

ABSTRACT

Title of Dissertation:

RADIATION CHEMISTRY IN
PRESSURIZED WATER NUCLEAR
REACTORS: H₂ GENERATION BY
¹⁰B(n,α)⁷Li, AND THE REACTION OF
BORATE WITH ·OH

Steven James Guerin, Doctor of
Philosophy, 2023

Dissertation directed by:

Professor Mohamad Al-Sheikhly,
Department of Materials Science
and Engineering,
University of Maryland, College Park

Nuclear power plants (NPPs) are complex engineering systems, with malfunctions having enormous potential to lead to widespread and extreme impacts on society and the environment as a whole. Their safe operation depends on a multitude of factors such as intelligent planning, proper design, quality components, high-level safety operations, and economic viability. Due to requiring high temperature and high pressure of an NPP's cooling fluid, one of the main concerns for further developing safe operating conditions and evaluating component lifetimes is improving our understanding on the issue of corrosion in nuclear systems. In the U.S., all commercially operated Pressurized Water nuclear Reactors (PWRs) are light-water reactors wherein their coolant waters can reach temperatures up to 350 °C. According to a report in 2005 in association with the U.S. Federal Highway Administration, an annual cost of \$4.2 billion was directly attributed to corrosion in NPPs in 1998, out of a total \$6.9 billion in the electrical utilities industry (Koch, et al., 2005).

Boron is added into commercial PWR primary water in the form of boric acid as a soluble chemical neutron “shim” in order to compensate for fuel burnup and allow smooth long-term reactivity control. After a boron nucleus captures a thermal neutron and becomes unstable, the energy of the recoil ions resulting from its fission accounts for up to 33 % of the total dose to the primary water. This event is an important source for H₂ and corrosive H₂O₂, so its product yields must be accurately included in models of the cooling water radiation chemistry.

H₂ produced in water from the $^{10}\text{B}(n,\alpha)^7\text{Li}$ fission reaction has been measured up to 300 °C to aid in quantification of the corrosive H₂O₂ from the same reaction. Thermal energy neutrons from the Rhode Island Nuclear Science Center 2 MW reactor interacted with boric acid contained in N₂O-saturated water in temperature-controlled high-pressure cells made from tubing of either titanium or zirconium alloy. After exposure for a minimum of one hour, the solution samples were extracted and sparged with argon. The H₂ entrained by the sparging gas was sampled with a small mass spectrometer. A small amount of sodium was included in the boric acid solution so that after sparging, samples could be collected for ^{24}Na activation measurements in a gamma spectrometer to determine the neutron exposure and thus the total energy deposited in solution. The G-value (μmol/J) for H₂ production was obtained for water at a pressure of 25 MPa, over a temperature range from 20 °C to 300 °C. These results have been complemented with Monte Carlo N-Particle® (MCNP®) simulations in collaboration with the National Institute of Standards and Technology, and have been compared with previous experimental results at room temperature and simulated results up to 350 °C.

Additionally, boric acid has thus far been accepted as a chemically nondisruptive additive, as it was confirmed long ago to have extremely low reactivity with the two main reactive species produced in reactor primary water by radiolysis, the solvated aqueous electron and the hydroxyl

radical (e_{aq}^- and $\cdot\text{OH}$). However, at the Electric Power Research Institute standard desired pH of 7.3 and the operational temperature of 350 °C, approximately 22% of the boron added in PWR primary water exists in the chemical form of the conjugate base, borate, not boric acid. Although borate was previously confirmed to have no appreciable reactions with e_{aq}^- , it was not adequately studied for reactions with $\cdot\text{OH}$ prior to this work.

We have observed a clearly apparent reaction between borate and $\cdot\text{OH}$. Current chemistry models are completely ignorant on both the existence of the resultant species and its reactions. The chemical reaction of $B(\text{OH})_4^-$ (borate) with $\cdot\text{OH}$ along with cross-reactions of the product species have been studied up to 200 °C to determine those reactions' rate constants and the products' spectra. The University of Notre Dame Radiation Laboratory's 8 MeV electron linear accelerator (LINAC) was configured to perform pulse radiolysis with pulse widths between 4ns to 20ns providing doses between 5.5 Gy and 62 Gy. High-energy electrons from the LINAC interact with the borated solution which has been N_2O -saturated and is continuously flowed through a 316 stainless-steel optical cell. The cell temperature was adjusted by resistive-heating silicon cartridges, and pressure was controlled by two syringe pumps to prevent boiling. The cell had two fused silica windows for transmitting light from a xenon arc lamp through the solution and out to a multichromatic spectrophotometer system. Time-resolved spectral data was obtained over nano- and micro-second timeframes, for wavelengths ranging from the deep UV and into the infrared spectrum (250 nm to 820 nm). The reaction rates and products' spectra were then obtained by analyzing the data using computational aids, namely IGOR Pro by Wavemetrics and KinTek Explorer by KinTek Corp. The product species of the reaction between borate and $\cdot\text{OH}$ is conjectured to be $\cdot\text{BO}(\text{OH})_3^-$, on the basis of *ab initio* calculations, which likely reacts with boric acid or borate to form a polymer radical.

RADIATION CHEMISTRY IN PRESSURIZED WATER NUCLEAR REACTORS:
H₂ GENERATION BY $^{10}\text{B}(n,\alpha)^7\text{Li}$, AND THE REACTION OF BORATE WITH $\cdot\text{OH}$

by

Steven James Guerin

Dissertation submitted to the Faculty of the Graduate School of the
University of Maryland, College Park, in partial fulfillment
of the requirements for the degree of
Doctor of Philosophy
2023

Advisory Committee:

Professor Mohamad I. Al-Sheikhly, Chair
Professor F. Patrick McCluskey, Dean's Representative
Professor David M. Bartels, co-advisor
Professor Lourdes G. Salamanca-Riba
Professor Isabel K. Lloyd

© Copyright by
Steven James Guerin
2023

Dedication

This work is dedicated to my parents **Kevin and Stacy Guerin**, for immortalizing the legacy of their supreme parentage in the quality of the lives of their three children. I am incapable of expressing the depths of my admiration in how you raised us all, or the heights of my pride in the man I have become through the support you've always given me.
I love you both.

And to my siblings **Nicholas Guerin** and **Katherine Archer** for their boundless encouragement, exceptional tenacity providing a contumelious coexistence as only siblings can, and our shared love. The ever-growing success you both have achieved fills me with joyful exhilaration. Nick, your bravery to embrace new experiences and brash determination in all pursuits has always inspired me with the fortitude to seek out and reach greater accomplishments. Katie, your elegant concern to all people and overflowing enthusiasm in your own endeavors always remain a striking influence to my outlook on life's many experiences.
I would not ask for a better brother or a better sister.

And to my timeless friend **Andrew Madura** for his indispensable camaraderie at the best of times and his steadfast alliance especially at the worst of times, throughout the entirety of both our lives. You're my best friend and I think of you as a brother.
Your genuine and your balanced outlook impressed, always.

And last, but certainly not least, to **Dr. Mark Driscoll** for his wise council throughout, and his untiring rallying of my best efforts. His doubtless endorsement carried me into the MSE Ph.D. program at UMD, through it, and beyond – without him I would not have achieved such noble recognition from academia, nor from myself.

Acknowledgements

I wish to express my profound gratitude and devotion to my advisor **Professor Mohamad I. Al-Sheikhly** at the Materials Science and Engineering Department for his leadership, kind-hearted encouragement, and endless support throughout this work's entirety. His advice and passion were a driving force before, through, and out of many tough times I experienced during my academic career path at the University of Maryland. It is thanks to his prolific success as both a teacher and a researcher that I have learned so much. My achievements here are a reflection of his dedication and perseverance as much as they are of my own.

No less so would I like to convey my deep and sincere appreciation to **Dr. David M. Bartels** at the Radiation Laboratory of the University of Notre Dame for his effective guidance and professional instruction, and for his extensive intellectual support. Performing my research entailed here would not have been feasible without his vast and comprehensive knowledge on water radiation chemistry always providing a solid foundation upon which to build. The opportunities I foresee in furthering my scientific interests are in many ways thanks to him.

I profoundly thank **Professor Lourdes G. Salamanca-Riba** and **Professor Isabel K. Lloyd** for both being part of my committee. I was taught by Prof. Salamanca-Riba in one of the four core MSE courses, as well as a theory and a lab course on transmission electron microscopy; I learned very much thanks to her exceptional teaching and careful training. I also enjoyed an elective class taught by Prof. Lloyd on additive manufacturing; her lectures were always insightful and stimulating, and they remain a fond experience. And I respectfully thank my other committee member **Professor F. Patrick McCluskey** for accepting the important role of Dean's Representative. I thank all of my committee members for their commitment to my career as a Ph.D. graduate student.

I offer tremendous thanks to **Dr. Alan Thompson** of the Neutron Physics Group at the National Institute of Standards and Technology for his contributions by providing many MCNP® simulations and calculations to give insight on the multitude of concerning aspects of this experiment, such as the dose contribution due to the compositions of the flow cells' tubing in the predicted radiation spectrum, as well as his overall subject matter expertise on radiation and its effects on matter.

I earnestly thank the staff at the Rhode Island Nuclear Science Center for their limitless willingness to provide me with assistance in any and all aspects necessary for the completion of my research at the facility. I thank the Director **Dr. Cameron Goodwin** for her vast delegation efforts and her continual support by her knowledge on the facility components as well as providing critical information well after my time at the facility was spent; I thank the principle Reactor Supervisor **Matthew Marrapese** for his unwavering cooperation and his enthusiasm in supplying any and all additional provisional materials I requested; and I thank the Assistant Director for Radiation and Reactor Safety **Sangho Nam** for his endless patience and his contributions by performing all of the gamma spectroscopy measurements we required as well as his expertise in this system's technical capabilities.

I thank as well the staff at the Radiation Lab at UND for their hard work and cooperation. I thank **Kiva Ford** at the Scientific Glassblowing Shop for his admirable craftsmanship in supplying us with the glass sparging apparatus; and I thank **Joe Admave** at the Machine Shop for his prompt services provided on the stainless steel optical flow cell.

I also thank my co-worker **Aiysha Ashfaq** for her long hours of dedication collaborating as a lab mate and friend. Her efforts working together with me in learning to control the mass

spectrometer and assessing its sufficient operation enabled the pursuit of much of this work, and will always be appreciated.

This work was supported by the Division of Chemical Sciences, Geosciences, and Biosciences, Office of Basic Energy Sciences of the U.S. Department of Energy through award DE-FC02-04ER15533.

Table of Contents

1 Introduction	1
1.1 Corrosion.....	1
1.1.1 Dry Corrosion	2
1.1.2 Wet Corrosion.....	2
1.1.3 Corrosion Rate varying with different conditions	2
1.1.4 Electrochemical Nature of Corrosion	3
1.1.5 Passivity	4
1.1.6 Corrosion Thermodynamics.....	5
1.1.7 Effect of the potential on activation energy	6
1.1.8 Corrosion process polarization	9
1.1.8.1 Activation polarization.....	11
1.1.8.2 Concentration polarization.....	12
1.1.8.3 Combined/Mixed Polarization (activation and concentration).....	14
1.2 Radiation	15
1.3 Neutron Scattering	21
1.3.1 Dosimetry by the Cadmium Ratio and Radiochromic Films.....	24
1.4 Linear Energy Transfer (LET).....	26
1.4.1 Low LET.....	26
1.4.1.1 Gamma/Photons.....	27
1.4.1.2 High energy electrons.....	30
1.4.2 High LET	31
1.4.2.1 Alpha Particles.....	32
1.5 Pulse Radiolysis.....	34
1.5.1 Transient Absorption Spectrophotometry	35
1.5.2 Ionic Strength Effect	37
1.6 Nuclear Power Plants (NPPs)	38
1.6.1 Pressurized Water nuclear Reactors (PWRs).....	39
1.6.2 Radiation-Induced Corrosion in PWRs	40

1.6.3 Radiolysis in PWRs	42
1.7 Boron in PWRs	43
1.7.1 Boron as a Neutron Shim	43
1.7.2 Boric Acid as an Inert Chemical Additive	47
1.7.2.1 Hydroxyl radical reaction with Boric Acid	48
1.7.2.2 Aqueous electron Reaction with Boric Acid	48
1.7.3 Borate in PWRs	50
1.7.4 Properties of Borate Solutions over Temperature	50
1.8 Other Considerations of Reactor Chemistry	58
1.8.1 Axial Offset Anomaly	58
1.8.2 Critical Hydrogen Concentration	63
1.8.3 Hydrogen embrittlement	65
1.8.4 Hydrated electron bimolecular reaction	67
1.9 Boron Neutron Capture Therapy	71
1.10 Previous Works on G(H ₂) for ¹⁰ B(n,α) ⁷ Li	74
1.10.1 Early work	74
1.10.2 Recent simulation work	76
1.10.3 Dietz et al., 2021	78
2 The Objective of This Work	83
3 Experimental Facilities, Materials, and Equipment	85
3.1 Hydrogen generation by ¹⁰ B(n,α) ⁷ Li	86
3.1.1 RINSC	86
3.1.1.1 Foils and gamma measurements	88
3.1.1.2 Power Trend Monitoring	89
3.1.2 System for Solution Containment & Transport	90
3.1.2.1 Irradiation Cells	90
3.1.2.2 Flow System	93
3.2 Borate reaction with Hydroxyl radical	95
3.2.1 NDRL	96
3.2.2 High-Pressure High-Temperature Flow System	97
3.2.3 Spectrometer System	99

4 Solution Selection.....	102
4.1 Solutions for Evaluating Hydrogen generation by $^{10}\text{B}(n,\alpha)^7\text{Li}$	102
4.1.1 RGA Calibration Solution.....	103
4.1.2 Gamma Background Solution.....	103
4.1.3 Boronated Experiment Solution.....	104
4.1.3.1 Boron-10 isotope concentration	105
4.1.3.2 Na_2CO_3 scavenger	105
4.1.3.3 NaNO_2 scavenger.....	106
4.1.3.4 LiOH	107
4.2 Solutions for Evaluating Borate Reaction with $\cdot\text{OH}$ Radical.....	107
4.2.1 Electron dosimetry	108
4.2.2 Discovery of a reaction in borax buffer solution	108
4.2.3 Identification of initial reactants	109
4.2.4 Attempts to evaluate the new radical's REDOX Potential	109
4.2.5 Reaction Evaluations	111
4.2.6 Searching for Ionic Strength Effect	111
5 Experimental Methods for Evaluating $^{10}\text{B}(n,\alpha)^7\text{Li}$ radiolysis product yields.....	112
5.1 Solution transport and analysis	112
5.2 RGA Signal Analysis by MATLAB.....	113
5.3 RGA Calibration	114
5.4 Boron Experiment.....	115
5.5 Gamma.....	116
5.6 Corrosion.....	118
5.7 Heater & LabVIEW PID program.....	119
5.8 RGA Mass Spectrometer	121
5.9 Sodium Activation	122
5.10 The G-value for H_2 by $^{10}\text{B}(n,\alpha)^7\text{Li}$	124
5.11 Predictive Simulations by MCNP.....	125

6 Experimental Methods for Evaluating Borate Reaction with •OH Radical	127
6.1 Electron Dosimetry	127
6.2 Path Length for Irradiated Solution Volume	128
6.3 Kinetic Data Analysis Methods using IGOR and KinTek	130
6.3.1 IGOR Pro	130
6.3.1.1 Borate radical first order reaction with •OH.....	130
6.3.2 KinTek Explorer	131
6.3.2.1 Kinetic Mechanism.....	132
6.3.2.2 Global fitting of time-resolved spectra via SVD.....	134
7 Results and Discussion.....	137
7.1 Hydrogen generation by $^{10}\text{B}(n,\alpha)^7\text{Li}$	137
7.1.1 Calibration, RGA precision	137
7.1.1.1 Change in calibration proportionality constant over time	140
7.1.2 Temperature Control Precision	141
7.1.3 Temperature Measurement Accuracy	142
7.1.4 Extreme Corrosion of Zirconium Alloy Cell.....	143
7.1.5 Corrosion of Titanium Cell at Above 200 °C	144
7.1.6 Gamma.....	146
7.1.6.1 MCNP Simulations for Gamma Background.....	147
7.1.6.2 Gamma Background experimental evaluation.....	148
7.1.7 Reactor Stability based on Power Trend readings	151
7.1.8 Power Trend vs Sodium Activation.....	154
7.1.9 Boron Shielding Effect	158
7.1.10 Room Temperature – effect of LiOH addition (pH).....	162
7.1.11 Error Analysis	164
7.1.12 G-value for H ₂	166
7.1.13 Comparing to Previous Works.....	167
7.2 General evaluation of Borate reaction with Hydroxyl radical.....	171
7.2.1 Discovering a mystery reaction taking place	172
7.2.2 Identifying initial reactants	174

7.2.3 Attempts to evaluate the new radical's REDOX Potential	176
7.2.4 <i>Ab initio</i> calculations for reactions of interest	177
7.2.5 Ionic Strength Effect Study.....	177
7.2.6 Calculating the pH of the two main borate solutions.....	182
7.3 Evaluation of Borate's Observed Reaction with $\cdot\text{OH}$	185
7.3.1 Initial Fits of the Borate Radical's Growth using IGOR	185
7.3.2 The Borate Radical's Growth and Decay, Fit using KinTek Explorer	189
8 Conclusions	204
9 Contribution to Science	207
9.1 H_2 generation by $^{10}\text{B}(\text{n},\alpha)^7\text{Li}$ for Reactor Chemistry Models	207
9.2 Critical Hydrogen Concentration.....	208
9.3 Reaction of Borate with $\cdot\text{OH}$ for Reactor Chemistry Models	208
9.4 Contribution to BNCT Research from H_2 generation by $^{10}\text{B}(\text{n},\alpha)^7\text{Li}$	210
9.5 Interference with N_2 for Gamma Dosimetry by Isopropyl.....	210
9.6 Interference with H_2 Measurements by Corrosion of Cell Materials	211
10 Future work	212
10.1 $^{10}\text{B}(\text{n},\alpha)^7\text{Li}$ Chemistry	212
10.2 Borate Kinetics	212

List of Abbreviations

AECL	Atomic Energy of Canada Limited
AIDE	Adsorption-Induced Dislocation Emission
AOA	Axial Offset Anomaly
BNCT	Boron Neutron Capture Therapy
BPR	Back Pressure Regulator
BWR	Boiling Water nuclear Reactor
CHC	Critical Hydrogen Concentration
DI	Deionized
EPRI	Electric Power Research Institute
G-value	radiation chemical yield
GWD	GigaWatt Days
HD	Hydrogen Degradation
HEDE	Hydrogen -Enhanced Decohesion
HELP	Hydrogen-Enhanced Localized Plasticity
HPGe	High Purity Germanium
IASCC	Irradiation-Assisted Stress Corrosion Cracking
ICP-OES	Inductively-Coupled Plasma Optical Emissions Spectrometer
LET	Linear Energy Transfer
LINAC	Linear Accelerator
MCNP®	Monte Carlo N-Particle®
MTU	Metric Ton of Uranium
NDRL	University of Notre Dame Radiation Laboratory
NIF	Neutron Imaging Facility
NIST	National Institute of Standards and Technology
NPP	Nuclear Power Plant
PID	Proportional-Integral-Derivative
PWR	Pressurized Water nuclear Reactor
RCF	Radiochromic film

REDOX	Reduction-Oxidation
RGA	Residual Gas Analyzer
RINSC	Rhode Island Nuclear Science Center
RSICC	Radiation Safety Informational Computational Center
SCC	Stress Corrosion Cracking
SHE	Standard Hydrogen Electrode
SNB	Sub-cooled Nucleation Boiling
SVD	Singular Value Decomposition
TOC	Total Organic Carbon
UHP	Ultra High Purity
VARIAC	Variable AC transformer

1 Introduction

Guidelines regulating the chemistry within nuclear reactor coolant are primarily concerned with 1) assuring the integrity of the primary system pressure boundary, 2) assuring integrity of the fuel rod cladding and achievement of design fuel performance, and 3) minimizing out-of-core radiation fields (EPRI, 1999). To adequately evaluate safe operating conditions and component lifetimes, one must understand: the process of degradation by corrosion both generally and in these specific environments, how radiation effects are extremely relevant as the source of many chemical species which alter/enhance the corrosion process, what provisional measures are engaged to control the nuclear reactivity and how they likewise will affect the chemistry, and the experimental methods regularly utilized to research the relevant reactions.

1.1 Corrosion

As mentioned above, it is critical for nuclear power plant (NPP) operation to adequately understand and work to mitigate corrosive reactions. Corrosion is an interfacial phenomenon, characterized by the deterioration of a material due to reactions with its environment through the activation of corrosive agents. Though most commonly associated with metals, as is the concern here, it should still be made clear that nonmetals such as ceramics, plastics, and rubbers can deteriorate under certain conditions, as practically all environments are corrosive to some degree (Fontana, 2005). Between the many different recognized types of corrosion of metallic materials, one of the ways to generally distinguish them is by classification into two types: dry corrosion and wet corrosion.

1.1.1 Dry Corrosion

Also referred to also as “hot” corrosion, dry corrosion occurs in environments devoid of any liquid (as in, with a dry gas) wherein a metal reacts directly with gaseous atoms. This is an accelerated type of oxidation, and is associated with metals heated to high temperatures (over 200 °C) (Eliaz & Latanision, 2007; Hancock, 1987). Common environments include gas turbines, boilers, power generation equipment, internal combustion engines, and industrial waste incinerators (Sidhu, et al., 2005).

1.1.2 Wet Corrosion

Wet corrosion occurs in the presence of a liquid electrolyte, such as an aqueous solution. It typically occurs as an electrochemical reaction between components in a system, so can be described as an analog to the electrochemical cell: an anodic reaction occurs on one metallic electrode (anode), a cathodic reaction occurs on another metallic electrode (cathode), both of which are immersed in an electrolyte that acts as an ionic conductor between the electrodes, and an electric potential along a conductive path between the electrodes drives the two reactions.

1.1.3 Corrosion Rate varying with different conditions

Corrosion, as a continual process, can be assigned a rate. In common literature, the corrosion rate is defined as “the amount of metal oxidized by unit of metallic surface over a certain period of time” (Andrade & Alonso, 2001). This rate can be expressed in units of millimeters per year (mm/yr) of growth of the oxide layer, and many models used to predict material failure have placed much significance on the corrosion rate (George, et al., 2004; Sidhu, et al., 2005; Peng & Zeng, 2015). The corrosion rate reflects the aggressiveness of an environment for deteriorating materials, and can be affected by the varying of conditions such as the temperature, pH, presence

of inhibitors, degree of passivity, concentration of reactive agents, electrode potential, an imposed driving electrical voltage, and so on.

1.1.4 Electrochemical Nature of Corrosion

Purely chemical reactions involve adding or removing elements from a chemical species without any change in their number of valence electrons, whereas electrochemical reactions involve chemical reactions where the valence is changed for at least one species and they are said to be oxidized (electrons removed) or reduced (electrons gained) (Kelly, et al., 2002). Again, wet corrosion can be considered a physical analog to the electrochemical cell, as it is driven by an electric potential difference between a metal and “redox” species (reactants that can be reduced or oxidized) within an electrolyte. The anodic reaction involves oxidation, where a metal atom releases at least one electron into the bulk conductive matrix, and the metal ion then dissolves into the electrolyte. The cathodic reaction involves reduction, where the free electron is assimilated by other species present in the electrolyte which will then become more reactive. In the presence of oxygen, the likely product from electron uptake into the electrolyte will be hydroxide (OH^-). This OH^- will react with the dissolved metal ion to form metal hydroxides that, due to their low solubility, will precipitate onto the metal surface as an oxide layer (Perez, 2004). This can be illustrated by the degradation of a divalent metal (M) in water containing O_2 , shown in Figure 1.

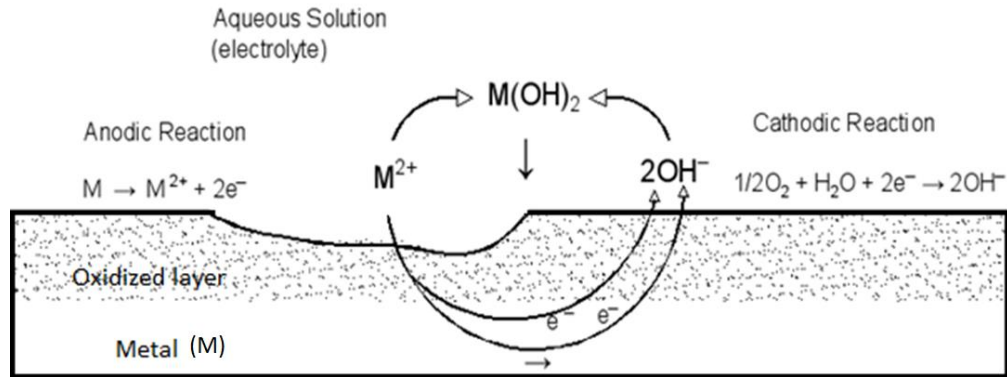


Figure 1. Schematic displaying corrosion of metal (M) in the presence of oxygen (figure adapted from (Bardal, 2003))

The overall rate of corrosion depends on the rates of both the forward anodic reactions and the reverse cathodic reactions, which in turn are limited both by the diffusion of the electrons and the oxidizing ions through the protective oxide layer and by the availability of redox species.

1.1.5 Passivity

Passivity involves the tendency of certain metals to lose chemical reactivity while they undergo electrochemical reduction in the presence of oxygen within the electrolyte, thus lowering the corrosion rate, due to metal oxide products from the reaction building up on the interface to form a dense, continuous, solid film with low ionic conductivity and low solubility, which functions as a barrier to the transport of reactants (oxygen and metal ions) (Fontana, 2005; Bardal, 2003; Was & Allen, 2019). As will be shown in more detail in the following sections, temperature and the concentrations of electrochemical reactants can alter the activation state of a metal, where some can transition from the immune and active (corroding) potentials into a passive state (Fontana, 2005). Typically, film growth can be promoted when the metal surface has greater access to oxygen from either high concentration in the electrolyte or strong convection, while growth can be hindered – or the film perhaps broken down – by the lack of oxygen (Bardal, 2003). However, a full understanding of the mechanisms involved in growth and breakdown of passivation layers

is incomplete for most cases. For the growth, it is difficult to differentiate between oxygen diffusion versus electrical conductivity in oxide films as to which is the rate limiting factor, since measuring potential across the oxide film as it develops without affecting the oxidation itself is problematic (Cox, 2005). Theories on the breakdown propose it could be a mechanical mechanism whereby changes in the morphology of the film then lead either to dielectric breakdown after its thickness is reduced below a critical level or the re-exposure of the substrate to the corrosive environment after cracking results from ever-increasing stress concentrations due to a mismatch in the crystallographic structure onto the metal (Tang & Ballarini, 2011; Bardal, 2003). Regardless, it is well known that a critical point during growth of oxide layers can be reached wherein a kinetic transition causes the oxide layer to lose its protective properties resulting in the corrosion rate increasing and returning to the kinetics for the bare metal (Ensor, et al., 2022). After this change in kinetics, referred to as the oxide transition, new oxide will continue to form either in a stable manner to become protective once more and breakdown again in a cyclic manner, or it will form in an unstable (e.g. non-planar) manner without providing any passivation effect and the metal then experiences “breakaway” corrosion (Ensor, et al., 2022) as it progresses at the maximum rate as the bare-metal kinetics do allow.

1.1.6 Corrosion Thermodynamics

A reconsideration of corrosion from the standpoint of thermodynamics can offer a better understanding of the driving forces behind these reactions, specifically the standard potentials for the anodic and cathodic reactions. For an electrochemical reaction to occur spontaneously, the change in the Gibbs free energy, ΔG , must be negative; if a reaction would change the state of a system to a state with a higher free energy ($\Delta G > 0$) then the reaction will not occur unless further energy is added to the system (not spontaneous) for it to achieve that state; and if there is no

difference in the free energy when the system is brought from one state to another ($\Delta G = 0$) then those states are in equilibrium. Therefore, it is understood that the Gibbs free energy is the energy that drives the spontaneous reactions inherent to the corrosion process, where ΔG can be calculated from the Faraday equation:

$$\Delta G = -nFE \quad (1)$$

where n is the number of electrons transferred (equiv/mol), F is the Faraday constant (C/equiv), and E is the electrochemical cell potential energy. This indicates that the free energy of corrosion depends mainly on the cell's potential. The potential of an electrochemical system E (in volts) is calculated by the Nernst equation:

$$E = E_0 + 2.3 \frac{RT}{nF} \log \frac{a_{ox}}{a_{red}} \quad (2)$$

where E_0 is the standard potential (V) of the half-cell at equilibrium, R is the ideal gas constant (J mol⁻¹ K⁻¹), T is temperature in Kelvin, and a_{ox} and a_{red} are the activities (alternatively, the concentrations) of the oxidizing and reducing species, respectively (Fontana, 2005). By this equation, the cell potential is determined to be positive when the concentration of oxidized species is higher than that of the reduced species, (*i.e.*, when the system has spontaneously provided more electrons than it consumed).

1.1.7 Effect of the potential on activation energy

Consider a generalized electrochemical reaction, where an oxidized species O can be reduced to R by accepting n electrons:



By representing the distance of the solvated metal ion from the interface as a reaction coordinate, depictions of the Gibbs free energy profile are shown below. The curves intersect at the transition state between the reactant/product states, and the height of the barrier between states determines the relative rates of the forward (reduction) and reverse (oxidation) rates (Bard & Faulkner, 2001). At equilibrium, energy of both states is the same and the requirements to cross the barrier in either direction are equivalent (Figure 2).

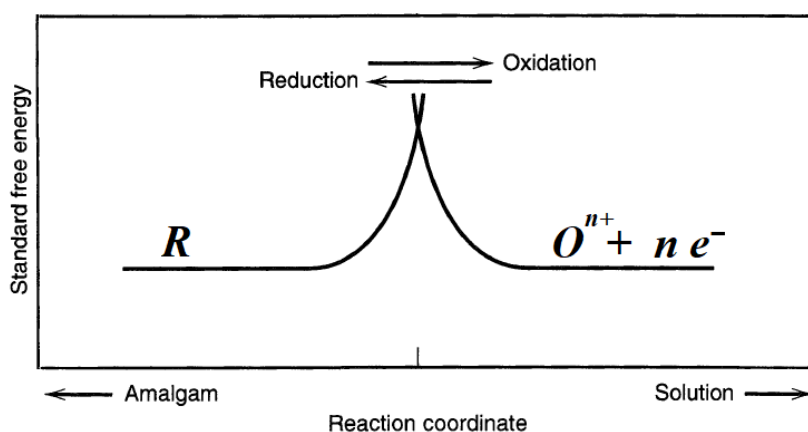


Figure 2. A system state at a potential corresponding to an equilibrium (adapted from (Bard & Faulkner, 2001))

By changing the potential to a more positive value (Figure 3), essentially the energy of the “reactant” electron is lowered (Bard & Faulkner, 2001) and therefore the more preferential configuration alters, driving up the rate of the backward reaction. This will result in a system with a higher concentration of oxidized species, in agreement with Equation (2).

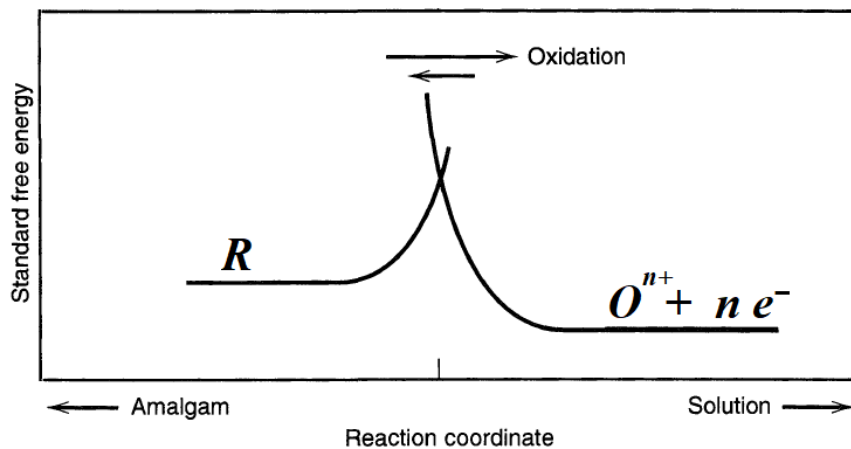


Figure 3. A system state at a more positive potential than the equilibrium (adapted from (Bard & Faulkner, 2001))

Alternatively, changing the potential to a more negative value (Figure 4) will increase the energy of the electron, and the barrier for reduction becomes less than the barrier for oxidation (Bard & Faulkner, 2001). Thus the rate of the forward reaction is increased, and the system shifts to a higher concentration of reduced species, as Equation (2) implies.

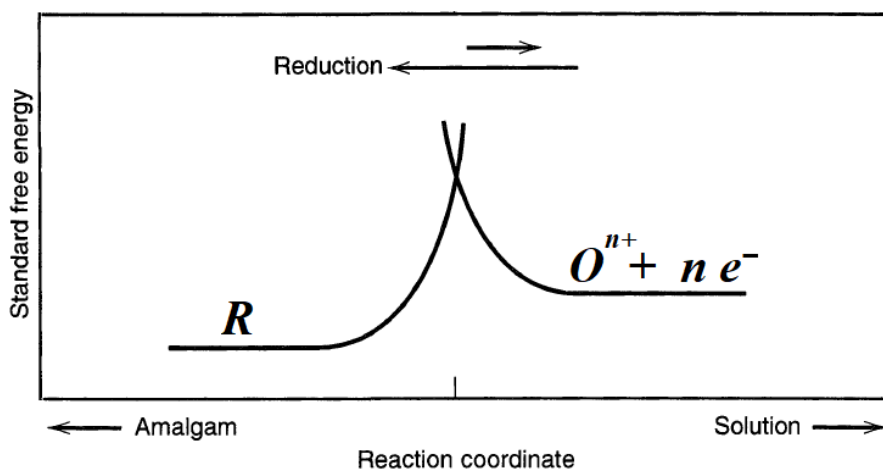


Figure 4. A system state at a more positive potential than the equilibrium (adapted from (Bard & Faulkner, 2001))

Reactions occurring in solutions or gas phases are called homogeneous reactions since they occur throughout the medium and at uniform rates, whereas these electrochemical reactions in

corrosive systems occurring at electrodes are called heterogeneous reactions and are usually more complex to interpret (Bard & Faulkner, 2001). The rates of the forward and backward reactions can be derived in terms of the current density from Faraday's Law (Fontana, 2005), and defined in terms of the conditions near the anode and cathode (Bard & Faulkner, 2001) as such:

$$r_f = \frac{i_c}{nF} = k_f C_{Red}(0, t) \quad (4)$$

$$r_b = \frac{i_a}{nF} = k_b C_{Ox}(0, t) \quad (5)$$

where r_f, r_b are the rates and k_f, k_b are the rate constants for the forward and backward reactions, respectively; i_c, i_a are the current densities at the cathode and anode; and C_{Red}, C_{Ox} are the concentrations of the reduced and oxidized species, expressed as a function of the distance x from the interface at time t , so the concentration at the interface is $C(0, t)$.

1.1.8 Corrosion process polarization

At equilibrium, the cathodic and anodic rates are equal, by definition. Similarly, the anodic and cathodic reactions' currents are equal and opposite and so there is no net current.

$$r_f = r_b = r_{eq} \qquad i_a = -i_c = i_0$$

$$r_{eq} = \frac{i_0}{nF} \quad (6)$$

where i_0 is referred to as the "exchange" current density as a convenient way to express the rate of oxidation and reduction at an electrode at equilibrium (Fontana, 2005). The exchange current density depends greatly on an electrode's reaction and material, the nature of the electrolyte, the temperature of the system, and concentrations of active species (Bardal, 2003), and so a change in any of these conditions can cause an imbalance in the rates and thus a shift in the electrochemical

cell potential. Such a shift is referred to as a polarization and the extent of this is measured in terms of the overpotential with respect to the equilibrium potential (Bard & Faulkner, 2001) as:

$$\eta = E - E_{eq} \quad (7)$$

This change in potential, as has been discussed above, will be accompanied by a net current in the direction of one of the reactions. There will always be some resistance acting against the current as it flows across the corrosion interface (Bardal, 2003), originating from limitations in the rates of the processes governing the electrode's overall reaction rate: mass transfer, electron transfer, chemical reactions preceding/following electron transfer, and other surface reactions (Bard & Faulkner, 2001) (as depicted in Figure 5). The two main types of electrochemical polarization are activation polarization and concentration polarization (Fontana, 2005).

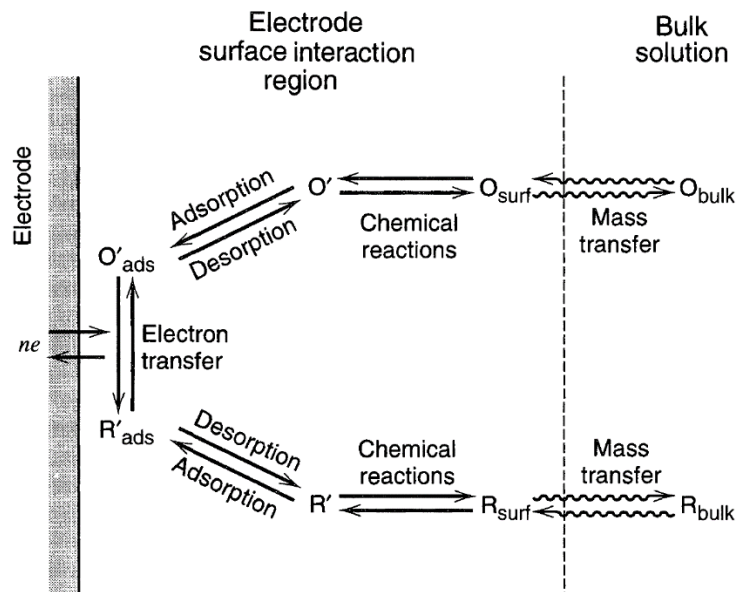
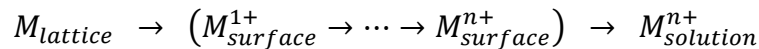


Figure 5. Pathway of a general electrode reaction (adapted from (Bard & Faulkner, 2001))

1.1.8.1 Activation polarization

An activation polarization corresponds to a situation where the corrosion is limited by the resistance against the reaction itself at the metal-electrolyte interface, due to species needing to overcome the energy barrier for transferring to a new state (Bardal, 2003). Metal ions must go through a sequence of oxidation reaction steps at the metal-electrolyte interface of the anode before dissolving into the solution bulk, written for a general case as:



where the number of successive electron losses depends on the metal (Perez, 2004). A simplified depiction of this is illustrated in Figure 6 for a hydrogen-evolution reaction on zinc during corrosion in an acidic solution.

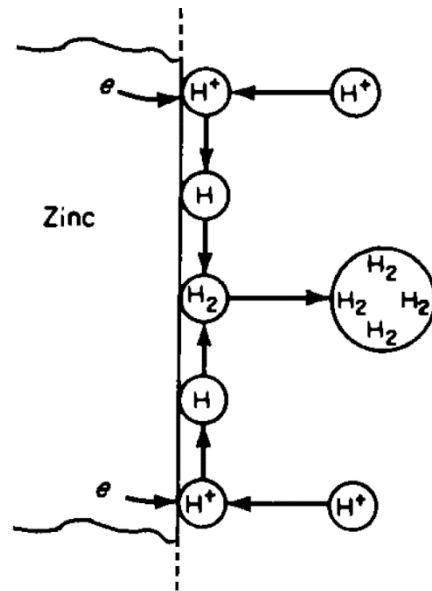


Figure 6. Schematic of hydrogen-reduction reaction on a zinc surface (adapted from (Fontana, 2005))

A reducible species must first attach (adsorb) on the metal-electrolyte interface, then an electron transfer occurs from the conductive metal bulk, the species undergoes a reduction reaction, after which it may then react with other species before removing and diffusing into the

solution bulk (Fontana, 2005). Any of these may act as the rate-determining step, depending on the conditions in the environment.

The overpotential is defined in terms of the current density (Fontana, 2005) and the rates for the electrochemical reaction at the electrodes (Bard & Faulkner, 2001) by the Tafel equation

$$\eta_{Act} = \pm\beta \log \frac{i}{i_0} \quad \text{where} \quad \beta = 2.3 \frac{RT}{\alpha nF}$$

At the anode:

$$\eta_{Act} = \beta \log \frac{i_a}{i_0} = 2.3 \frac{RT}{\alpha nF} \log \frac{r_b}{r_{eq}}$$

At the cathode:

$$\eta_{Act} = -\beta \log \frac{i_c}{i_0} = -2.3 \frac{RT}{\alpha nF} \log \frac{r_f}{r_{eq}}$$

where β is known as the Tafel constant, for which α (called the symmetry coefficient) is determined by the shape of the rate-controlling energy barriers.

For a system with a typical β of 0.1 V, a change in the oxidation and reduction reaction rates corresponding to a standard hydrogen electrode (SHE) change by an order of magnitude will require merely a 100 mV change in the overpotential (Fontana, 2005), ergo the rate of an electrochemical reaction is very sensitive to small changes in electrode potential.

1.1.8.2 Concentration polarization

A concentration polarization corresponds to a situation where the corrosion is limited by the mass transport properties of the electrolyte governing the diffusion of species between the bulk solution and the electrode surface interaction region (as depicted in Figure 7), which can lead to either a shortage of reactants at the surface or a buildup of reaction products in the electrolyte (Bardal, 2003). For the case of a metal submerged in an aerated solution, where the reduction of oxygen is made significant as it is unique to corrosive environments in nature, a high enough

reaction rate for oxygen can lead to a shortage of this reducing species due to a limiting diffusion rate (Bardal, 2003).

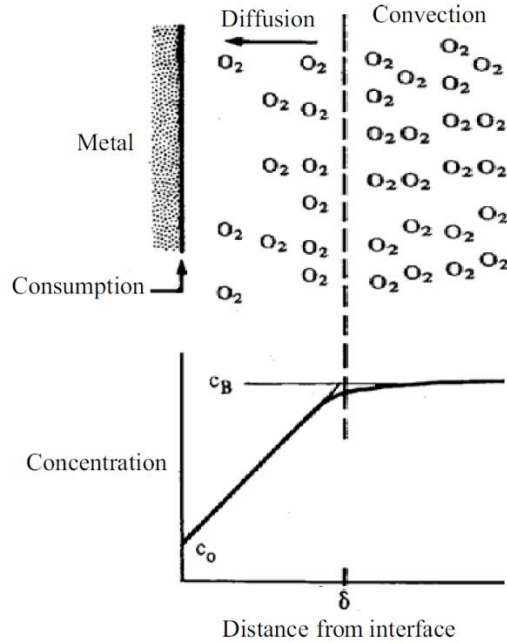


Figure 7. Oxygen concentration as a function of distance from the metal-electrolyte interface (adapted from (Bardal, 2003))

A simplified depiction of this situation is illustrated in Figure 7, where beyond a certain distance δ out from the interface (the diffusion layer thickness) the concentration is effectively constant, while at shorter distances the concentration of unreduced oxygen is determined by diffusion (Bardal, 2003), following Fick's law:

$$\frac{dn}{dt} = -D \frac{dc}{dx} \quad (8)$$

where $\frac{dn}{dt}$ is the mass transport rate in the x-direction ($\text{mol cm}^{-2} \text{s}^{-1}$), D is the diffusion coefficient ($\text{cm}^2 \text{s}^{-1}$), and c is the concentration (mol cm^{-3}). The current density of oxygen reduction can then be expressed in general by applying Faraday's laws, and it can be expressed as the diffusion

limiting current density i_L for the case where the maximum transport rate and reaction rate are achieved and thus the concentration at the interface approaches zero:

$$i = DnF \frac{c_B - c_0}{\delta} \quad \text{where } c_0 \rightarrow 0 \text{ gives } i_L = DnF \frac{c_B}{\delta}$$

where c_B is the reducing species' concentration in the bulk and c_0 is the concentration at the interface. Combined with the Nernst equation, the overvoltage due solely to concentration polarization is:

$$\eta_{Conc} = 2.3 \frac{RT}{nF} \log \left(\frac{c_0}{c_B} \right) = 2.3 \frac{RT}{nF} \log \left(1 - \frac{i}{i_L} \right) \quad (9)$$

from the books by Fontana and by Bardal.

1.1.8.3 Combined/Mixed Polarization (activation and concentration)

Both activation polarization and concentration polarization are important for reduction reactions at the cathode where concentrations are low, particularly for the reducible species in the electrolyte, whereas for metal dissolution at the anode the concentration polarization can be neglected since there is a nearly unlimited supply of metal atoms for dissolution and so activation polarization dominates (Fontana, 2005; Bardal, 2003). The total overpotentials are sums of each type of overpotential in effect, and so become:

At the anode:

$$\eta_a = \eta_{Act}$$

$$\eta_a = 2.3 \frac{RT}{\alpha nF} \log \frac{i}{i_o}$$

At the cathode:

$$\eta_c = \eta_{Act} + \eta_{Conc}$$

$$\eta_c = -2.3 \frac{RT}{nF} \left[\frac{1}{\alpha} \log \left(\frac{i}{i_o} \right) - \log \left(1 - \frac{i}{i_L} \right) \right]$$

These equations present the best tools available for describing the electrode reaction kinetics using simple terms for well-defined physical constants and easily-determined variables

for particular systems, as all electrochemical corrosion processes are comprised of at least one anodic reaction and at least one cathodic reaction (Fontana, 2005; Bardal, 2003).

1.2 Radiation

It has been nearly 130 years since humanity began the earnest studying of radiation and exploitation of its effects after William Roentgen published his discovery of x-rays, though observations of natural radiation chemistry phenomena have been reported in the past as early as the poet Homer writing about lightning producing a sulfurous smell in the air (Roentgen, 1896; Zimbrick, 2002). Indeed, we are surrounded by radiation at every moment. This is visualized particularly well in simple Wilson cloud chambers which display the passage of ionizing radiation as mist-like trails of condensation directly visible to the eye, as in the cloud chamber on display in the Physics Building at Syracuse University in New York. Electromagnetic radiation heats our planet's atmosphere, provides an immense spectrum of colors for vision, and is the source driving photosynthesis as the main form of energy metabolism for life on Earth. And particles like protons, neutrons, and electrons are constantly being produced by spallation in our atmosphere as well as through the natural radioactive decay of unstable nuclides of certain elements, such as the popularly known uranium-238 atom. Radiation by particles or photons with high enough energy above a certain threshold are considered ionizing radiation since at such energies these particles can remove electrons from atoms they interact with while traversing a medium, and are generally differentiated as being either charged or uncharged. The unpaired electrons and positive ions in the bulk irradiated material resulting from such interactions will enact chemical reactions which would not have occurred without this involvement of radiation.

Radiation chemistry is the primary field investigating the effects of radiation on materials, and is distinguished from radiochemistry wherein radiation is used to generate new elements. There are many different types/classes of ionizing radiation and they are commonly characterized by which accelerated particle is irradiating the target and by the origin of the particle, e.g. proton, neutron, electron, alpha, beta, X-ray, and gamma. How the particle interacts with a material can vary widely since the exact nature of interaction is dependent on many factors such as the particle's charge and mass as well as the target material's state of matter, density, and temperature (Spinks & Woods, 1990). One part of this work is focused on elucidating certain effects of neutron radiation and more specifically the consequent radiation by heavy particles like alpha, while we also recognize gamma radiation as an additional contribution to the overall chemistry; and the other part of this research is focused on utilizing electron radiation to induce an enhanced state of chemistry for studying reactions of intrigue.

Neutrons are one of the two constituents of the atomic nucleus (the other being protons), lacking a charge and having a mass of 1.0087amu (slightly more than the proton), and when unbound from the atomic nucleus they typically are travelling at speeds with enough energy to break atomic bonds – which is the driving force behind nuclear fission and therefore the foundation of nuclear engineering as a field of study (Al-Sheikhly, 2017).

Electrons are found in the atomic orbit, having a negative unit charge and mass of 5.4858×10^{-4} amu, and can become unbound through several processes such as beta decay and secondary electron formation, or artificially by linear accelerators using high electric potentials to collect and accelerate packets of electrons at a target (Al-Sheikhly, 2017). Their small mass allows them to penetrate deeply into materials and their charge allows for more significant reactions than a neutron would exhibit thanks to prospective coulombic interactions.

An alpha particle is a form of highly energetic helium-2 nucleus, lacking its electrons. Possessing two positively charged protons and two neutrons gives it a relatively large mass and high charge, which causes these particles to be highly ionizing due to them rapidly transferring their energy when traversing a medium, therefore achieving low penetration ranges compared to other forms of radiation. They are commonly produced during decay of most larger radioactive nuclides, or can come from lower elements which have been made unstable through interactions with other particles.

The energy of a particle at rest and its relativistic total energy are defined in terms of its rest mass m_0 and its velocity v by:

$$E_0 = m_0c^2 \quad (10)$$

$$E = \frac{m_0c^2}{\sqrt{1 - \frac{v^2}{c^2}}} \quad (11)$$

and the particle's kinetic energy is defined as the difference between its total energy and its energy at rest, while we use an approximation for particles traveling at non-relativistic speeds:

$$K = E - E_0 = m_0c^2 \left(\frac{1}{\sqrt{1 - \frac{v^2}{c^2}}} - 1 \right) \quad (12)$$

$$\text{for } (v \ll c) \text{ we approximate } K = \frac{1}{2}m_0v^2 \quad (13)$$

where c is the speed of light in a vacuum (2.998×10^8 m/s) (Al-Sheikhly, 2017; NIST, 2019).

Photons are quanta of electromagnetic radiation, as such they are considered particles without mass or charge that travel at the speed of light, and their energy is defined in terms of their wavelength by the Planck-Einstein relation:

$$E = h\nu = \frac{hc}{\lambda} \quad (14)$$

where E is the photon's energy (eV), h is Planck's constant (4.136×10^{-15} eV s) (NIST, 2019), ν is the photon's frequency (s^{-1}), and λ is the photon's wavelength (m). Lower frequency light such as visible and infrared does not have the energy to ionize, whereas photons such X-rays and gamma rays are higher energy and are of interest in radiation engineering and chemistry. X-rays are produced when electrons which have been excited to higher energy states in the valence shell then drop to lower energy levels, while gamma rays are produced by reactions within atomic nuclei such as radioactive decay. They are electrically neutral so do not steadily lose energy to any coulombic interactions as charged particles do. As such, they travel considerable distances before undergoing more "catastrophic" interactions – perhaps by transferring their energy to electrons, either partially or totally, and these newly excited electrons will ultimately deposit their energy in the medium. Gamma rays have the shortest wavelength of the electromagnetic spectrum, between 3×10^{-11} m and 3×10^{-13} m, corresponding to the highest energy levels with a wide range between 40 keV to 4 MeV, and so they are the deepest penetrating photons (Spinks & Woods, 1990).

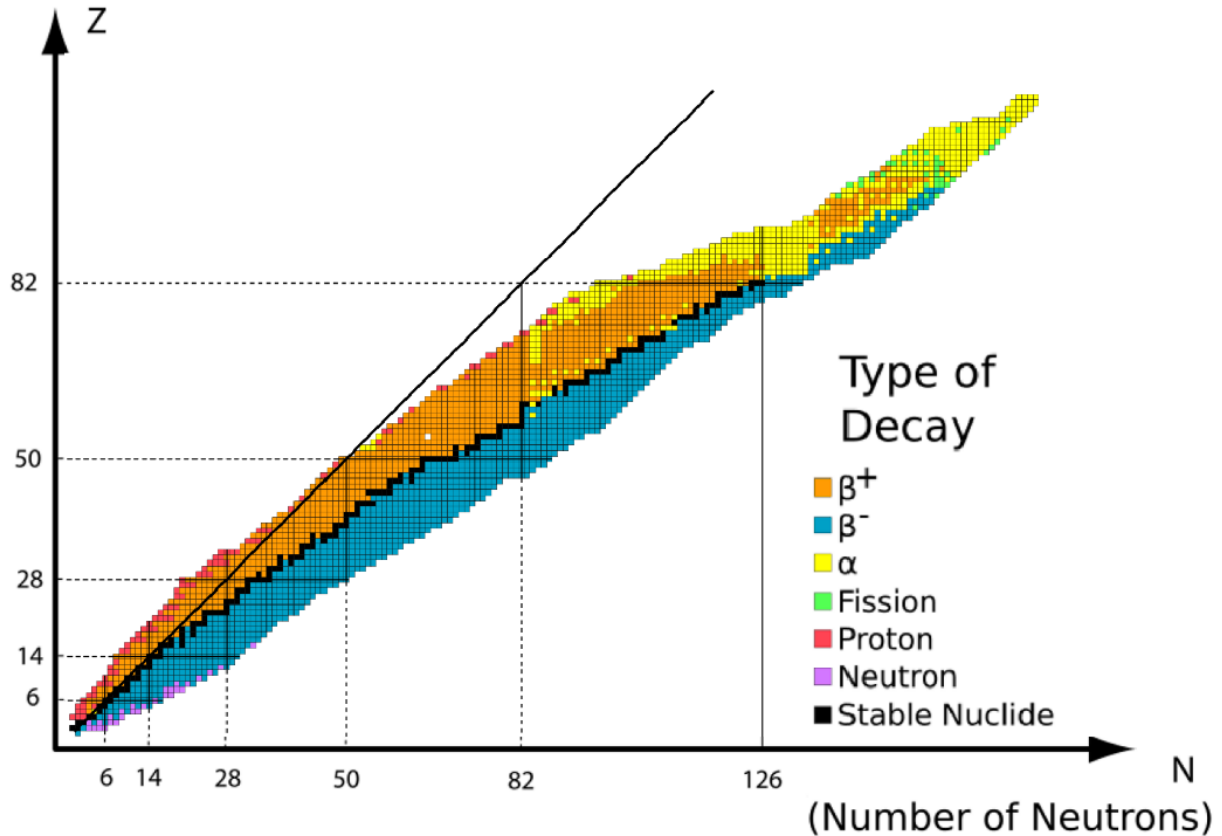


Figure 8. Main decay mode of radioactive nuclides (adapted from (Özbay, 2016)).

When an atom's constituents are not arranged in the lowest possible potential energy state and so it is unstable, part of its matter/energy is likely to randomly dis-integrate itself from the whole in a nuclear reaction to transform the main nucleon into a more stable form/energy state, and the original atomic form is said to be radioactive. The unit for quantifying radioactivity was originally defined as a curie (Ci), being the number of disintegrations per second occurring in a mass of 1 gram of radium in equilibrium, named in honor of Marie and Pierre Curie (Rutherford, 1910) who coined the French term "radio-actif" with the prefix from the Latin *radius* for "ray". The official unit was changed in 1975 at the 15th General Conference on Weights and Measures, giving official status as the SI unit of activity to the becquerel (Bq), being defined as one aperiodic decay event per second (BIPM, et al., 2001). The unit Bq was named in honor of Henri Becquerel, who shared a Nobel Prize in Physics in 1903 with the Curie's for their work together on

radioactivity. There are several methods by which radioactive isotopes can undergo decay, and some nuclides have more than one possible process or “mode” they may decay through. For example, bismuth-212 is radioactive and 64% of its decays are emission of a beta electron while 36% of its decays are alpha particle emissions (Kondev, et al., 2021). The likeliest type of decay for most known nuclides are shown in Figure 8, and the decay formula for radium is shown below.



$$1\text{Ci} = 3.7 \times 10^{10} \text{ s}^{-1} = 37 \text{ GBq}$$

The ionizing energy deposited into systems by radiation is quantified as the dose, with units of energy deposited per unit of mass for which the SI standard unit is the gray (Gy), equivalent to one Joule per kilogram (J/kg). The nuclear fission of uranium produces large amounts of energy, where 80–85% manifests in the kinetic energy of recoiling fission fragments, 5–6% appears as the energy of neutrons and gamma rays emerging from the fission reaction, and 5–6% as energy stored in the unstable fission fragments which will be freed as beta or gamma radiation upon their decay (Spinks & Woods, 1990).

The main mechanisms by which particles will interact with matter are either by nuclear capture or by scattering. Nuclear capture results in a compound nucleus being formed, whereas scattering involves an interaction where the particle maintains its identity. Scattering can be elastic or inelastic, as determined when the kinetic energy of both the particle and the target is conserved or when the kinetic energy is not conserved, respectively. One of the inelastic methods that energy can be transferred to a system by is Bremsstrahlung, wherein the electromagnetic force experienced between a penetrating high energy electron and positively charged nuclei it passes transforms some of the electron’s kinetic energy which is emitted out as bremsstrahlung radiation

in the form of X-rays. Alternatively, the ionizing radiation can affect changes on the atoms or molecules themselves as some kinetic energy is transformed to potential energy contained by electrons in higher orbital energy states or by the nuclear forces within the nucleus, leading to the destabilization of chemical species and subsequent release of free radicals along the track of a specific particle. With this case, different types of energetic particles will transfer different amounts of energy, and the local rate of energy deposition along a track is defined by the Linear Energy Transfer (LET) of that particle, which is expressed in terms of energy loss per unit distance travelled ($\text{keV}/\mu\text{m}$).

The quantity of chemical species produced by ionizing radiation effects is defined as a species' G-value (or g-value, where the typical connotation is that "g" is used for known yields which have been defined and "G" is used for measured yields, however the reverse has also been used in literature). This radiation-chemical yield has units of amount produced per energy deposited in the medium, which is expressed as either number of molecules per 100eV deposited ($\#/100\text{eV}$) or, more commonly, as (micro)moles produced per Joule deposited ($\mu\text{mol}/\text{J}$).

1.3 Neutron Scattering

The neutron occupies a central position in the modern world of radiation engineering, as their self-replicating interactions with fissile materials are the driving force behind the fission reactions powering nuclear reactors. They are most copiously produced in such reactors, though can also be generated in particle accelerators by means of similar nuclear reactions. Neutrons are typically classified according to their energy level, though the conventions are often not precise. Relativistic neutrons are said to have energies higher than 25 MeV, fast neutrons have roughly 10–20 MeV, and neutrons with approximately 0.01–0.1 MeV are referred to as

slow/intermediate/resonance neutrons (Turner, 2008). A “thermal” neutron is said to be in approximate thermal equilibrium with its surroundings, where their most probable energy in the distribution at room temperature is given as 0.025 eV, and these are of primary concern to part of this work. Epithermal neutrons have more energy than thermal neutrons but not as much as fast neutrons, with energy roughly between 0.025–0.4 eV (again, the conventions are not precise and often overlap each other). They are considered incompletely thermalized, but are expected to become thermalized relatively soon.

Neutrons have a spin and thus a magnetic moment along with a nonzero distribution of electric charge, despite being defined as electrically neutral, and so can weakly interact with electrons through electromagnetic forces; though they mainly interact with protons and other neutrons, doing so through the strong nuclear force. Fast neutrons will gradually lose their energy as they traverse matter mainly through a series of elastic scattering events, becoming more and more likely to instead be captured by a nucleus, and this process is generally referred to as neutron moderation or thermalization. Thermal neutrons diffuse about randomly in matter until captured, and they gain and lose only small amounts of energy with each interaction, being in near-equilibrium.

Cross sections for nuclear interactions represent the likelihood of the interaction occurring, for which atomic nuclei are assigned a representative cross-sectional area (denoted σ) to express these probabilities. The standard unit is the barn, equal to 1×10^{-24} cm², which was coined during the Manhattan Project with rumors that this terminology was related to the idiom “couldn’t hit the broad side of a barn” and it outlasted the less favored unit, the “shed,” equal to 1×10^{-24} barn (Baker & Holloway, September, 1944). The total capture cross section represents the sum of all probabilities for each possible interaction process which any nuclide is capable of participating in.

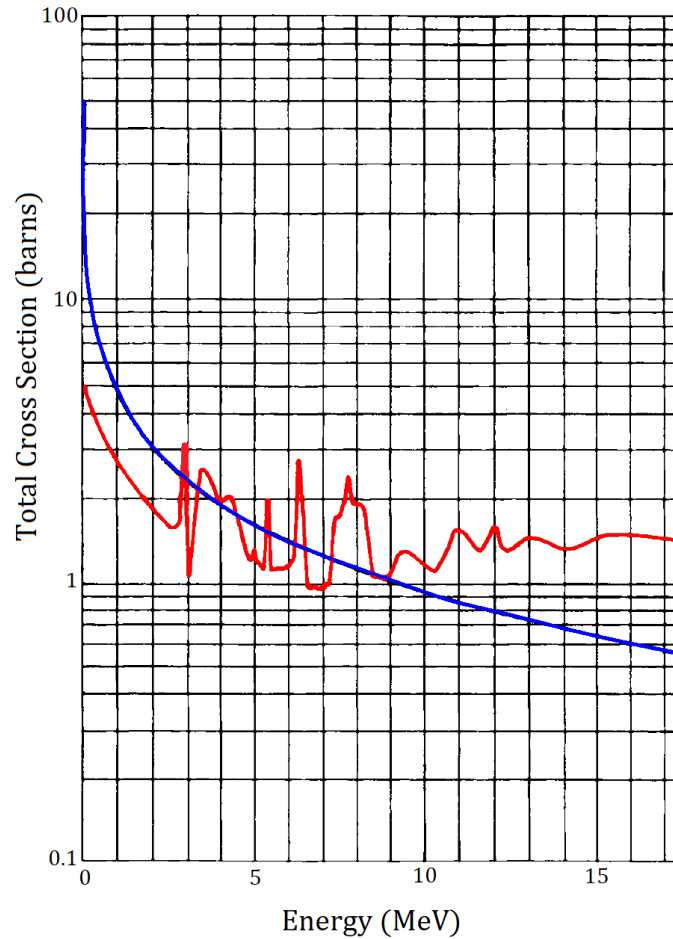


Figure 9. Total cross section for neutrons interacting with hydrogen (blue) and carbon (red) as functions of energy (adapted from (Turner, 2008)).

The lone proton of a hydrogen nucleus has no excited states, and so its total cross section is representative of prospective elastic scatterings and neutron captures only; whereas a carbon nucleus can attain multiple discrete excited energy states and so the separate potentials of elastic scattering, inelastic scattering, and neutron capture each vary with the energy of the incident neutron, thus enhancing/depressing the total cross section over a range of energies (as depicted in Figure 9). As it turns out, the greatest amount of energy can be transferred from an incident neutron to a target nucleus when the latter has the same or similar mass as the neutron, meaning that elements of lower atomic mass are more effective moderators. This can be shown through consideration of the laws for conservation of kinetic energy and of momentum, whereby the

average of the fractional kinetic energy transferred per collision for a neutron elastically scattering with a nuclide, integrated in three dimensions over all possible angles, is defined as:

$$\xi = 1 - \frac{(m - 1)^2}{2m} \ln \left(\frac{m + 1}{m - 1} \right) \quad (16)$$

where m is the mass of the target nuclide (University of Cambridge, 2023). This is part of the justification behind using water as the main moderator in nuclear reactors, since the hydrogen atom's proton is the elemental nucleus with the closest mass to a neutron. Graphite is another popular neutron moderator for several reasons: it is easily obtainable, its mass number of twelve legitimizes various approximations in theory such as the Fermi continuous slowing-down model and the assumption of isotropic neutron scattering, and its small absorption yet large slowing-down time yields slow temporal variation of neutron density (Nishina, et al., 1979). These characteristics have made it highly relevant for use in pulse neutron techniques to determine the mean free path of thermal neutrons through different materials and the thermal neutron cross sections of different nuclides (Price, 1964; Mitsui & Siguyama, 1973), as well as for use in research facilities where the consequences of thermal neutron absorption reactions are of interest (Auden, et al., 2019), as is one aim of this work.

1.3.1 Dosimetry by the Cadmium Ratio and Radiochromic Films

The relative density of thermal neutrons within a neutron flux consisting of a spectrum of energies is referred to as the thermal index. This is most commonly measured using the cadmium ratio, wherein the activity of a neutron-absorbing material is compared to its activity when shielded by cadmium (Sekine & Baba, 1980). Cadmium almost completely absorbs thermal neutrons and transmits epithermal neutrons (Zangirolami, et al., 2010), and so the cadmium ratio can be used to determine the fluence purely by thermal neutrons.

Radiochromic films (RCFs) are a standard dosimetry media, wherein the structural characteristics of their crystalline sensitive element(s) will be modified by exposure to ionizing radiation (Casolaro, et al., 2019). Typically, the ionization of a film’s monomer elements will result in a polymerization process, this in turn is reflected by a macroscale color change, the degree of which can then be related to the radiation dose experienced by the RCF. These dosimetric characteristics are described by a dose-response curve, which could be a plot of net optical density read out at certain wavelengths against the dose (though such curves are not linear, usually the best fits are polynomial), and they can depend on many factors such as film type, radiation type, the readout system (wavelength, transmission/reflection, resolution, etc.), and time between irradiation and readout (Butson & Niroomand-Rad, 2017).

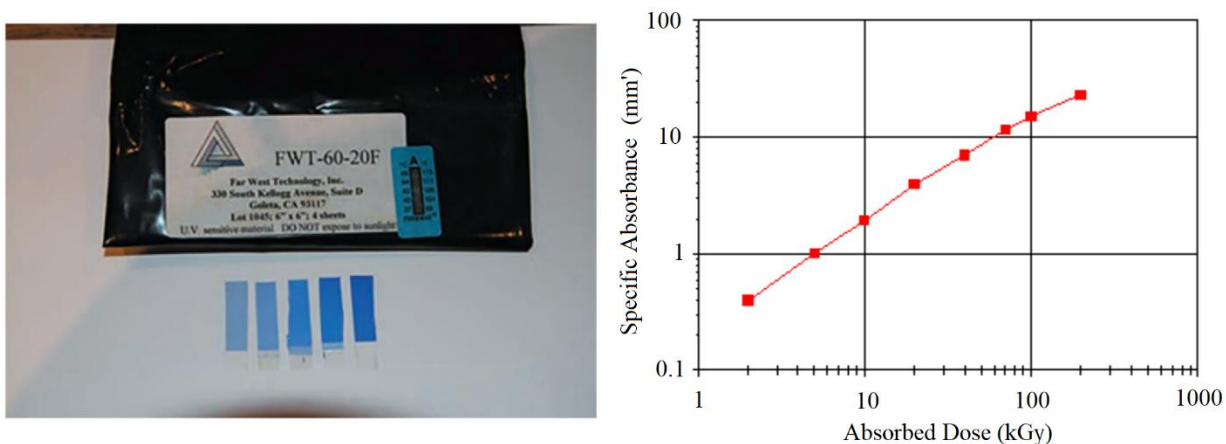


Figure 10. Left: image of Far West Technology FWT-60 film package, and cut film samples irradiated with increasing dose from left to right (adapted from (Butson & Niroomand-Rad, 2017)); Right: typical dose-response curve for FWT-60 dosimeters as measured with Radiachromic readers manufactured by FWT (adapted from (Far West Technology, Inc., 2002)).

Far West Technology manufactures RCF media based on colorless derivatives of the hydrophobic family of amino-triphenylmethane (the FWT-60 series use hexa(hydroxyethyl)) that change from clear to a deep blue in relation to absorbed dose (Far West Technology, Inc., 2002),

which are commonly used for high-dose applications though lack the sensitivity for medical applications, and they are one of the oldest RCF manufacturers still available.

1.4 Linear Energy Transfer (LET)

Charged particles moving through a material exert Coulombic forces on many atoms simultaneously, where a single charged particle can interact with a tremendous number of electrons (millions) as it travels. Each interaction has its own probability for occurrence and for a certain energy loss, and an average energy loss is calculated per unit distance traveled, known as Linear Energy Transfer (LET), with units of keV/ μm . There are certain limiting cases over the continuum of LET, referred to as Low and High LET, distinguishable depending on the type of energetic ionizing particle and consequently how it interacts with the medium when it is depositing energy. These divergent LET cases exhibit fundamentally different performances when considering the structure of the speciation event and its resulting “escape” products. In general, individual radiolytic events of ionized molecules are formed non-homogeneously as clusters of reactive ionized species, which are referred to as “spurs” (Zimbrick, 2002).

1.4.1 Low LET

In the case of Low LET, this deals with gamma rays and low-mass ions such as high energy electrons. The majority of radiation dose in reactor cooling water occurs via Low LET gamma radiolysis, producing a large yield of the free radicals $\cdot\text{OH}$, $\cdot\text{H}$, and e_{aq}^- .

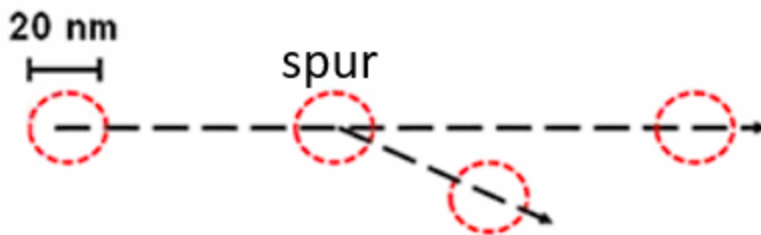


Figure 11. Graphic displaying spur spacing for a Low LET particle.

Most spurs along a Low LET particle's track are spaced far from other spurs, which allows the reactive ionized species to escape immediate recombination with each other because of their low initial density. Therefore the degree of diffusion to infinity of these species is high and the escape yield of the initial radicals is large. Being generally low-mass, they easily scatter to large angles, and as a result they exhibit a zig-zag trajectory.

1.4.1.1 Gamma/Photons

Although lacking a net electric charge, photons such as gamma rays are by nature electromagnetic and can therefore interact with the bound electrons of atoms as well as directly with the nucleus in multiple ways, including coherent scattering, Compton scattering, pair production, Rayleigh scattering, Bragg scattering, photodisintegration/photoneuclear reaction, and by the photoelectric effect. Depending on the energy of the photon and the properties of the medium it is traveling through, several modes of interaction may be possible – at which point prediction of the exact mode that will manifest becomes impossible.

Coherent scattering describes interactions where the photon loses little energy due to several effects combining coherently, as in by the addition of their amplitudes. Rayleigh scattering involves interactions with the atomic electrons and is the main process by which coherent scattering occurs, though it can be neglected in radiation chemistry since it typically occurs in an energy range where the far more-potent photoelectric effect is highly likely as well.

Compton scattering is an example of incoherent scattering, as there is a random phase relationship between the incident and scattered radiation which causes the scattering effects here to combine discordantly and interfere. It involves an incident photon interacting with an electron, bound or free, by transferring some of its energy to accelerate the electron. The result is the deflection of the photon with reduced energy and the emission of a recoil electron. This interaction predominates in water for photon energies between 1–5 MeV (Spinks & Woods, 1990).

Pair production involves the formation of two recoil particles, an electron and an anti-electron (positron), following the complete absorption by an atomic nucleus of a photon with a minimum energy above $2m_e c^2$ (the rest energy of an electron/positron). The remainder of the photon's energy above this level is divided evenly between the two recoil particles as kinetic energy. The positron, being the antimatter counterpart to the electron, will eventually combine with one and annihilate to produce two gamma rays of equal energy $m_e c^2 = 0.511$ MeV (Spinks & Woods, 1990).

The photoelectric effect also involves the absorption of a photon's energy in its entirety, but in this case it is transferred to a bound electron which is subsequently ejected from its orbital. The kinetic energy of this "photoelectron" is the difference between the energy of the incident photon and the binding energy of the electron in its orbital. Photons with sufficient energy will eject the most tightly bound electrons in the K-shell orbital for about 80% of their interactions; and although photons exhibiting the photoelectric effect are generally low-energy, the binding energy of the inner electrons for water is of the order of 500 eV, which is relatively small (Spinks & Woods, 1990).

The later three interactions described above are the most likely, and the predominating effect between them can be roughly determined based on the absorbing material's atomic number

and the energy of the incident photon as shown in Figure 12. Although other modes of interaction were mentioned above, they are not of particular concern in this work and so no further introduction or discussion on them will be presented.

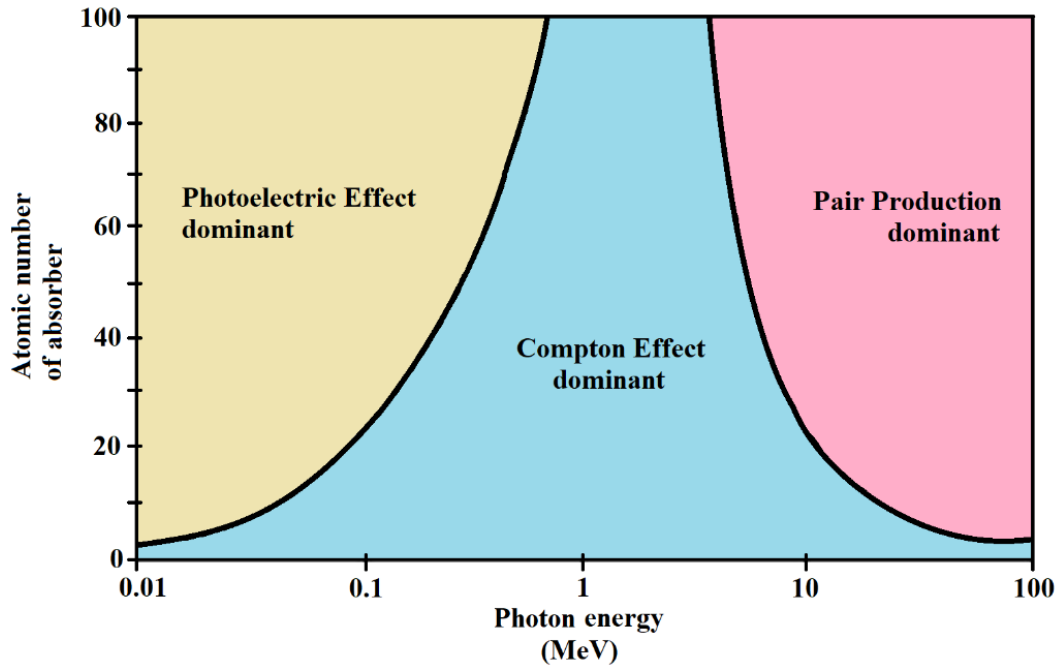


Figure 12. Dominance of the three most likely photon interactions (adapted from (Al-Sheikhly, 2017)).

These interactions generally result in the photon losing a relatively large amount of its energy; however they occur very infrequently, which leads to photons having high penetration. Thus, dissimilar to the representation for likelihoods of neutron interactions as a cross sectional area, the concept of a material's "photon cross section" is not entertained unless the interaction coefficient is on the order of 10^{-28} m^2 . Instead, the intensity of a flux of photons is considered to be "attenuated" to a different degree depending on the mode of interaction, represented by attenuation coefficients associated with specific modes. The total linear attenuation coefficient is often given as:

$$\mu = \tau + \sigma + \kappa \quad (17)$$

where τ , σ , and κ are the linear attenuation coefficients in units of cm^{-1} for the photoelectric, Compton, and pair production modes, respectively (Spinks & Woods, 1990). The contributions from coherent scattering and photonuclear reactions are relatively small and therefore are usually omitted.

1.4.1.2 High energy electrons

Electrons interact with matter either by emission of electromagnetic radiation or by elastic and inelastic collisions through coulombic interactions with the electrons within the target material. Using relativistic quantum mechanics, Hans Bethe derived an expression for the stopping power of a uniform medium for an incident charged particle (Turner, 2008), and we express here the collisional stopping-power formula for an electron through water as:

$$\left(-\frac{dE}{dx}\right)_{col} = \frac{4\pi k_0^2 e^4 n}{m_e c^2 \left(1 - \frac{1}{(\tau + 1)^2}\right)} \left[\ln \left(\frac{m_e c^2 \tau \sqrt{\tau + 2}}{I \sqrt{2}} \right) + \frac{1}{2(\tau + 1)^2} \left[1 + \frac{\tau^2}{8} - (2\tau + 1) \ln 2 \right] \right] \quad (18)$$

Using Coulomb's constant $k_0 = 8.99 \times 10^9 \text{ N m}^2 \text{ C}^{-2}$, the electron charge $e = 1.60 \times 10^{-19} \text{ C}$, the number of electrons per unit volume $n = 3.34 \times 10^{29}$ (per cubic meter of water), and the electron rest mass $m_e = 9.11 \times 10^{-31} \text{ kg}$, Equation (18) can be approximated as:

$$\left(-\frac{dE}{dx}\right)_{col} = \frac{0.1695}{\left(1 - \frac{1}{(\tau + 1)^2}\right)} \left[\ln \left((3.61 \times 10^5) \tau \sqrt{\tau + 2} \right) + \frac{1}{2(\tau + 1)^2} \left[1 + \frac{\tau^2}{8} - (2\tau + 1) \ln 2 \right] - \ln I_{eV} \right] \quad (19)$$

where I_{eV} is the mean excitation energy of the medium (for water, $\ln I_{eV} \approx 4.31$), and τ is define as $\frac{E}{m_e c^2}$ such that for an electron $m_e c^2 = 0.511 \text{ MeV}$ and E is the kinetic energy of the electron

(eV). Calculations for the rate of energy loss $-\frac{dE}{dx}$ (MeV/cm) and the penetration depth of an electron traveling through water have been plotted as functions of its incident energy (eV) in Figure 13.

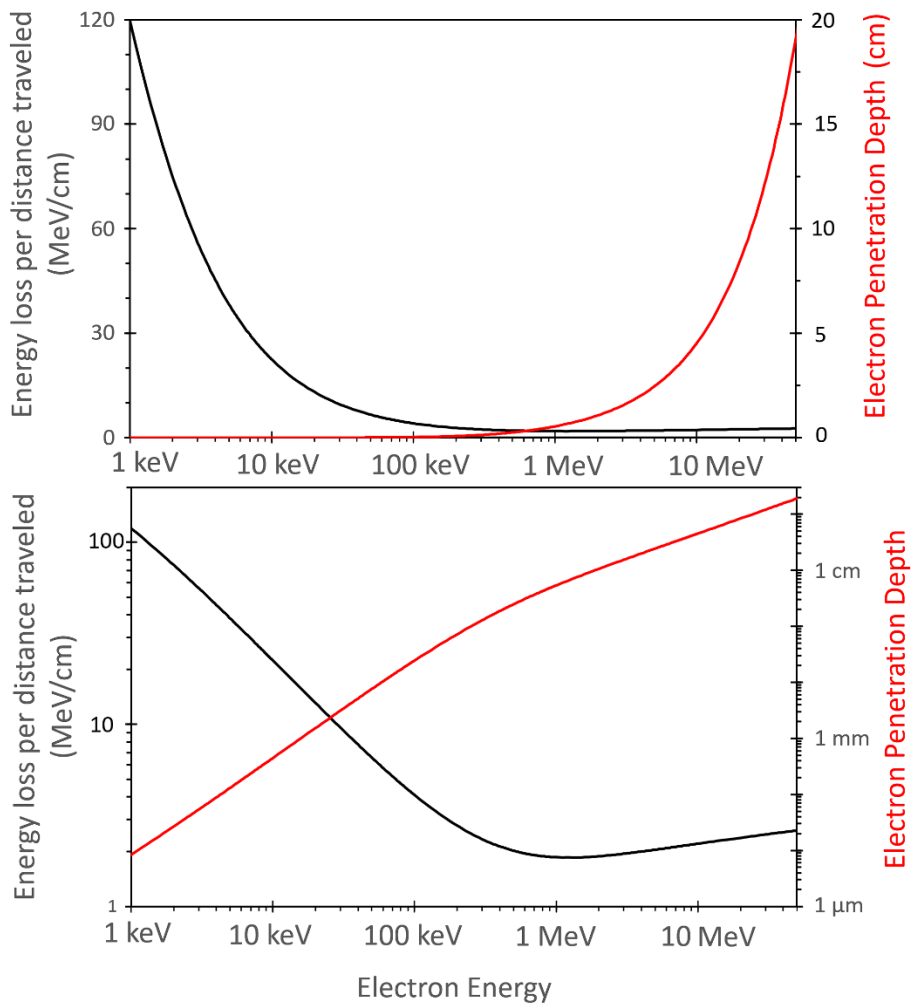


Figure 13. Stopping power of water (black) and electron penetration depth (red), as a function of incident electron energy, displayed linearly (top) and on log scale (bottom), calculated by approximation of the Bethe equation as it was presented in (Turner, 2008).

1.4.2 High LET

The behavior of energy transfer into a traversed medium is very different for a heavy charged particle (such as alpha particles and fission products), and is characterized by High LET. On average, such particles lose similar amounts of energy per collision as compared to Low LET

particles. However, the distance between each collision is much shorter for a heavy particle than for a low-mass particle.

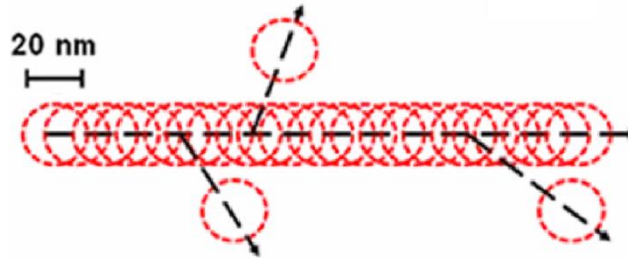


Figure 14. Graphic displaying spur spacing for High LET particle.

This close proximity between spurs results in almost no diffusion to infinity for any of the initial reactive ionized species, due to most of them recombining to form stable molecular products such as H_2 and H_2O_2 . Though these products are considered stable, they are still quite reactive in terms of corrosion chemistry and so quantifying the yields of these species in any irradiated aqueous system, such as those found in PWRs, becomes very important for assessing safe operating lifetimes of components.

1.4.2.1 Alpha Particles

The rate of energy loss is inversely related to the velocity of a particle, and so an alpha particle will have several hundred times more ionization events per unit distance traveled than a low-mass particle with the same kinetic energy, since they are not traveling at relativistic speeds. Alpha particles have an electric charge and so interact with matter by the same methods as electrons do, by bremsstrahlung emission as well as inelastic and elastic scattering effects. However, their energies are typically well below the TeV order where bremsstrahlung becomes important; and Equation (16) indicates the fraction of energy transferred in elastic collisions is greatest between particles of similar mass (although this equation was derived specifically for collisions with neutrons, the general relation is applicable for any pair of particles with mass) and

therefore, conversely, the alpha particle possessing ca. 7,400 times the mass of an electron implies that elastic scattering will be negligible. Thus they travel in essentially straight paths.

Bethe similarly derived an expression for the stopping power of a uniform medium for an incident heavy charged particle (Turner, 2008), and we express here the collisional stopping-power formula for an alpha particle through water as:

$$\left(-\frac{dE}{dx}\right)_{col} = \frac{4\pi k_0^2 z^2 e^4 n}{m_e c^2 \left(1 - \frac{1}{(\tau + 1)^2}\right)} \left[\ln \left(\frac{2m_e c^2 ((\tau + 1)^2 - 1)}{I} \right) + \frac{1}{(\tau + 1)^2} - 1 \right] \quad (20)$$

Using the atomic number of the heavy particle $z = 4$, the proton rest mass $m_p = 1.673 \times 10^{-27}$ kg, and the neutron rest mass $m_n = 1.675 \times 10^{-27}$ kg, this equation can be approximated similarly as was done for Equation (18) as:

$$\left(-\frac{dE}{dx}\right)_{col} = \frac{2.711}{\left(1 - \frac{1}{(\tau + 1)^2}\right)} \left[\ln((7.512 \times 10^9)((\tau + 1)^2 - 1)) + \frac{1}{(\tau + 1)^2} - 1 - \ln I_{eV} \right] \quad (21)$$

where I_{eV} is the mean excitation energy of the medium (for water, $\ln I_{eV} \cong 4.31$), and τ is define as $\frac{E}{m_\alpha c^2}$ such that for an alpha particle the energy at rest is $m_\alpha c^2 = 3.727$ MeV and E is the kinetic energy of the particle (eV). Calculations for the rate of energy loss $\frac{dE}{dx}$ (MeV/cm) by an alpha particle, compared with an electron, both traveling through water have been plotted as functions of their incident energy (eV) in Figure 15.

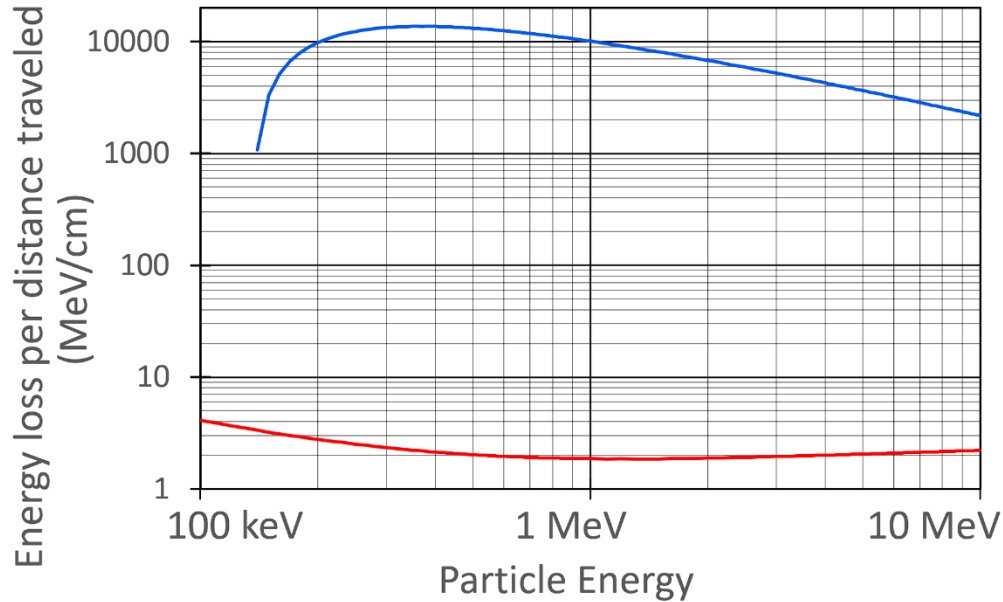


Figure 15. Stopping power of water for electrons (red) and alpha particles (blue), calculated by approximation of the Bethe equation as it was presented in (Turner, 2008).

As is clear by the comparison, alpha particles and other heavy charged particles lose energy much faster than electrons do as they travel through water. Particularly important to note is the peak behavior arising at lower energies. From the high energy range, as $\tau \rightarrow 0$, the factor in front of the bracket in Equation (21) increases, but then at a low enough energy the decrease of the logarithmic term dominates which leads to a maximum in the rate of energy loss, referred to as the Bragg peak (Turner, 2008), wherein particles will rapidly “dump” all of their remaining energy into a very small volume.

1.5 Pulse Radiolysis

In pulse radiolysis, a linear accelerator delivers a burst of high energy electrons to a sample cell over a pulse width less than 100ns, which perform radiolysis characterized by Low LET. Unlike photolysis, wherein energy absorption depends on an absorbing molecule’s excitation wavelengths, energy transferred by the Coulombic effect of radiolytic LET is less selective and so the major species of molecules being ionized is dependent on the relative concentration in the

irradiated medium. Thus, for an aqueous solution undergoing pulse radiolysis, a high concentration of the initial reactive transient species from ionized water decomposition ($\cdot H$, $\cdot OH$, e_{aq}^-) can be produced to interact with other present chemical species initially dissolved in the water. These reactions of interest often occur over a period of time less than 100 μ s.

1.5.1 Transient Absorption Spectrophotometry

One of the methods utilized to study the progression of chemical reactions in non-scattering homogeneous solutions, such as those relevant to water radiolysis, is absorption spectrophotometry. Its theory is based off of the Beer-Lambert Law:

$$\log_{10} \left(\frac{I_0}{I} \right) = A \quad (22)$$

$$A = \epsilon \ell c \quad (23)$$

where the fraction of light intensity transmitted through a reference sample (I_0) versus the intensity when transmitted through a sample containing an absorbing species (I) is calculated as the absorbance (A), which is related to the length of the path that light has traveled through the absorbing medium (ℓ), the concentration of the absorbing species (c), and the species' efficiency for attenuating light as it passes through a solution of the homogeneously dispersed species (ϵ). Absorbance is a unitless quantity, while ℓ commonly has units of distance (cm), c has units of molarity (mol/L, or M), and ϵ (known as the molar attenuation coefficient or the molar extinction coefficient) has units of $M^{-1} \text{ cm}^{-1}$. A basic diagram representation for the progression of the steps involved is shown in Figure 16 to highlight the three main contrasted states of the system.

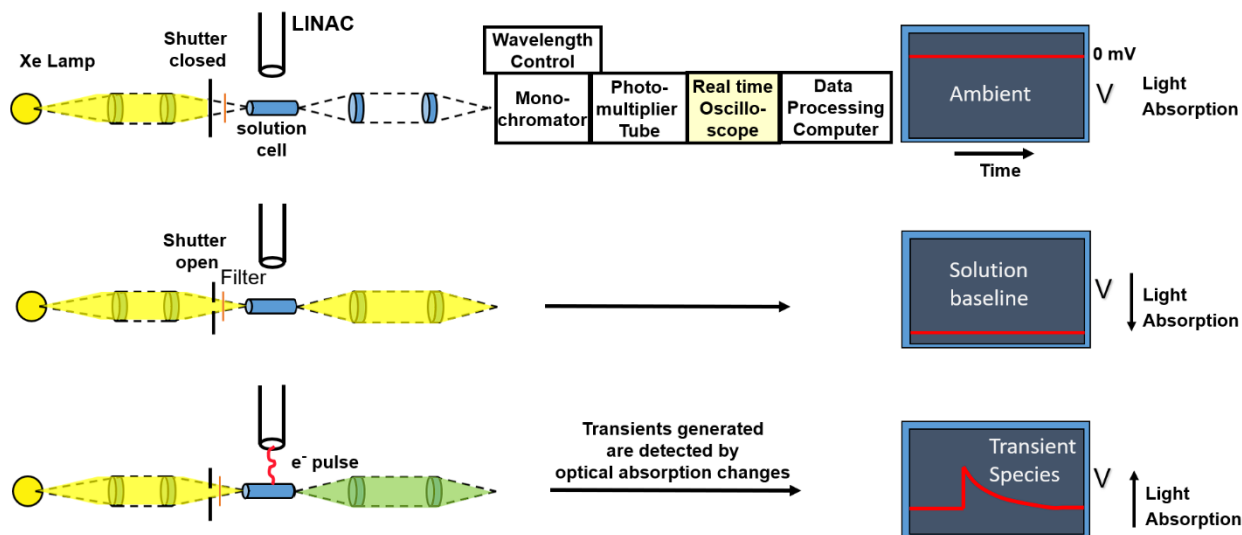


Figure 16. Diagram representation of the stages involved in spectrophotometry: establishing ambient conditions, evaluating baseline absorption in the unirradiated solution, and detection of transient species produced by an e-beam pulse reacting rapidly with other available species.

Spectrophotometry is the study of such interactions between light and matter. Different chemical species will absorb a certain intensity of light at specific wavelengths, determining their own unique absorption spectrum that can be used to identify a particular species when performing spectrophotometry over a wide enough range of select wavelengths. A prevalent technique for observing the generation and reactions of radiolytic species in an aqueous solution by spectrophotometry is pulse radiolysis, wherein the progression of the chemical interactions within the irradiated solution can then be monitored via a UV-Visible beam from a Xe-arc lamp to produce white light which passes perpendicular to the e-beam through the solution both before and immediately following the irradiation, as has been done here. The two differing spectra of transmitted light intensity can then be monitored and compared as a function over time to evaluate the absorption spectra for any radiolytic absorbing species present at any time intermediate to their production and consumption, and thus the kinetics involved therein. An example of a time-resolved absorption spectrum is shown below.

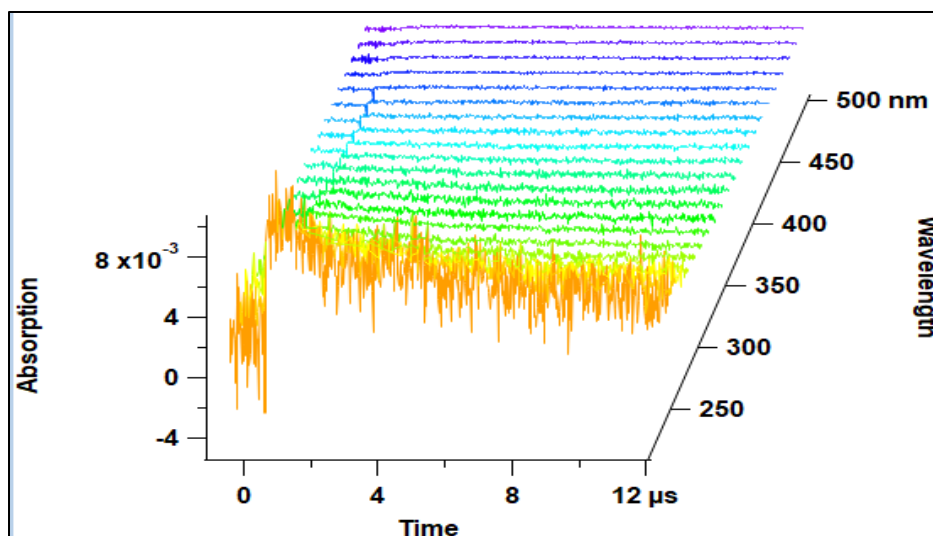


Figure 17. Time-resolved absorption spectrum obtained during pulse radiolysis of an aqueous borax solution by spectrophotometry.

Briefly the baseline conditions precluding the e -beam pulse are shown plotted at negative times, the LINAC is pulsed at $t=0$, the rapid growth of initially produced radicals appears as an increase in absorption, which then decays as these transient species are consumed.

1.5.2 Ionic Strength Effect

The ionic strength effect is a characteristic effect on the kinetics of solutions which can be observed in the presence of charged particles. Ionic strength is representative of the concentration of chemical species with a non-zero charge in solution, and is given by the following equation (Arnaut, et al., 2006):

$$I = \frac{1}{2} \sum_i^n c_i Z_i^2 \quad (24)$$

where c_i is the concentration of the i -th species with charge Z_i in solution. In solutions with low ionic strength, as are those used in the second part of this work, using the model of the Debye-Hückel theory it is understood that an ion is surrounded by an atmosphere of oppositely charged ions all with the same charge that thus lower the chemical potential of the central ion by

neutralizing its charge (Arnaut, et al., 2006), or the cloud and central ion have the same charge and the chemical potential is thus enhanced by this charge pairing. The ionic strength effect can then be described by the Brönsted-Bjerrum Equation (Hay, 2000) for a generic reaction between two species $[A] + [B] = [AB]$ as:

$$\log(k) = \log(k_0) + Z_A Z_B \sqrt{I} \quad (25)$$

where k_0 is the rate constant at infinite dilution and k is the rate constant at the specified ionic strength, I . It is thus demonstrated from these two equations that the rate constant is decreased when dealing with ions of opposite charge in solution as the ionic strength is increased by raising the concentration of the charged species.

1.6 Nuclear Power Plants (NPPs)

Nuclear power plants (NPPs) utilize the excess energy from nuclear fission in the form of heat by transporting it to an adjacent system for conversion to an electric output. In essence, a nuclear reactor system is a thermodynamic engine, transferring energy as heat between two thermal reservoirs and converting some of that energy into work. It is understood from the second law of thermodynamics that not all of the energy meant to perform work can be harnessed as such, in an ideal system the maximum efficiency of any thermodynamic engine is known as the Carnot Efficiency, given by:

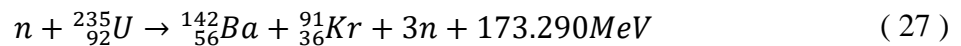
$$\eta_{Carnot} = 1 - \frac{T_{cold}}{T_{hot}} \quad (26)$$

where T_{cold} and T_{hot} are the absolute temperatures of the cold reservoir and hot reservoir, respectively. It follows that an NPP's efficiency is greater for larger temperature differences between the thermal reservoirs. This is the theoretical reasoning providing the background support

for why nuclear power plants are desired to operate at the highest temperatures allowed by current material limitations. The lower limit on the cold reservoir's temperature is dependent on the heat rejection capacity at the condenser into a heat sink, which is limited by the environment since reactors most often radiate their excess heat out into the air or large bodies of water. The temperature of the hot reservoir in current reactors is limited to below the critical point of water (374 °C), since for supercritical conditions not enough is yet known about the changes in radiation-induced chemistry in water and how the limiting corrosion processes on the materials of the primary cooling loop would be affected (Guzonas, et al., 2017).

1.6.1 Pressurized Water nuclear Reactors (PWRs)

Pressurized Water nuclear Reactors (PWRs) are a class of light-water (as opposed to deuterium dioxide, or “heavy” water) commercial reactors similar to the previously more common Boiling Water nuclear Reactors (BWRs), designated as Generation II reactors and built until the end of the 1990s. Such reactors utilize the excess energy in the form of heat which is produced during chain reactions from standard uranium neutron capture fission reactions to produce electricity. One such fission reaction is shown below, wherein a thermal neutron is captured by a uranium-235 nucleus, destabilizing it, which then fissions into barium and krypton nuclei along with more neutrons, all with a total of 173.290MeV kinetic energy. The neutrons can go on to interact with other ^{235}U nuclei to continue this reaction.



These reactions occur in the heavy fissionable material contained within a reactor's fuel rods, and the kinetic energy of the fission products is then absorbed by cladding materials sheathing the fuel rods, consequently heating this outer layer of the rods. Once the heat conducts to the outer

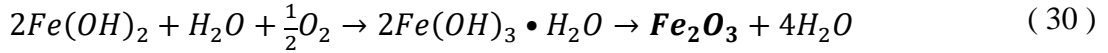
surface of the cladding, it then transfers to the working fluid flowing around it. Cladding materials are commonly composed of aluminum, stainless steel, and zirconium alloys. This cladding serves to prevent corrosion of the fuel by the coolant, contain the radioactive fission products from escaping the rods, and provide structural support for the fuel material. The working fluid consists of two separate bodies of water: the primary loop and the secondary loop. The primary loop is in direct contact with and flows around the cladding of the fuel rods, and thus is heated by the cladding while also being irradiated by neutrons that have escaped capture in other fissile nuclei. The primary loop transfers its heat energy to the secondary loop, which in turn boils and drives steam turbines, while the primary loop is kept under pressure to prevent boiling. To provide better long-term control over the rate of fission reactions within the reactor, neutron poisons and other chemicals are added to the chemistry of the primary water loop. Along with these additives are other chemical species produced from the decomposition of water molecules due to their ionization as the fluid is irradiated. A significant amount of these species cause corrosion, such as on the surface of the fuel rod cladding, and so can decrease the safe operational lifetime of PWR components via anodic corrosion.

1.6.2 Radiation-Induced Corrosion in PWRs

As mentioned in Section 1.1, corrosion is an electrochemical process driven by an electric potential difference between a metal and redox species within an electrolyte. For a metal in an oxygenated aqueous solution, the anodic and cathodic reactions progress as such: metal atoms release their electrons, the ions dissolve into the electrolyte, the free electrons react with redox species in the electrolyte to form OH^- , which reacts with metal ions to form metal hydroxides that precipitate to form an oxide layer on the metal surface. In most PWRs, the primary coolant is only in contact with austenitic stainless steel, zircalloy-2 or other zirconium alloys, and Inconel (Jenks

& Griess, 1967). Therefore, a commonly corroded metal in PWRs is steel, and the prevalent radiolysis leads to production of additional redox species.

Proposed Anodic Reactions:



Proposed Cathodic Reactions:

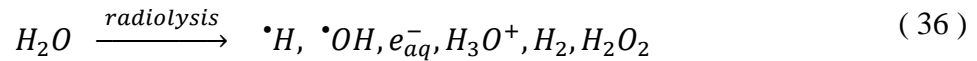


where the **R** reaction numbering scheme is taken from the Atomic Energy of Canada Limited (AECL) review on reactions for simulation of water radiolysis by Elliot and Bartels in 2009 (Elliot & Bartels, 2009). In the early days of nuclear power systems, corrosion issues were most commonly attributed to improper water chemistry control leading to the propagation of crack formations in stainless steel components held under significant stresses. The cooperation between corrosion effects and static tensile stresses to form cracks in materials is referred to as stress corrosion cracking (SCC) (Bardal, 2003; Fontana, 2005). As our understanding of the factors involved in corrosion within reactors improved, innovations were developed to counteract them in the form of alterations to component materials and designs, and to the water chemistry. These changes in turn allowed for extended operated lifetimes along with higher maximum reactivity and fluence rates. As a result, the susceptibility of alloys to SCC has shifted to be increasingly pertinent

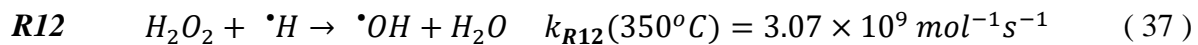
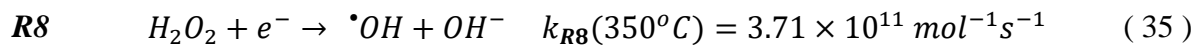
in irradiated components over those considered nonirradiated, due to irradiation-assisted stress corrosion cracking (IASCC), which has been said will become the most important corrosion issue in the future of aging NPPs (Was & Allen, 2019). As has been well-established in Section 1.1, the rate of corrosion can be said to depend greatly on the concentrations of the involved redox species, which is determined largely via water radiolysis.

1.6.3 Radiolysis in PWRs

These radiolytic events occur when an energetic particle interacts with the aqueous medium surrounding the fuel rods, thus depositing some of its energy to water molecules. These ionized molecules are unstable and decompose into a multitude of reactive species, which can in turn recombine to form other more stable products.



Yields for these species must be accurately calculated to be included in reactor chemistry models since information on local corrosion potentials and crack propagation rates caused by this electrochemical process is necessary when determining safe operating conditions and reactor component lifetimes. Hydrogen peroxide (H_2O_2) is one of the main stable products from recombination of radiolytic species and is easily oxidized or reduced at very high reaction rate constants (as shown in the reactions listed below), so it can participate in both the forward anodic and the reverse cathodic reactions simultaneously.



As was discussed in Section 1.1 and its subsections, the electrochemical cell potential can be polarized by an imbalance in the rates for the anodic and/or cathodic reactions which may lead to the suppression of the overall corrosion process. The presence of H_2O_2 will inherently balance

an increase in both the forward anodic and the reverse cathodic reactions simultaneously, thus counteracting polarization effects and considerably raising the rate of corrosion. Even small concentrations can allow it to dominate the limiting rates for both the reducing and oxidizing reactions.

1.7 Boron in PWRs

Control rods in commercial reactors operate to halt neutrons from continuing the fission chain reaction. They are repositioned mainly only during startup and shutdown. However, inherent to the nature of their design, they perform only as localized, nonhomogeneously dispersed regions of depressed neutron flux. A measure taken to enforce homogeneous neutron flux depression around the fissile material is by including chemical “shims” dissolved within the primary loop water itself, which will provide a smoother flux throughout. This also delivers better long-term control over the rate of fission reactions within the reactor, as the concentration of these chemicals can be adjusted easily.

1.7.1 Boron as a Neutron Shim

One of the aforementioned additives included in the primary water loop within PWRs is Boron-10, due to its relatively high thermal neutron capture cross section. The term “neutron cross section” refers to the likelihood of interaction between a target nucleus and an incident neutron, and is equated to a cross-sectional area which is measured in barns ($1 \text{ b} = 1 \times 10^{-28} \text{ m}^2$). Thermal neutrons refer to neutrons which have kinetic energy (K_E) on the order of 0.025eV at room temperature, equating to a speed of roughly 2200 m s^{-1} , and our interaction of interest is when such an incident neutron is captured by boron. Kinetic energy can be calculated using the Boltzmann constant k_B as:

For $k_B = 8.617 \times 10^{-5} \text{ eV/K}$ and $T = 290\text{K}$,

$$K_E = k_B T \text{ yields } K_E = 0.025 \text{ eV} \quad (38)$$

^{10}B is injected (as boric acid) into commercial nuclear reactor primary water as a soluble neutron poison, or chemical “shim,” due to its relatively large thermal neutron capture cross section (763 barns) (Sauerwein, et al., 2012) in order to compensate for fuel burnup and smooth over the neutron flux over the course of a fuel cycle for long-term reactivity control. Reactivity is a relative measure comparing the current state of a reactor to the state when the rate of neutron production is equal to neutron losses, allowing the chain reaction to be self-sustaining, known as critical state. At the beginning, the fuel rods are “fresh” and so reactivity is high, meaning that enough neutrons are being produced to overcome the rate of losses to boron and the control rods and continue the fission reactions. As boron is dissolved all throughout the primary water coolant loop, it can act as a homogeneously dispersed absorber of thermal neutrons, compared to the heterogeneously dispersed regions of decreased neutron flux resulting from the inserted control rods. The homogeneous dispersal of such a neutron absorber provides a smoother flux profile throughout the core to sustain a more stable level of reactivity than control rod insertion does provide.

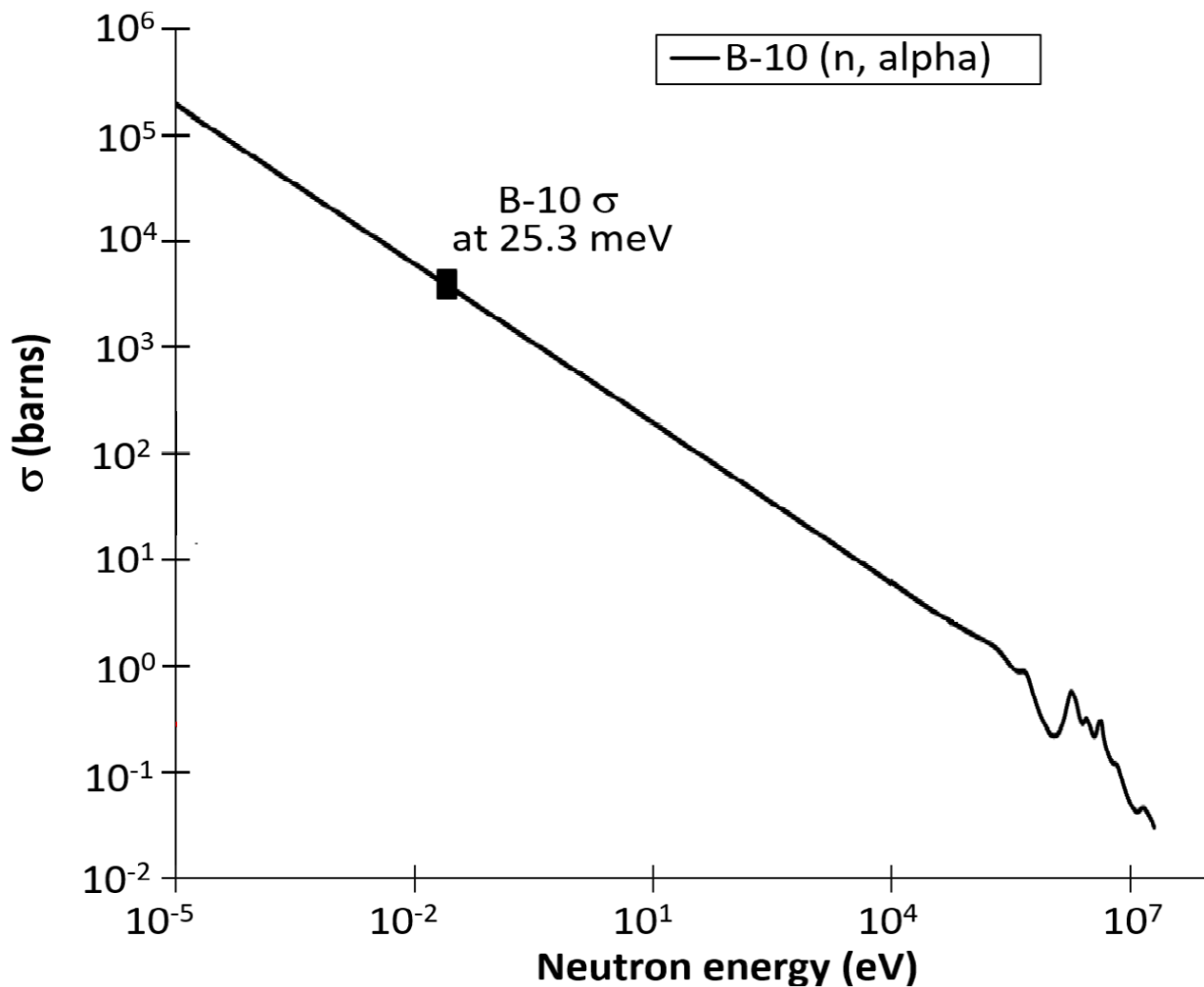


Figure 18. Boron-10 nuclear reaction cross section (adapted from (Auden, et al., 2019)).

As the amount of unspent fuel in the rods decreases, the reactivity decreases as their capacity for neutron production lowers, requiring boron concentration to be reduced to compensate. The aim is to maintain a stable rate of neutron interactions within the main heavy fissile fuel and thus a stable power output. As per guidelines by the Electric Power Research Institute (EPRI), the concentration of boron in commercial power generating PWRs is adjusted over a full 525-day fuel cycle as shown in the figure below, from 0.14 mol L^{-1} at the start of the cycle down to 0 mol L^{-1} before the end as the fuel is slowly spent and the reactivity decreases (EPRI, 2014).

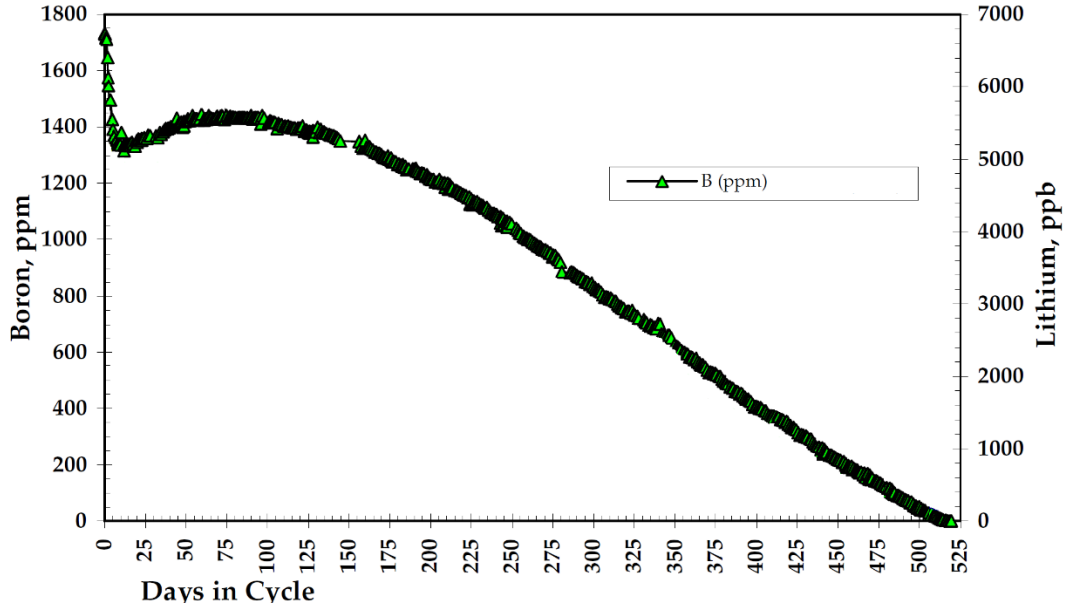
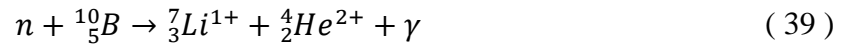


Figure 19. Boron concentrations used over the course of a fuel cycle (adapted from (EPRI, 1999)).

In order to perform as a neutron shim, boron is expected to capture some of the thermal neutrons traveling through the water from one fuel rod to another so as to prevent them from interacting with any further ^{235}U nuclei and thus continue the fission chain reaction. When boron captures a neutron, its nucleus similarly becomes unstable and it fissions into an alpha particle and a lithium ion. The $^{10}\text{B}(n,\alpha)^7\text{Li}$ fission reaction usually produces a $^4\text{He}^{2+}$ ion with kinetic energy 1.473 MeV and $^7\text{Li}^{1+}$ ion with kinetic energy 0.841 MeV (with emission of a 0.479 MeV gamma ray); while there is also a 6% probability for the reaction to instead produce a 1.778 MeV $^4\text{He}^{2+}$ ion and a 1.015 MeV $^7\text{Li}^{1+}$ ion and no gamma (Auden, et al., 2019).



These heavy ions are High LET particles and so quickly lose energy by ionization of the water medium, resulting in water radiolysis and production of H₂, H₂O₂, ·OH radicals, ·H atoms, and e_{aq}^- in dense tracks (Mozumder, 1999). At the beginning of a fuel cycle, dose from the ¹⁰B(n,α)⁷Li fission products can amount to 33% of the total radiation dose in the core (Christensen, 1995). The dose-average LETs of the 1.473 MeV α particles and 0.841 MeV ⁷Li ions have been calculated to be 196 and 216 eV/nm, respectively (Islam, et al., 2017). The stable “escape” products from the High LET tracks are mainly H₂ and H₂O₂ (LaVerne, 2000; LaVerne, 2004), in nearly equal amounts. Given the importance of this source for corrosive H₂O₂ (Macdonald, 1992; Lin, 2000; Raiman, et al., 2017), the product yields of this event should be accurately included in models of the cooling water radiation chemistry (Elliot & Bartels, 2009).

1.7.2 Boric Acid as an Inert Chemical Additive

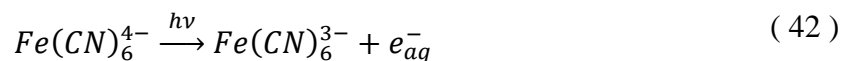
The boron atom has only three external electrons for its four bonding orbitals and is therefore considered electron deficient. Thus, boric acid exists in thermodynamic equilibrium with its conjugate base by the reaction below, where it is seen exhibiting Lewis acidity instead of the typical Brønsted acidity, wherein it is not a typical acid operating primarily by H⁺ donation, rather it is an OH⁻ acceptor.



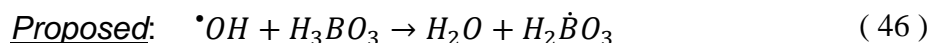
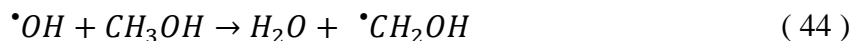
Two of the main reactive species produced from water radiolysis, the aqueous electron (e_{aq}^-) and the hydroxyl radical (·OH), have been evaluated for their reactions with boric acid (Buxton & Sellers, 1987) so as to establish boron’s viability as a chemically nondisruptive additive in that form for acting as a buffer for use in radiation chemical studies and as a neutron shim for use in PWR primary coolant.

1.7.2.1 Hydroxyl radical reaction with Boric Acid

In their 1987 study, Buxton and Sellers photolytically generated e_{aq}^- from hexacyanoferrate(II), the $Fe(CN)_6^{4-}$ ion, in a nitrous oxide (N_2O) saturated aqueous solution, in turn generating $\cdot OH$ radicals.



By allowing boric acid to compete with methanol (CH_3OH) and $Fe(CN)_6^{4-}$ as $\cdot OH$ scavengers according to the chemical reactions below, they found no dependence on boric acid concentration on $Fe(CN)_6^{4-}$ yields. Their conclusion was there is no appreciable reaction between boric acid and $\cdot OH$, and estimated reaction rate is $k(\cdot OH + B(OH)_3) \leq 1.0 \times 10^6 \text{ dm}^3 \text{ mol}^{-1} \text{ s}^{-1}$.



1.7.2.2 Aqueous electron Reaction with Boric Acid

Buxton and Sellers also used pulse radiolysis to study the reaction of boric acid with e_{aq}^- by monitoring the decay rate of the electron. They observed a small increase in decay with increased boric acid concentration (Figure 20-a), corresponding to an apparent rate constant of $k(e_{aq}^- + B(OH)_3) = (2.7 \pm 0.3) \times 10^4 \text{ dm}^3 \text{ mol}^{-1} \text{ s}^{-1}$. They concluded this was more likely a reaction with a common impurity within boric acid, such as nitrate. Furthermore, they observed no marked effect of pH on the decay of the hydrated electron (Figure 20-b). An expected result, if it is reacting with an impurity, though unlikely if there is any reaction of e_{aq}^- with boric acid

since in this pH range it exists in at least five different forms and it would be remarkable if each one reacted with e_{aq}^- at the same rate.

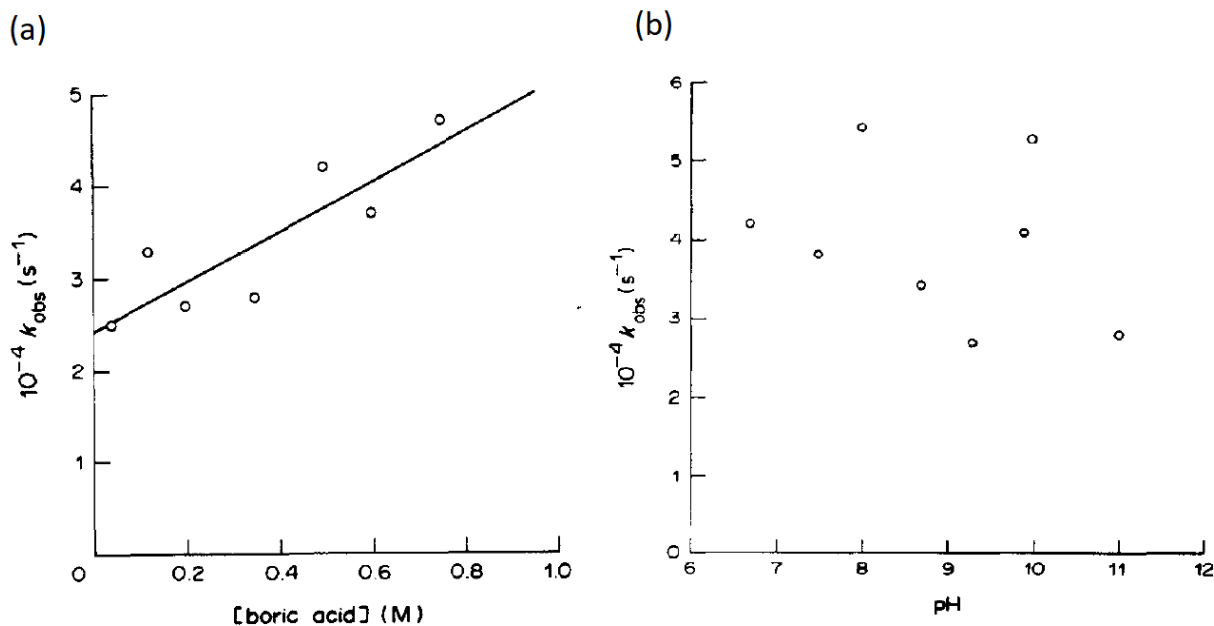


Figure 20. (a) the effect of boric acid concentration on the decay of the hydrated electron in deaerated solutions at pH 6.7, (b) the effect of pH on the decay of the hydrated electron in deaerated solutions containing 0.5 mL dm^{-3} (Buxton & Sellers, 1987)

Thus, the accepted assumption was there would be no marked effect on the radiation chemistry within PWRs when using borax as an additive. Such extremely low reactivity of the boric acid with e_{aq}^- and $\cdot\text{OH}$ would make boric acid “an ideal buffer for use in radiation chemical studies, even at high concentrations” (Buxton & Sellers, 1987). However, they note that boric acid exists in at least five different forms within their pH range: boric acid, borate, a dimer, a cyclic trimer, and a cyclic tetramer. To be clear, they reported no appreciable reactions of e_{aq}^- with any of these species, but no reactions with $\cdot\text{OH}$ only pertaining to the boric acid form.

1.7.3 Borate in PWRs

Buxton and Sellers' research's less thorough evaluation pertaining to the borate form's possible reactivity could be a significant oversight for PWR water chemistry models when considering how much of the boric acid added to the primary water loop is converting to the chemical form of borate. Boric acid and lithium hydroxide are added to the primary water within a PWR to obtain the EPRI standard desired pH of 7.3 at the operational temperature of 350 °C (EPRI, 1999). The acid dissociation constant K_a is a quantitative measurement of how readily an acid (generically, HA) dissociates into a proton (H^+) and its conjugate base (generically, A^-), the equation for which can be rearranged to solve for the ratio of concentration of the conjugate base to its acid form for a given pH and the known K_a of boric acid, 1.1×10^{-8} , as shown below:

$$K_a = \frac{[H^+][A^-]}{[HA]} = \frac{[H^+][borate]}{[boric\ acid]} \quad (47)$$

$$pH = -\log_{10}[H^+] \quad (48)$$

$$\frac{[borate]}{[boric\ acid]} = \frac{K_a}{[H^+]} = \frac{1.1 \times 10^{-8}}{10^{-7.3}} = 0.219 \quad (49)$$

$$\frac{[borate]}{[^{10}B]} = \frac{\left(\frac{[borate]}{[boric\ acid]}\right)}{\left(\frac{[borate]}{[boric\ acid]}\right) + 1} = 0.180 \quad (50)$$

As shown, approximately 18% of the added boron exists in the chemical form of borate, not boric acid, which was not adequately confirmed by Buxton and Sellers to be a nonreactive species with $\cdot OH$.

1.7.4 Properties of Borate Solutions over Temperature

The chemistry and physical properties of boron-containing aqueous solutions at the high-temperature, high-pressure conditions in PWRs are more complex relative to other acid-base

equilibria due in part to a high degree of speciation, wherein boric acid $B(OH)_3$ undergoes ionization reactions to form borate $B(OH)_4^-$ along with metaborates and polyborates. Modeling the transport by dissolution and precipitation reactions of these boron-containing species and their effects on the pH in such conditions, as well as their potential to disrupt the desired power distribution in PWRs (as will be discussed in the next section), requires accurate determination of their thermodynamic properties. The intensity of formation of polyborates depends on the temperature and pH of the solution, as well as the initial concentration of boric acid. Although the formation of at least 10 different borate and polyborate species are known to occur in aqueous boric acid solutions (the structures of the main species discussed here are shown schematically in Figure 21) and their thermodynamic properties have been studied extensively over a wide range of temperatures and pressures, the identities and structures of some polyborates are still under investigation.

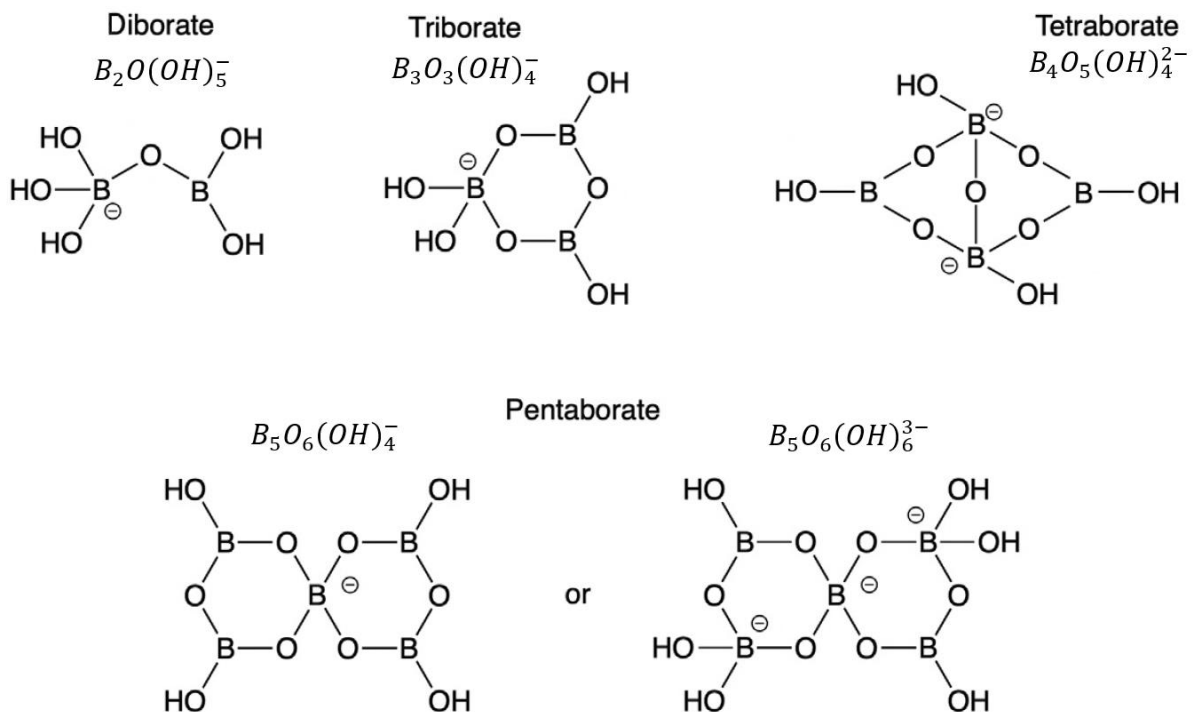
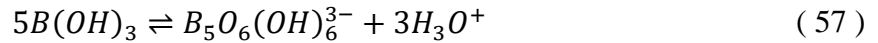
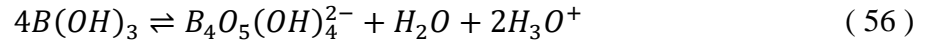
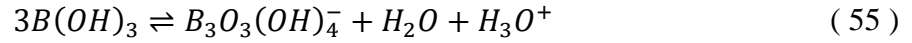
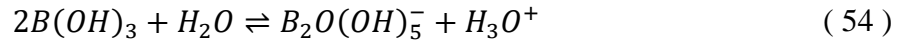
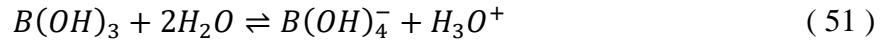


Figure 21. The major forms arising from the speciation reactions present in boric acid solutions.

In 2013, Wang et al. compiled a comprehensive thermodynamic database based on the mixed-solvent electrolyte (MSE) activity coefficient model together with critically evaluated literature results to calculate phase equilibria, speciation, pH, solubility, and vapor-liquid equilibrium due to the effects of chemical speciation, temperature, and concentration (Wang, et al., 2013). Their model includes the following equilibrium ionization reactions to form the borate ion, metaboric acid, boron trioxide, and four of the major polyborate species:



Using their accumulated model parameters, Wang et al. reproduced the solubility of boric acid with satisfying accuracy to previous experimental results (Kracek, et al., 1938; Blasdale & Slansky, 1939). The result is shown in Figure 22, where they chose to present the x-axis as $x_{B(OH)_3}^{0.5}$ to emphasize the details at the lower boric acid concentration range.

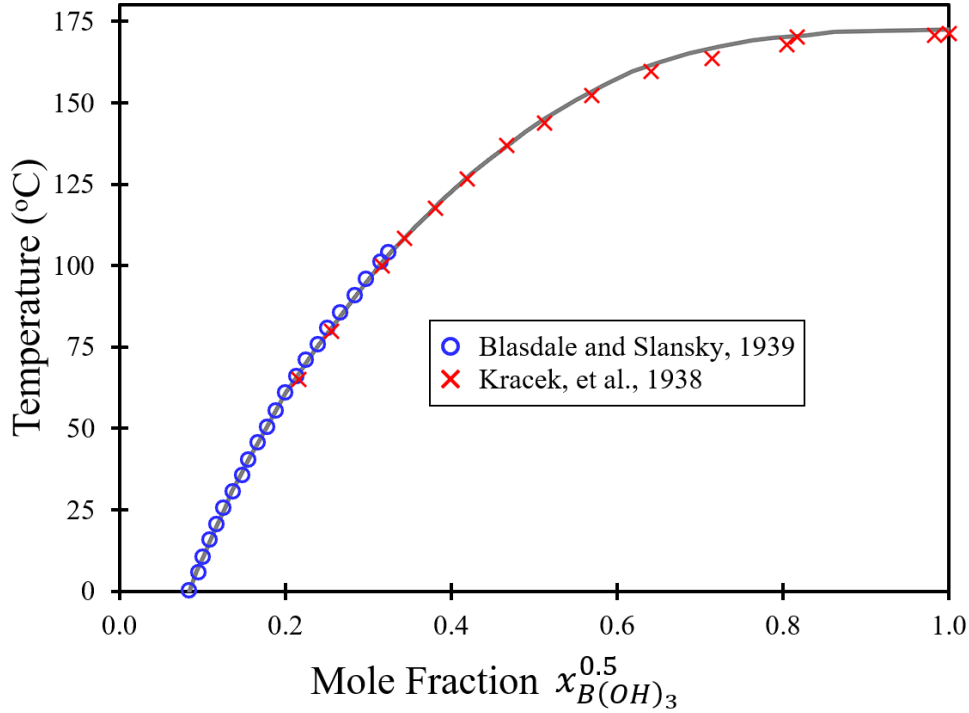
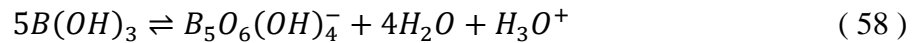


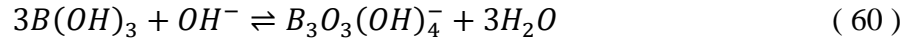
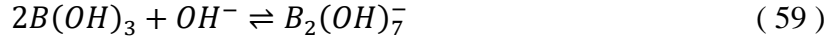
Figure 22. Solubility of boric acid in water as a function of temperature, where the symbols are experimental data and the line is calculated from the MSE model by Wang et al. (data taken from (Wang, et al., 2013))

Contrary to the model used by Wang et al., evidence was reported in 2011 by Zhou et al. for the formation of a *monovalent* pentaborate species at room temperature using Raman spectroscopy, by the reaction:



while also confirming the existence of the triborate $B_3O_3(OH)_4^-$ and tetraborate $B_4O_5(OH)_4^{2-}$ species in concentrated solutions (Zhou, et al., 2011). The existence of a pentaborate species was further confirmed later by Applegarth et al. in 2017 using Raman spectroscopy, and their *ab initio* studies confirm its identity as the monovalent anion $B_5O_6(OH)_4^-$ (Applegarth, et al., 2017).

According to more recent experimental results on boron-containing aqueous solutions at PWR conditions, the diborate $B_2O(OH)_5^-$ and triborate $B_3O_3(OH)_4^-$ species are the main products of the ionization reactions of boric acid which form based on the following equilibria:



where triborate has been found as the main anionic species from 10 to 150 °C, while it is postulated that diborate would be the main species from 200 to 300 °C (Ferguson, et al., 2019).

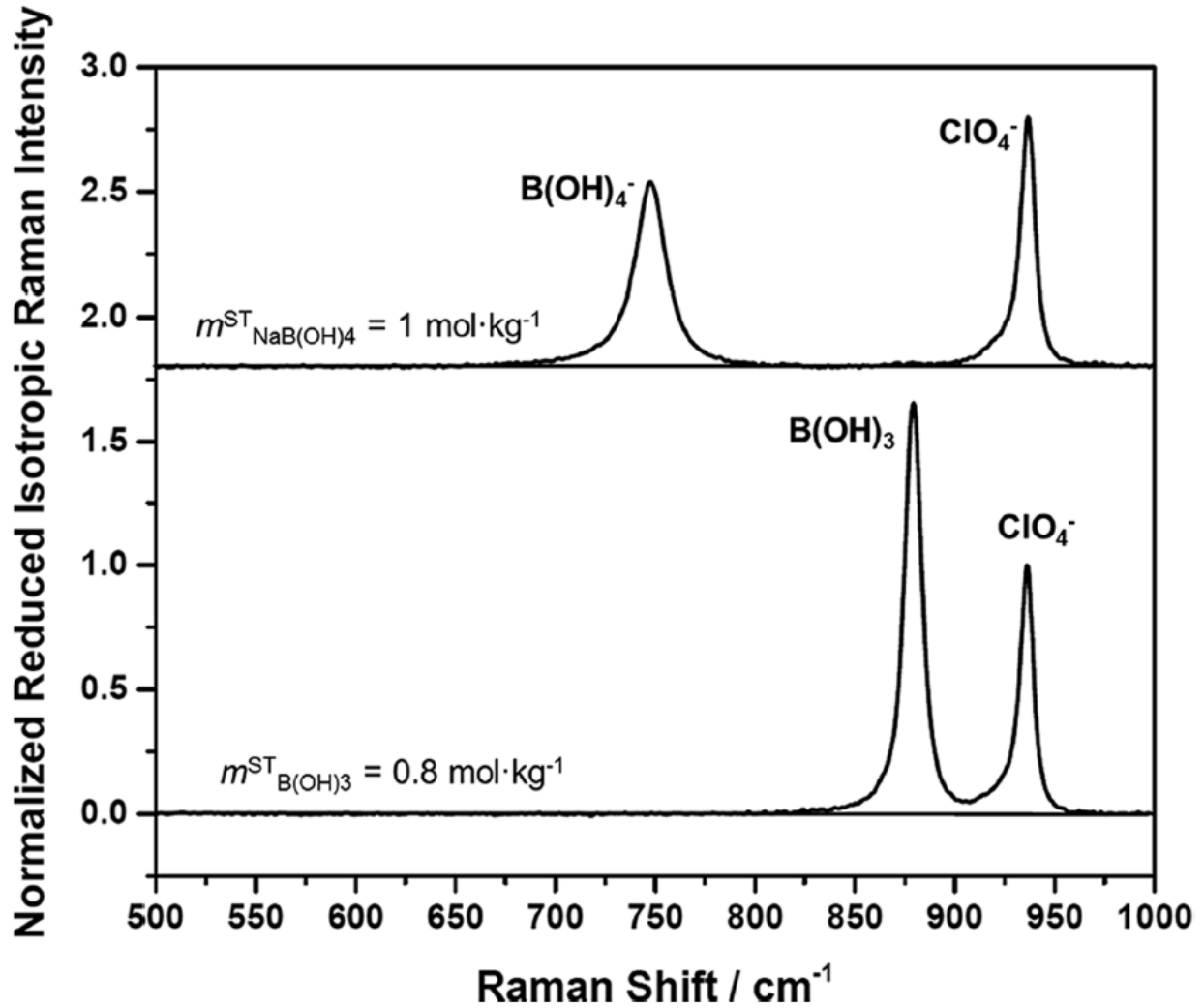


Figure 23. Reduced isotropic Raman spectra of a 1 mol kg⁻¹ sodium borate aqueous solution and a 0.8 mol kg⁻¹ boric acid aqueous solution, both with 0.087 mol kg⁻¹ NaClO₄ present as an internal standard, measured at 25 °C and 20 MPa (from (Sasidharanpillai, et al., 2019)).

Further studies on the speciation have been published by Tremaine and his collaborators, and in 2019 they published a study using Raman spectroscopy at high pressure (20 MPa) and up

to high temperature (300 °C) (Sasidharanpillai, et al., 2019). As shown in Figure 23, at room temperature there is only the borate ion signal present for nominally 100 % borate solutions and only the boric acid signal present in nominally 100 % boric acid solutions, and this behavior was confirmed for the boric acid solution up to 300 °C (which contradicts the claim by Wang et al. that metaboric acid HBO₂ would be significant and in equilibrium with the boric acid above 200 °C (Wang, et al., 2013)). However, in solutions with NaOH added as a buffer at a concentration ratio with the boric acid of $0 \leq R \leq 1$ they observe signals from the polyborate species, where the triborate ion $B_3O_3(OH)_4^-$ was found to be the major species present in the range of 25 to 300 °C for those boric acid-rich solutions.

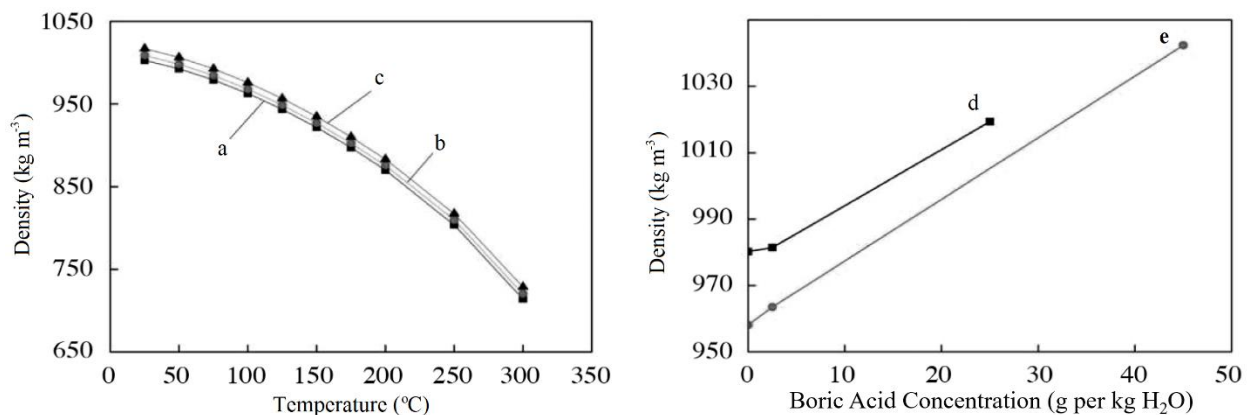


Figure 24. Density of boric acid solutions as a function of temperature (left) at pressure 10 MPa and boric acid concentrations 3.1 (a), 18.6 (b), and 43.4 g kg⁻¹ (c), and as a function of concentration (right) at pressure 0.1 MPa and temperatures 65.6 (d) and 100 °C (e) (adapted from (Morozov, et al., 2019)).

Morozov and his collaborators published several papers around 2019, detailing experimental results from their research on the physicochemical properties of boric acid solutions over a range of parameters (temperature, pressure, and acid concentration) characteristic of PWR conditions, including the density, viscosity, pH, and thermal conductivity (Morozov, et al., 2018; Morozov, et al., 2019; Morozov, et al., 2020). As shown in Figure 24, the density of a boric acid solution will decrease with temperature and increase with boric acid concentration. As seen by

Figure 25, the viscosity of a boric acid solution will decrease with temperature and increase with boric acid concentration. The degree of the pH decrease with increasing boric acid concentration is shown in Figure 26, and it is apparent the thermal conductivity of boric acid solutions will increase with temperature though decreases with the concentration of boric acid.

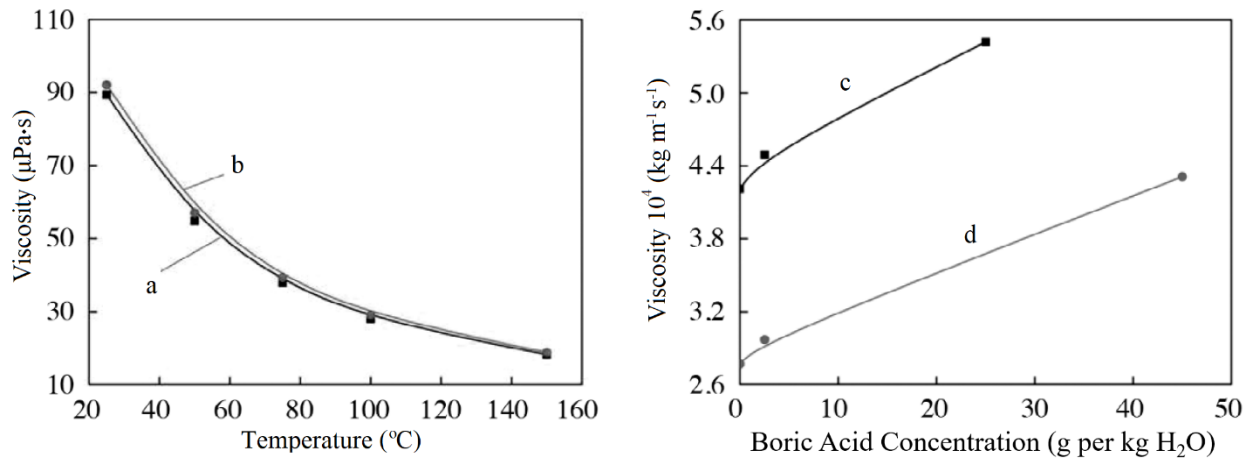


Figure 25. Viscosity of boric acid solutions as a function of temperature (left) at pressure 1 MPa and concentrations 2 (a) and 20 g kg^{-1} (b), and as a function of concentration (right) at pressure 0.1 MPa and temperatures 65.6 (c) and 100 $^{\circ}\text{C}$ (d) (adapted from (Morozov, et al., 2019)).

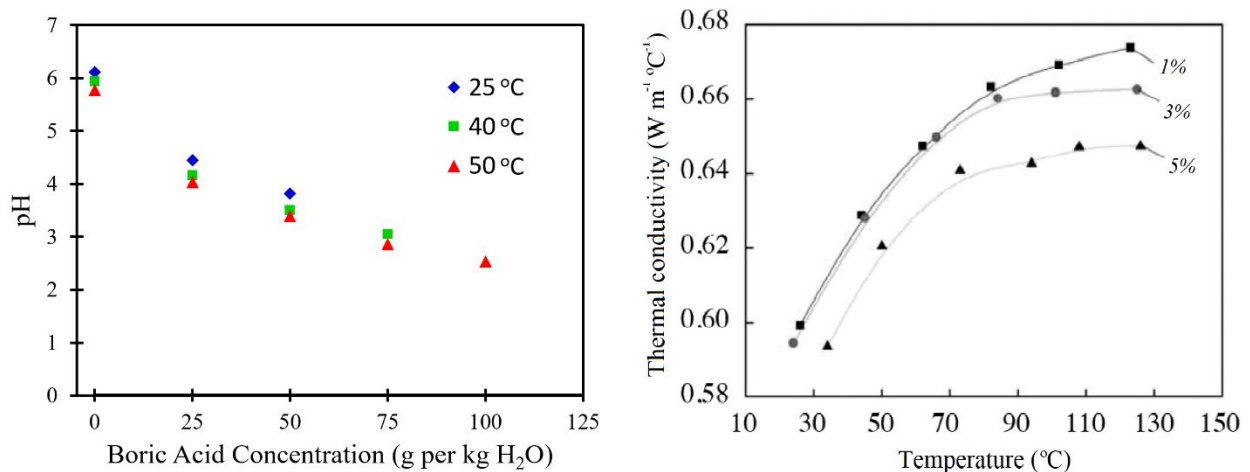


Figure 26. pH of boric acid aqueous solutions as a function of concentration (left) at three temperatures (data taken from (Morozov, et al., 2020)), and thermal conductivity as a function of temperature (right) at pressure 10 MPa and boric acid concentrations 1, 3, and 5 % (adapted from (Morozov, et al., 2019)).

Additionally, aqueous boric acid buffer solutions are commonly mixed (as is the case in the second half of this work) using “borax,” known more accurately as sodium tetraborate

decahydrate ($Na_2B_4O_7 \cdot 10H_2O$), which will readily dissolve in the water, dissociating to boric acid, borate, and sodium ions. In solutions of such a nature, it is well-known that the positively charged Na^+ ions can associate with the negatively charged $B(OH)_4^-$ borate ions to form ion pairs (Pokrovski, et al., 1995), by the reaction:



The association constant K_A is defined by the ratio of paired/unpaired ion concentrations by:

$$K_A = \frac{[NaB(OH)_4^0]}{[Na^+][B(OH)_4^-]} \quad (62)$$

$$pK_A = \log_{10}[K_A] \quad (63)$$

The association constants for $NaB(OH)_4^0$ experimentally obtained by Pokrovski et al. as a function of temperature as well as a curve they generated using the revised Helgeson-Kirkham-Flowers equation of state model are shown in Figure 27.

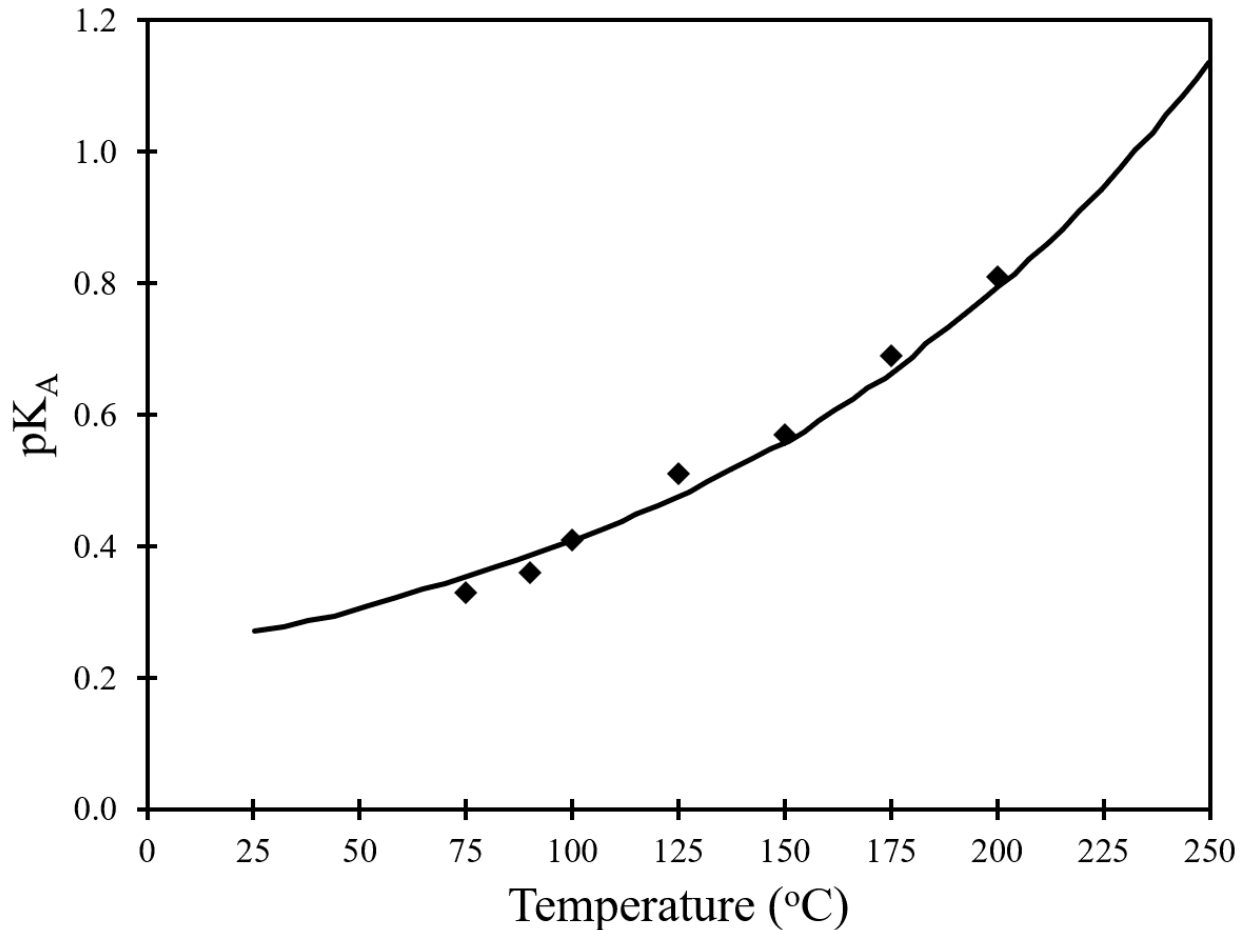


Figure 27. Logarithm of the association constants for $\text{NaB}(\text{OH})_4^0$ as a function of temperature at saturated vapor pressure for experimental data (diamond symbols) as well as a curve generated by the revised Helgeson-Kirkham-Flowers equation of state model (data taken from (Pokrovski, et al., 1995)).

1.8 Other Considerations of Reactor Chemistry

More accurate determinations of the $^{10}\text{B}(\text{n},\alpha)^7\text{Li}$ product yields up to high temperatures as well as the elucidation of the borate reaction with $\cdot\text{OH}$ radicals would both be highly beneficial contributions to efforts in resolving other closely related aspects of NPP water chemistry. Those for which this work is most relevant are described presently.

1.8.1 Axial Offset Anomaly

A reactor is overall a non-isothermal system, heated by means of forced convection. Typical nuclear reactors have their fuel rods oriented vertically and flow low temperature coolant

water upwards along them from the bottom, and this thermal gradient results in an “axial offset” which is defined by a difference in power between the top half of the core and the bottom half as:

$$Axial\ Offset\ \% = \frac{(P_{top} - P_{bottom})}{(P_{top} + P_{bottom})} \times 100 \quad (64)$$

where P_{top} and P_{bottom} are the integrated power in the top and bottom halves of the core (Deshon, 2004). Historically, any core-wide deviation greater than 3 % has been considered significant, and an Axial Offset Anomaly (AOA) is defined by the EPRI to be a significant deviation of the measured axial offset from its predicted performance (Deshon, 2005).

The power shift characteristic of AOA has a number of serious safety implications and can threaten to alter the full power shutdown margin, thereby forcing a costly down-rating of the reactor’s power output. As of 2004, among eighteen different PWRs in the U.S., there have been 37 fuel cycles confirmed to have experienced AOA (Deshon, 2004), up from 20 as of 2001, with one case being serious enough that the plant was derated to 75 % power for several months over the final third of its operating cycle, culminating in an estimated economic penalty of ca. \$20 million (Frattoni, et al., 2001; Deshon, 2004).

An example of the effect of AOA on the axial offset as experienced over a portion of the fuel cycle in a Westinghouse NPP, wherein the AO is measured more negative than the predicted values due to a shift in the power output towards the bottom of the core resulting from a suppression of the neutron flux in the upper regions of the core. The root cause has been identified as the buildup of corrosion product (often referred to as “crud”) depositions on the fuel cladding assemblies as a result of Sub-cooled Nucleate Boiling (SNB), wherein the soluble boron neutron absorbers are incorporated into the developing porous structures at concentrations high enough to cause a decrease in the neutron flux.

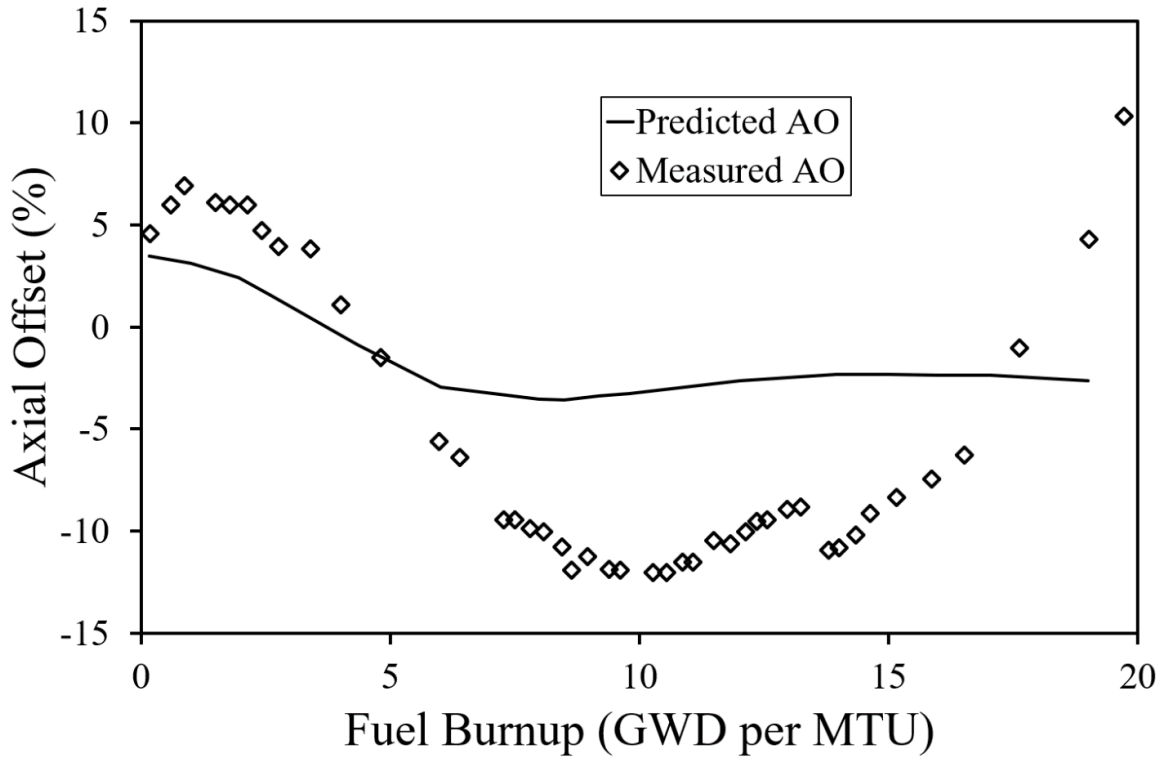


Figure 28. Data from a Westinghouse plant exhibiting Axial Offset Anomaly, plotted as the Axial Offset in the core versus the degree of Fuel Burnup in the reactor (GigaWatt Days per Metric Ton of Uranium) (adapted from (Deshon, 2004)).

In a typical PWR, the coolant temperature at the core's inlet is below 50 °C and is heated primarily by forced convection with a very high heat flux from the cladding. SNB is a highly localized phenomenon, occurring when the heated fuel cladding walls in contact with the liquid water coolant exceed the saturation (boiling) temperature, and when encountering a nucleation site the superheated liquid will briefly evaporate. A schematic showing this process is given in Figure 29. This evaporation promotes the deposition of corrosion products onto the cladding, thus increasing the availability of surface imperfections for the coolant to boil upon.

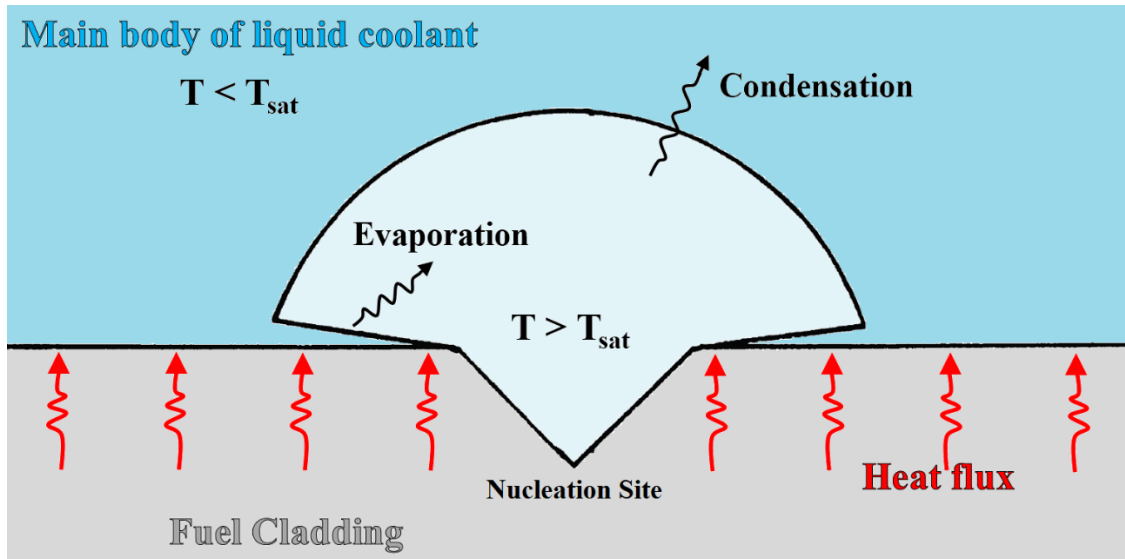


Figure 29. Schematic of Sub-cooled Nucleate Boiling at a nucleation site on the fuel cladding (adapted from (Deshon, 2004)).

The amount of crud deposition is roughly proportional to the degree of SNB, and the generation of an evolving porous “chimney” structure has been observed in the formation of these deposits, as shown in Figure 30. The thermal hydraulic behavior of these chimneys is often modeled based on Cohen’s one dimensional Wick Boiling model (Cohen, 1974; Henshaw, et al., October 2006), wherein capillary forces at the coolant-chimney interface draw coolant through interconnected channels to the cladding surface, the subsequent vapor formed then escapes out the chimney and this drives the capillary action. Corrosion products as well as coolant additives like boric acid are drawn in as well via this capillary action to the cladding interface.

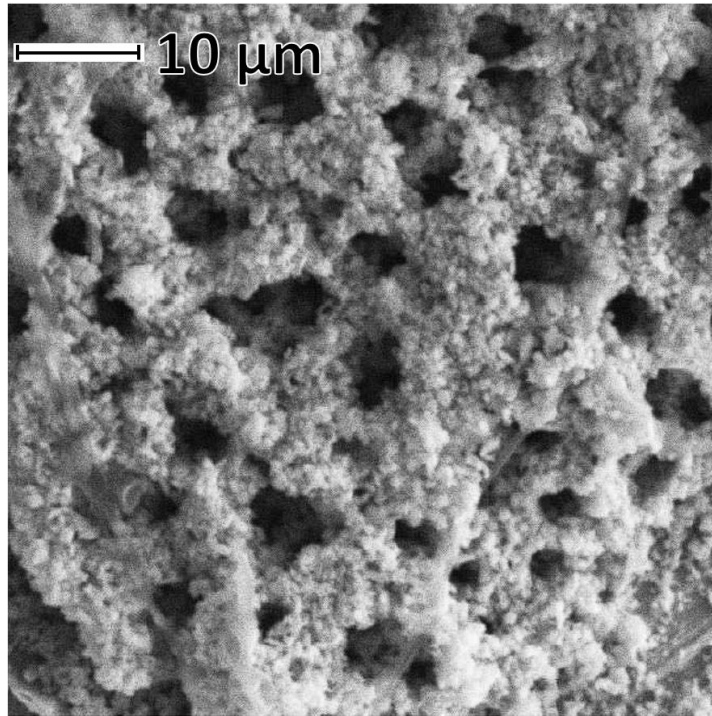
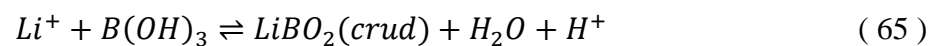


Figure 30. SEM of a crud flake exhibiting boiling chimneys (adapted from (Deshon, 2004)).

Among several other boron “hideout” mechanisms which will not be discussed, the modeling work of Henshaw et al. in 2006 supports precipitation of lithium metaborate as a significant mechanism (>99 %) for boron uptake within porous layers of crud by the reaction:



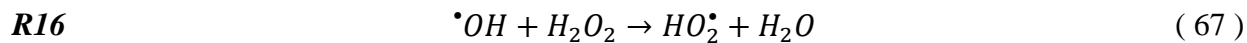
at much smaller crud thicknesses than previous models predict because their model accounted for the rise in saturation temperature towards the bottom of the crud structures and since the solubility of LiBO_2 decreases with rising temperature it thus precipitates in such conditions (Henshaw, et al., 2006). The AOA phenomenon is therefore attributed to the crud deposition serving as the substrate for concentrating boron species which then act to depress the neutron flux in the upper sections of the fuel assembly. AOA will be an increasingly pervading issue as PWRs are continuing to be uprated, and so it is of major concern to this field of study that the radiolysis chemistry of water,

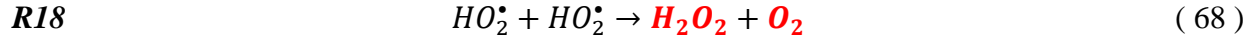
in particular the alpha dose from the $^{10}\text{B}(n,\alpha)^7\text{Li}$ reaction, as well as the boric acid chemistry in the chimney regions are better understood.

1.8.2 Critical Hydrogen Concentration

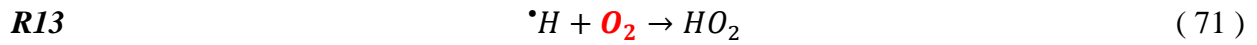
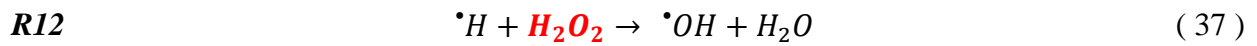
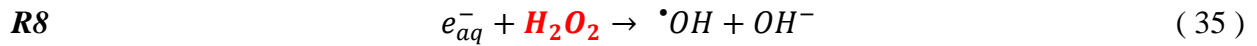
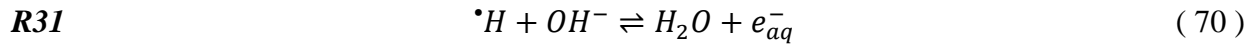
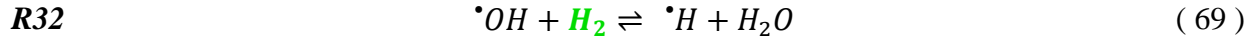
Oxidative corrosion is an extremely important aspect of the aqueous chemistry that occurs in a nuclear reactor, as was discussed in Section 1.6.2. The concentrations of oxidants and reductants are not what intrinsically controls stress corrosion cracking susceptibility, rather it is the corrosion potential (Was, et al., 2011). Significant changes in corrosion potential are in most cases accompanied by large changes in crack growth (i.e., IASCC), e.g. an electrode potential change from an oxidative state with 2 ppm O_2 (0.15–0.20 V_{SHE}) to a reductive state with 0.02–0.20 ppm H_2 (-0.50–0.54 V_{SHE}) (Was, et al., 2011), since the rate of an electrochemical reaction is very sensitive to small changes in electrode potential, as was discussed in Section 1.1.8.1.

In order to curb the production of oxygen and hydrogen peroxide in the primary coolant system of a power plant, a small amount of hydrogen is typically dissolved in the water (Macdonald, 1992). Through chemical kinetics, this addition of hydrogen suppresses the production of oxygen and other oxidative species, resulting in no net radiolysis as the longer-lived molecular products are destroyed by the short-lived radicals in a chain reaction. The minimum value of hydrogen required to completely suppress the production of these oxidative species is called the Critical Hydrogen Concentration (CHC). The dissolved H_2 reacts with the oxidizing $\cdot\text{OH}$, converting it to a reducing $\cdot\text{H}$ atom. The relevant chemical reactions for the production of these oxidative species are shown below:





where, again, the **R** reaction numbering scheme is taken from (Elliot & Bartels, 2009). The destruction of these species is carried out by the following reactions:



The EPRI guidelines instruct the addition of H₂ to PWR coolant at concentrations between 25–50 scc/kg (EPRI, 1999). However, experimental research indicates that the CHC is somewhat less than 10–15 scc/kg (Bartels, et al., 2012), with some results as low as 0.5 scc/kg (Elliot & Stuart, 2008) as shown quantitatively in Figure 31; furthermore, modeling research by Bartels et al. that was based on the most recent experimental chemical kinetic data at high temperatures (>300 °C) also suggests this minimum required level of dissolved hydrogen for preventing the net radiolytic breakdown of the water is “well below 10–15 scc/kg” (Bartels, et al., 2012).

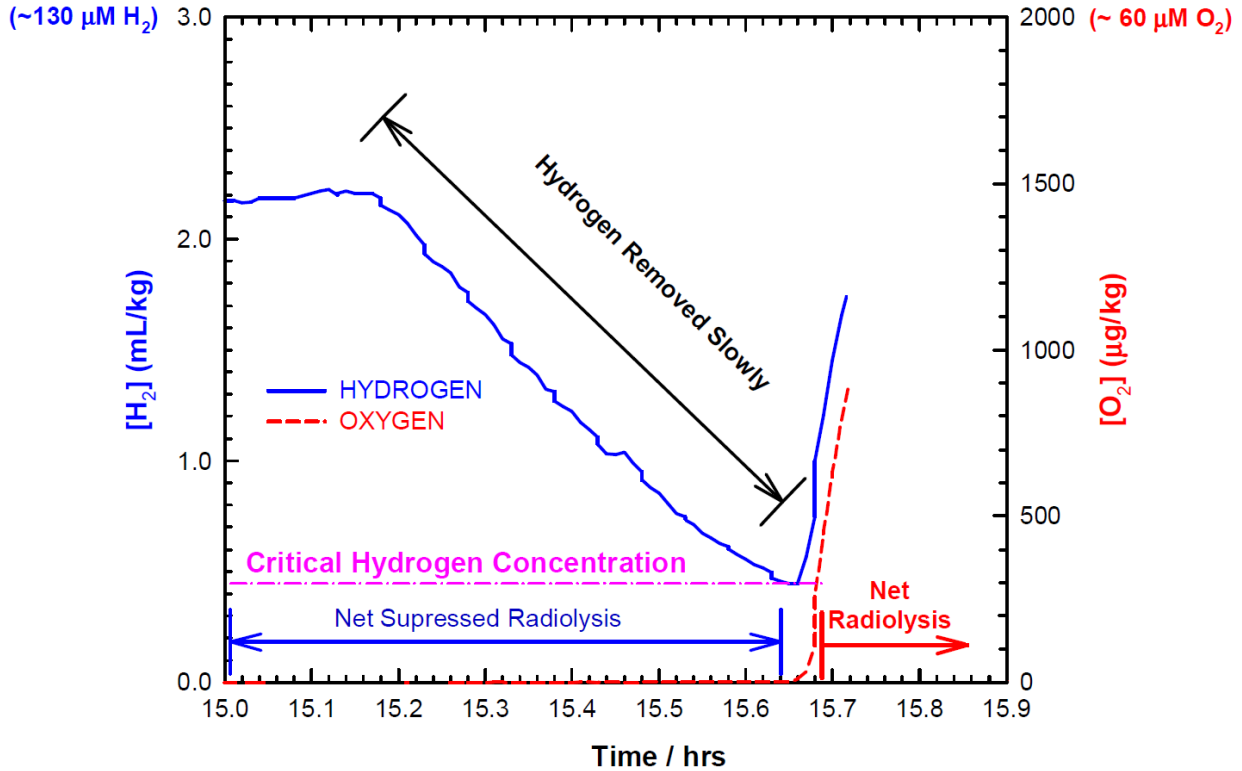


Figure 31. Experimental results by Elliot & Stuart on measuring the CHC for suppression of net radiolytic production of H₂ and O₂ for non-boiling water in the Chalk River NRU reactor U-2 loop (adapted from (Elliot & Stuart, 2008)).

Modeling shows at 300 °C and higher that the CHC is determined almost entirely by the equilibrium constant of the **R32** reaction (69) (Kanjana, et al., 2013); moreover, the ratio of yields of radicals versus the molecular products H₂ and H₂O₂ by radiolysis is a significant determining condition, and unfortunately their G-values for non-gamma radiolysis are by far the largest uncertainty in the modeling of these systems (Bartels, et al., 2013).

1.8.3 Hydrogen embrittlement

The upper limit on the concentration of added hydrogen in PWR primary coolant is determined mainly by concerns over another degenerative process, commonly known as “hydrogen embrittlement,” affecting stainless steel components and the zircalloy fuel-cladding material (Zieliński & Sobieszczyk, 2011). Although this terminology is representative for

macroscopic scale, it may be judged unsuitable when considering the mechanisms involved. Penetration of atomic hydrogen into metal surfaces can lead to the “dissolved” hydrogen reacting to form brittle hydride compounds, or interactions between the hydrogen and the metal matrix such as the movement of dislocations at nanoscale (known as “slipping”) and micro-void coalescence (Fontana, 2005; Zieliński & Sobieszczyk, 2011). Stress corrosion cracking (SCC) will involve crack progression transgranularly, intergranularly, or a combination of these, and the further development and growth of cracks depends on the material and its environment, wherein hydrogen can assist transgranular crack development and growth (Bardal, 2003). As this process involves the degradation of a material through interactions with its environment, it should be considered more generally a corrosive process, as “hydrogen degradation” (HD). Although the main mechanism of HD is unclear and the debate is still ongoing, the most responsible mechanisms agreed upon are hydrogen-enhanced decohesion (HEDE), adsorption-induced dislocation emission (AIDE), and hydrogen-enhanced localized plasticity (HELP) (Dwivedi & Vishwakarma, 2018).

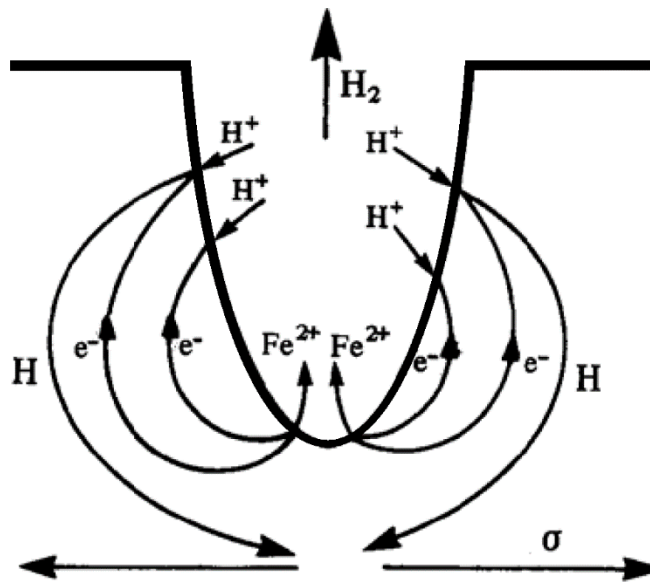


Figure 32. Process of the hydrogen degradation mechanism at crack front (adapted from (Bardal, 2003)).

In the case of nuclear reactors, the mechanism of most concern is HEDE as it is associated with a decrease in atomic bond strength at a grain boundary due to hydrogen segregation, reducing the cohesive strength of such interfaces and thus initiating/propagating cracks along them when applied stresses exceed the material's cohesive strength (Katzarov & Paxton, 2017). The stress intensity at the crack tip is the determining quantity for whether a crack will propagate and can be expressed as the stress intensity factor K by the following equation:

$$K = Y\sigma\sqrt{\pi x} \quad (72)$$

where σ is the nominal stress, x is the crack length, Y is a geometrical function that depends on the shape of the component and orientation of the load relative to the crack, and there exists a critical value K_C above which the crack will propagate (Bardal, 2003). A simple depiction is shown in Figure 32, where at the site of a crack in a hydrogen ion-rich environment there are hydrogen atoms from a cathodic reaction which diffuse into the metal (particularly in front of the crack since that is where tensile stress is highest) making it more brittle by obstructing plastic deformation thus increasing stress concentration at the tip (Bardal, 2003).

1.8.4 Hydrated electron bimolecular reaction

In the early stages of studying radiation chemistry of water, among the many steps clarified in the radical mechanism thus confirming the existence of reactive species besides $\cdot\text{H}$, $\cdot\text{OH}$, and H_2O_2 was the additional complication that there appeared to be two types of hydrogen atoms which possessed different reactivities (Jonah, 2010). After being dissuaded from an electron having any significant chemical lifetime, Frederick Dainton and co-workers measured the ionic strength effect dependence and showed the second "H atom" had a negative unit charge (Collinson, et al., 1962). The observation and measurement of an absorption in the 700 nm range by what came to be

identified as this electron as well as the subsequent acquisition of the full spectrum were both major milestones for pulse radiolysis, and thus allowed direct measurements of the rate of its reactions with an ever-increasing variety of inorganic and organic species (Jonah, 2010). The spectrum used for electron dosimetry analysis as part of this work, for which the methodology is detailed in Section 6.1, is shown in Figure 33. It has been experimentally and theoretically confirmed in many ways that when generated in aqueous solutions: their charge density is considered localized in a cavity of radius ca. 2.5 Å (1 angstrom is 0.1 nm, and the hydrogen atom is considered to have a radius of 0.25 Å (Slater, 1964)), and they are surrounded by ca. 4 water molecules (two are bonded to the electron and the others participate in the water-water network) (Novelli, et al., 2023). This electron is therefore considered to be “dissolved” within the solution, and thus is referred to as a fully relaxed, solvated, or hydrated electron, or simply as e_{aq}^- (as is the case throughout this work). Its nature as the simplest case of a quantum particle existing in a complex thermochemical system continues to compel scientific intrigue towards understanding its fundamental characteristics and interactions.

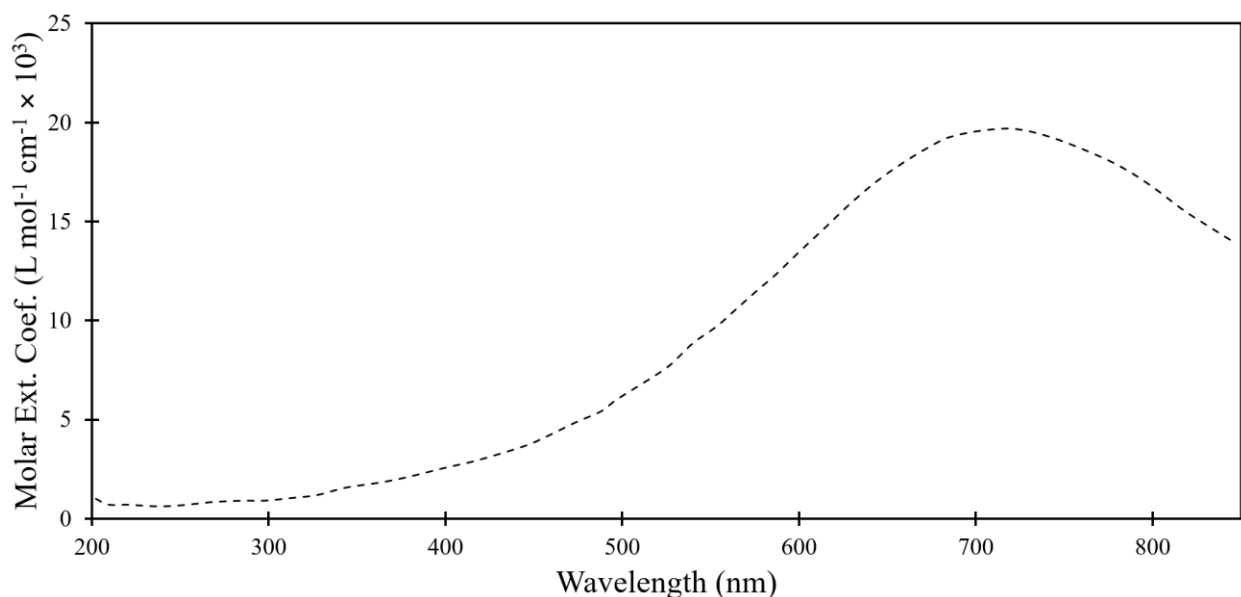
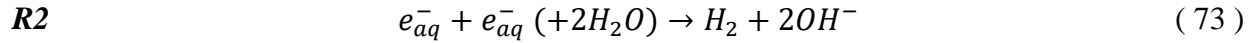


Figure 33. The molar extinction coefficient of the hydrated electron as a function of wavelength at room temperature (data taken from (Torche & Marignier, 2016)).

One of the main mechanisms for the production of H_2 in the radiolysis of water, which is important for correctly predicting radiation effects in primary coolant systems of PWRs, is the reaction between two e_{aq}^- in a bimolecular recombination reaction as:



However, this reaction has long been considered puzzling from a mechanistic viewpoint due in part to the peculiar nature of e_{aq}^- itself, specifically that reaction **R2** experimentally lacks an observed ionic strength effect at room temperature (Schmidt & Bartels, 1995) and exhibits a decrease in the reaction rate above 150 °C in alkaline conditions (Christensen & Sehested, 1986; Marin, et al., 2007).

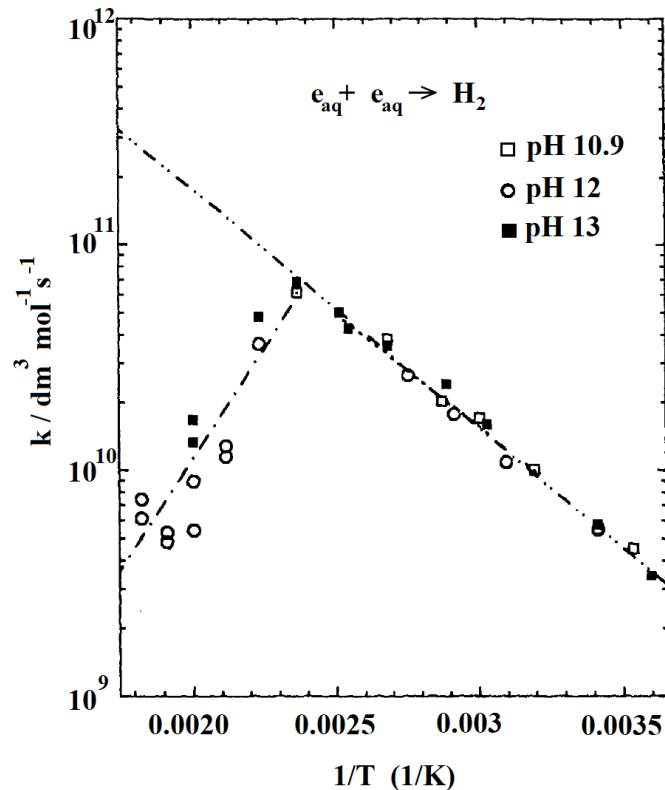


Figure 34. Arrhenius plot of data for reaction (73) in alkaline conditions. The fit above 150 °C is shown for alkaline conditions, as well as the Arrhenius fit below 150 °C and its extrapolation to higher temperatures (figure adapted from (Elliot, 1994) who uses data from (Christensen & Sehested, 1986)).

Deliberation on these issues and their root causes are on-going. Previous suggestions included: the reversible formation of a dielectron $(e_2^{2-})_{aq}$ which would slow the decay of e_{aq}^- from competition of its protonation and dissociation (Christensen & Sehested, 1986), the dielectron decaying solely via protonation and subsequently forming a hydride cation (H^-) which reacts with water to form the H_2 and OH^- products (Swiatla-Wojcik & Buxton, 1995) to explain the differing behavior between alkaline and non-alkaline systems (where protonation would be favored), and the dielectron pairs being solvent-separated and less stable at high temperatures which decreases the probability of protonation (Marin, et al., 2007). However, work by Savolainen et al. in 2014 using optical-pump-terahertz-probe transient spectroscopy showed that the signal of a delocalized pre-solvated electron decays within ca. 0.2 ps, followed by its localization/solvation to e_{aq}^- (Savolainen, et al., 2014). With such an extremely short lifetime for the dielectron (if indeed that can be confirmed as the species detected, though to be clear this is not yet the case), then the inclusion/omission of a mere 1×10^{-4} M concentration of KOH (as used in kinetics experiments to scavenge protons to provide alkaline conditions (Marin, et al., 2007)) could not possibly make any difference to the reaction probability. The reaction should thus be considered as occurring with the water itself.

In summary, experimental results so far obtained have not given rise to a satisfying consensus in the radiolysis community on the appropriate mechanism, on the rates in nonalkaline conditions at temperatures above 150 °C, nor on their significance in Low- vs. High-LET track recombination and escape yields. The results obtained in part of this work are expected to prove promising in offering further insight pertaining to the last.

1.9 Boron Neutron Capture Therapy

A more accurate determination of the $^{10}\text{B}(n,\alpha)^7\text{Li}$ product yields at room temperature could also be a valuable contribution to efforts in less directly related branches of research. One such field is in medicine, for a specific modality which has been shown effective in combatting some of the most malignant and aggressive forms of cancer.

Boron has also been utilized in neutron cancer treatment as part of a re-emerging therapy technique known as Boron Neutron Capture Therapy (BNCT). Radiation has long been known to induce many chemical changes in biological systems. Ever since the proposed therapeutic potential of neutron irradiation published in 1935 by Gordon Locher, it has been extensively confirmed as an effective treatment with new innovations continuously being investigated for improvement. Radiation therapy is required in the treatment of at least 50% of all cancer patients (Wang, et al., 2022). BNCT employs a binary system, where the delivery of boron compounds acting as radiosensitizers to tumor tissues is combined with a targeted neutron radiation technique. This makes it theoretically superior to conventional radiotherapy modalities since it enables the manipulation of either component independently, and promotes the *selective* irradiation of cancer cells (Barth, et al., 1990; Yokoyama, et al., 2006). The neutron fluence is considered non-ionizing, using either thermal neutrons ($E_{\text{th}} < 0.4\text{eV}$) or deep tissue-penetrating epithermal neutrons ($0.4\text{eV} < E_{\text{epi}} < 10\text{keV}$) that will be slowed to thermal levels by collisions with atoms (primarily hydrogen), which will then be captured by boron (Coderre & Morris, 1999). The thermal neutron capture cross section of ^{10}B (3835 barns) is relatively high compared to other elements common to normal tissues in humans, as seen in Table 1, and is favored over other nuclides with similar relatively high cross sections since ca. 20% of natural boron is ^{10}B , making it readily available, and because the $^{10}\text{B}(n,\alpha)^7\text{Li}$ fission products' path lengths are 10-14 μm , which is approximately one cell diameter

(Barth, et al., 1992). Additionally, boron is the only non-metal Group 13 element and is capable of forming covalent bonds much like carbon and silicon, though it is considered electron deficient as it has only three external electrons for its four bonding orbitals. This particular electron configuration makes it easy to incorporate into organic compounds, leading to a diverse, complex, and extensive variation of nontoxic chemical forms, which makes the element even more attractive for use in neutron capture therapy (Sauerwein, et al., 2012). These ^{10}B -labeled compounds are likely to be incorporated at higher concentrations within tumors compared to neighboring tissue due to the cancer cells' accelerated metabolism along with other possible influential factors, e.g. a compromised/absent blood-brain barrier, and so will result in an immense dose gradient between tumor cells and normal cells (Barth, et al., 1990; Nedunchezian, et al., 2016).

Table 1. Thermal neutron capture cross-section values of normal tissue elements, given in barns (from (Barth, et al., 1990)).

Element	Cross-section	Element	Cross-section
H	0.332	N	1.75
Na	0.536	P	0.19
K	2.07	O	<0.0002
Mg	0.069	S	0.52
Ca	0.44	Cl	33.8
C	0.0037	Fe	2.62

DNA strand and double-strand breaks are closely correlated with radiation-induced cell death (Holley, et al., 1990) and can be brought about through either (a) direct action, where energy is deposited straight onto the DNA sugars and bases thus disrupting the molecular structure, or (b) indirect action, where radicals created by energy deposition on water molecules (radiolysis) will go on to abstract hydrogen from the DNA thus causing a break. The rate of hydrogen abstraction from DNA by $\cdot\text{H}$ is much less than by $\cdot\text{OH}$ (Chatterjee & Holley, 1990). However, $\cdot\text{OH}$ can be lost to reactions with other water radicals, and so all of them must be taken into consideration when

evaluating overall chemical and biochemical processes. The majority of damage to DNA by High or Low LET radiation is thought to arise indirectly through production of reactive oxygen species, however radiotherapy with Low LET requiring oxygen to enhance the effects of biological radiation can be hindered by the malignant tumor cells' aggressive proliferation rapidly consuming oxygen, effecting radioresistance in these cells (Allen, et al., 2011). As water represents ~65% of human weight, it is a major constituent in all cells and so the High LET α -particle and lithium ion can enact the same devastating effect on cells in either oxygen-rich or hypoxic environments (Hada & Georgakilas, 2008). While $\cdot\text{OH}$ reacts efficiently with proteins that comprise ~20% of human weight, other products in the dense ionization tracks from High LET (such as H_2O_2 , e_{aq}^-) would be trapped by oxygen to create superoxide ($\text{O}_2^{\cdot-}$) which hardly reacts with proteins, and so the mechanisms of BNCT may be enhanced in hypoxic conditions (Kusumoto & Ogawara, 2019). Hydrogen peroxide is toxic to the DNA structure, undergoing a Fenton reaction ($M^+ + \text{H}_2\text{O}_2 \rightarrow M^{2+} + \text{OH}^- + \cdot\text{OH}$) with a variable valency metal ion bound to the DNA to produce $\cdot\text{OH}$ which will cause a strand break, where the yield of strand breaks is expected to be linearly dependent on the H_2O_2 concentration (Ward, et al., 1987). These strand breaks occur when hydrogen is abstracted from one of the five carbon positions on the deoxyribose moiety (the group of atoms responsible for characteristic chemical reactions) and double strand breaks are considered to be when there are breaks on opposite strands within 10 base pairs, where the High LET of $^{10}\text{B}(n,\alpha)^7\text{Li}$ products yields very clustered DNA damage which is difficult (if not outright impossible) for a cell at any cancer cycle phase to repair and survive (Chatterjee & Holley, 1990; Wang, et al., 2022). As with modeling of NPP PWR water chemistry, simulations for dosimetric results of BNCT (such as in (Brandão & Campos, 2009)) could be improved by additional data for yields of H_2 and H_2O_2 by the $^{10}\text{B}(n,\alpha)^7\text{Li}$ reaction.

1.10 Previous Works on G(H₂) for ¹⁰B(n,α)⁷Li

As previously mentioned, there is a scarcity of radiation yield measurements for the ¹⁰B(n,α)⁷Li reaction in aqueous solutions. Although H₂O₂ was previously declared here as a primary species of concern in PWR water chemistry for its troublesome enhancement of the degradative corrosion process, quantifying its production at high temperatures and high pressures is challenging because it catalytically decomposes on metal surfaces and thus is lost to the very same corrosion reactions which make its presence a concern. However, the H₂ yield from the radiolysis induced by the ¹⁰B(n,α)⁷Li fission event is expected to be virtually identical, as can be demonstrated by simple mass balance:



and is adequately stable for reliable, accurate quantification. Furthermore, the other considerations in NPP reactor chemistry described in Section 1.8 indicate that H₂ is as well a primary species of concern in PWR water chemistry by its own right, particularly for its beneficial suppression of the H₂O₂ as well as other oxidative species. These fundamental characteristics are the driving force behind the interest for part of this work to be measuring this H₂ yield at conditions corresponding to those found in PWRs. Herein is a report on the values currently available which have been obtained in previous works for the H₂ produced by the ¹⁰B(n,α)⁷Li recoil ions.

1.10.1 Early work

Barr and Schuler reported yields for G(•H), G(•OH), and G(H₂O₂) by the ¹⁰B(n,α)⁷Li reaction in an aqueous 0.4 M sulfuric acid solution using spectrophotometric detection of the oxidation of ferrous ions (Fe²⁺) (Fricke dosimetry) and reduction of ceric ions (Ce⁴⁺) both with and without the presence of dissolved oxygen, arriving at a value of G(-H₂O) = 0.367 μmol/J for the net water decomposition yield (Barr and Schuler, 1956; Schuler and Barr 1959). Yokohata and

Tsuda calculated $G(e_{aq}^-)$ from the $^{10}\text{B}(n,\alpha)^7\text{Li}$ radiolysis in a neutral aqueous solution by measuring the N_2 generated through the reaction of hydrated electrons with N_2O (Yokohata & Tsuda, 1974). Later, LaVerne and Schuler reported on the same product yields in the Fricke dosimeter solution generated from individual accelerator-produced alpha particles and $^7\text{Li}^{1+}$ ions, and their results are comparable with the yields by Barr and Schuler with a value of $G(-\text{H}_2\text{O}) = 0.293 \mu\text{mol/J}$ (LaVerne & Schuler, 1987).

In 2006, Hilbert Christensen gave a report on the state of the art of radiolysis in nuclear reactors, including a compilation and assessment on the available values of important parameters for computer simulations of these processes. For H_2 production by $^{10}\text{B}(n,\alpha)^7\text{Li}$, he lists experimental and simulation results at room temperature from several sources (Jenks & Griess, 1967; Lefort, 1958) and provides his own recommended value of $0.145 \mu\text{mol/J}$ (Christensen, 2006), as well as calculated results for ca. 300°C (Bjergbakke, et al., 1984; Lundgren, et al., 2004). These reported values are displayed in Figure 35.

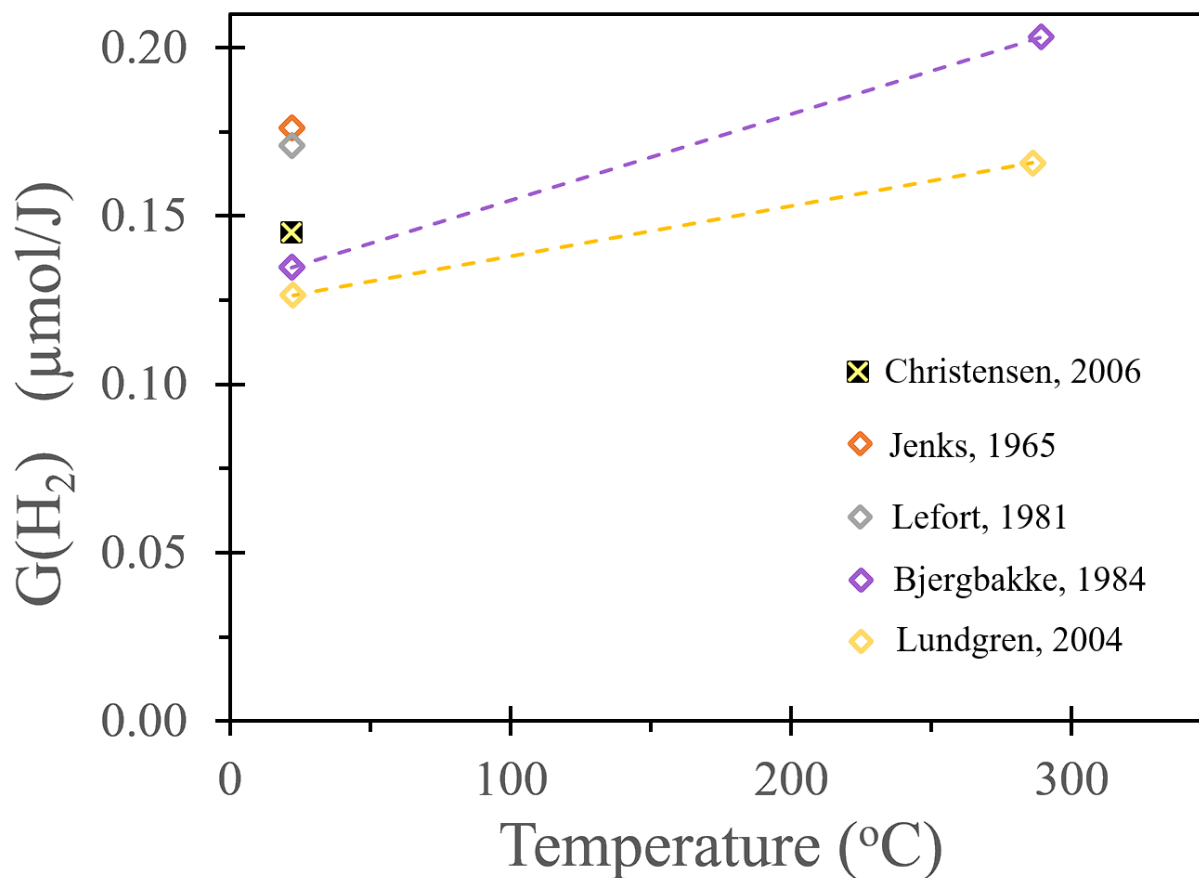
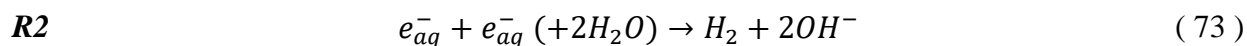


Figure 35. Values in the report by Christensen for early works on determining $G(H_2)$ from $^{10}B(n,\alpha)^7Li$ at room temperature and ca. 300 °C (Christensen, 2006).

1.10.2 Recent simulation work

Monte Carlo track chemistry simulations on the radiolysis yields from the $^{10}B(n,\alpha)^7Li$ reaction in aqueous solutions up to 350 °C were carried out by Islam et al. at Sherbrooke University in 2017 (Islam, et al., 2017). They performed simulations using two different rates above 150 °C for the bimolecular reaction of the hydrated electron.



As was mentioned during the discussion in Section 1.8.4 on the hydrated electron, reaction **R2** was measured above 150 °C in alkaline conditions by Christensen & Sehested and exhibited a decrease in the reaction rate (Christensen & Sehested, 1986). A.J. Elliot later used the results by Christensen

& Sehested to make an Arrhenius extrapolation to higher temperatures (Elliot, 1994), as shown previously in Figure 34. The rates calculated via this methodology have been employed repeatedly in models for comparison with the experimental alkaline rates. The AECL review by Elliot & Bartels in 2009 gave recommended rates updated based on the more recent experimental values for alkaline conditions (pH >10) of Marin et al. in the year prior, and it was these rates which Islam et al. applied in their simulation (Marin, et al., 2007; Elliot & Bartels, 2009; Islam, et al., 2017). The experimental rates and the rates calculated from the lower temperature rates by Arrhenius extraction up to above 150 °C which they use are shown in Figure 36, and the simulation results for G(H₂) are shown compared to other recent results in Figure 39.

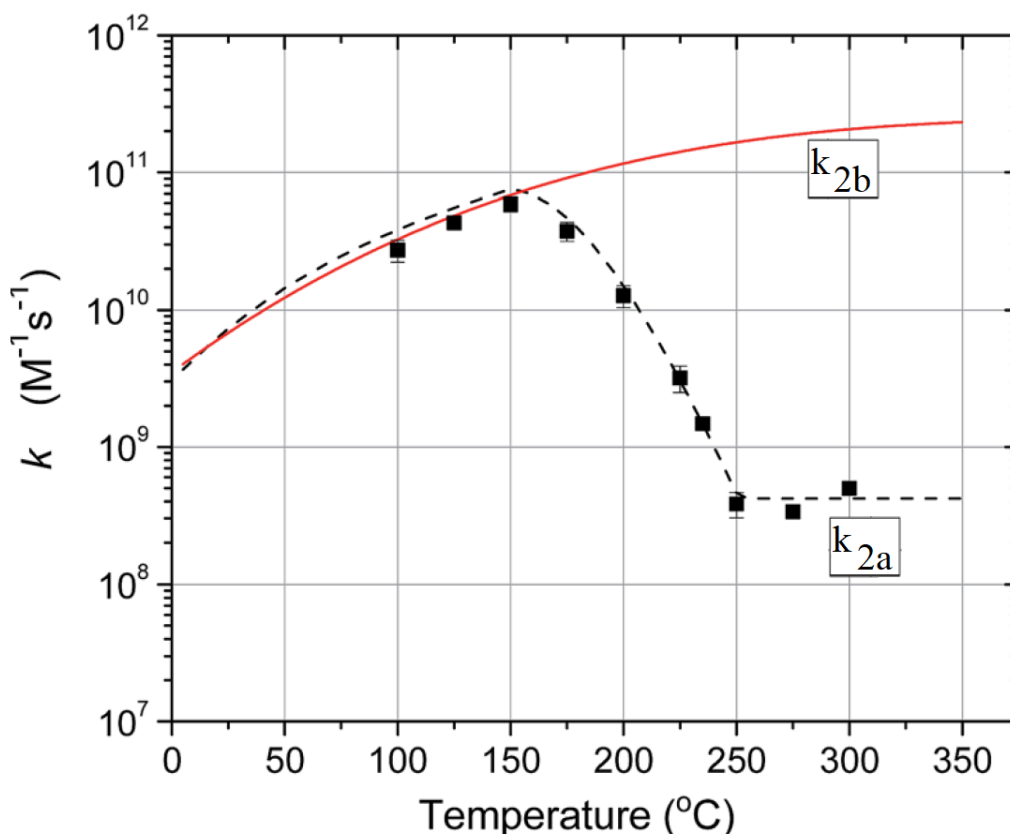


Figure 36. rate constants for the bimolecular reaction of the hydrated electron as a function of temperature obtained by experimental measurements in alkaline conditions (k_{2a}) and by an Arrhenius extrapolation procedure on lower temperature data (k_{2b}) (adapted from (Islam, et al., 2017)).

Zakaria et al. published in 2021 a continuation on these Monte Carlo simulations at Sherbrooke to investigate the effects of multiple ionization of water on the G-values of the Fricke dosimeter (Zakaria, et al., 2021). It was generally considered that the ionization of water molecules which initiates High LET radiolysis was mono-electronic; however, to assuage a disagreement between previous Monte Carlo simulations on the production of HO_2^{\bullet} and experimental results, the hypothesis of multiple ionization of a single molecule or of nearby neighboring molecules was suggested as necessary to be invoked (Ferradini & Jay-Gerin, 1998). Zakaria et al. investigated the inclusion of this hypothesis, and their simulation results for $G(H_2)$ are shown compared to other recent results in Figure 39.

1.10.3 Dietz et al., 2021

In the precursor to the present work, Dietz et al. reported on the molecular hydrogen yield by the $^{10}B(n,\alpha)^7Li$ reaction in a neutral-pH boric acid solution at room temperature (Dietz, et al., 2021). Our system for measuring H_2 yield by $^{10}B(n,\alpha)^7Li$ up to high temperature and pressure is based on their experimental setup used at the NIST Center for Neutron Research BT-2 Neutron Imaging Facility (NIF). This experiment had several aspects ripe for improvement: the mass spectrometer was not operated at optimal settings, they suffered significant gamma background from the cell block material used, the form/design of the cell coupled with a frontal-beam neutron exposure scheme lead to a significant decrease in the neutron fluence experienced by a majority of their solution volumes, and their scavenger system was not adequate for scavenging some problematic species.

The Residual Gas Analyzer (RGA) mass spectrometer was not operated at optimal settings (due to legitimate concerns about degrading its components) and so the S/N ratio was lower than desired, and the thermal neutron flux density at NIF was measured at an average of only $8 \times 10^6 \text{ s}^{-1}$

1 cm^{-2} . Overcoming these issues required long hours of irradiation with a high concentration of boric acid (0.65M, more than four times the concentration used in PWRs) to produce a detectable level of H_2 .

As will be discussed in detail later on, we obtained results at room temperature, which indicate a comparable G-value to the work done by Dietz et al. Thanks to an average neutron flux density at the Rhode Island Nuclear Science Center reactor of $3 \times 10^8 \text{ s}^{-1} \text{ cm}^{-2}$ (nearly $\times 40$ higher than at NIF) and an alternative flowcell construction ($1/4$ -inch tubing), we were able to generate similar levels of H_2 at a much faster rate (requiring less than one-tenth the time for irradiation) and with a much smaller gamma contribution estimated.

Additionally, the materials and structure of the cell were found to be not ideal for neutron irradiation or for high pressure. First, they failed to anticipate the significant gamma background from neutron capture by titanium in the cell block used. In order to recover a $G(\text{H}_2)$ number, they carried out their own complementary MCNP simulations which indicated that gamma dose accounted for 29% of the total energy deposited in solution due to neutron absorption and prompt fluorescence by the major (75%) ^{48}Ti isotope, translating to a -16% adjustment of their G-value from $(1.37 \pm 0.05)/100\text{eV}$ down to $(1.18 \pm 0.10)/100\text{eV}$ (Dietz, et al., 2021). This issue compounded further difficulties due to the NIF neutron fluence being collimated in a frontal beam along the lengthiest axis of the cell, with the thick titanium outer walls inadvertently acting to shield the boron solution further back in the cell as depicted in Figure 37.

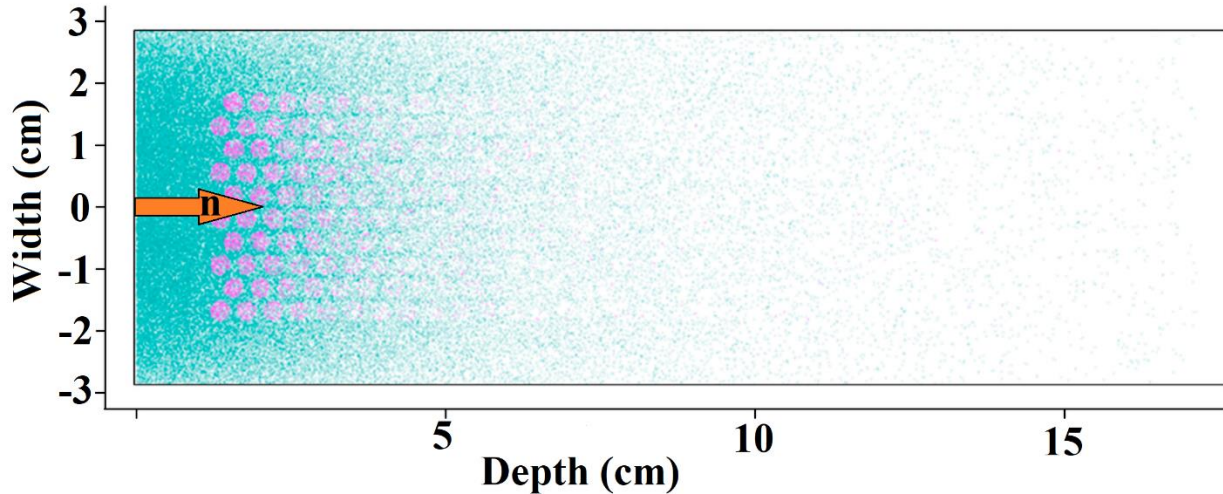


Figure 37. A center cross section mapping the MCNP-simulated neutron captures by the titanium (blue) and by ^{10}B (magenta) in Dietz et al.'s flow cell, with the orange arrow to indicate direction of the collimated neutron beam (adapted from (Dietz, et al., 2021)).

Secondly, the cell's design proved inadequate for high pressure experimentation. It was designed as a three-part sandwich structure where a honeycomb pattern of through-channels was machined into the central piece and the two "caps" had sections milled out to link each channel in a single continuous path (see Figure 38). In anticipation of this cell no longer being viable for continued experimentation, a destructive test was performed to evaluate the sturdiness of the cell's sandwich-design for use in high pressure, above 20 MPa. The weld seam between the top and central pieces failed at 22.5 MPa, indicating that using tubing instead to contain and flow the solution would be more practical.

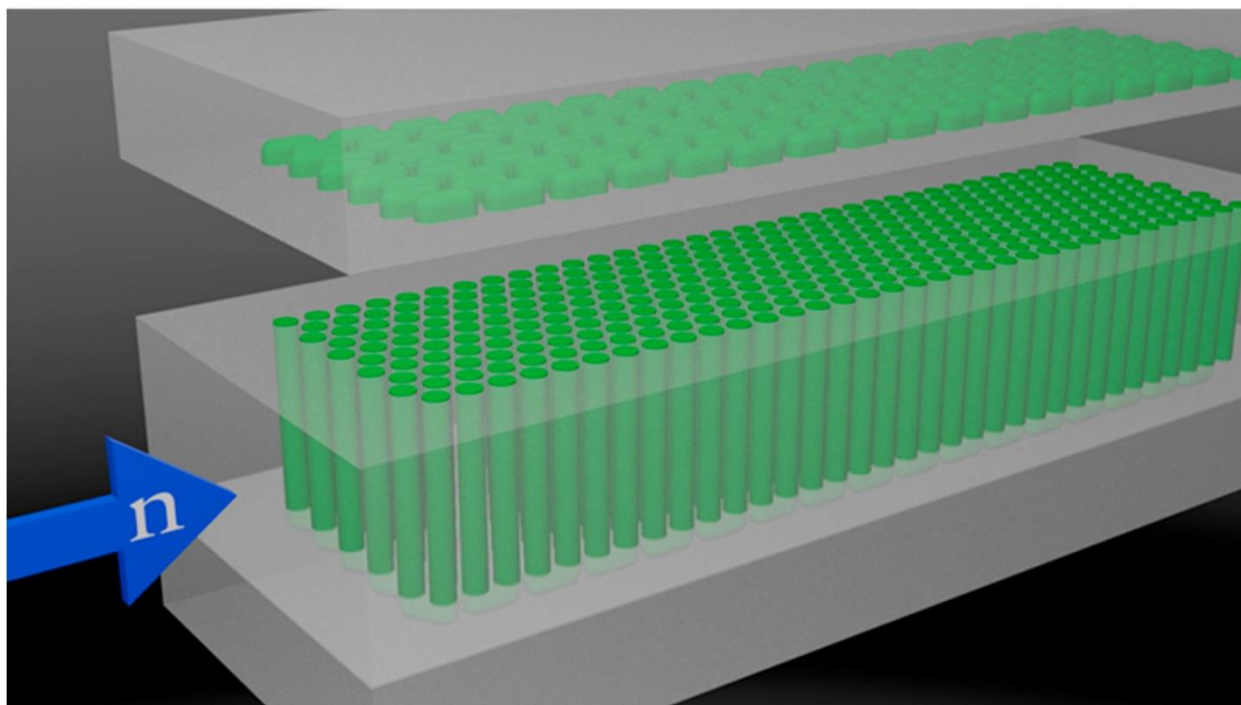
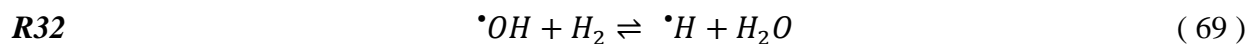
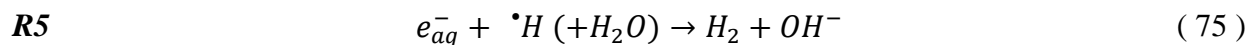
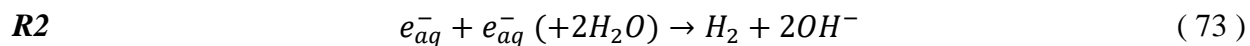


Figure 38. Schematic of the three-part sandwich construction of the precursor flow cell (from (Dietz, et al., 2021)).

To add uncertainty, they included no adequate scavenger for $\cdot\text{H}$ atoms or $\cdot\text{OH}$ radicals, nor for e_{aq}^- resulting from gamma radiation. They sparged only with argon instead of including some scavenger for e_{aq}^- , such as N_2O , which will lead to an overproduction of H_2 by reaction **R2** below. The $\cdot\text{H}$ atom will similarly lead to H_2 overproduction by reaction **R5** below without a scavenger present, such as nitrite (NO_2^-). Any $\cdot\text{OH}$ present will have the opposite effect, potentially consuming their H_2 by reaction **R32** below, unless a scavenger were included such as carbonate ($\text{CO}_3^{=}$) or nitrite.



Their final reported $G(\text{H}_2)$ at room temperature was $(0.12 \pm 0.01) \mu\text{mol}/\text{J}$, which is plotted

together with the simulation results by Islam et al. and by Zakaria et al. up to 350 °C in Figure 39.

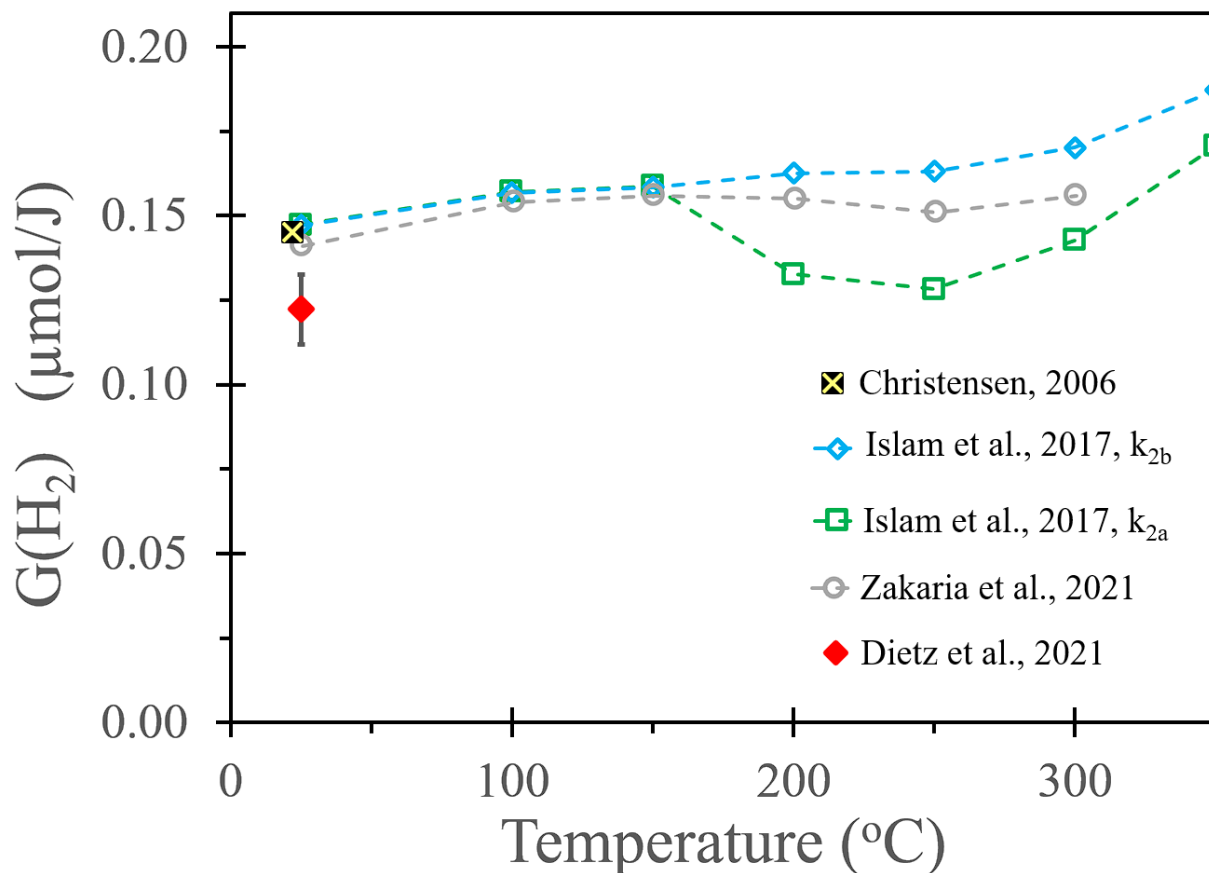


Figure 39. Recent simulation and experimental results (Christensen, 2006; Islam, et al., 2017; Zakaria, et al., 2021; Dietz, et al., 2021).

Important to note in Figure 39 is the “dip” appearing at 150 °C, a direct result from the significance placed on reaction **R2** in the model used along with the different rate constants entered, as discussed in the previous section. The significance of this dip will be addressed later in the discussion comparing our experimental results obtained for this work to those generated via simulation by Islam et al., in Section .7.1.13.

2 The Objective of This Work

The “escape” products from the radiolytic events produced by prompt recombination of radicals along dense High LET tracks of the $^4\text{He}^{2+}$ and $^7\text{Li}^{1+}$ ions produced from the ^{10}B neutron absorption event are mainly H_2 and H_2O_2 (LaVerne, 2000; LaVerne, 2004). Given the importance of this source for corrosive H_2O_2 (Macdonald, 1992; Lin, 2000; Raiman, et al., 2017), the product yields of this event should be accurately included in models of the cooling water radiation chemistry (Elliot & Bartels, 2009). However, a literature search indicates that there exist no measurements of any product yields for this radiolysis event in high temperature water, and almost no measurements at room temperature (Barr & Schuler, 1959; Yokohata & Tsuda, 1974; Dietz, et al., 2021). Unfortunately, accurately measuring H_2O_2 at high temperature and pressure is challenging because it catalytically decomposes on metal oxide surfaces and is easily lost to corrosion reactions (Lin, et al., 1991; Satoh, et al., 2004; Kanjana, et al., 2013). However, the H_2 yield is far easier to measure reliably, and should be virtually identical to the H_2O_2 yield due to mass balance (Edwards, et al., 2007; Janik, et al., 2007; Sterniczuk, et al., 2016). Therefore, estimating the total energy deposited into the cooling water from the $^{10}\text{B}(n,\alpha)^7\text{Li}$ reaction is straightforward when given the nuclear cross-section of boron (Carlson, 2011; Carlson, et al., 2018; Brown, et al., 2018), the neutron flux, and the boron concentration in the water (EPRI, 1999), but only if other radiolytic events are minimized or avoided entirely. Part of this work presents measurements of the H_2 yield from the $^{10}\text{B}(n,\alpha)^7\text{Li}$ reaction, at a pressure of 25 MPa and over a temperature range from 20 °C to 300 °C.

At the EPRI standard desired pH of 7.3, approximately 22% of the boric acid added will be converted to borate. Although boric acid was confirmed to be adequately chemically inert for use as both a buffer and a neutron shim (Buxton & Sellers, 1987), borate was not sufficiently

studied for reactions with the $\cdot\text{OH}$ radical that is prevalent in PWR coolant. While performing collaborative research at the University of Notre Dame's Radiation Laboratory, a clearly evident reaction between the conjugate base form, borate, and the $\cdot\text{OH}$ radical at an initially apparent rate of approximately $3 \times 10^6 \text{ dm}^3 \text{ mol}^{-1} \text{ s}^{-1}$ was observed at room temperature via multichromatic spectrophotometry. This contradicts the widely accepted theory that using boric acid as an additive in the primary water loop would not result in significant reactions of any of boron's present chemical forms with any of the other important and prevalent radiolytic species found in the water chemistry of PWRs. Current chemistry models are therefore completely ignorant on both the existence of the resultant species and its reactions. Part of this work presents measurements of the reaction of $\cdot\text{OH}$ with borate over a temperature range from 25 °C to 200 °C.

3 Experimental Facilities, Materials, and Equipment

The first half of this work is concerned with H_2 produced in water from the $^{10}B(n,\alpha)^7Li$ reaction, which utilized a temperature-controlled high-pressure flow system to perform tests with an aqueous boric acid solution irradiated with thermal neutrons from the thermal column of the 2 MW reactor at the Rhode Island Nuclear Science Center (RINSC). The flow system is a continuation on previous work with improvements made on an experimental setup used at the National Institute of Standards and Technology (NIST) Center for Neutron Research BT-2 Neutron Imaging Facility, wherein acceptable results were obtained at ambient conditions (Dietz, et al., 2021). The original aim of this work was to obtain data up to the 350 °C and 20 MPa conditions that exist in PWRs, using an updated system and the alternate facility which have both been confirmed through means of Monte Carlo N-Particle® (MCNP) transport code simulation results to perform at an improved capability as expected.

The second half of this work is concerned with a newly discovered reaction between borate and $\cdot OH$, which similarly used a temperature-controlled high-pressure cell to perform tests on an aqueous borate solution, however certain aspects of the cell design along with the facilities and techniques used are quite different from those used in the first half of this work. The solution in the cell was irradiated by several-nanosecond duration pulses of high-energy electrons from the University of Notre Dame Radiation Laboratory's 8 MeV electron linear accelerator (LINAC). The optical cell, flow system, and LINAC facility have been described elsewhere and utilized with similar techniques in a multitude of other works (Takahashi, et al., 2000; Cline, et al., 2002; Janik, et al., 2007; Kanjana, et al., 2015; Lisovskaya & Bartels, 2019). The original aim of this work was to obtain time-resolved spectral data at wavelengths between 250nm to 820nm of this reaction in liquid water, and then analyze the data with computational aids to identify the chemical

composition of the product radical and the reactions through which it forms and decays, along with the rate constants of the relevant reactions and spectra of the relevant species, up to 200 °C.

3.1 Hydrogen generation by $^{10}\text{B}(\text{n},\alpha)^7\text{Li}$

Herein is a description of the facilities, materials, and equipment that were employed to measure the radiolytic yield of H_2 by the $^{10}\text{B}(\text{n},\alpha)^7\text{Li}$ event in an aqueous solution at 25 MPa and at temperatures up to 300 °C.

3.1.1 RINSC

Neutron irradiations were carried out in the thermal neutron column of a 2 MW open-pool light-water research reactor with a low-enriched uranium core. The Rhode Island Nuclear Science Center (RINSC), headquarters for the RI Atomic Energy Commission and located on the Narragansett Bay Campus of the University of Rhode Island, houses the state's only nuclear reactor. It has been in operation since 1964 and has been described in detail elsewhere (Crow, et al., 1995; Tehan, 2000; RIAEC, January 2017). Its available research facilities include a Thermal Column (Figure 40) for thermal neutron use, favorable for this proposed experiment. We need to limit the amount of energy deposited in our system from any radiation source other than the ions produced by the $^{10}\text{B}(\text{n},\alpha)^7\text{Li}$ reaction. Neutrons from the reactor must travel through a 6ft deep stack of graphite blocks, which will scatter high energy neutrons as has been described in Section 1.3. This will result in a thermalized spectrum at the end of the column.

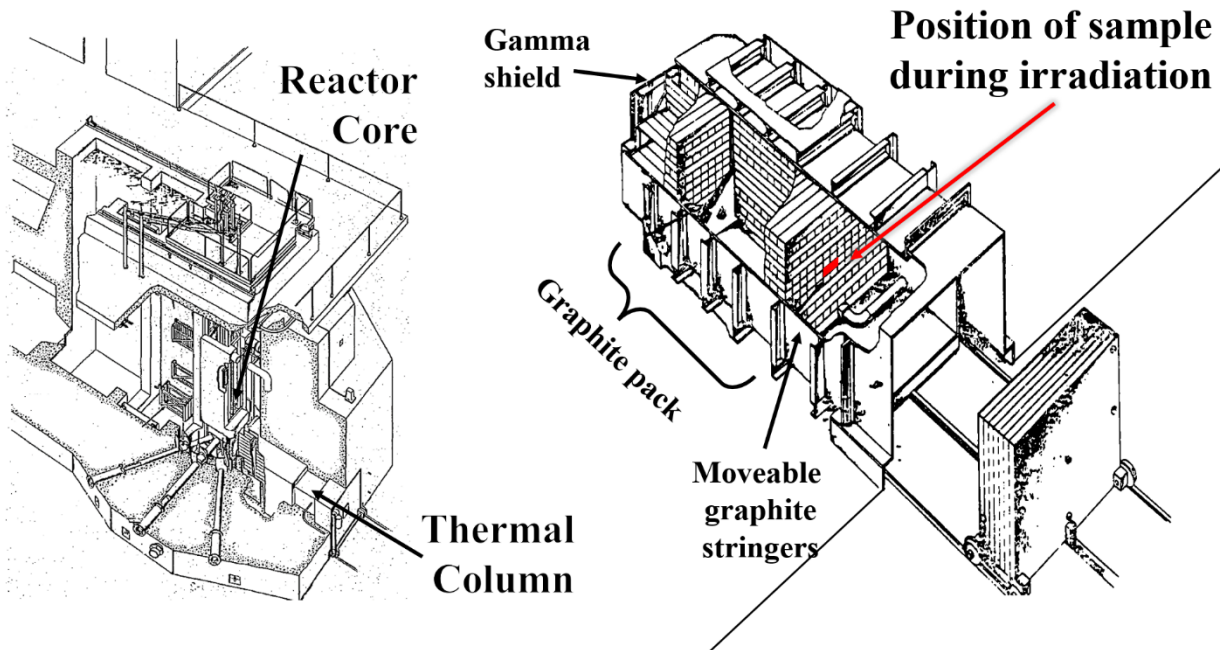


Figure 40. Left: overview of 2 MW nuclear pool-type reactor at RINSC (adapted from (RIAEC, January 2017)). Right: cutaway diagram of thermal column (adapted from (RINSC, 2023)).

Two of these long 4-inch-by-4-inch graphite blocks can be repositioned 8 inches towards the reactor core to form a cavity that is 4 inches tall, 8 inches wide, and 8 inches deep on the accessible outer face of the stack, where a sample can be placed and would be expected to get irradiated via a diffuse neutron flux “glow” coming from the five surrounding faces of graphite uniformly. A simplified graphic of this setup is displayed in Figure 41.

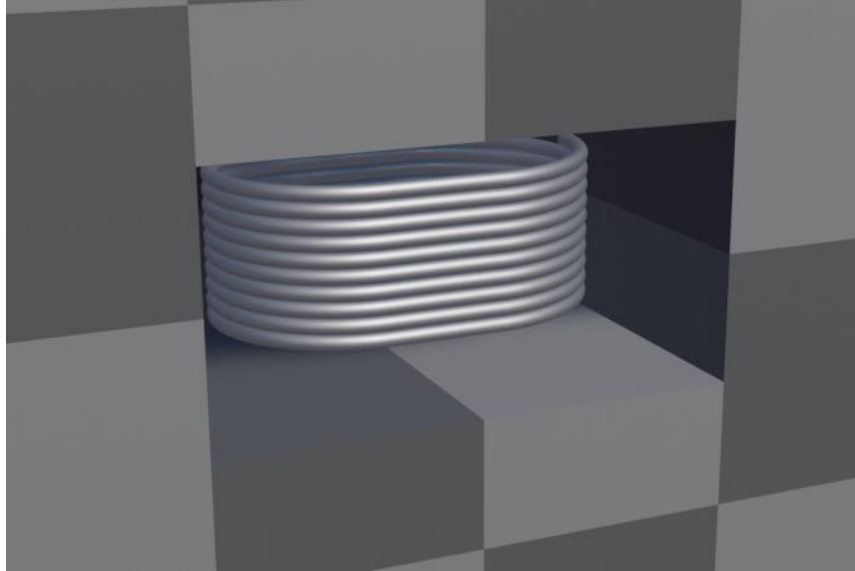


Figure 41. Graphic of modeled zirconium tubing solution containment cell placed within modeled cavity of graphite blocks at end of RINSC thermal column.

3.1.1.1 Foils and gamma measurements

A high rate of thermal neutron flux is desirable to obtain an acceptable signal-to-noise ratio for the relatively low concentrations of H₂ expected (roughly 0.12 μmol/J at room temp, based on calculations with data obtained from (Dietz, et al., 2021)) over an amount of time reasonable for the facility's capabilities. Daily start-up and shut-down procedures at the RINSC reactor allow for a maximum of approximately six hours at full power. The neutron flux was measured prior to the experiment to determine the neutron spectrum's thermalization which the experimental solution will be exposed to by using the cadmium-ratio method. Gold foils both with and without a cadmium cover were placed at the location desired for the experimental cell within the thermal column, then irradiated over the course of one day and analyzed on the next. The neutron flux density can be calculated from the analysis of the foils' activations, as described in Section 1.3.1; the Au foils showed a flux density for thermal and epithermal neutrons of $9.71 \times 10^7 \text{ s}^{-1} \text{ cm}^{-2}$, and the Au+Cd foils showed a flux density for thermal neutrons of $3.11 \times 10^5 \text{ s}^{-1} \text{ cm}^{-2}$. This equates to a cadmium ratio of 310, therefore we can expect a flux density for thermal neutrons of 9.68×10^7

$\text{n s}^{-1} \text{ cm}^{-2}$.

Low gamma background is necessary to isolate the boron fission H_2 from any gamma H_2 . At room temperature $G_\gamma(\text{H}_2) = 0.045 \mu\text{mol/J}$ (Spinks & Woods, 1990). Using radiochromic film from Far West, Inc. as described in Section 1.3.1, the gamma background is estimated as 1.5–2 Gy/hr.

3.1.1.2 Power Trend Monitoring

A diagram of the RINSC reactor core's structure is shown in Figure 42. When the reactor is in an off state, four boron-aluminum (“boral”) control blades are lowered between low enriched uranium fuel elements to absorb thermal neutrons and thus prevent higher levels of progression of the nuclear chain reaction. When the control rods are retracted, they no longer impede the neutrons, which allows far more to reach beryllium reflectors and be redirected back towards the center, where these neutrons can be captured by uranium nuclei and thus increase the reactivity in the core. There is also a stainless steel regulating rod which is inserted/withdrawn from the core area to suppress/enhance the neutron field, allowing for finer adjustment of the reactivity level than the boral blades allow.

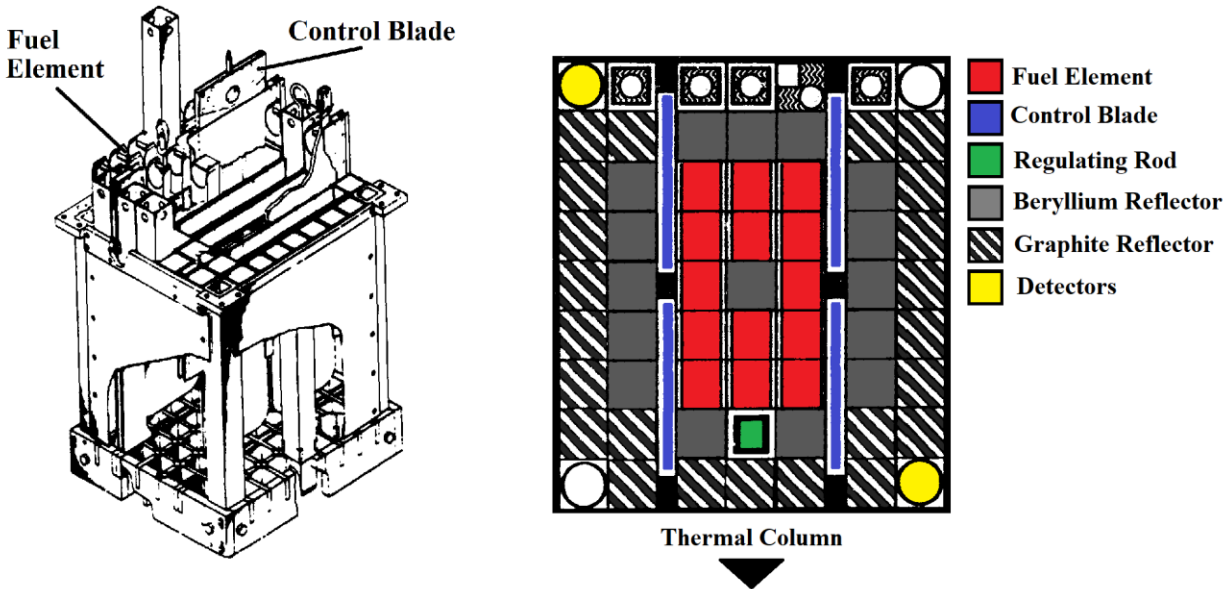


Figure 42. Diagram of RINSC reactor core structure, and top-down view of core element arrangement showing the four boron control blades, fuel elements, and the stainless steel regulating rod (both adapted from (RIAEC, 1992)).

The RINSC facility includes two compensated ion chamber detectors located within the pool near the reactor core to monitor the reactivity level in real time. A reading is logged every 5 seconds as a percentage of the maximum 2 MW power output.

3.1.2 System for Solution Containment & Transport

A high-pressure high-temperature flow-through cell unit was connected to a pump for controlling solution flow rate, was next wrapped in resistive heating tape and insulated to allow temperature control, was then attached with thermocouples to monitor the temperature, and was finally inserted within the RINSC Thermal Column for irradiation.

3.1.2.1 Irradiation Cells

Two irradiation cells were constructed, both for high temperature and high pressure, consisting of three tubing sections, each 1.52 m long with a 6.35 mm outer diameter and 4.45 mm inner diameter, plumbed together with 316 stainless steel Swagelok union fittings. The tubing was bent into a rectangular coil ca. 15 cm across to enhance the coupling between the liquid target and

the neutron field, and still allow fast quantitative removal of the irradiated liquid by utilizing a flow-through geometry. Total liquid volume of the flow cell is ca. 75 mL. The two cells differ only in the material selected for the main three sections of tubing, with the first cell made of Zircadyne® 702 alloy and the second made of Commercially Pure Grade 2 Titanium. The compositions of these materials are given in Table 2. MCNP simulations (discussed in more detail later) predict the zirconium alloy to undergo less neutron activation than the titanium tubing, which will introduce error in the G-value of H₂ from delayed gamma fluorescence; titanium is expected to be less likely to corrode at temperatures above 200 °C, wherein the metal oxidation reaction would also interfere as a source of H₂ overproduction.

Table 2. Compositions of the two materials used for flow cell tubing (Zircadyne and titanium information acquired from (ATI, 2012) and (MatWeb, 2023), respectively).

<u>Zircadyne 702[®] composition</u>		<u>Titanium Grade 2 composition</u>	
<i>UNS Designation</i>	<i>R60702</i>	<i>UNS Designation</i>	<i>R50400</i>
<u>Element</u>	<u>Weight</u>	<u>Element</u>	<u>Weight</u>
Zirconium + Hafnium, min	99.2 %	Titanium	≥ 98.885 %
Hafnium, max	4.5 %	–	–
Iron + Chromium, max	0.20 %	Iron	≤ 0.300 %
Hydrogen, max	0.005 %	Hydrogen	≤ 0.015 %
Nitrogen, max	0.025 %	Nitrogen	≤ 0.030 %
Carbon, max	0.05 %	Carbon	≤ 0.10 %
Oxygen, max	0.16 %	Oxygen	≤ 0.250 %
		Other, total	≤ 0.300 %

The cell tubing is wrapped with high temperature heating tape, along with a layer of aluminum foil and a layer of fused silica batting to insulate the cell while heating up to a maximum of 350 C. A main thermocouple is in contact with the tubing metal at the cell inlet to monitor the liquid for temperature control over the full duration of all irradiations, and a secondary thermocouple monitors the temperature of the main body of air contained within the cell insulation

layers to verify temperature uniformity. All other tubing used in the flow system was composed of 316 stainless steel. These internals of the experimental cell are displayed in Figure 43.



Figure 43. Photograph of the zirconium alloy irradiation cell tubing, wrapped in heating tape, along with a layer of aluminum foil and of fused silica batting insulation.

The cell tubing, the heating tape, the thermocouples, the aluminum foil wrapping, and the silica batting insulation are all contained within a lidded tray made of aluminum sheet metal as a full experimental cell “unit” to simplify transportation and installation into the thermal column. This unit’s placement within the cavity on the front face of the graphite pack is shown in Figure 44.

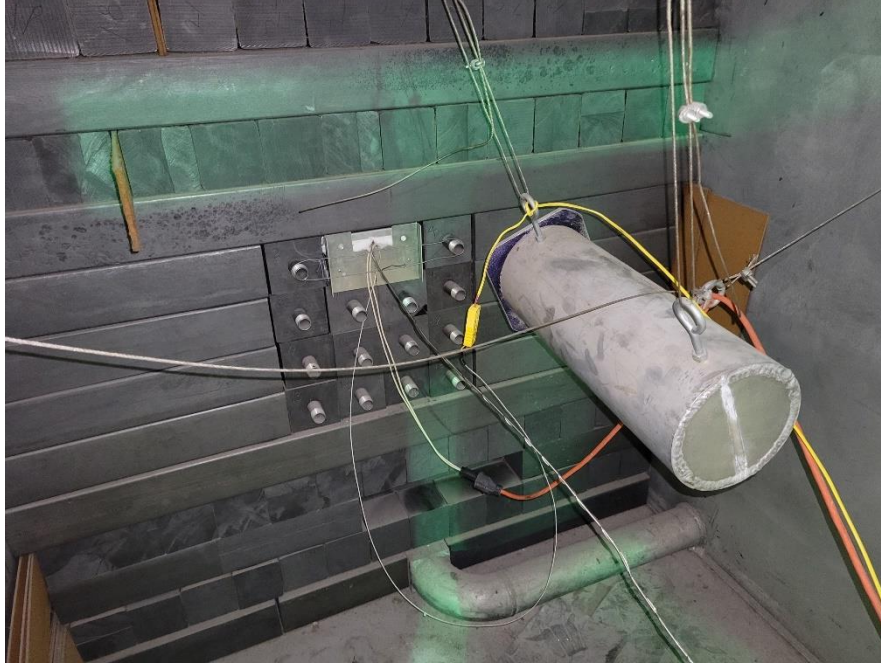


Figure 44. Photograph of the lidded aluminum transport tray containing the cell, installed in place within the irradiation cavity at the end of the graphite face of the thermal column.

3.1.2.2 Flow System

The flow system apparatus begins with an argon-saturated, pH balanced lithium hydroxide and boric acid solution that is loaded into a syringe pump, which will increase the pressure of the system down-line up to a maximum of 25 MPa. The liquid will proceed into the flow cell where the borated solution is then irradiated, producing H_2 dissolved in the solution. After irradiation, the solution is flowed out of the cell and into a glass sparging apparatus. The dissolved gases are sparged out of solution via a feed of UHP Argon gas, which then flows past a Residual Gas Analyzer (RGA) mass spectrometer to determine concentrations of gases that were dissolved in the sparged volume of irradiated solution.

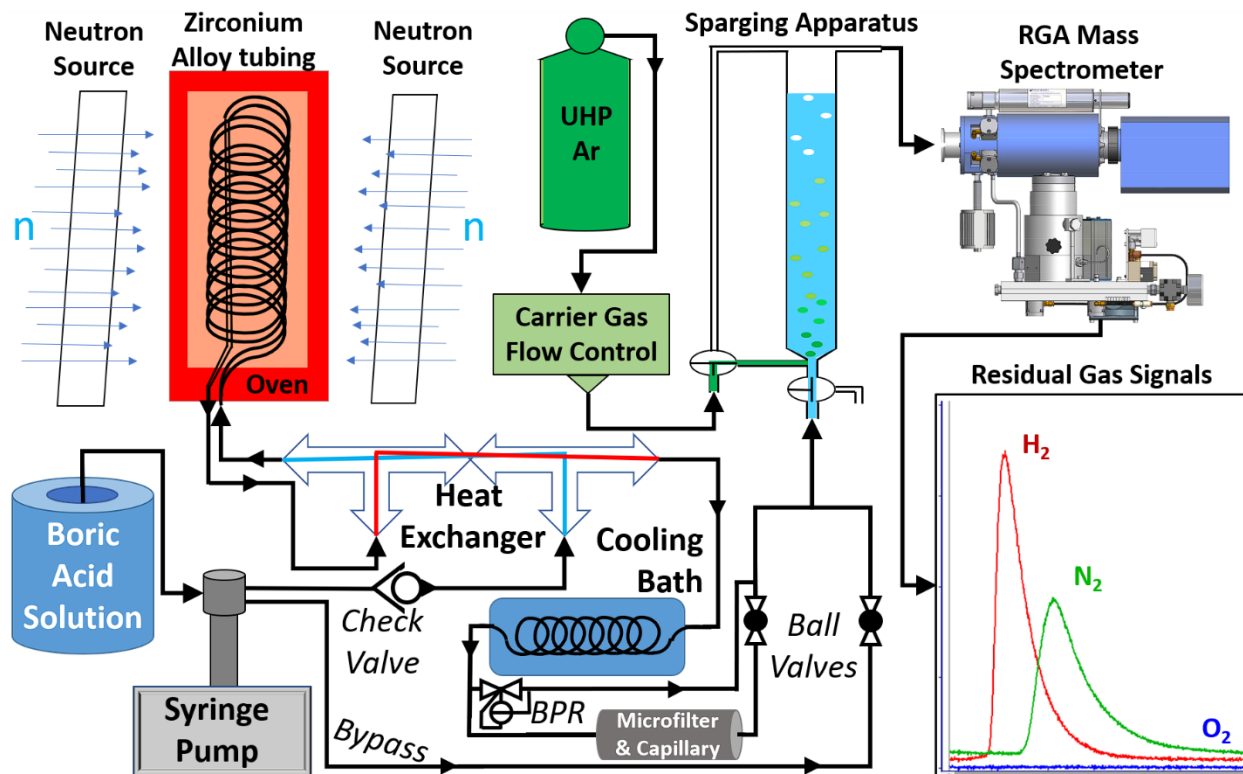


Figure 45. Schematic of system used for flowing experimental solution, containment and heating during irradiation, collection, and sparging to quantify hydrogen content.



Figure 46. Pictures of the original 20mL glass sparging apparatus (left) (adopted from (Dietz, et al., 2021)), and the larger 150mL glass sparging apparatus custom made for this project (right).

A schematic of the apparatus used to irradiate solution, collect it, and test it for hydrogen is shown in Figure 45. The irradiation cell is located within the thermal column enclosure, and all other components of the full experimental apparatus are located ca. 3 meters away within a simple commercially available greenhouse enclosure to mitigate the effects on the sensitive equipment by large unavoidable temperature fluctuations which are common within the RINSC facility's reactor vault. The water and chemicals are added to a glass reservoir which is sealed off from the atmosphere and mixed by a magnetic stir bar for at least 30 minutes while being degassed. The solution is then drawn from its reservoir into a Teledyne ISCO 260D liquid syringe pump, which can then force solution to flow out either of its two outlets. One outlet is routed to bypass the rest of the system and leads directly to the glass sparging apparatus, shown in Figure 46, to avoid unwanted irradiation of select solution volumes while the reactor is powered up. The other main outlet is routed out of the greenhouse enclosure and towards the cell in the thermal column. After flowing through the cell, the solution is routed through a section of tubing that is coiled and submerged in a room temperature water bath acting as a heat sink to bring down the solution's temperature. The water then passes through a microfilter and capillary tube, dropping the pressure from over 25 MPa to less than 1.5 MPa, before it flows into the glass sparging apparatus. A back pressure regulator (BPR) relief valve (model Idex P-880) is included in the line after the bath, in parallel with the microfilter and capillary tube. The BPR is set to 28 MPa, to prevent overpressurization of the cell when the system valves are sealed and a freshly injected volume of room temperature water is trying to expand while it is heated.

3.2 Borate reaction with Hydroxyl radical

Herein is a description of the facilities, materials, and equipment that were employed to obtain time-resolved spectral data for the apparent reaction between $B(OH)_4^-$ (borate) and $\cdot OH$

(hydroxyl radical), along with cross-reactions of product species, studied at ca. 2.5 MPa and at temperatures up to 200 °C.

3.2.1 NDRL

The University of Notre Dame Radiation Lab (NDRL) owns and operates a Titan Beta Model TB-8/16-1S electron linear accelerator (LINAC), designed to output pulses of 8 MeV electrons for performing pulse radiolysis. In this work, it is configured to supply pulse widths ranging between 5ns to 20ns, delivering a dose-per-pulse in the range of 5–50 Gy on flow-controlled aqueous solutions. This system was previously described elsewhere (Whitham, et al., 1996; Kanjana, et al., 2015; Lisovskaya, et al., 2020). It has been designed to dependably satisfy the following fundamental conditions which are key for radiation chemistry water radiolysis: short pulses to study chemical processes occurring with high reaction rates, a large enough dose of high energy electrons contained in single pulses to generate a detectable chemical change, no current supplied outside of the principal pulse width to avoid further complications in data analysis, and a minimal background current generated while the electron gun is off by additional electrons unintentionally introduced into the accelerating RF standing wave for observations carried out over longer times (greater than ms-scale).

The LINAC system begins with a 130-140 kV gridded electron gun, 60% of the charge is then compressed into the accelerator guide, comprised of a series of aligned Helmholtz coils, which transport and focus the electron beam to a diameter of ca. 5 mm at the output. For this work, a “line focus” is applied to the beam such that when it reaches the aqueous solution it is vertically focused down to ca. 3 mm and horizontally dispersed over 25 mm, centered on a slot machined into the cell. The beam’s horizontal profile is gaussian with a sigma parameter of ca. 8.1 mm, the effects of which will be discussed further on in Section 6.2.

It is significant to note that from one day's operation to another the LINAC will supply different dose rates despite equivalent settings, varying by 40–60 % (depending on which distinct arrangement of settings is used) as experienced during this study. This is due to a compounding combination of general instabilities in multiple features, inherent to the operation of such complex systems, such as changes in the power output by the Klystron amplifier of the radio frequency used to accelerate the electrons affecting both the energy and focus of the *e*-beam. However, the emission is expected to not change significantly during a full day's run, no more than by 5 %. The drift from day to day makes it necessary for each day's set of acquired data to be accompanied with dosimetry measurements using the electron signal, as outlined in Section 6.1.

3.2.2 High-Pressure High-Temperature Flow System

The high energy electrons are directed at a “window” slot machined through the bulk of the stainless steel, a recess 11 mm deep into the cell body, leaving a 1mm-thick outer “wall” of steel for the electrons to pass through and into the solution volume. Two Teledyne ISCO 260D liquid syringe pumps allow for a mixture of two solutions to be mixed at a tee connection at preferred ratios accurate to 1%, which is flowed at a constant rate of ca. 3 mL/min through a preheater and then into a 316 stainless steel high-pressure high-temperature optical cell with a 25 mm path length. A diagram of the cell is shown in Figure 47.

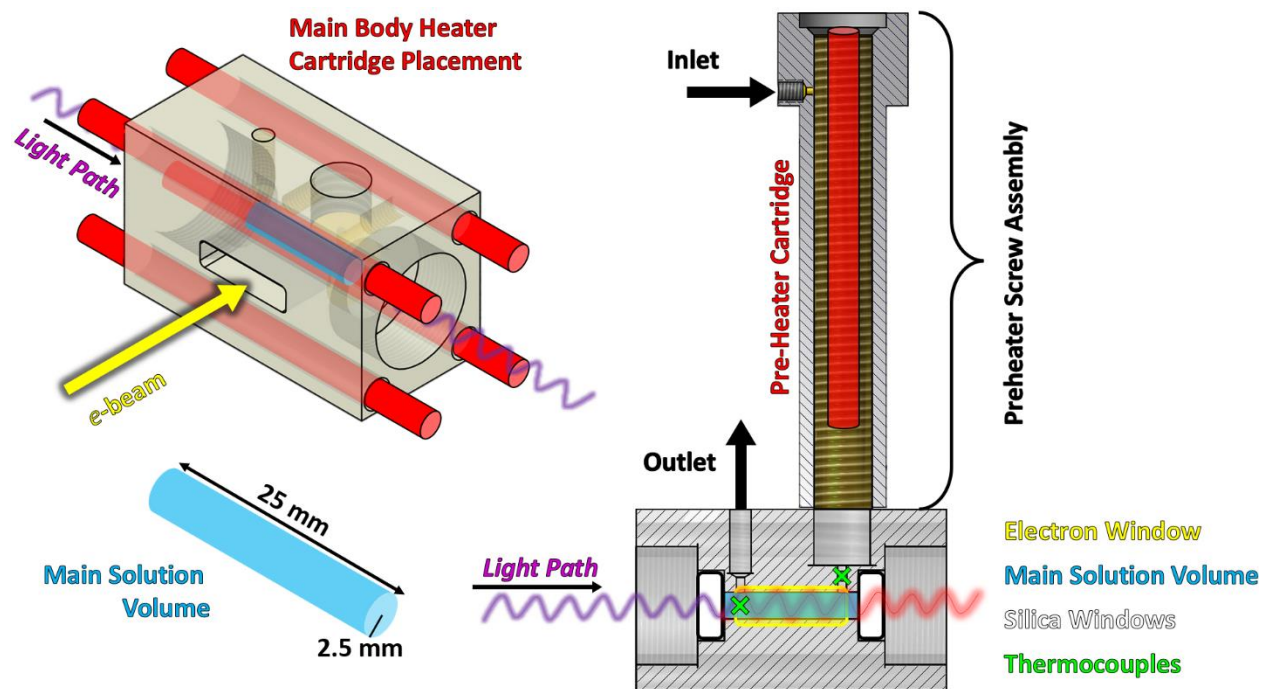


Figure 47. Notre Dame Radiation Laboratory Bartels Group stainless steel high-pressure high-temperature irradiation flow cell (the three depictions are not displayed at the same scale).

The temperature of the main irradiated volume of solution is monitored with a programmable temperature controller (PTC-10) from Stanford Research Systems by two K-type thermocouples (Omega Engineering, Inc) which gave 0.01 °C stability but ± 2 °C accuracy, with one located at the inlet from the preheater screw assembly and one near the main volume outlet. The temperature of the continuously-flowing solution is adjusted by five resistive-heating silicon cartridges: one is located within the preheater screw assembly, and four are inserted into holes through the stainless steel comprising the bulk of the cell body in order to uniformly surround the irradiated solution volume. The cell is insulated from the ambient atmosphere by a ca. 1 inch thick casing made of calcium silicate board to fit firmly around the cell, with cutouts for the electron window and analyzing light.

The solution pressure is monitored by an Omega brand precision pressure transducer and passively controlled via the flow rate (3 mL/min) through a temperature-controlled capillary tube

on the outlet side of the cell. The capillary tube is submersed in a heated bath kept at a temperature of ca. 40 °C, which maintains a pressure of ca. 2.5–3.0 MPa to prevent boiling when experimenting at temperatures up to 200 °C.

The sample cell has two fused-silica windows, resistant to high temperature water, to transmit light from a pulsed xenon arc lamp through the solution in the cell and out to a multichromatic spectrophotometer system, with 24 channels of time-resolved data being read out to an IGOR Pro acquisition program.

3.2.3 Spectrometer System

The short-lived products were detected using a UV-Vis transient detection system consisting of a 1 kW Xe arc lamp light source and a recently-constructed-multichannel detection system capable of measuring transient species absorption vs. time over a full spectrum. The analyzing lamp light is dispersed by an Acton SP2300 f/3.9 30 cm imaging spectrograph onto an array of twenty-four UV-transmitting fiber optic bundles, each 50 cm in length. Bundles are shaped at the spectrograph end into a rectangle approximately 1.1 mm in width and 3 mm in height, and terminate at the surface of a 2 mm diameter UVG50 silicon photodiode with a -100V bias. The resolution is determined by the 1.1 mm fiber “slit width” and the grating selection, and comes to be 11.9 nm per channel, with the center of the spectrum set by the spectrograph. Each photodiode is directly coupled to a home-built programmable two-stage operational amplifier assembly with 500 MHz bandwidth; all photodiode channels are set to a 100 Ohm load resistance, and each amplifier stage can be individually switched under computer control between 3.3, 10, 33, and 100× gain to provide an optimal light signal voltage between 0.1 and 1.0 V for the oscilloscope digitizers. Six Tektronix TDS5034 digital oscilloscopes with four 8-bit 350 MHz channels are used to collect data for a minimum sampling period of 0.8 ns. The oscilloscopes are triggered by

auxiliary triggers, and their amplifier offsets and full scale are adjusted to optimize for the best signal amplitude resolution of a given transient. The controlling computer with the IGOR Pro acquisition program issues commands to and receives data from the oscilloscopes via direct ethernet connections using the VISA protocol. A diagram of the overall experimental setup is given in Figure 48.

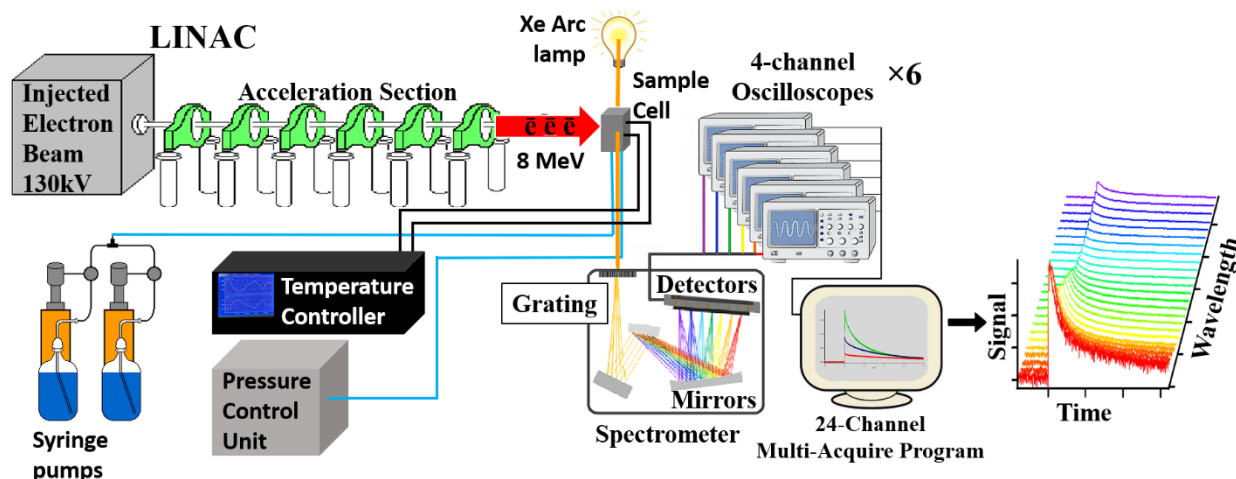


Figure 48. Block diagram of the experimental 8 MeV LINAC at NDRL with solution flow system, spectrometer, and data acquisition components.

As discussed in Section 1.5.1, the absorbance of a transient species is calculated from the Beer-Lambert Law:

$$\log_{10} \left(\frac{I_0}{I} \right) = A \quad (22)$$

This system does not allow for the light intensities with transient species (I) and without (I_0) to be measured simultaneously. Instead, the lamp is current-pulsed while the LINAC alternates between providing a pulse or not, and these interleaved pairs of trace sets are averaged and ratioed to obtain the time-resolved transient species absorption. Typically 16–25 pairs of traces are acquired together, all traces in either set can be evaluated to identify and remove outliers, and the approved remainder are averaged and ratioed. The system is limited by the recovery time of the pulsed lamp

to a repetition rate of ca. 0.3–0.5 Hz, and the nature of this experiment further limits the rate down to 0.14 Hz to allow for the full irradiated volume (ca. 0.5 mL) to be largely replaced between each lamp pulse with fresh solution at the maintained 3 mL/min flowrate.

4 Solution Selection

Normal “tap” drinking water can contain a plethora of organics, ions, disinfectants, disinfectant byproducts, and other such contaminants. The Total Organic Carbon (TOC) is an indirect analysis of the presence of organic carbon atoms in water, and is recognized as a suitable index for a “global indicator” of quantitative and qualitative water purity (Visco, et al., 2005), and in drinking water the typical TOC concentration can range up to 25 ppm (Thermo Electron Corporation, 2003). As has been discussed, the species initially produced by water radiolysis are highly reactive radicals. The radicals will react with many of these contaminants, and if these reactions occur at a faster rate than the reactions we are interested in then they will dominate over the generation of any of the products that are critical to our work. Since both parts of this work are focused on studying precise yields via *water* radiolysis, both parts required a source of very pure water that has been distilled and deionized.

4.1 Solutions for Evaluating Hydrogen generation by $^{10}\text{B}(n,\alpha)^7\text{Li}$

Three distinct solution mixtures were prepared for the majority of the experiments performed at RINSC. The RINSC facility is equipped with a water treatment system that produces >10 M Ω -cm deionized (DI) water filtered to <100 ppb TOC. A typical calibration solution was prepared by deaerating a volume of DI water with a gas mixture containing measured amounts of hydrogen and nitrogen gas in argon. Another standard solution was prepared for evaluating gamma background levels by deaerating a volume of DI water with a nitrous oxide gas mixture in argon, along with a scavenger system to allow accurate dosimetry by analyzing production of hydrogen and nitrogen gases. The standard experimental boronated solution is prepared by mixing boric acid into DI water deaerated with a nitrous oxide gas mixture in argon, along with a scavenger system

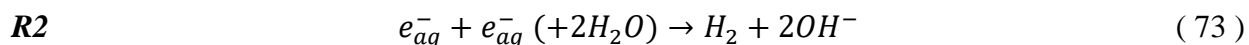
included to prevent over-production/consumption of H₂. Solutions are deaerated to avoid reactions with oxygen, and to prevent atmospheric nitrogen from interfering with detecting the experimentally generated nitrogen to allow its quantification as a gamma dosimeter.

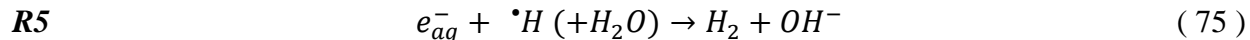
4.1.1 RGA Calibration Solution

A volume of DI water was saturated for ≥30 minutes with a gas mixture of (5.0 ± 0.1) % hydrogen and (5.0 ± 0.1) % nitrogen in argon (Airgas Inc.) while being stirred. Known volumes of this solution are sparged and the ion current peak areas resulting from RGA mass spectrometry analysis were evaluated to acquire the proportionality factor for relating moles of dissolved gas to signal peak area read out by the RGA.

4.1.2 Gamma Background Solution

The contribution to H₂ production both from the thermal column's low gamma radiation background and from prompt fluorescence gamma of the flowcell materials (titanium, Zircadyne 702 alloy, and stainless steel) was measured to correct the ¹⁰B fission results. A zero-boron "blank" solution was used, containing similar concentrations of ²³Na for an *in situ* neutron flux dosimeter as in the boron experimental solutions, but with the addition of 1.0–5.0mM isopropyl alcohol (70% in purified water, Pro Advantage, USP Grade) as a scavenger of the hydroxyl radical •OH and the •H atom. Solution volumes were deaerated for ≥30 minutes with a (2.50 ± 0.05)% N₂O in argon gas mixture (Airgas Inc.) while being stirred. Based on its solubility, this should give a 0.57 mM concentration of N₂O to scavenge any aqueous electrons ($k_{(89)} = 9.62 \times 10^9 \text{ M}^{-1} \text{ s}^{-1}$ at 260 bar, (Takahashi, et al., 2004)) and prevent recombination reactions which might produce additional H₂ by the following reactions:

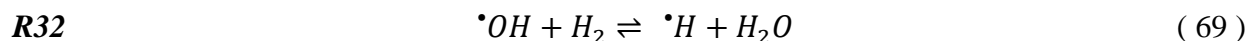




4.1.3 Boronated Experiment Solution

The standard experimental borated solution is prepared by mixing 36.680 g of boric acid (Sigma, BioUltra grade, ≥ 99.5 % trace metal basis), 0.0292 g of sodium carbonate (Fisher, ACS grade, ≥ 99.5 % trace metal basis), and 2 L of >10 M Ω -cm deionized water filtered to <100 ppb TOC. This ideally yields a solution of 0.3 M of natural boron, with 0.276 mM of ^{23}Na ions, though at 300 °C only 0.15 M boron was used to more accurately resemble PWR conditions.

Solution volumes are deaerated with the same (2.50 ± 0.05) % N_2O gas mixture in argon as used for the gamma blank solutions and so should have the same concentration of N_2O adequate to scavenge aqueous electrons and prevent H_2 over production by reactions **R2** and **R5**. And similar as for the gamma blank solutions, we expected to measure the N_2 level produced from N_2O reacting with solvated electrons to quantify the gamma dose.



The $\cdot\text{OH}$ radicals are expected to react with the CO_3^{2-} ions, preventing them from consuming (by reaction **R32**) any of the H_2 from the $^{10}\text{B}(n,\alpha)^7\text{Li}$ reaction. Alternative experimental solution mixtures substituted 0.0243 g of sodium nitrite (Sigma-Aldrich, >99 %) instead of sodium carbonate (to better scavenge $\cdot\text{OH}$ and especially $\cdot\text{H}$ atoms that manage to escape the tracks), and some include 0.143 g of enriched lithium-7 hydroxide monohydrate (Aldrich, 99.95 % trace metal basis) to ascertain any significant effect from the pH level at room temperature and to more accurately resemble the chemistry in a PWR at temperatures ≥ 200 °C. No effect on H_2 production was noted upon changing these scavengers for the minor radiolysis species, presumably because the gamma background is small.

4.1.3.1 Boron-10 isotope concentration

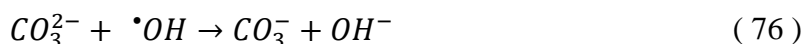
A sample of the boric acid used for the first part of this work was shipped to a Notre Dame facility for isotopic ratio analysis of $^{10}\text{B}/^{11}\text{B}$ measured by mass spectroscopy, and the ratio in our boric acid sample was confirmed as the natural fractional abundance of 0.199 ± 0.007 listed in many sources (NIST, 2022).

4.1.3.2 Na_2CO_3 scavenger

The concentration of sodium ions chosen to be present in our solutions was determined by the expertise of the technician operating the gamma spectrometer, Sangho Nam, and this technique will be discussed later in Section 5.9. He advised that obtaining a sodium activation in the range of roughly 1 nCi to be generated per hour of exposure would best suite our desired measurement accuracy based on the capabilities of the equipment used. Based on the average thermal neutron flux density measured as $9.68 \times 10^7 \text{ s}^{-1} \text{ cm}^{-2}$ (Section 3.1.1.1) impinging on the solution as well as the decay rate of ^{24}Na and its thermal neutron capture cross section, we determine (by Equation (98), introduced later) an adequate concentration of ^{23}Na to be ca. 0.27 mM. For the sake of repeatability as well as enabling precise quantification of the concentration, a “sodium standard” solution was prepared by adding 1.459 g of Na_2CO_3 ($105.99 \text{ g mol}^{-1}$) to 1 L of DI water. This would then get diluted as two aliquots of ca. 10 mL added into 2 L of boronated solution freshly prepared each day for experimentation. Annoyingly, the glass syringe used for volumetric appraisal and transferal of said aliquots was determined to be inaccurately labeled – by simply weighing a nominal “ten milliliters” of sodium standard solution, we determined such an aliquot equated to 10.23 mL. Furthermore, the precise Na^+ density within our Na_2CO_3 standard solution was calibrated relative to a commercial $(1000 \pm 3) \mu\text{g cm}^{-3} \text{ Na}^+$ density standard using ICP-OES (Inductively-Coupled Plasma Optical Emissions Spectrometry), thus determining it to be $0.939 \times$

the expected concentration. All in all, the typical concentration of ^{23}Na obtained by diluting four aliquots of the sodium standard solution into 2 L of DI water is 0.265 mM.

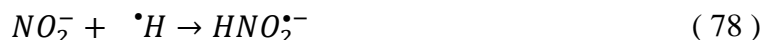
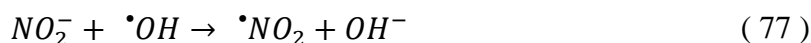
Additionally, the CO_3^{2-} ions are expected to react with the $\cdot\text{OH}$ radicals, thus preventing H_2 consumption, by the following reaction:



where this occurs at a rate of $4.2 \times 10^8 \text{ M}^{-1} \text{ s}^{-1}$ at room temperature and the rate increases with Arrhenius behavior up to 300 °C with an activation energy of 23.6 kJ mol⁻¹ (Buxton, et al., 1988).

4.1.3.3 NaNO₂ scavenger

Sodium nitrite was selected to provide Na⁺ ions for thermal neutron dosimetry as well as NO_2^- ions to act as a more effective scavenging system. The later are expected to react with $\cdot\text{OH}$ radicals faster than the CO_3^{2-} and are able to scavenge $\cdot\text{H}$ atoms as well, by the following reactions:



where the $\cdot\text{OH}$ scavenging has been measured at a rate of $1 \times 10^{10} \text{ M}^{-1} \text{ s}^{-1}$ at room temperature (Buxton, et al., 1988), and the $\cdot\text{H}$ scavenging has been measured at a rate of $1.62 \times 10^9 \text{ M}^{-1} \text{ s}^{-1}$ at room temperature and has Arrhenius behavior up to 86 °C with an activation energy of 15.6 kJ mol⁻¹ (Mezyk & Bartels, 1997).

Similar to the sodium standard solution prepared with Na₂CO₃ for repeatable dilution into experimental solutions made fresh daily, a standard solution was prepared with 1.221 g of NaNO₂ (68.995 g mol⁻¹) added to 0.5 L of DI water. This would be diluted as a single “10 mL” aliquot

into 2 L of solution, and this standard solution was calibrated relative to the same commercial $(1000 \pm 3) \mu\text{g cm}^{-3} \text{Na}^+$ density standard using ICP-OES as the sodium carbonate standard was. Based on the accurate aliquot volume of 10.23 mL and the determined $0.974\times$ calibration factor, the typical concentration of ^{23}Na in experimental solutions is 0.176 mM when NaNO_2 was used.

4.1.3.4 LiOH

Along with the boric acid added to PWR primary water, lithium hydroxide (LiOH) is added to obtain the EPRI standard desired pH of 7.3 (EPRI, 1999). Due to a limited amount available for these experiments, some of the measurements performed in this part of the work did not include LiOH. However, little-to-no effect by its inclusion/omission on the production of H_2 is expected as per Buxton and Sellers' study on reactions with e_{aq}^- and $\cdot\text{OH}$ in boric acid solutions over a pH range between 6 and 11 (Buxton & Sellers, 1987), and this is confirmed in our work for at room temperature. To more accurately resemble PWR conditions at high temperatures $\geq 200\text{ }^\circ\text{C}$, 0.143 g of enriched lithium-7 hydroxide monohydrate is added to 2 L of DI water and 0.3 M boric acid (and half as much was added to the 0.15 M boric acid solution used at $300\text{ }^\circ\text{C}$).

4.2 Solutions for Evaluating Borate Reaction with $\cdot\text{OH}$ Radical

For the other part of this work, the majority of these experiments used a mixture between a pure DI water solution saturated with N_2O and a solution of sodium tetraborate decahydrate ($\text{Na}_2\text{B}_4\text{O}_7 \cdot 10\text{H}_2\text{O}$) (hereby referred to as "borax") that was alkalized by the addition of sodium hydroxide (NaOH) in DI water which was similarly degassed with N_2O . This alkalization converts most (up to 99.5%) of the boric acid into borate, and so this is often referred to here as a "borate" solution. Solutions for electron dosimetry were prepared by deaerating a volume of DI water with argon. An attempted study on the redox potential of the borate radical $\cdot\text{B}(\text{OH})_4$

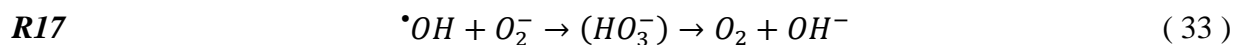
previously suspected of being formed was carried out with solutions of borax with bromide, azide, carbonate, and iodide. A study of the pH effect on the first order chemistry was investigated using mixtures of the borate solution with a borax solution that was not neutralized by NaOH. And lastly, an investigation on the ionic strength effect for the radical was investigated using a mixture between a pure DI water solution and the borax solution without NaOH. The NDRL facility is equipped with a water treatment system that produces 18 MΩ-cm deionized (DI) water filtered to <10 ppb TOC.

4.2.1 Electron dosimetry

At the beginning of a day of experimentation, a volume of DI water was saturated with an Ultra High Purity (UHP) argon gas (Airgas Inc). This solution is then irradiated with the LINAC settings adjusted to match the conditions to be used for the duration of that day, in particular the set pulse widths of 4, 8, and 15 ns typically used during experimentation. The detected electron signal is then fit with a model to calculate a dose and dose rate, as will be described in more detail in Section 6.1.

4.2.2 Discovery of a reaction in borax buffer solution

What came to be understood as a reaction between the $\cdot\text{OH}$ and borate was originally discovered when investigating the reaction of $\cdot\text{OH}$ with O_2^- as follows:



where, again, the **R** reaction numbering scheme is taken from (Elliot & Bartels, 2009). This was measured using a 2 mM borax buffer solution to maintain pH and convert HO_2 to O_2^- quickly. The water was air-saturated so that the O_2 concentration is low enough to use the “escape yields” as calculated from our typical modeling software.

4.2.3 Identification of initial reactants

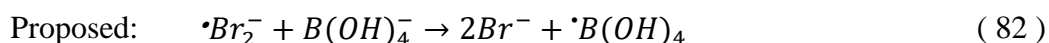
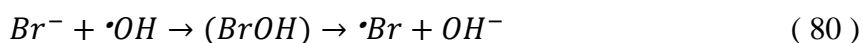
We moved ahead with the suspicion that one of the reactants is the $\cdot\text{OH}$ radical. In an effort to determine the identity of the other reacting species we performed a pH study with a borax buffer solution saturated with 100 % N_2O for converting all e_{aq}^- to $\cdot\text{OH}$ and OH^- by the reaction given in Equation (89). Two solutions are prepared with 2 mM of borax – one is alkalized with 7.2 mM sodium hydroxide (NaOH) and the other is acidified with 7.2 mM of perchloric acid (HClO_4). The mix ratio of these two solutions was varied, and analyzing the signals thus obtained made it clear that borate was the species which is reacting with $\cdot\text{OH}$.

4.2.4 Attempts to evaluate the new radical's REDOX Potential

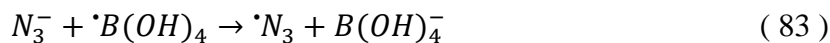
At first we assumed the reaction between borate and the $\cdot\text{OH}$ was an electron abstraction:

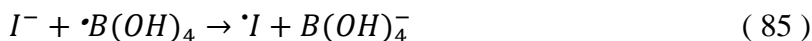


whereby the borate is oxidized. And so we attempted to evaluate the reduction/oxidation (REDOX) potential of the produced radical. We investigated whether borate could be oxidized by an alternative species, bromine, for which the supposed reactions are as follows:



as well as whether the radical could oxidize some other species, thereby reducing itself back to borate, using the chemical agents azide, carbonate, iodide, and sulfite for which the supposed reactions are as follows:





Solutions for this experimentation were prepared with various concentrations of these agents, mixed with 0.1 M of borax in DI water that was saturated with N₂O. Sodium bromide (Mallinckrodt®, reagent grade, ≥99.5 % pure) was used at 0.01 M, with and without borax; sodium azide (Mallinckrodt®, reagent grade, ≥99.5 % pure) was used at 1–3 μM; anhydrous sodium carbonate (Acros Organics, ≥99.95 % pure) was used at 0.01 M; potassium iodide (Matheson Coleman & Bell, reagent grade, ≥99.5 % pure) was used at 1–3 μM; and anhydrous sodium sulfite (Mallinckrodt®, reagent grade, ≥99.5 % pure) was used at 2 μM.

Table 3. REDOX potentials of the various chemical agents used for evaluating the borate radical (values obtained from (Armstrong, et al., 2015)).

Reaction	Electrode Potential / V
$\cdot OH + e^- \rightarrow OH^-$	+1.902 ± 0.017
$O_{2(aq)} + e^- \rightarrow O_2^-$	-0.18 ± 0.02
$\cdot Br_2^- + e^- \rightarrow 2Br^-$	+1.63 ± 0.02
$\cdot N_3 + e^- \rightarrow N_3^-$	+1.33 ± 0.01
$\cdot CO_3^- + e^- \rightarrow CO_3^{2-}$	+1.57 ± 0.03
$\cdot I + e^- \rightarrow I^-$	+1.35 ± 0.02
$\cdot SO_3^- + e^- \rightarrow SO_3^{2-}$	+0.73 ± 0.02
$\cdot B(OH)_4 + e^- \rightarrow B(OH)_4^-$?

No effect on the kinetics of the growth or decay of the absorbing radical were observed in the presence of any of the selected chemical agents. Possible reactions and the potential products were reevaluated via *ab initio* calculations, and a new likely product was identified.

4.2.5 Reaction Evaluations

The initial reaction rate of the borate and the $\cdot\text{OH}$ was studied along with the second order decay of the product radical. Both solutions used in this investigation were saturated with N_2O to convert e_{aq}^- to $\cdot\text{OH}$ and OH^- . One solution was mixed with 0.05 M of borax in DI water, and thus contained 0.1 M boric acid and 0.1 M borate. Having identified the borate as the initial reactant, we convert most all of the boric acid to borate by alkalizing with 0.1 M of NaOH. The pH was measured at 10.65, indicating that >96 % of the original 0.1 M of boric acid was converted to borate (the appropriate formulae for this value's calculation will be given later in Section 7.2.6). This solution was then mixed and diluted with pure DI water at select ratios. The solution mix was irradiated in the LINAC using low dose to study the initial reaction of borate with $\cdot\text{OH}$ and with high dose and multiple concentrations (two-four) to study the second order decay.

4.2.6 Searching for Ionic Strength Effect

The new product identified by *ab initio* calculations that was found more likely to be forming was $\cdot\text{BO}(\text{OH})_3^-$ via hydrogen atom abstraction, which as a charged particle was expected to exhibit an ionic strength effect as outlined in Section 1.5.2. No such effect was observed during the studies performed to evaluate the initial reaction and the subsequent decay of the product (or products). We suspected the lack of evidence was due to ion pairing between $\text{B}(\text{OH})_4^-$ and Na^+ ions. Both solutions used to investigate this suspicion were saturated with N_2O to convert e_{aq}^- to $\cdot\text{OH}$ and OH^- , one solution contained 0.05 M of borax in DI water (and thus contained 0.1 M boric acid and 0.1 M borate) without any NaOH included (pH was measured at 9.30), and that solution was then mixed and diluted with pure DI water at select ratios.

5 Experimental Methods for Evaluating $^{10}\text{B}(n,\alpha)^7\text{Li}$ radiolysis product yields

The experiment for the first part of this work is comprised of two essential measurements: the amount of dissolved molecular hydrogen that was produced from the High LET fission products' water radiolysis, and the amount of ^{24}Na activation in the same volume which is proportional to the thermal neutron exposure of the ^{10}B . The hydrogen produced can then be normalized to the number of ^{10}B capture events to deduce a radiation chemical yield, or G-value.

5.1 Solution transport and analysis

As part of each daily start-up procedure, ca. 10 mL of solution is sent out the secondary port of the syringe pump through the bypass route to waste to confirm removal of any bubbles, and at least 500 mL of solution is flushed through the cell flow system to replace any impure solution remaining from previous runs. Once the reactor has achieved full power output, a fresh volume of solution is flowed into the cell. The total volume of the flow system from the exit port of the syringe pump, through the cell, to the glass sparging apparatus inlet is estimated to be approximately 100 mL; therefore, for each instance when loading a new volume to be irradiated and/or when extracting an irradiated volume for testing, a total volume of 120 mL is made to flow to ensure full quantitative transfer.

After a sample volume has been irradiated and is ready for analysis, a new sample volume is pumped into the cell to simultaneously extract the entire irradiated volume into the glass sparging apparatus. The sparger is routed to allow a continuous stream of argon gas (99.999 % purity, Airgas Inc.), monitored by a flow controller (model Masterflex 32907-59), flowing either through a bypass route or bubbling up through the column of irradiated solution to sparge out the

dissolved hydrogen and nitrogen. This mixed gas exits out the sparger, flows through two parallel moisture traps, and passes a Residual Gas Analyzer (RGA) mass spectrometer for analysis. The RGA measures the ion current of select gases (we monitor hydrogen, nitrogen, and oxygen) as a function of time, and integration of each gas's ion current signal peak area is proportional to the concentration of that gas dissolved within the solution.

5.2 RGA Signal Analysis by MATLAB

The raw data from the RGA mass spectrometer is exported as signal (nA) versus time (s), and is read into a custom MATLAB script for analysis. The user defines the periods of signal to be designated as "baseline" noise both before and after the sample's gas signal is acquired, as shown in the left plot of Figure 49 for an example experiment signal obtained at ca. 160 °C. The right plot shows the fitting of the baseline trend by linear regression.

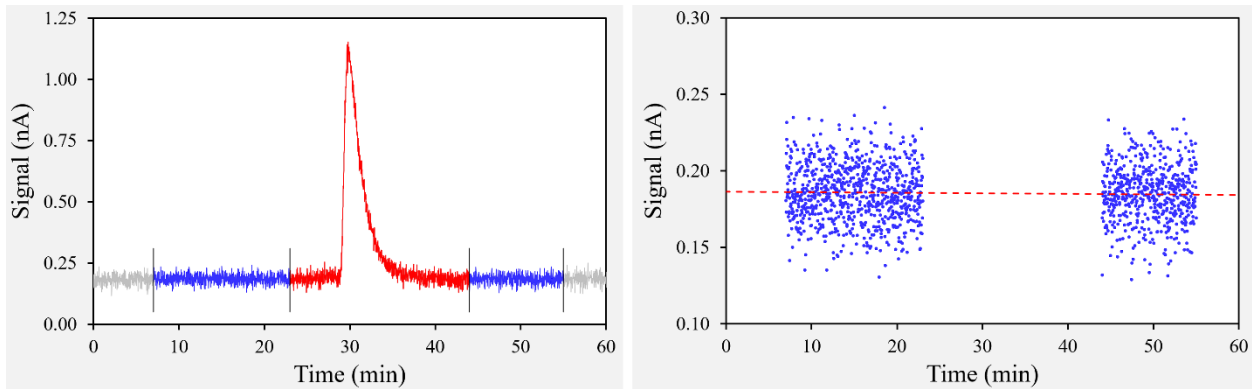


Figure 49. Left: selection for distinguishing signal "baseline" (blue) from "sample" signal (red). Right: fitting by linear regression to baseline trend.

The linear baseline trend fit is then used to subtract out the baseline noise level from the original signal of the sample, where Figure 50 shows a plot of the end result. The area of this true signal data is then calculated using Simpson's 1/3 Rule of Integration. The essential concept behind this rule is that triplets of points on the curve are fitted by quadratic interpolation and the area

under these points is calculated by integrating the parabolic functions along all points of the curve, though this explanation is rather simplistic.

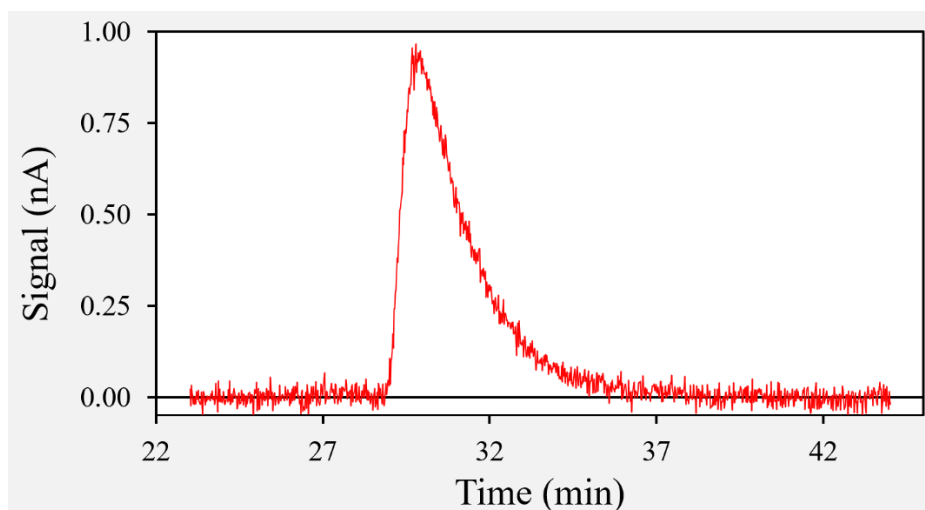


Figure 50. Plot of signal from Figure 49, with baseline noise level subtracted out to integrate over the peak and obtain the signal area.

This fitting method yields excellent repeatability, even when the baseline region bounds are varied by several minutes. The effect of variations of the chosen bounds has been investigated and confirmed to result in variations of the final integrated signal peak area by less than 0.1 %. This accuracy is consistent for all signals analyzed throughout this part of the work, so long as the user can adequately distinguish within reason when the signal is deviated from baseline noise levels, particularly as the H₂ finishes dissipating and the signal returns to baseline.

5.3 RGA Calibration

Measuring the proportionality constant as a value of peak-area-per-mole of select gas was carried out daily. A volume of DI water is saturated with a gas mixture of (5.0 ± 0.1) % hydrogen and (5.0 ± 0.1) % nitrogen in argon (Airgas Inc). Saturated solution is drawn into the syringe pump, and select volumes (reported by the ISCO syringe controller to 0.1cc accuracy) are flowed into the glass sparging apparatus. Volumes from 40 mL to 120 mL of solution are collected and sparged,

and the resulting H₂ and N₂ signals are integrated to establish a linear relationship between the area of the signal peaks and the concentration of both gases. The concentration of each gas is expected to vary day-to-day due to temperature fluctuations (between 16–24 °C over the course of this experiment) in the experimental facility and so is calculated by Henry's Law, shown below.

$$k_H(T) = k_H^o \times e^{\left[\frac{d(\ln k_H)}{d(1/T)} \times \left(\frac{1}{T} - \frac{1}{298.15} \right) \right]} \quad (87)$$

$$C_{H_2} = p \times k_H(T) \times m_{H_2O} \times \rho_{H_2O}(T) \quad (88)$$

where k_H^o is Henry's Law constant at 298.15 K (mol g⁻¹ atm⁻¹), $\frac{d(\ln k_H)}{d(1/T)}$ is the temperature dependence parameter for the Henry's Law constant, T is the temperature of the solution, p is the partial pressure of a select gas in the mixed gas (atm), m_{H_2O} is the molar mass of water (g mol⁻¹), and $\rho_{H_2O}(T)$ is the density of water as a function of temperature (mol L⁻¹). The values for the Henry's Law constant and their temperature dependence were obtained from the NIST Chemistry WebBook SRD 69 (Lemmon, et al., 2021) for both hydrogen gas (7.8×10^{-4} and 500) and nitrogen gas (6.5×10^{-4} and 1300).

5.4 Boron Experiment

Experimental runs with boronated solutions were commonly performed at a target temperature on a given day, with conditions repeated for three measurements. RGA calibration is performed first, then irradiation of a sample, followed by its H₂ content measurement and ²⁴Na activation analysis while the next sample is irradiated. The G-value for H₂ by the ¹⁰B(n,α)⁷Li reaction is directly calculated from the total quantity of H₂ present divided by the energy deposited in the solution by the reaction's product ions. The concentration of H₂ sparged out of each

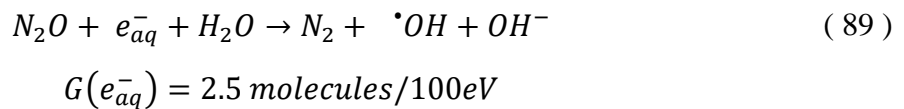
irradiated boric acid solution sample is calculated based on the daily calibrations, as described previously.

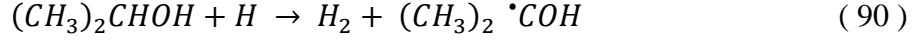
5.5 Gamma

It was expected and confirmed that the thermal column at RINSC would not result in a perfectly thermalized neutron spectrum entirely devoid of any background gamma radiation. Additionally, some of the materials used to construct the flowcell setup were expected to undergo neutron activation and fluoresce, namely: stainless steel Swagelok unions, ^{48}Ti neutron capture in the titanium cell tubing (one of the major issues faced in the precursor work (Dietz, et al., 2021)), and hafnium in the Zircadyne 702 cell tubing.

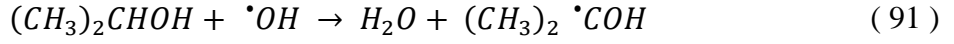
The contribution to H_2 production both from the thermal column's low gamma radiation background and from prompt fluorescence gamma of the flowcell materials was measured to correct the ^{10}B results. The zero-boron "blank" solution described in Section 4.1.2 was used, with ^{23}Na for an *in situ* neutron flux dosimeter, isopropyl alcohol as a scavenger of the hydroxyl radical $\cdot\text{OH}$ and $\cdot\text{H}$ atom, and deaerated with the N_2O in argon gas mixture as an e_{aq}^- scavenger.

These samples were irradiated in the flow cell for durations similar to the boron experiment samples, and their dissolved gas contents analyzed all with the same procedure. The chemistry induced by the gamma is very well known (Spinks & Woods, 1990; Elliot & Bartels, 2009; Sterniczuk, et al., 2016), producing e_{aq}^- , $\cdot\text{H}$ atoms, and $\cdot\text{OH}$ radicals which can react quantitatively with the scavengers as follows:

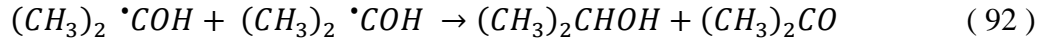




$$G(\cdot H) = 0.60 \text{ molecules}/100eV$$



$$G(\cdot OH) = 2.5 \text{ molecules}/100eV$$



as well as directly producing H₂, where at room temperature the G-value of H₂ for gamma radiation is 0.45 molecules/100eV. Additionally, as N₂O reacts with solvated electrons it will increase N₂ levels, which we expected to also measure for additional gamma dose quantification. We therefore expect in this system a measured $g(H_2) = G(H) + G(H_2) = 0.60 + 0.45 = 1.05$ molecules/100eV and $g(N_2) = G(e_{aq}^-) = 2.5$ molecules/100eV solely from the Low LET gamma. Multiplying a G-value in molecules/100eV by 0.1036 converts to units of $\mu\text{mol}/\text{J}$.

While we expect that the ¹⁰B experimental solution is exposed to some small levels of gamma radiation directly from the core (based on the RCF measurements as described in Section 3.1.1.1), we assume that some gamma radiation also results from neutron-capture fluorescence in the surroundings and thus is proportional to the measured neutron flux density in the sample. Based on the total content of hydrogen gas within an irradiated “gamma blank” sample, the total dose rate of gamma radiation can then be calculated by the following equation:

$$D_\gamma = \frac{H_2}{V_{Irr} \times g_\gamma(H_2) \times \rho_{H_2O} \times t_{Irr}} \quad (93)$$

where D_γ is the gamma dose rate (Gy/hr), H_2 is the amount of dissolved hydrogen (mol), V_{Irr} is the volume of the irradiated solution (L), $g_\gamma(H_2)$ is the g-value of molecular hydrogen for gamma at room temperature (mol/J), $\rho_{H_2O}(T)$ is the density of water at a given temperature (kg/L), and

t_{irr} is the duration of irradiation (hr). The density of water must be taken into account here; and although there is a corresponding change with temperature in the concentrations of boron and sodium in the boric acid experiment, their ratio remains constant and so the calculated yield of H_2 per $^{10}B(n,\alpha)^7Li$ event is independent of the density of water, as is apparent in Equation (100) which is derived later.

5.6 Corrosion

Both metal alloys that the two types of flow cells were constructed of are known to undergo some degree of oxidation by the following reactions. This oxidative corrosion process typically leads to the formation of a passivation layer of metal oxide (Was & Allen, 2019). The passive layer still has a non-zero corrosion rate, but the production of hydrogen becomes small.



The first irradiation cell made of the zirconium alloy Zircadyne 702 was used for approximately two months, subjected to thermal cycling as well as irradiation during initial testing and later in experimental runs. Unfortunately, this cell material was found to undergo an extreme degree of oxidation at temperatures of 200 °C and higher, producing an overabundance of molecular hydrogen in the solution, as will be further discussed in Section 7.1.4.

The titanium cell was conditioned and tested for corrosion similar to the zirconium cell's treatment. After conditioning for several days, reactor experiments could be carried out. During the boron experiments to measure $G(H_2)$ at higher temperatures on a given day, prior to reactor power-up, a sample of the boric acid solution was flowed into the titanium cell while it is held at a target temperature and 25 MPa. This “corrosion blank” is kept within the cell for ca. 1 hour, then

analyzed to quantify the hydrogen produced solely via corrosion during that time. A second blank is taken to confirm that the corrosion rate is constant. This yield at the target temperature is then used as an estimate for how much hydrogen must be subtracted as “corrosion yield” from the raw hydrogen content measured in samples irradiated by neutrons at the same cell temperature, as a correction in the calculation of the final “boron yield” hydrogen.

5.7 Heater & LabVIEW PID program

The temperature of the tubing at the inlet to the cell is monitored with a K-type thermocouple whose voltage is read out through a LabJack model U6 DAQ into a LabVIEW program. The program is set to take a reading every 0.25 seconds to be fed into a digital proportional-integral-derivative (PID) controller, which is configured to output through the LabJack a control voltage signal between 0–5 V based on the simple equation below:

$$V(t) = k(S - T(t)) \quad (96)$$

where S is the setpoint temperature and $T(t)$ is the temperature reading at time t .

A power controller module, consisting in part of a Crydom PMP2425W proportional control solid state relay set to Phase Angle mode A, is connected to a standard 120 VA power socket of the RINSC facility. This controller module proportionally scales an output based on the 0–5 V control voltage input from the LabJack, where the output % can be calculated by the equation:

$$Out\% = \sin\left(\frac{\pi}{2} \times \frac{V}{5}\right)^{5/2} \quad (97)$$

where V is the control voltage from the LabJack. This scaling is displayed in Figure 51.

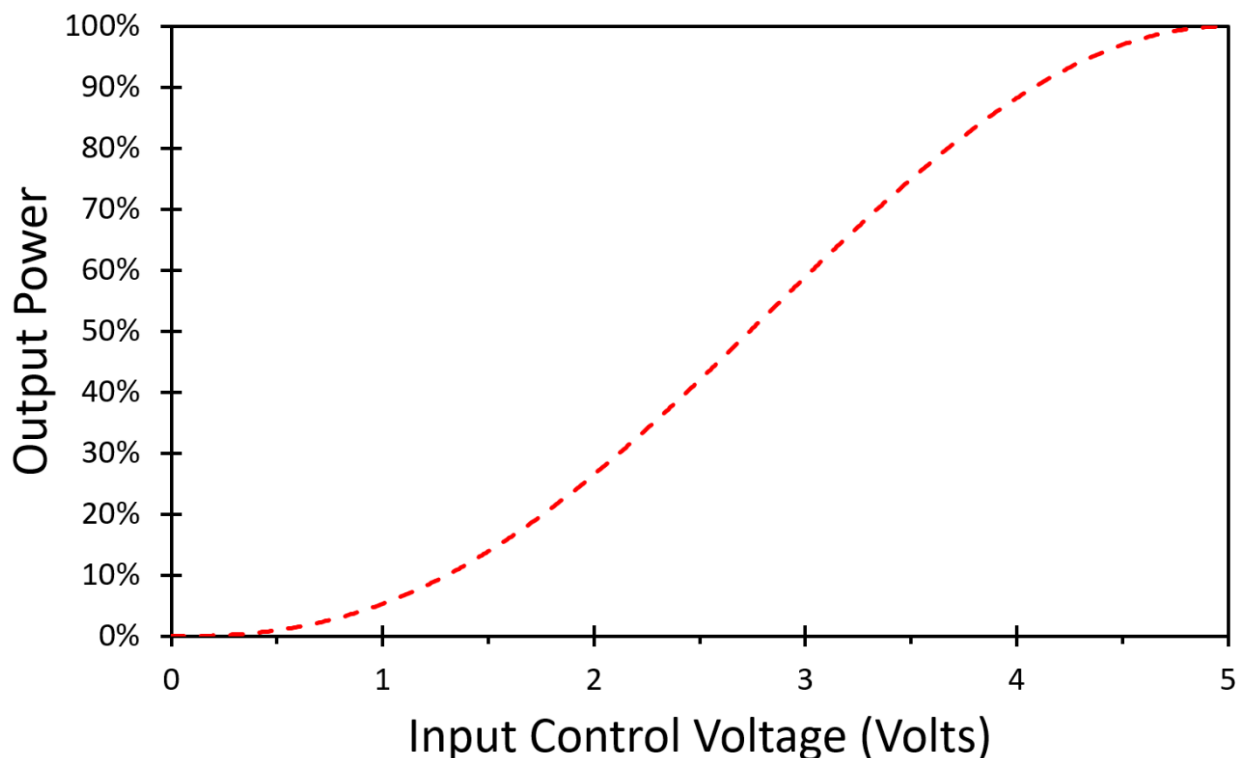


Figure 51. Crydom PMP2425W proportional control solid state relay transfer characteristics for output power Phase Angle Control by 0–5 VDC input.

The scaled output from the controller module is connected to a Staco Energy model 3PN1010B variable AC transformer (or “VARIAC”) as a proportional control allowing simple manual linear adjustment for fine-tuning the output. This was found necessary due to inherent operational limitations in the Crydom SSR control module system, namely that it would not register control voltage inputs below 0.25 V, which caused massive oscillations in temperature unless the proportionality constant k in Equation (96) were large while the control module output % were scaled down by the VARIAC. The resistive heating tape wrapped around the cell was then powered directly from the final output of the VARIAC. A plot of the program’s monitored behavior during a full day’s three experimental runs at ca. 160 °C is displayed in Figure 52, where the sudden decreases in cell temperature (red) are caused when fresh solution is flowed from the

room temperature syringe pump into the heated cell and the corresponding increase in the output power (yellow) can be seen.

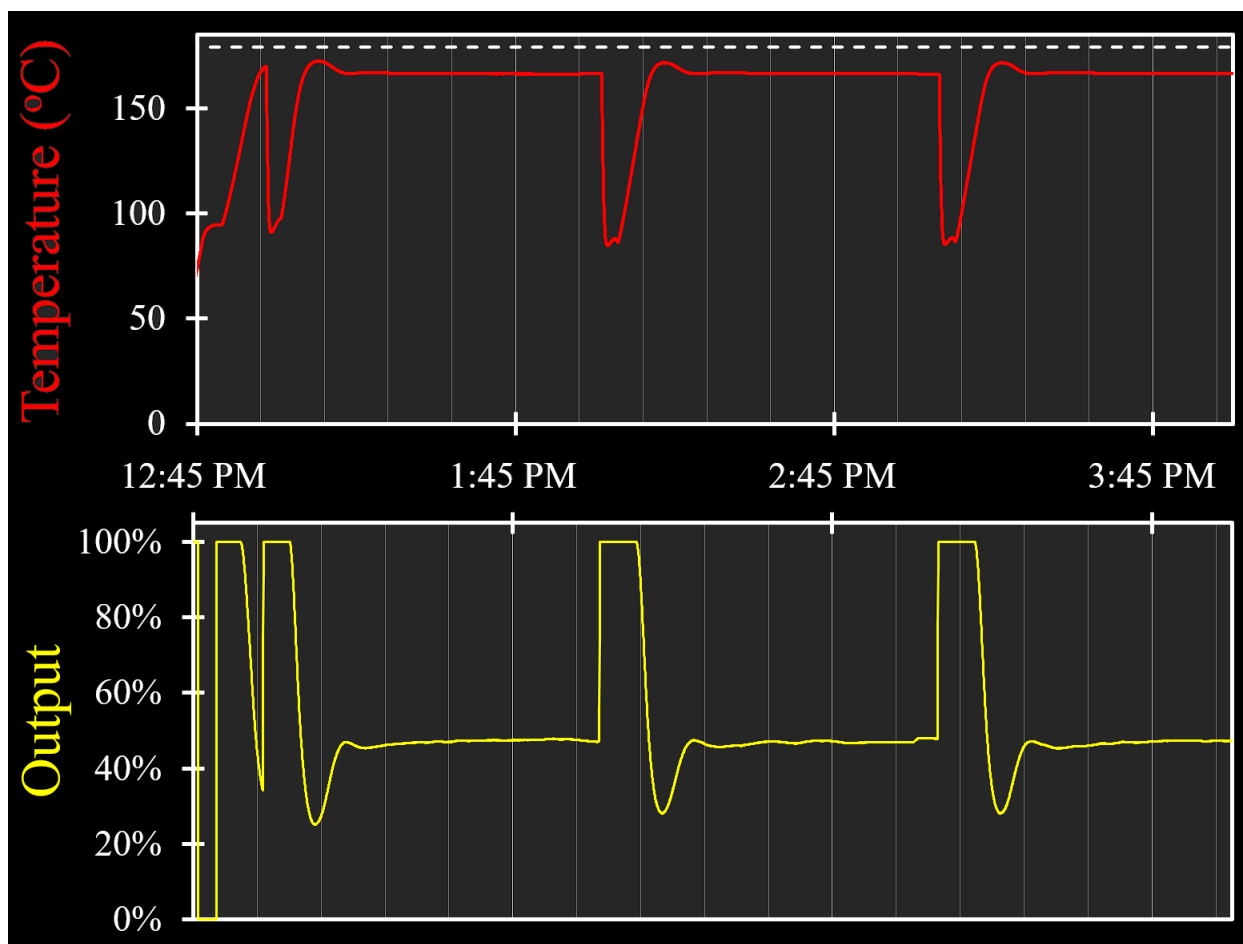


Figure 52. Plot from LabVIEW temperature control program data of cell temperature (red) and setpoint (white dashed line), and output % from the power control module (yellow) to the heating power supply.

5.8 RGA Mass Spectrometer

An Inficon Transpector 2 Compact Process Monitor Residual Gas Analyzer (RGA) mass spectrometer measures the ion current of select masses (amu 2, 28, and 32 for hydrogen, nitrogen, and oxygen, respectively) as a function of time. Integration of each gas's ion current signal peak area is proportional to the concentration of that gas dissolved within the solution. The mixed gas exiting out the sparger is mainly UHP argon as a carrier gas, as well as small amounts of hydrogen

that was dissolved in the water from the $^{10}\text{B}(n,\alpha)^7\text{Li}$ reaction. This mixed gas first flows through two parallel Restek Molecular Sieve S-Traps to remove moisture, and then reaches a tee connection. The gas flow splits to either go out a 4-foot-long exhaust of ¼-inch copper tubing to be vented to the atmosphere, or be drawn through a capillary tube to be sampled by the RGA. The exhaust tube is included so as to contain a large volume of argon between the tee inlet to the RGA and the atmosphere beyond, to act as a buffer and prevent the atmosphere which can be drawn in backwards when the outward flowrate of gas is interrupted (even briefly, such as when switching the valves on the sparger to reroute gas flow) from reaching the RGA and disrupting the baseline, which takes up to several hours to settle down and attain acceptable levels.

5.9 Sodium Activation

For irradiated samples, after analysis of all dissolved gases, the entire 120 mL sample volume of irradiated solution is collected from the glass sparger apparatus and diluted with additional DI water to precisely 500 mL in a Marinelli beaker to be analyzed for ^{24}Na activation to determine the total neutron exposure sustained by the sample.. Activity in the Marinelli beaker is then counted for 30 minutes on a Canberra high purity germanium (HPGe) detector model operating with 30 percent efficiency, using a Lynx Multichannel Analyzer, and analyzed using Genie™ 2000/Apex® spectroscopy software. The ^{24}Na activity is based on a weighted average of the area under the peak located at 1368 keV. Since the decay of radioactive nuclides is random, calculating an activation level of a sample based on the counted number of decays over a given duration is not exact; however, nuclear events follow a distribution curve which approaches a Gaussian distribution around the “real” activation level as the number of counts increases. This software generates a representative average activation along with an uncertainty based on a user-defined value of the standard deviation σ (Canberra Industries, Inc., 2017); and here we have set

$\sigma=1$, meaning that the average activation it provides represents the value we are 68% confident of obtaining if the measurement is repeated and that the uncertainty value represents the width of the Gaussian distribution around that average value (or its “error”).

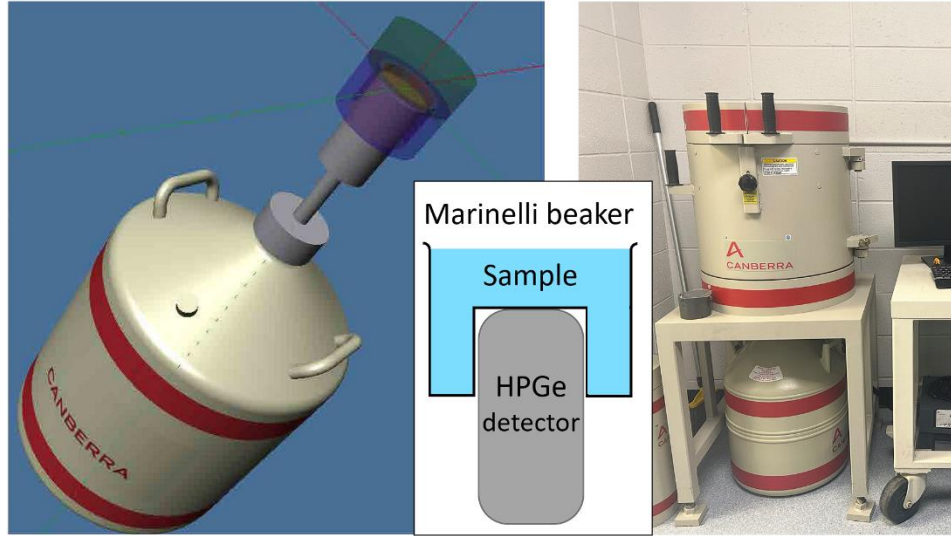


Figure 53. Left: model of a Canberra HPGe detector model, showing placement of the Marinelli beaker onto the detector, adapted from (Canberra Industries, Inc., 2017); Center: cross-section depicting the sample uniformly surrounding the detector; Right: a photograph of the RINSC setup, including the shielding unit over the detector.

Based on the total ^{24}Na produced during the irradiation (roughly 1 nCi is generated per hour of exposure for the concentrations of sodium ion used), we calculate the average neutron flux density within the solution volume:

$$\Phi_n = \frac{A_c e^{\lambda_{Na-24} \Delta t}}{\sigma_{Na-23} (1 - e^{-(\lambda_{Na-24} t_{irr})}) c_{Na-23} V_{irr} N_A} \quad (98)$$

where Φ_n is the neutron flux density ($\text{s}^{-1} \text{cm}^{-2}$), A_c is the counted activity of ^{24}Na (Bq), λ_{Na-24} is the decay rate of ^{24}Na ($1.287 \times 10^{-5} \text{s}^{-1}$), Δt is the decay time from the end of irradiation to the end of activation counting (s), σ_{Na-23} is the thermal absorption cross section of ^{23}Na ($(5.33 \times 10^{-29} \text{m}^2 (0.533 \text{barn}))$), t_{irr} is the irradiation duration (s), c_{Na-23} is the concentration of ^{23}Na (mol L^{-1}), V_{irr} is the volume of irradiated solution (L), and N_A is Avogadro’s number. It is

assumed the flux is near-constant during the course of each sample's irradiation, as it is expected to be very closely monitored and accurately maintained as an inherent condition of the RINSC reactor facility's safe operation, and this is confirmed via the Power Trend logs as discussed further on.

5.10 The G-value for H₂ by ¹⁰B(n,α)⁷Li

The High LET ions have a total of 2.793 MeV for 6% of the neutron capture events, and 94% of the events yield 2.314 MeV along with a 0.48 MeV gamma (Auden, et al., 2019). This gamma has a mean free path estimated to be 30 cm through water, which agrees with our simulation results showing very little absorbed dose from this gamma. Therefore it is omitted from the G-value calculation presented here, giving a weighted average of 2.343 MeV deposited in the solution per ¹⁰B(n,α)⁷Li neutron capture fission event.

The thermal neutron capture cross section of ¹⁰B is $3.835 \times 10^{-25} \text{ m}^2$ (3835 barn) (Sauerwein, et al., 2012), and the boric acid used in these experiments was confirmed via mass spectrometry to contain the natural isotopic fraction as 0.199 of ¹⁰B (De Laeter, et al., 2003), within measurement uncertainties. Therefore, our effective thermal neutron capture cross section is $7.63 \times 10^{-26} \text{ m}^2$. The number of ¹⁰B neutron capture fission events can be calculated using the average neutron flux density obtained from the ²³Na activation analysis by the following equation:

$$N_{Evt} = t_{irr} \Phi_n \sigma_{B-nat} c_{B-nat} V_{irr} N_A \quad (99)$$

where N_{Evt} is the number of ¹⁰B neutron capture events, t_{irr} is the duration of irradiation, σ_{B-nat} is the thermal absorption cross section of natural boron, and c_{B-nat} is the concentration of natural boron. This value can then easily be used to calculate the energy deposited in the solution by the

$^{10}\text{B}(n,\alpha)^7\text{Li}$ event. Using equations (98) and (99), the equation for $G(\text{H}_2)$ becomes:

$$G(\text{H}_2) = \frac{\sigma_{\text{Na-23}} c_{\text{Na-23}}}{\sigma_{\text{B-nat}} c_{\text{B-nat}}} \times \frac{(1 - e^{-(\lambda_{\text{Na-24}} t_{\text{irr}})})}{t_{\text{irr}} A_c e^{\lambda_{\text{Na-24}} \Delta t}} \times \frac{H_2}{E_{\text{Evt}}} \quad (100)$$

where H_2 is the amount of hydrogen detected by the mass spectrometer (moles), and E_{Evt} is the energy deposited in solution per neutron fission event (3.754×10^{-13} J). However, as is discussed later on, this value must be corrected due to a small amount of H_2 produced by the gamma background instead of by the $^{10}\text{B}(n,\alpha)^7\text{Li}$ High LET recoil ions, as well as by oxidation of the metal tubing components which also generates excess H_2 interfering with our evaluations.

5.11 Predictive Simulations by MCNP

Monte Carlo N-Particle® (MCNP®) is a general-purpose Monte Carlo radiation-transport code designed to track many particle types over broad ranges of energies, maintained by the Radiation Safety Informational Computational Center (RSICC) at Oak Ridge National Laboratory. Thanks to the collaborative efforts of Dr. Alan Thompson at NIST, his simulations confirmed that the geometry and materials used in our fluid containment and transport system would be adequate to provide the results necessary for this research.

The radiation spectrum in the RINSC thermal column was simulated using the Monte Carlo neutron transport code MCNP 6.2 (Werner, 2017) applied to a geometrically simplified model of the experimental flowcell, accurate to recent measurements performed by our collaborator Dr. Cameron Goodwin, the director of the Rhode Island Neutron Science Center. The neutron flux density was also simulated by MNCP to make a comparison with the flux density obtained during the precursor experiment at NIST's Neutron Imaging Facility beamline (Dietz, et al., 2021).

The energy deposited into the aqueous solution by gamma irradiation due to the activation

of surrounding materials is distinguished from the energy deposited by all events, including the heavy ion products of the $^{10}\text{B}(n,\alpha)^7\text{Li}$ fission event. The MCNP analysis evaluates the sum energy deposition probabilities, which are used to establish a ratio between the energy deposition by only photons versus that by all events. These ratios were assessed for both flow cell materials, one relating to the industrially available Zircadyne® 702 zirconium cell alloy and the other to the Titanium Grade 2 material.

6 Experimental Methods for Evaluating Borate Reaction with $\cdot\text{OH}$ Radical

This part of the work involved first irradiating samples of the solutions of interest to obtain their time-resolved spectral data, followed by thorough analysis of said data using computational aids. Analyzing the evolution of the absorbance at any wavelength over time along with the known initial concentrations of active species (such as the borax buffer and N_2O) and calculated concentrations of radicals generated from Low LET pulse radiolysis allows for the establishment of the rates at which initial species are consumed and product species are generated, whereas analysis across multiple wavelength channels allows for the identification and quantification of species whose spectra are known (such as the $\cdot\text{OH}$ radical and carbonate) and establishment of the as-yet unknown spectra for the other species involved in the reactions.

6.1 Electron Dosimetry

The e_{aq}^- signal was detected at 710 nm and its concentration within the first 6 μs was calculated from a fitting model using the extinction coefficients given by Torche and Marignier (Torche & Marignier, 2016) with the limiting escape yield for e_{aq}^- taken to be $G(e_{aq}^-) = 0.26 \mu\text{mol/J}$ (Janik, et al., 2007). The dose is applied as a delta-pulse in the model and the expected homogeneous chemistry is calculated, then the time-dependent spur decay function given by Bartels et al. is used to correct to larger absorbance (Bartels, et al., 2000). This result is convolved with a rectangular function to represent the LINAC pulse width along with an exponential function representing the photodiode rise time, which is finally fit precisely to the rise time and amplitude of the signal.

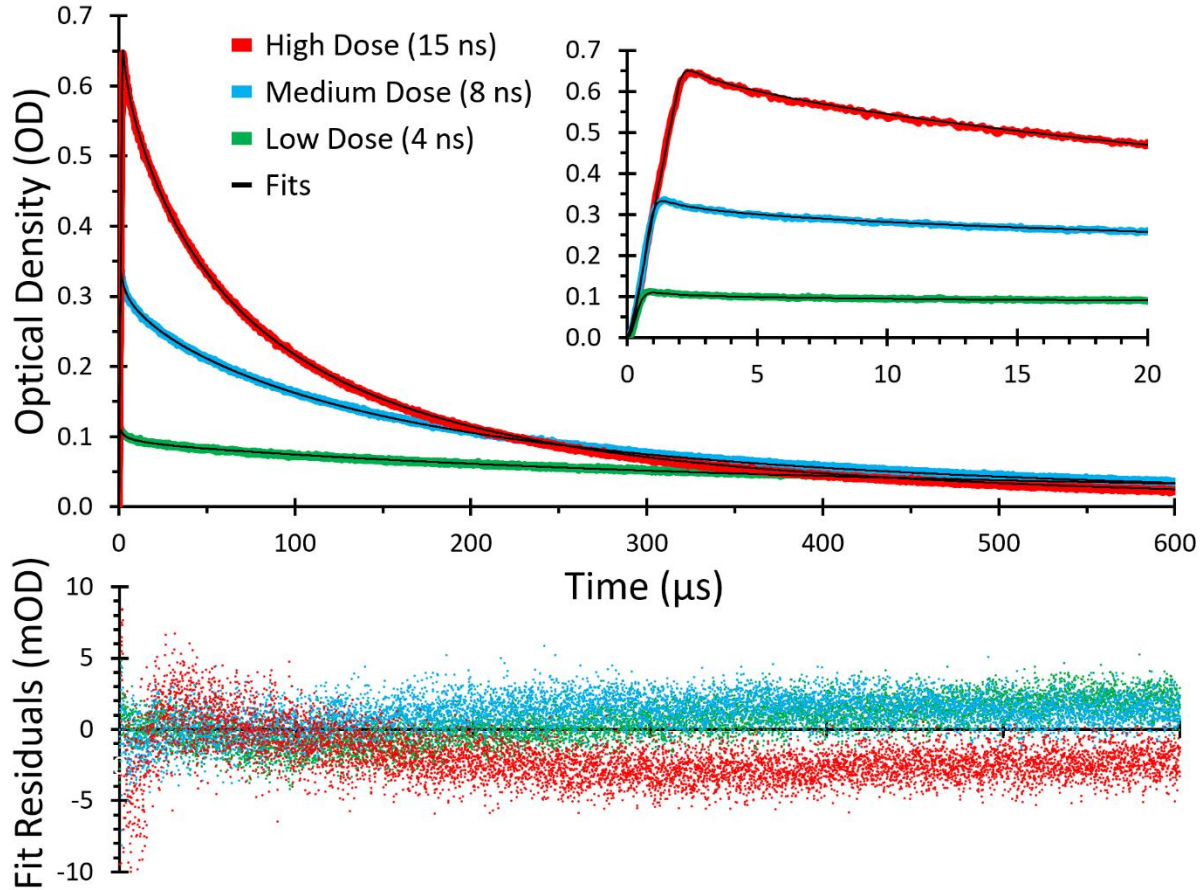


Figure 54. Fits to the e_{aq}^- signal at 710nm for electron dosimetry using the fitting model (top, with short time scale shown in upper right), and the residuals for each fit (calculated as Signal-minus-Fit) showing good agreement (bottom).

6.2 Path Length for Irradiated Solution Volume

There has been concern for some time at NDRL about the concentration gradient that does exist along the light pulse's path within the cell caused by the Gaussian spread of the e -beam along that axis, as originally mentioned in Section 3.2.1. The electromagnetic lenses generated from the Helmholtz coils are set such that they focus the beam in the vertical dimension through the "window" slot into the flow cell and spread the beam over 25 mm in the horizontal dimension to a Gaussian shape with a sigma parameter of ca. 8.1 mm. This is illustrated in Figure 55.

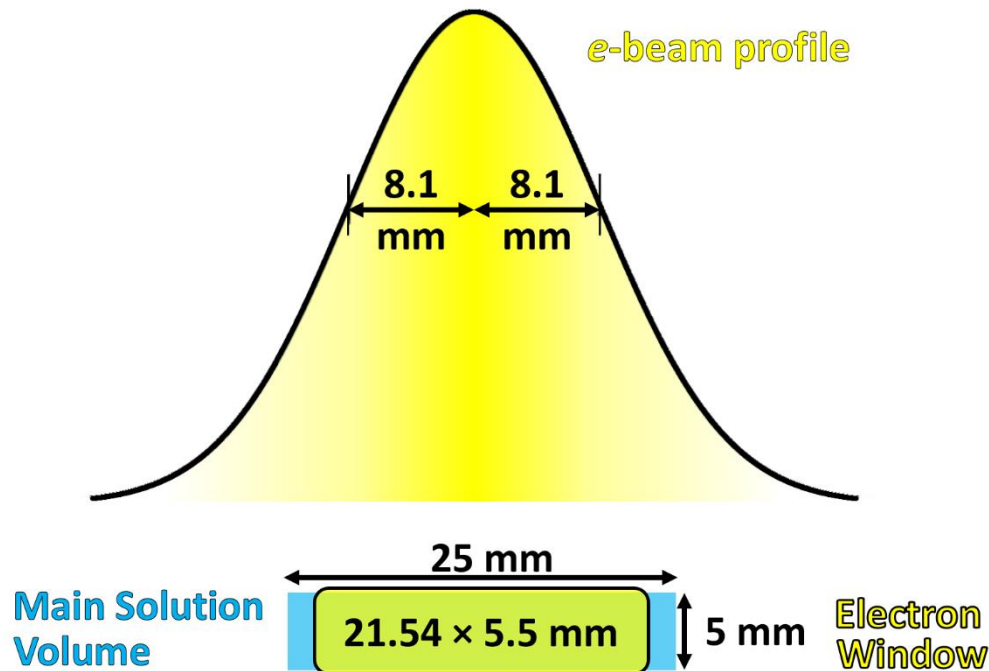


Figure 55. NDRL LINAC e -beam profile (upper) incident on the solution within the flow cell through the “window” slot machined in the stainless steel body (lower, frontal view).

Although this beam spread results in a large concentration gradient across the pulsed light’s 25 mm path length and therefore leads to very different kinetics at the outer edges compared to the center, thankfully an integration over the concentration gradient looks almost identical to modeled results using the average of the total dose computed as constant across the path length, as supported with the fittings shown in the previous section on electron dosimetry. Still, it could be expected to make a difference in some systems.

However, a second concentration gradient becomes a concern due to the ca. 21.5 mm window cutout to let in the e -beam being shorter than the 25 mm distance from the inner face of one fused silica window to the other. Simple mathematical integration of a Gaussian distribution centered on 0 with $\sigma = 81$ mm from +12.5 to -12.5 mm yields 87.75, whereas integration from +10.75 to -10.75 mm (the window width is ca. 21.5 mm) yields 81.65, thus the distinction between these two cases represents a 7% change in the assumed experienced dose. Which path length

should be used? Based on fittings for the electron dosimetry, it seems that defining the path length to be 20 mm instead of 25 mm is the better decision, though this assumes all modeled pure water rate constants, doses, and extinction coefficients are correct.

6.3 Kinetic Data Analysis Methods using IGOR and KinTek

6.3.1 IGOR Pro

IGOR Pro is a powerful and versatile commercially available scientific and engineering data analysis software developed and maintained by WaveMetrics, Inc. since 1989 as an interactive numerical computing environment with a fully functional programming language and compiler. It is completely programmable for analyzing data, which it stores in arrays of up to four dimensions referred to as “waves”, and is well known for its graphics capabilities. Its built-in functions are also extendable with external operations to allow data acquisition from, manipulation of, and communication with external devices; and in principle can perform any task that can be programmed in the C or C++ programming languages.

6.3.1.1 Borate radical first order reaction with $\cdot\text{OH}$

Data on the initial risetime obtained using multiple concentrations were fit in IGOR Pro to the following equation of an x-offset exponential rise function:

$$y(x) = y_0 + Ae^{-\left(\frac{x-x_0}{\tau}\right)} \quad (101)$$

The initial risetime behavior was expected to be representative of first order reactions, and so the fitted time constant, τ , was then used to obtain an Arrhenius plot for what was later determined to be the growth of the borate radical, as:

$$[A] = [A_0]e^{-(kt)} \quad (102)$$

where $[A]$ is the concentration at time t , and k is the rate constant, commonly defined as $k = \frac{R}{C}$ where R is a reaction's rate at a concentration of C , and the rate is calculated as $R = \frac{1}{\tau}$ by the time constant computed from the exponential fitting.

6.3.2 KinTek Explorer

KinTek Explorer is a proprietary software developed and maintained by KinTek Corporation as a dynamic chemical kinetics simulation and data-fitting program (Johnson, et al., 2009), and is steadily being improved through collaboration with numerous organizations from their active research, including this work. It is capable of modeling complex systems numerically by generating differential equations for arbitrary reaction schemes from descriptions as simple as “A + B = C” without simplifying its mathematical approximations. Any signal (optical, chemical, electrical, etc.) can be dynamically simulated from parameters (concentration, titration, voltage, pH, etc.) alterable in real time, allowing for experimental data obtained from multiple conditions to be fit simultaneously to a single globally unified model. This technique for fitting data to a model can be tailored to link the rates of different reactions, set limits on rates and concentrations, and provide detailed error analysis as confidence contours onto fitted parameters.

There are two main challenges faced in fitting data to a digital simulation, and they are in direct competition with each other: a model is required to be complete enough to adequately describe the physical mechanism at play without relying on unsupported simplifications, but it cannot be overly complex beyond the support of the data's information content (Johnson, 2009). The simulation requires provision of four fundamental ingredients: the minimal model of reactions, the set of reaction rate constants, the system's initial conditions (dose, concentration, mixing time),

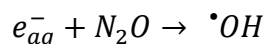
and the set of observable output functions (what species' behaviors are expected to be perceived); and this can then be fit to multiple sets of experimental data.

6.3.2.1 Kinetic Mechanism

Again, KinTek is able to use arbitrary reaction schemes in its modeling, where the only chemical species necessary to be defined in a simple "A + B = C" scheme are those which are considered "observables" in the data or those which play some part in the kinetics of said observables. For example, the reaction of nitrous oxide with aqueous electrons of course produces N₂ along with OH⁻ and •OH, by the equation:



However, N₂ is not considered an observable for the purposes of KinTek to fit the kinetics of the borate radical reaction in this case, as it is not an absorbing species detectable by this transient spectroscopy method, nor is the OH⁻. Therefore, Equation (43) is represented in a simplified form to be entered in KinTek's model as:



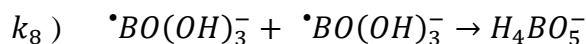
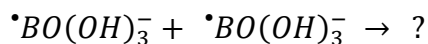
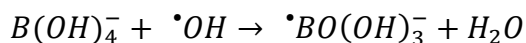
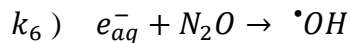
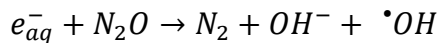
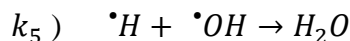
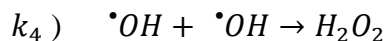
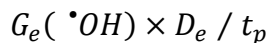
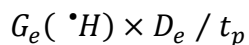
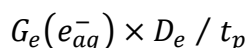
Furthermore, KinTek is not inherently well-adjusted for simulating the kinetics induced by pulse radiolysis. Therefore, in order to allow simulation of induced radiolysis by the *e*-beam pulse we include a stand-in precursor variable called "doserate" representing the well-known Low LET γ -radiolysis yields in water, which generates the most pertinent species.

Based on the results of the analysis by IGOR detailed later in Section 7.3.1, we suspect that the borate radical generated from the reaction between borate and •OH undergoes a bimolecular recombination which generates a secondary absorbing radical species. We also provide N₂O in solution as an e_{aq}^- scavenger, and thus their reaction in its simplified form. We also include

simplifications for the two most impactful reactions between the unscavenged species, though omit many of the other known reactions in such a chemical system for the sake of further simplicity, as well as to not unnecessarily strain the intended capabilities of KinTek. The real-world radiolytic yields and equations for the reactions chosen to be represented in KinTek as well as the simplified equivalent reactions included in its model are thus:

Real Representation

Simplified KinTek equivalent



where G_e is the corresponding product yield by electron radiolysis (mol J^{-1}), D_e is the electron dose (Gy), and t_p is the width of the electron pulse (s).

For the sake of clarity in further discussions, we have assumed that perhaps the borate radical's self-recombination results in an oxygen abstraction and the formation of $H_4BO_5^-$ a peroxyborate. However, it should be made clear that this has not yet been supported analytically and therefore should be considered here as nothing more than a simple placeholder for use in our analysis.

Each rate constant k_i is allowed an entry for both the forward and the reverse reaction, though here we specify no equilibrium reactions. The rate constants of the first three reactions correspond to the g -values of the generated species by Low LET γ -radiolysis, the values for which are obtained from the review by Elliot and Bartels as well as the rate constants k_4 and k_5 all dependent on the temperature (Elliot & Bartels, 2009). Based on the individual experimental run conditions, we enter the initial concentrations of the N_2O and the borate, and define the appropriate *doserate* and time regime values to simulate the e -beam pulse contribution to the chemistry model. This achieves an entirely acceptable model for use in fitting our data.

6.3.2.2 Global fitting of time-resolved spectra via SVD

Upon importing a 3-dimensional array for time-resolved spectra, KinTek automatically performs Singular Value Decomposition (SVD), deconvoluting the multiple overlapping spectra of many present species changing concentration with time in order to define the unique spectrum of individual species and obtaining the time-dependence for each's signal (Johnson, 2018). The theory of SVD is embedded in linear algebra, and further explanation of this process can be found in (Hendler & Shrager, 1994). In brief summary from their description: one species' spectrum can be represented as a vector (a column of numbers with each element signifying absorbance at a particular wavelength), the overall spectrum at a given time in a mixture of species is the sum of each's absorbance scaled by their concentration at that time (as discussed in Section 1.5.1), thus a matrix containing raw time-resolved spectra would have (in linear algebra terms) a distinct row space (absorbance) and a distinct column space (wavelength), and the process of SVD separates the two spaces into individual matrices along with a third matrix informing on the eigenvalues which are scalar factors for the eigenvectors in the previous two matrices and each corresponds to a supposedly distinct species. A visual representation of the process can be seen in Figure 56 and

Figure 57, wherein time-resolved spectra data for the reactions involved in the catalyzation of EPSP synthase are plotted, and the SVD results (corresponding to the absorbance and wavelength matrices) automatically generated by KinTek are shown in separate plots for the relative spectra of the three present species as well as the relative signal amplitudes/concentrations of the three species evolving over time. These data plots are adapted from the Spectra-ES-EI-EP example data included in KinTek's download files, which are available at <https://kintekcorp.com> and a more in-depth explanation of their detailed analysis is provided by the program's developer Kenneth A. Johnson in (Johnson, et al., 2009).

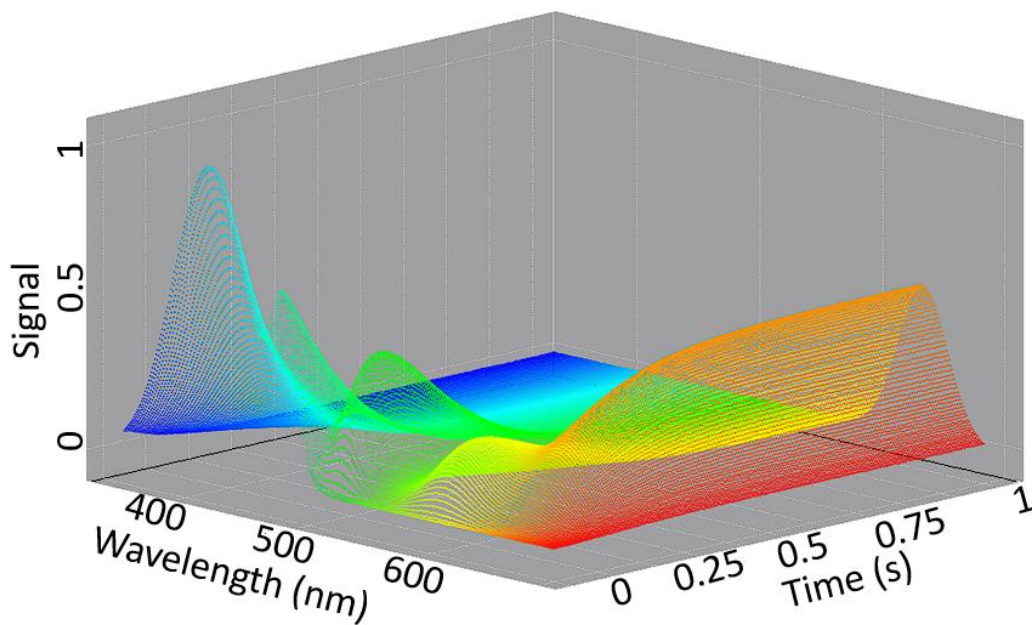


Figure 56. Plot of full time-resolved spectral data, adapted from the Spectra-ES-EI-EP example data included in KinTek's online download files on reactions of catalyzed EPSP synthase.

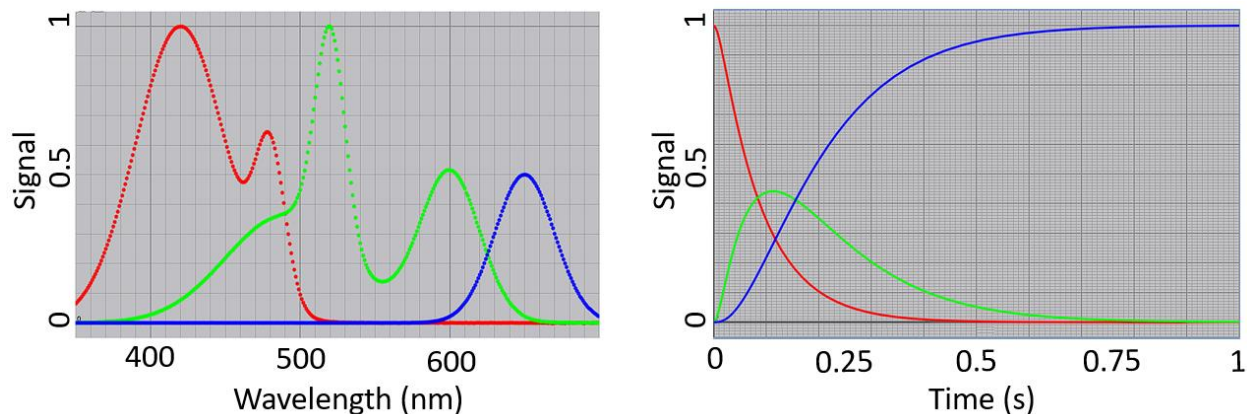


Figure 57. Plots of relative spectra of the three present species, as calculated by KinTek's SVD method (left); and relative signal amplitudes/concentrations of the three species' spectra evolving over time (right), as calculated by KinTek's steady-state kinetics model, both included in KinTek's download files on reactions of catalyzed EPSP synthase.

We found KinTek Explorer admirably advantageous in its allowance of any model entered by a user to be applied to the resulting time dependence matrix of signals for fitting by numerical integration of the provided rate equations, and for its capacity to fit multiple sets of user-specified experimental conditions to be fit globally to a single model (Johnson, 2009). In comparison to utilizing KinTek, the task of performing similar fittings with IGOR was determined to be a far less favorable ordeal due to the multivariant conditions inherent in our measurements, including the daily changes in dose rates by the LINAC at NDRL (despite equivalent settings on each day), along with of course the purposefully varied doses and concentrations among all experimental runs' collected data made.

7 Results and Discussion

7.1 Hydrogen generation by $^{10}\text{B}(n,\alpha)^7\text{Li}$

7.1.1 Calibration, RGA precision

Measuring the proportionality constant as a value of peak-area-per-mole of select gases was carried out daily, typically by measuring three calibration samples on each day. Either the same 120 mL volume as an experimental solution was repeated in order to avoid any change in the water column height within the sparger affecting a change in the argon flowrate and thus a change in the gas split ratio for mass spec sensitivity, or multiple different volumes were measured to confirm signal peak area linearity with differing concentrations of sparged gases.

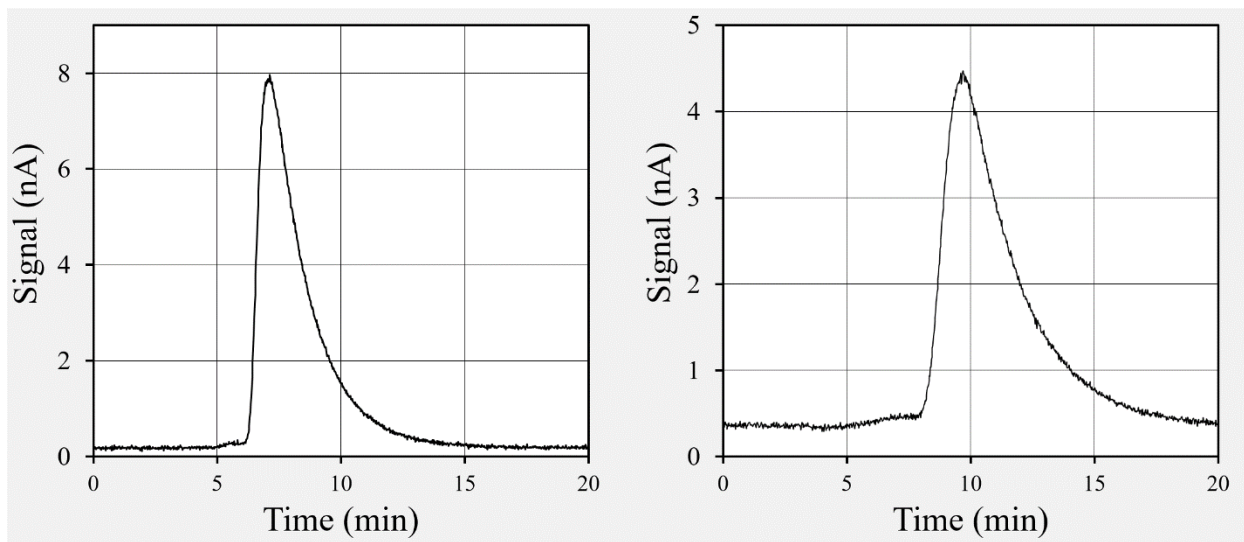


Figure 58. Ion current signal peaks of hydrogen (left) and nitrogen (right) for a typical 120mL calibration sample volume containing a calculated content of 4.87 and 4.22 μmol of H_2 and N_2 , respectively, dissolved in deionized water.

A pair of typical calibration signals from one sample for hydrogen and for nitrogen are shown in Figure 58. As is apparent by the signal behaviors in the figure, the S/N noise ratio is entirely adequate for accurate analysis. A set of signal peaks obtained for hydrogen and nitrogen from three different volumes of solution for one day's calibration are shown in Figure 59,

confirming good linearity with gas concentration and negligible effect from changes in water column height within the sparger.

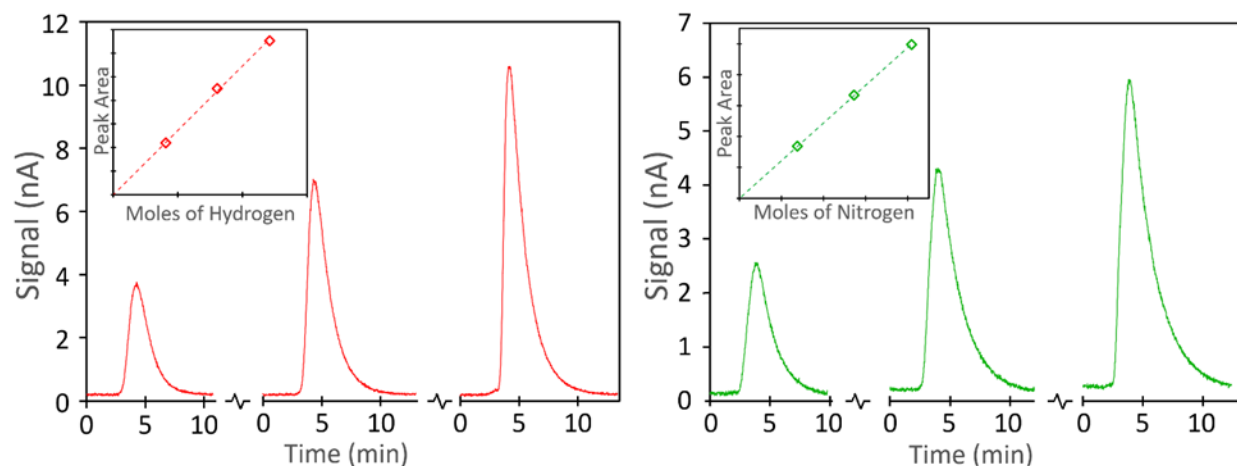


Figure 59. RGA ion current signal peaks for hydrogen (red) and nitrogen (green) for typical calibration sample volumes of 40mL, 80mL, and 120mL, with the 120mL sample containing 4.83 μmol of H_2 and 4.09 μmol of N_2 . Linearity is demonstrated in the upper left corners. Error bars of the signal integration are smaller than the size of the points.

Low concentrations of products' yields from the $^{10}\text{B}(\text{n},\alpha)^7\text{Li}$ event have been an important challenge to overcome for obtaining data. Thankfully, this system operated with a sensitivity high enough to measure our experiment's minute quantities of resulting hydrogen gas dissolved in the 120 mL solution sample volumes at concentrations as low as between 4–9 $\mu\text{mol/L}$, with a Signal-to-Noise level that has proven to be high enough for confident detection of H_2 content levels down to 0.5 μmol . A comparison is later made in Figure 81 between the H_2 signals typically obtained for the work done by Dr. Travis Dietz, my predecessor, and the signals obtained in this work, which demonstrates clear improvement on the detection of this gas product.

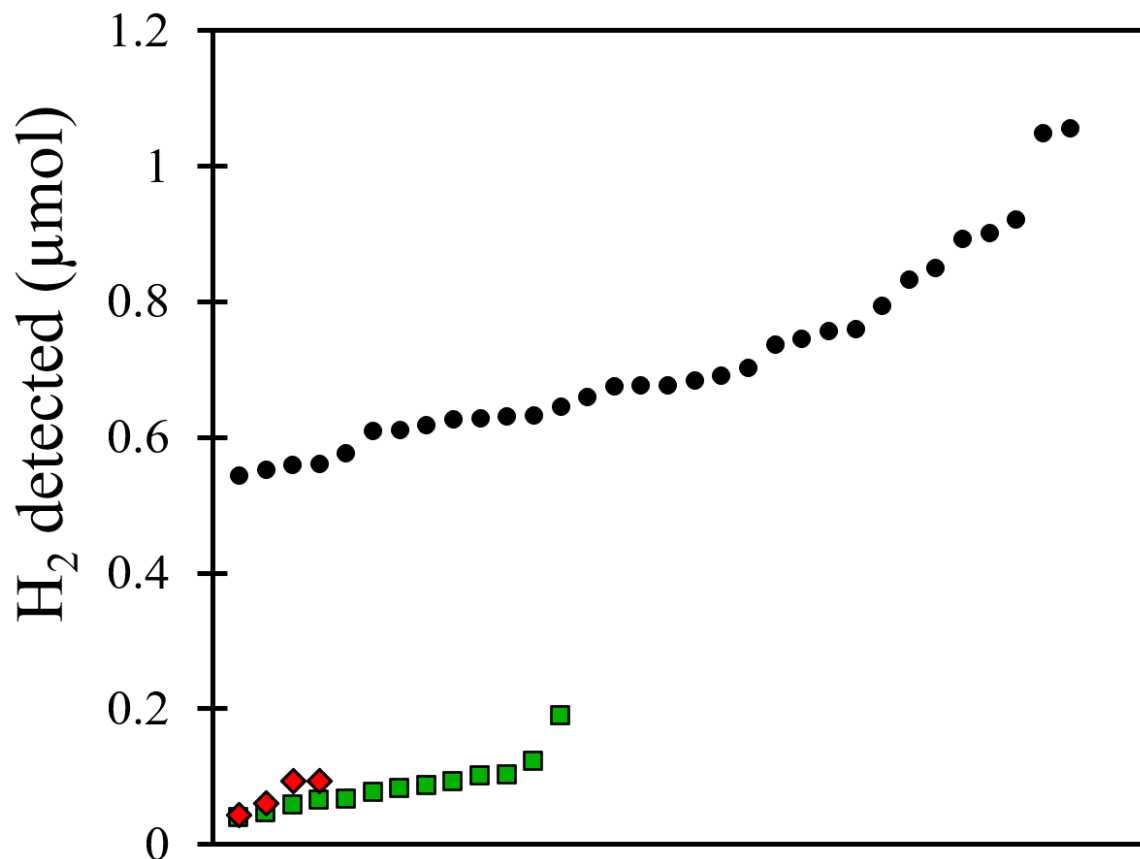


Figure 60. Plot of all H₂ content levels detected in all sample solutions, arbitrarily sorted from smallest to largest. Three sets of samples are distinguished: main experiment solutions containing ¹⁰B which were irradiated (black circles), gamma “blank” samples without boron which were irradiated (green squares), and corrosion “blank” samples containing ¹⁰B which were not exposed to any irradiation but held at high temperature (red diamonds).

Figure 60 shows a plot of the total H₂ content detected in nearly every single evaluated experimental solution sample. Not displayed are the calibration solution samples’ H₂ content, as they are typically an order of magnitude larger than the H₂ content in the boronated irradiated solutions. The RGA signals detected for the smallest gamma and corrosion samples’ contents were at the limit of our system’s detection capabilities. The smallest signal of the corrosion sample set was obtained from solution held in the titanium cell for one hour while maintaining a temperature of 200 °C, and contained a calculated 0.04 μmol of H₂. The signal was only just above the noise level, as can be seen in Figure 61.

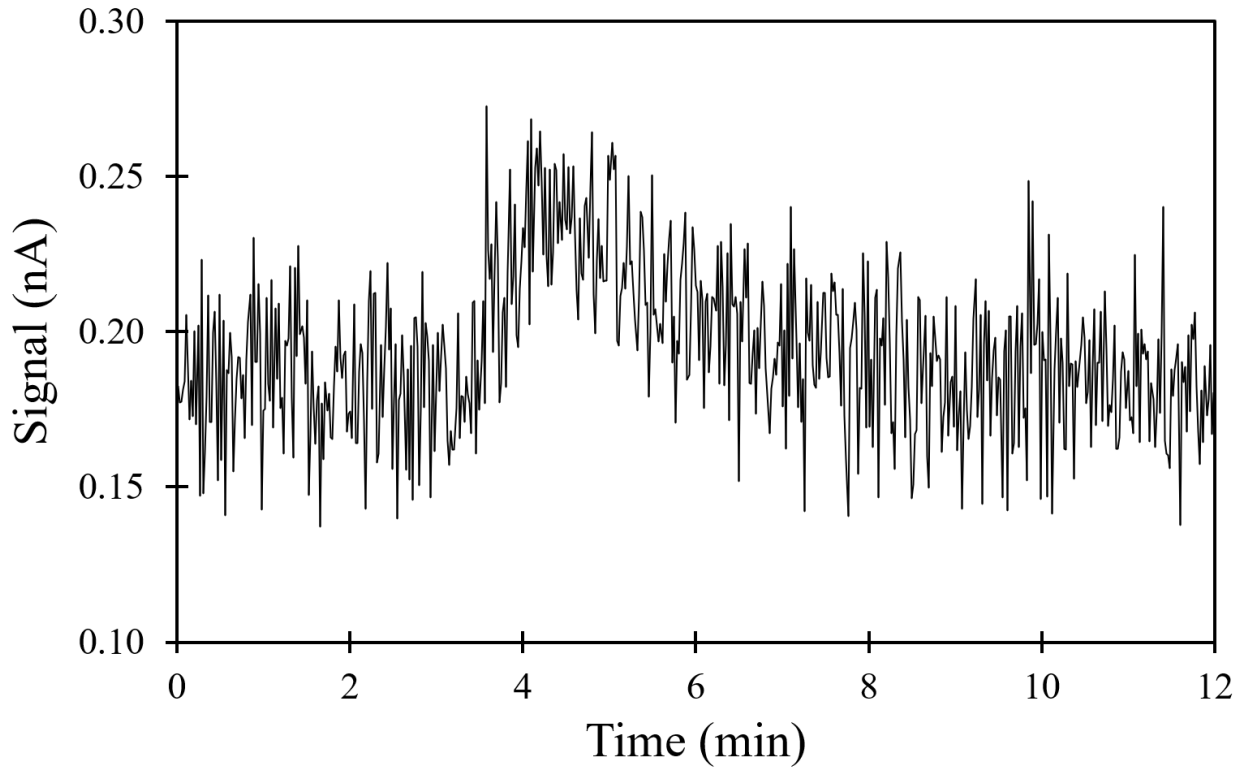


Figure 61. Plot of the RGA raw signal obtained for a corrosion "blank" sample held in the Zircadyne 702 cell at 250 °C for one hour, containing a calculated content of 0.04 μmol of H_2 dissolved in 120 mL of solution.

7.1.1.1 Change in calibration proportionality constant over time

The proportionality constant was measured on every day in which experimental measurements were obtained, and a plot of its behavior over the full course of this experimental campaign during the 2022 year is given in Figure 62. Although explaining this erratic behavior is beyond the scope of this work, it clearly indicates the need for RGA calibration to be performed daily.

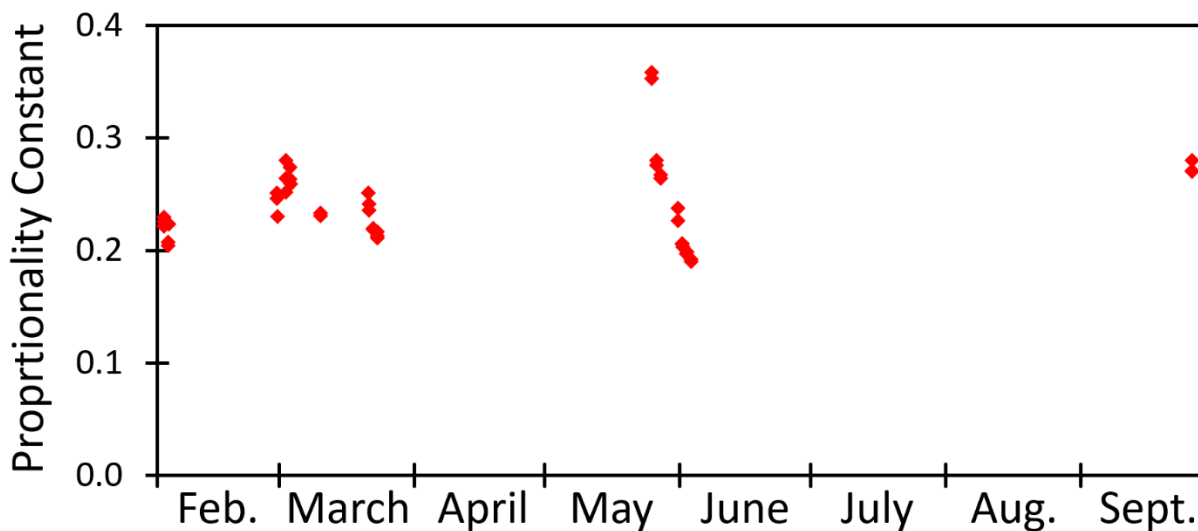


Figure 62. Plot of the RGA mass spectrometer proportionality constant obtained for H_2 on each day in which experimental results were obtained.

7.1.2 Temperature Control Precision

The LabVIEW program used to monitor the flow cell temperature and electrical control systems used to supply power to the resistive heating tape all performed in a highly reproducible manner. The highest temperature at which the $G(H_2)$ from $^{10}B(n,\alpha)^7Li$ was measured was ca. 300 °C; the change in cell temperature caused by flowing fresh room temperature water into the heated cell was at its largest here, and the thermocouple readings for three irradiation durations are shown overlaid in Figure 63.

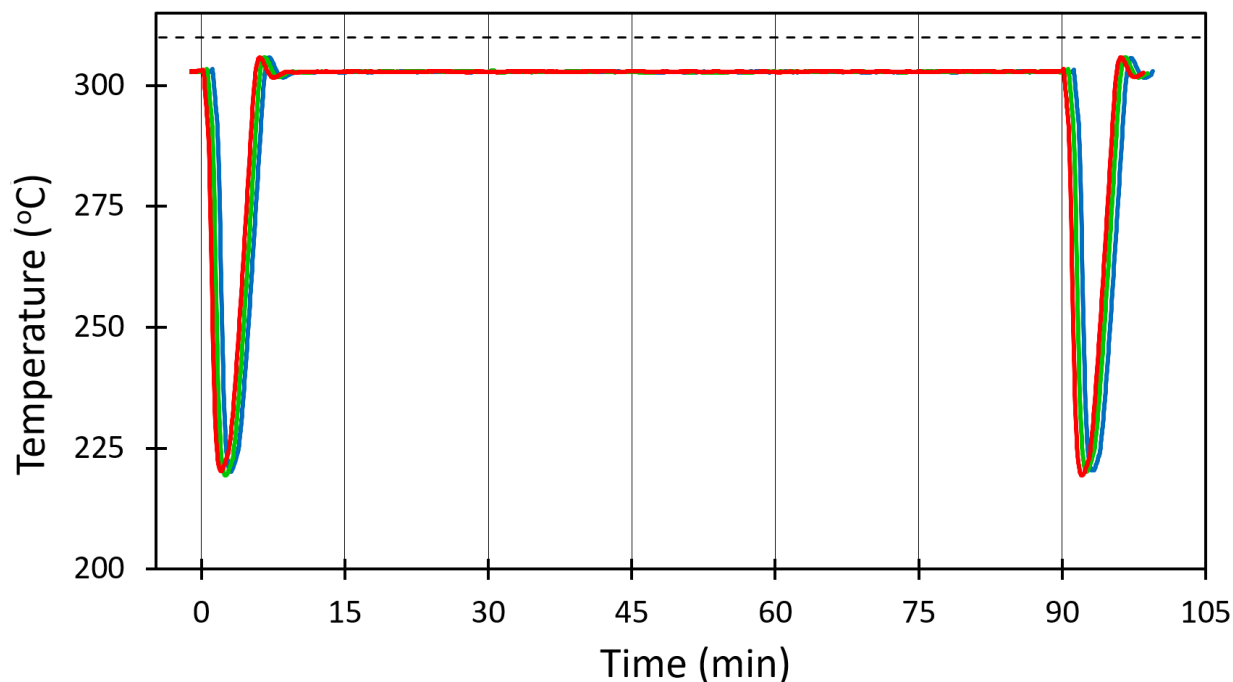


Figure 63. Plots of LabVIEW temperature readings from thermocouple on the cell inlet, showcasing temperature control and reproducibility. The first sample (red) has no offset, the second (green) sample was given an offset of +30sec, and the third (blue) sample as given a +60sec offset. The setpoint temperature of 310 °C is indicated (dashed line).

At time-zero, fresh solution begins flowing into the cell and the irradiated solution is simultaneously extracted. As the thermocouple is in contact with the metal tubing at the flow cell's inlet, the response by the control system is able to be almost immediate and the “downtime” during which the cell temperature is being recovered is minimalized. The full 120 mL of solution is finished flowing within ca. 3 minutes, which in this plot corresponds to the turning point when the cell begins increasing in temperature – though at lower temperatures the power supplied is able to overcome the cooling effect of the fresh solution and the response time is faster.

7.1.3 Temperature Measurement Accuracy

Unfortunately, the thermocouple wire extensions used for the cell thermocouples were not all connected in the proper orientation until almost the end of these experiments. There were four additional dissimilar metal-metal junctions at various adapter/union plugs, and the voltages in

series were paired so as to nearly subtract out of the electrical voltage measurement, such that the problem was not easily recognized. In retrospect, we believe the temperature readout on any given day may have been inaccurate by ± 5 °C, based on the behavior of these thermocouples observed over the course of this experimental campaign as well as from qualitative comparison with facility thermostats monitoring the ambient air temperature and the temperature of the water in the reactor pool. Fortunately the $G(\text{H}_2)$ proves to have very weak temperature dependence so that this problem was not critical.

7.1.4 Extreme Corrosion of Zirconium Alloy Cell

The first irradiation cell made of the zirconium alloy Zircadyne® 702 was used for approximately two months, subjected to thermal cycling and irradiation during initial testing and later in experimental runs. Unfortunately, this cell material was found to undergo an extreme degree of oxidation at temperatures of 200 °C and higher, producing an overabundance of molecular hydrogen in the solution, as is demonstrated in Figure 64.

During initial testing at the system's maximum temperature, pure water was flowed into the cell then held at 25 MPa at 300 °C for ca. 30 minutes, with the reactor powered off. When the sample volume was being extracted into the glass sparging apparatus, fully formed bubbles could clearly be seen flowing in with the water from the cell. The gas was confirmed by the RGA mass spectrometer to be mainly hydrogen, rather than an air leak in our solution tubing as we initially expected. Signal analysis indicated hydrogen concentrations $>150\times$ higher than the concentrations typical for the irradiated boric acid solutions at room temperature.

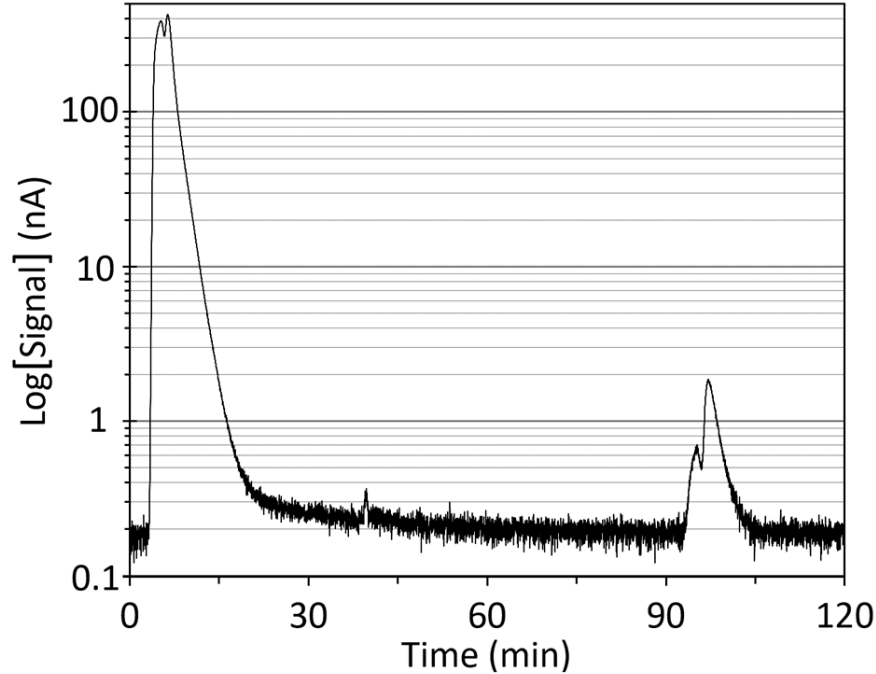


Figure 64. Log scale plot of the hydrogen signals obtained when breakaway corrosion was first observed during irradiation of a solution with 10 % boron concentration (0.03 M) in the Zircadyne 702 cell; the first sample was irradiated for 1.5 hours at 300 °C while the second sample was irradiated for 1 hour at 150 °C.

The cause has been judged to likely involve breakaway corrosion exhibited by the zirconium alloy tubing material (Ensor, et al., 2022) by the oxidation reaction:



Therefore, it was necessary to replace the zirconium tubing with the Grade 2 Titanium cell for higher temperature experiments. The amount of hydrogen produced in the zirconium cell by this corrosion was confirmed to be negligible (<1 %) when compared to the hydrogen resulting from the $^{10}\text{B}(n,\alpha)^7\text{Li}$ recoil ions at 175 °C and was not distinguishable at lower temperatures.

7.1.5 Corrosion of Titanium Cell at Above 200 °C

The titanium cell was conditioned and tested for corrosion similar to the zirconium cell's treatment. The new cell was filled with pure water, pressurized to 25 MPa, and heated to 300 °C, then held at those conditions for two days to encourage the formation of the oxidized passivation

layer. After this conditioning period, several pure water samples were flowed in and held for approximately one hour at 300 °C and 25 MPa to then be analyzed for hydrogen content generated by the oxidation reaction:



The signal analysis indicated manageable levels of hydrogen content in the titanium cell, much lower than those produced in the Zircadyne 702 cell. During the boron experiments to measure $G(H_2)$ at higher temperatures, on a given day, prior to reactor power-up, a sample of the boric acid solution was flowed into the titanium cell while it is held at a target temperature and 25 MPa. This “corrosion blank” is kept within the cell for ca. 1 hour, then analyzed to quantify the hydrogen produced solely via corrosion during that time. This yield at the target temperature is then used as an estimate for how much hydrogen must be subtracted as “corrosion yield” from the raw hydrogen content measured in samples irradiated by neutrons at the same cell temperature later in the day, as a correction in the calculation of the “boron yield” hydrogen.

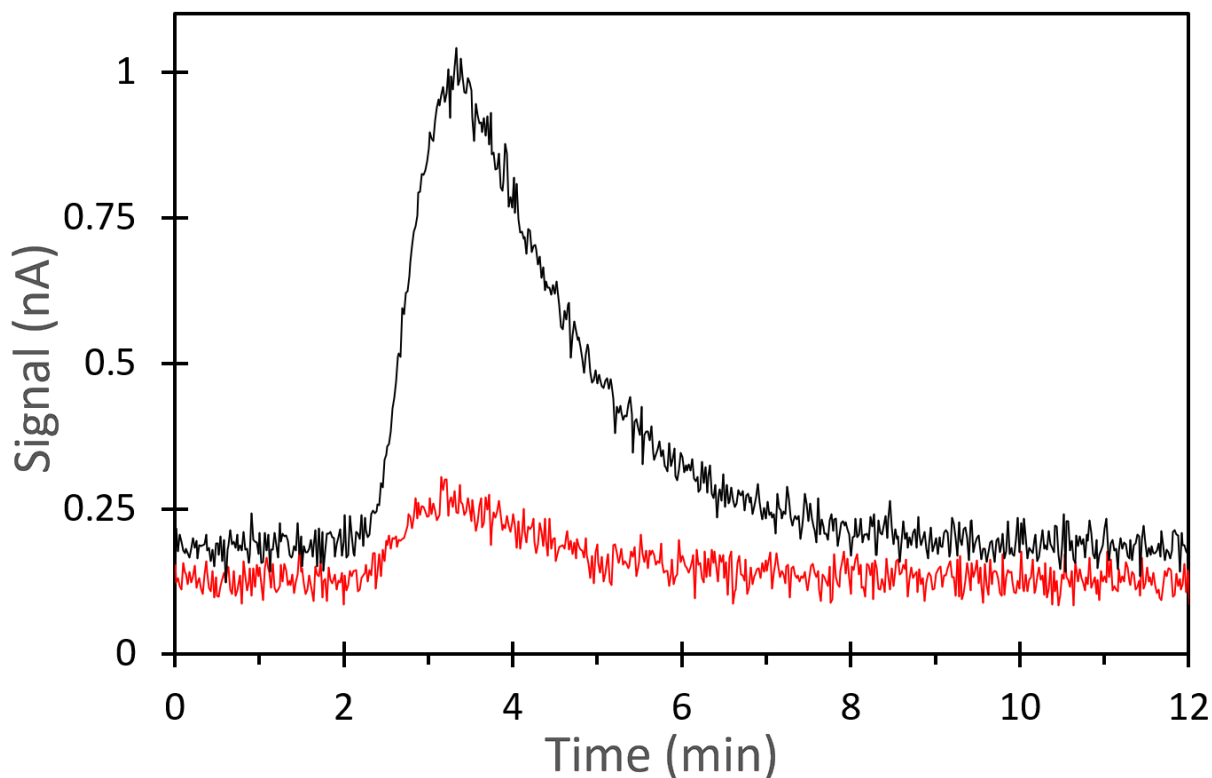


Figure 65. Example hydrogen signals for a corrosion blank (red) and experimental sample (black), both obtained at 300 °C over a one-hour duration. The corrosion signal has been given an offset of -0.05nA.

Figure 65 compares the signals of a corrosion blank and a boron experiment sample, where both were heated to 300 °C and held at 25 MPa for one hour. Experiments at 300 °C used half of the typical concentration of boric acid (0.15 M) to more accurately resemble the concentrations used in PWRs while running at this temperature. With the titanium cell, the amount of hydrogen produced in “corrosion blank” samples compared to the total hydrogen detected in irradiated samples was ca. 17% at 300 °C, 8% at 250 °C, and only 1% at 200 °C.

7.1.6 Gamma

While we expect that the ^{10}B experimental solution is exposed to some small levels of gamma radiation directly from the core, we assume that some gamma radiation results from neutron-capture fluorescence in the surroundings and thus is proportional to the measured neutron

flux density in the sample. The content of hydrogen gas produced within an irradiated “gamma blank” sample is used to calculate the total dose rate of gamma radiation expected to be experienced by the boron samples.

7.1.6.1 MCNP Simulations for Gamma Background

The radiation spectrum in the RINSC thermal column was simulated accurately to recent measurements using the Monte Carlo neutron transport code MCNP 6.2 applied to a geometrically simplified model of the experimental flowcell, assessed for both the Zircadyne 702 and the Titanium Grade 2 flow cell materials. A ratio for the energy deposited into the aqueous solution was established between the energy deposition by only photons (gamma radiation) versus that by all events (including the heavy ion products of the $^{10}\text{B}(n,\alpha)^7\text{Li}$ fission event). It was indicated from these simulations that by using the zirconium and titanium alloys to contain the solution during irradiation that the percentage of energy deposited in the boric acid solution from photons alone would be only 2.0 % and 3.1 %, respectively, of the total energy deposited. This is a significant improvement from the ratio of almost 30% in the precursor experiment due to activation of titanium flow cell material (Dietz, et al., 2021). The minor gamma dose contribution to be accounted for as part of the total energy deposited in the samples indicated by these simulations was confirmed by experimental evaluations of the gamma radiation background in the thermal column.

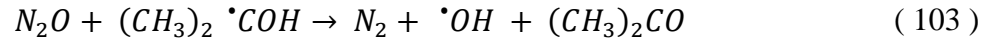
Additionally, the neutron flux density found in the RINSC reactor environment was successfully modeled in MCNP, and these simulations indicated this facility would provide a thermal neutron flux density of $2.4 \times 10^8 \text{ s}^{-1} \text{ cm}^{-2}$ to our flowcell at its intended location within their thermal column – another significant improvement as an increase from the average $8 \times 10^8 \text{ s}^{-1} \text{ cm}^{-2}$ obtained at NIST’s Neutron Imaging Facility beamline in the precursor experiment (Dietz,

et al., 2021).

7.1.6.2 Gamma Background experimental evaluation

As was discussed in Section 5.5, we expected in this system a measured $g(\text{H}_2) = G(\text{H}) + G(\text{H}_2) = 0.60 + 0.45 = 1.05$ molecules/100eV and $g(\text{N}_2) = G(e_{aq}^-) = 2.5$ molecules/100eV solely from the Low LET gamma.

For this experimental investigation into the contribution of any H_2 overproduction due to background gamma radiation, we were surprised to measure in several repeat experiments that the ratio of N_2/H_2 signals is around 4–8 in these solutions rather than the expected ratio of $g(\text{N}_2)/g(\text{H}_2) = 2.4$. After some consideration, we realized the additional N_2 comes from a reaction of the isopropanol radicals with N_2O as:



Note that reaction (103) produces another $\cdot\text{OH}$ radical, meaning the N_2 is released in a chain reaction, with $(\text{CH}_3)_2 \cdot\text{COH}$ as the carrier. The isopropanol radicals are well-known to be powerful reducing species, but typically the rate constant for reduction of the N_2O is too low to be competitive with the self-disproportionation reaction (92) in a gamma source (several Gy per second dose rate). In the present case of several Gy per hour dose rate, the second-order self-disproportionation is slow, and reaction (103) becomes important. We estimate a reaction rate on the order of $k_{(103)} = 1 \times 10^3 \text{ M}^{-1}\text{s}^{-1}$ can explain our observation. It means we should use the measured value for $g(\text{H}_2)$ to evaluate the gamma background dose rate for calculating our gamma correction factor rather than the measured value of $g(\text{N}_2)$.

Figure 66 shows a typical plot of the raw signal obtained by the RGA mass spectrometer from a gamma blank sample as compared to a standard boron sample. The gamma blank was

irradiated for 120 minutes and sodium activation measurement implies a neutron flux density of $4.50 \times 10^8 \text{ s}^{-1} \text{ cm}^{-2}$, whereas the boron sample was irradiated for 60 minutes at $3.80 \times 10^8 \text{ s}^{-1} \text{ cm}^{-2}$. The extended duration used for gamma blanks was necessary to obtain sufficient S/N for dependable analysis, which demonstrates how minor the H₂ contribution from our materials' fluorescence is.

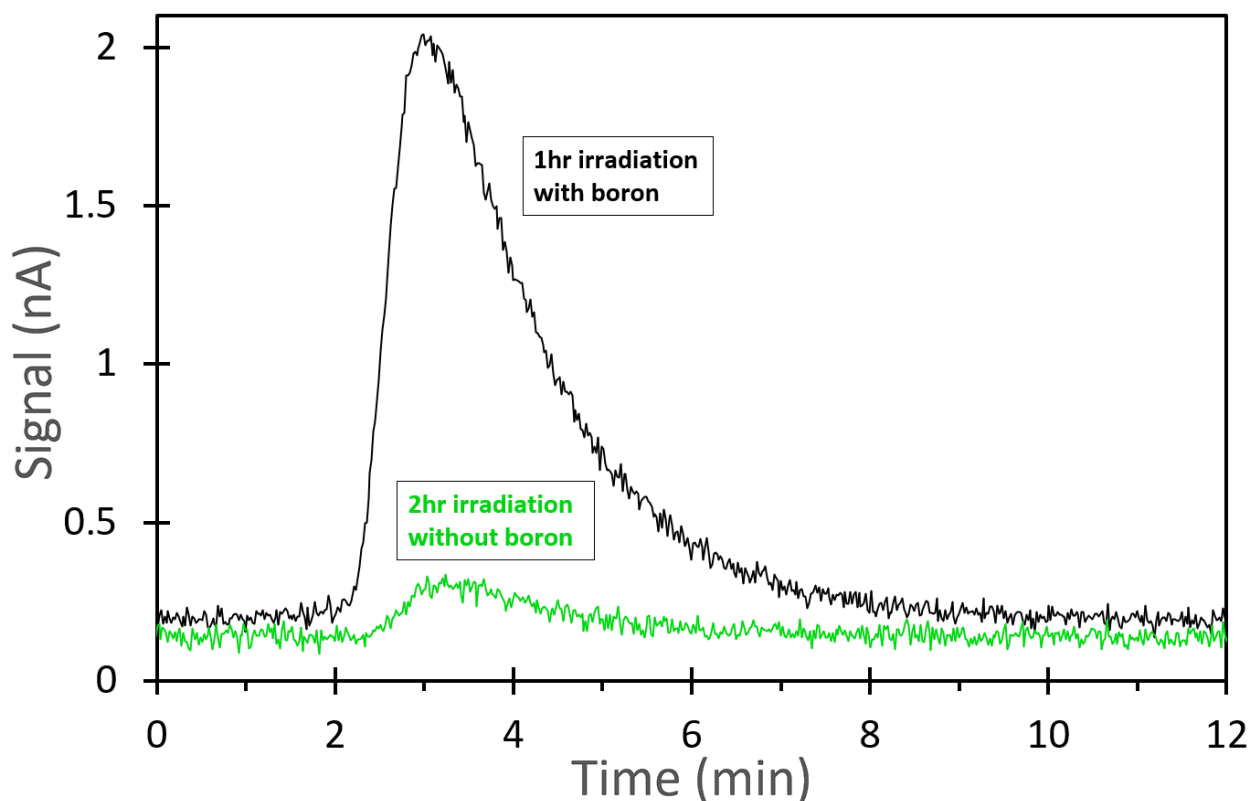


Figure 66. Comparison of the hydrogen signals obtained in a sample for measuring gamma contribution (green) and an experimental boron sample (black), both irradiated at room temperature. According to sodium activation measurements, the gamma sample experienced a higher neutron dose compared to the boron sample by a factor of 2.43. The gamma blank signal has been given an offset of -0.05nA.

Over the course of this several-month experimental campaign, the configuration of the flow cell, its containment, and the surroundings were altered in minor aspects (such as the type of heating tape used, along with other assorted materials and components) as well as by changing more significant features (such as alternating the tubing material between the zirconium and

titanium alloys). Therefore, several measurements were made to evaluate the gamma background once the cell was configured in a particular arrangement and continual experimentation was performed. Figure 67 displays the ratio of gamma dose (measured by generated hydrogen content) to the neutron flux density the sample experienced (measured by sodium activation) for the three main configurations of the flow cell used. According to this evaluation, at room temperature the D_γ is calculated by Equation (93) to be 4.3 and 5.2 Gy/hr for the Zircadyne 702 cell material in two different arrangements, and ca. 7.9 Gy/hr with the Grade 2 Titanium cell material.

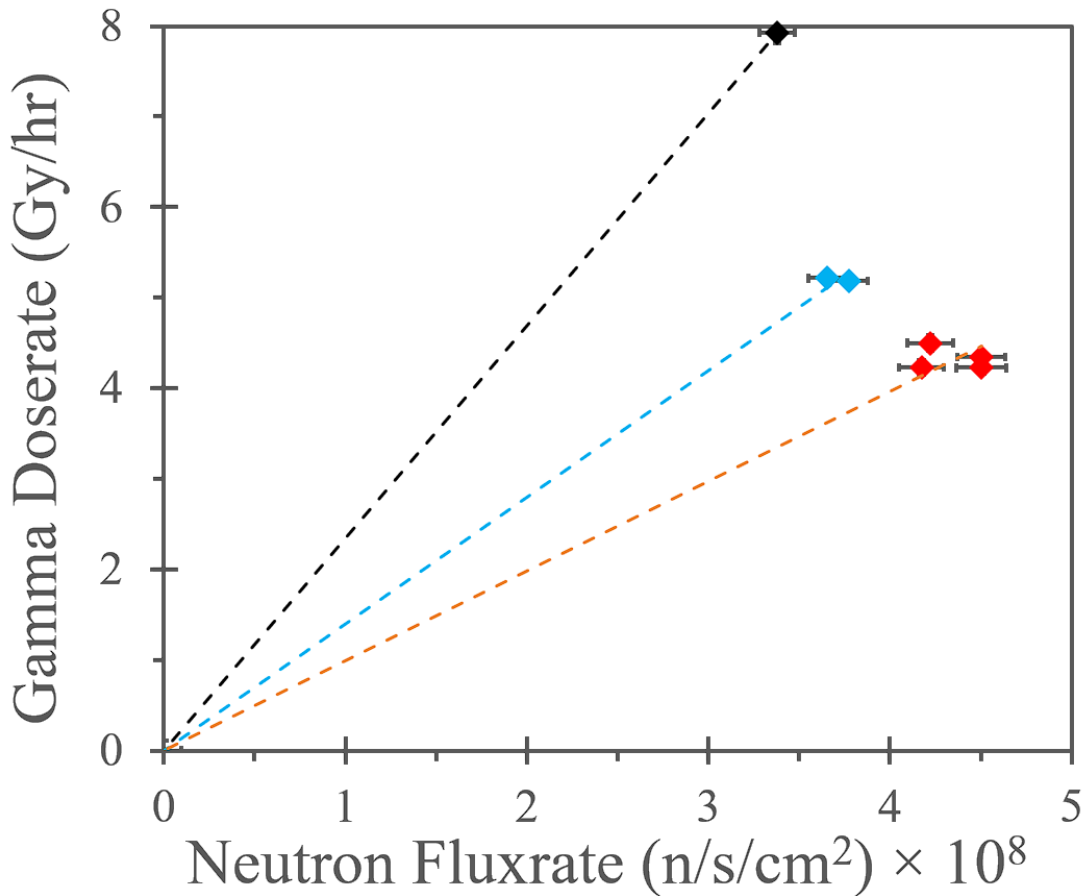


Figure 67. Gamma doserate versus neutron flux density, calculated from quantity of hydrogen produced and level of sodium activity, respectively, for different flowcell configurations throughout the experimental campaign: early experiments using Zircadyne cell (blue), midway experiments using titanium cell (black), later experiments again using Zircadyne cell (red). Error bars for gamma doserate are smaller than the size of the points.

In the boric acid experiments, the $\cdot\text{H}$ reacts with H_2O_2 product or with NO_2^- and does not contribute to the measured H_2 level. There was no change observed with or without the NO_2^- scavenger. Given the gamma dose rate deduced from the room temperature alcohol “blank” experiments, we use the following published equation (Elliot & Bartels, 2009) to calculate the radiation yield of H_2 produced by gamma background as a function of temperature:

$$g_\gamma(\text{H}_2) = 0.419 + (8.712 \times 10^{-4}) T - (4.971 \times 10^{-6}) T^2 + (1.503 \times 10^{-8}) T^3 \quad (104)$$

$$D_\gamma = \frac{H_2}{V_{Irr} \times g_\gamma(\text{H}_2) \times \rho_{\text{H}_2\text{O}} \times t_{Irr}} \quad (93)$$

where T is the temperature of the aqueous matrix ($^\circ\text{C}$) and $G(\text{H}_2)$ is in units of molecules/100eV (we multiply by 0.1036 for conversion to units of $\mu\text{mol}/\text{J}$). This G-value calculation is used in conjunction with Equation (93) to compute the value of H_2 for subtraction from the raw measured quantity, where this gamma contribution accounted for ca. 2 % of the total hydrogen detected at the lowest temperatures and up to ca. 6 % at the highest temperatures.

7.1.7 Reactor Stability based on Power Trend readings

A plot demonstrating the reactor stability during a daily run is shown in Figure 68, where three sample irradiation periods have been indicated. The average of the three neutron flux densities calculated from Equation (98) are plotted to show their relative deviation compared with the behavior of the power trend readings during their associated irradiation durations.

During the first half of this experimental campaign at RINSC, there were occasional “spikes” in power (for example the one shown in Figure 68, at 12:50pm just before the first sample is injected). These power spikes are unavoidable consequences due to the inherent design and operation of the reactor coupled with the fact that the data displayed in Figure 68 were acquired at

a late stage of the RINSC reactor's fuel cycle. This is indicative of the more-depleted fuel elements having built up fission products with large thermal neutron cross sections which thus act as neutron poisons, lowering the efficiency of the reactor. To compensate for this loss of efficiency while still operating to maintain the desired power level, the stainless steel regulating rod is adjusted at a faster rate than would be necessary with fresh fuel. At a high enough rate, it reaches its maximum extractable range before an entire day of operation at full power is completed, necessitating the manual adjustment of one or more of the boron control blades to increase the lower limit of reactivity which the regulating rod can provide when fully inserted. This compensational process causes a brief increase in power, due to a mismatch in the automatic adjustment speed capabilities between the rod and the plates, before the regulating rod can begin to counteract it, which results in the observed power spikes.

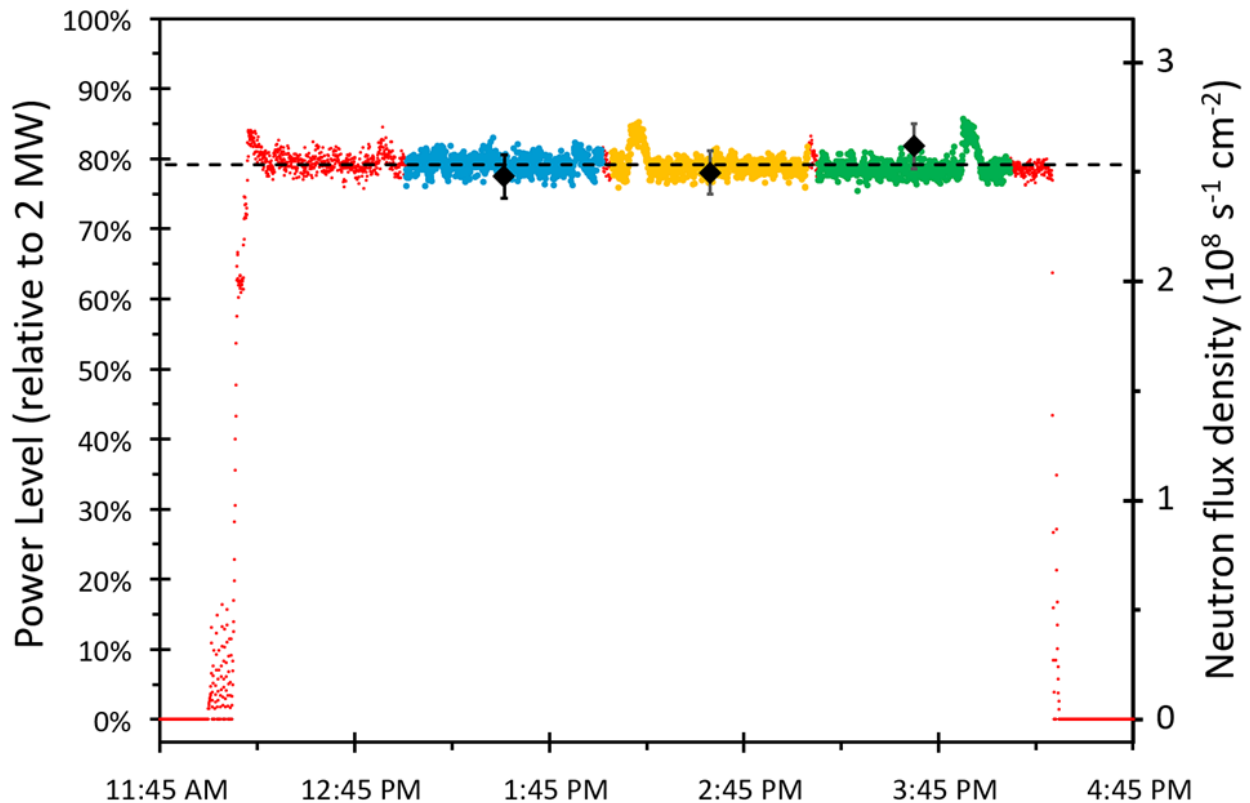


Figure 68. Plot of the data from power trend readings logged by the compensated ion chamber detectors. The points associated with the first (blue), second (yellow), and third (green) experimental samples' irradiations are distinguished from the readings during reactor power-up and shutdown (red). Also shown are the neutron flux densities calculated by sodium activation in each sample (black). The average of the three flux density values (2.51×10^8 n/s/cm²) has been plotted equivalent to the average of the relative power level for all samples (79.1%) (dashed line).

A refueling was performed on 18 April 2022, after the initial period of data acquisition in March but before the following periods of data acquisition in June and in September of that same year. Some of the effects from refueling can be seen in Figure 69. The fresh fuel prevents overall reactivity from declining as quickly, therefore the regulating rod does not reach its limit within the 6 hour time window the reactor is being held at full power and so there are no longer spikes in the power trend. It can also be noted that the reactivity level is at a slightly higher average value (previously 79%, after refueling 83%) and exhibits somewhat larger variation (standard deviation

of the power level during irradiation of the first samples are 1.2% on March 21 and 3.1% on May 25).

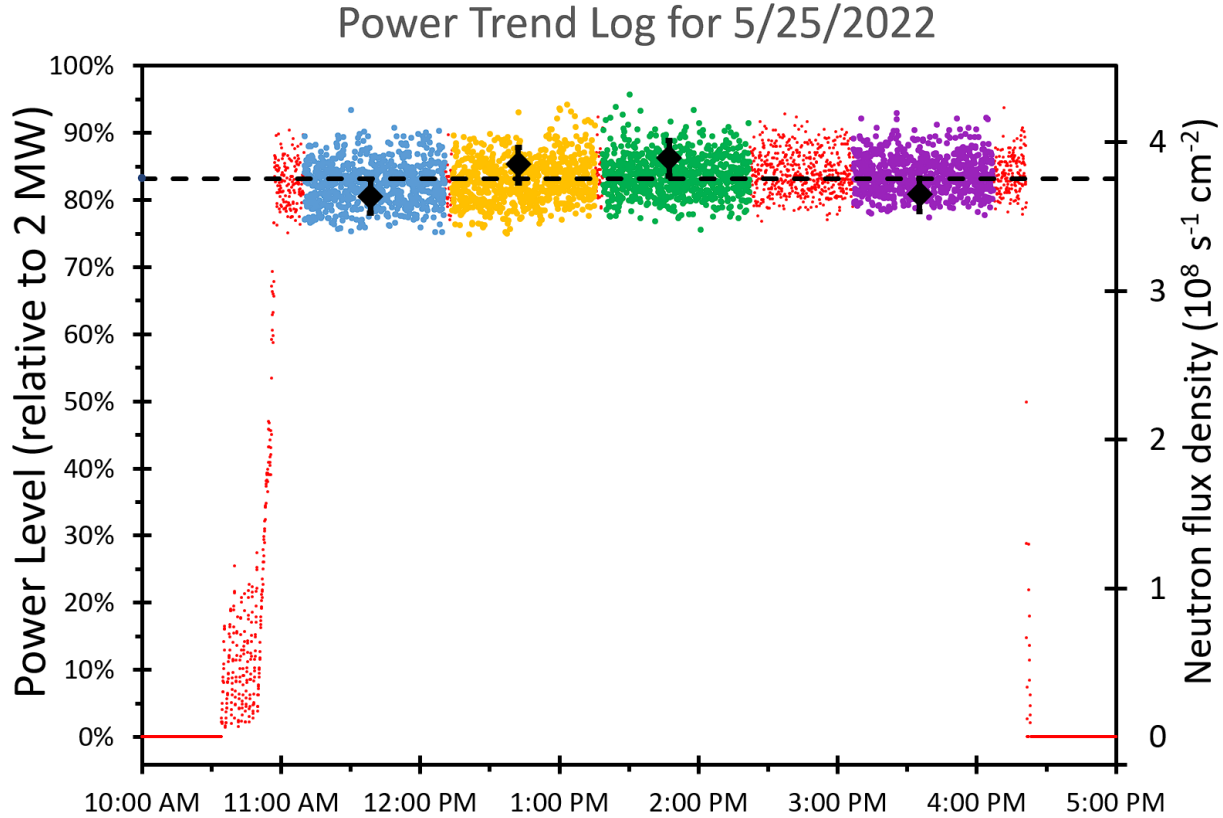


Figure 69. Plot of the data from power trend readings logged by the compensated ion chamber detectors. The points associated with the first (blue), second (yellow), third (green), and fourth (purple) experimental samples' irradiations are distinguished from the readings during reactor power-up and shutdown (red). Also shown are the neutron flux densities calculated by sodium activation in each sample (black). The average of the four flux density values ($3.76 \times 10^8 \text{ n/s/cm}^2$) has been plotted equivalent to the average of the relative power level for all samples (83.2%) (dashed line).

7.1.8 Power Trend vs Sodium Activation

Based on the total ^{24}Na produced during the irradiation (roughly 1 nCi is generated per hour of exposure for the concentrations of sodium ion used), we calculate the average neutron flux density within the solution volume:

$$\Phi_n = \frac{A_c e^{\lambda_{Na-24} \Delta t}}{\sigma_{Na-23} (1 - e^{-(\lambda_{Na-24} t_{irr})}) c_{Na-23} V_{irr} N_A} \quad (98)$$

where Φ_n is the neutron flux density ($s^{-1} cm^{-2}$). This value is used to calculate the energy deposited in the solution by the $^{10}B(n,\alpha)^7Li$ event, which is then used along with the amount of hydrogen detected to calculate $G(H_2)$.

The measurements of the reactor's relative power output logged by the compensated ion chamber offer a secondary method for quantifying the neutron exposure each sample experiences, since the neutron flux density is expected to be proportional to the reactivity measured in the core of the reactor. The power trend data are summed over the exposure period of each sample by the following equation:

$$\Psi = \sum_{i=1}^n P(t_i) \times e^{(-\lambda_{Na24} \times (t_{end} - t_i))} \quad (105)$$

for comparison with the Φ_n values calculated from the ^{24}Na activation levels, where $P(t_i)$ is the power reading at time t_i from the compensated ion chamber detectors and t_{end} is the timestamp of the last power reading attributed to the corresponding sample's irradiation. For the purposes of these comparisons, we included within this summation equation the exponential decay factor to normalize with respect to the sodium activation. These summation values are displayed in Figure 70, plotted versus an ID number each sample was assigned chronologically. Different stages of this experimental campaign are also indicated, where most experiments with the Zircadyne 702 cell below 200 °C were completed in the early stages, the reactor refueling occurred between the early and middle stages, all experiments with the titanium cell at 200 °C and above were completed in the middle stage, and the late stage involved final necessary assessments at room temperature

of miscellaneous Zircadyne cell aspects, such as elucidating the cause behind the confusing results for the ratio of N₂/H₂ produced in the gamma background as described in Section 7.1.6.2.

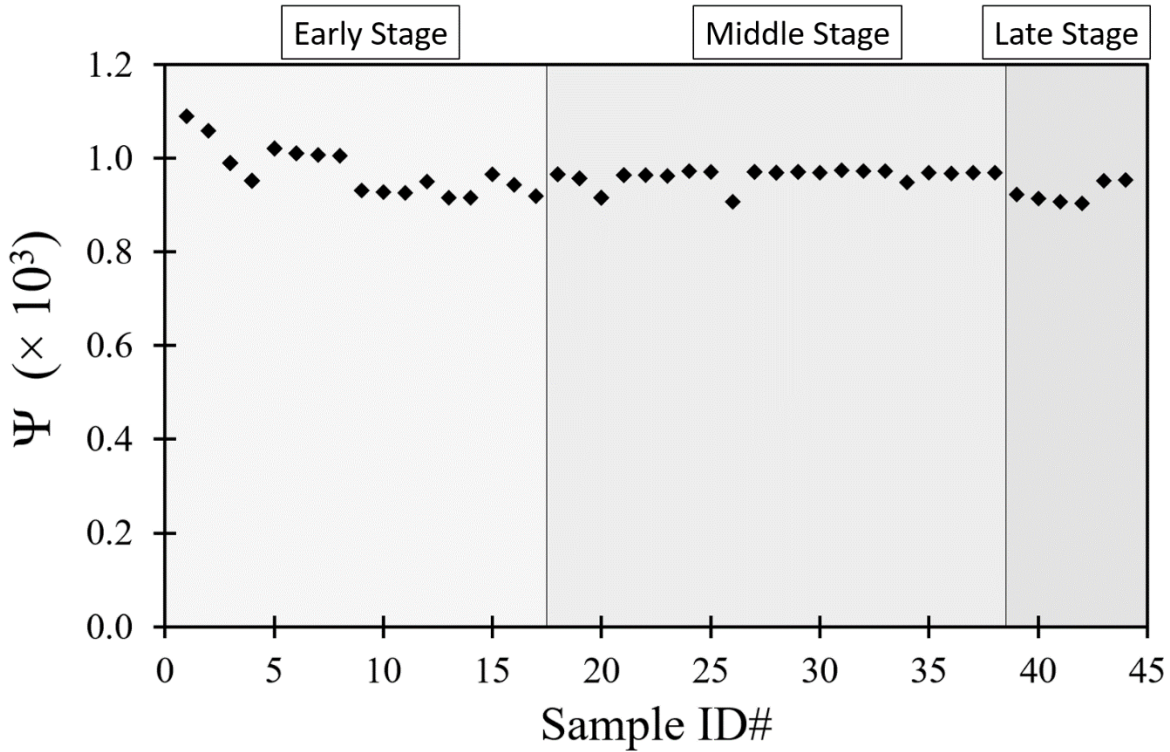


Figure 70. Plot of all power-trend-data-summation Ψ values for all samples where sodium activation was measured. The different stages of this experimental campaign (early, middle, late) are indicated. Sample ID numbers were assigned chronologically.

For this comparison between the *in situ* sodium dosimeter and the RINSC facility's reactivity detection system, an additional consideration is necessary to be accounted for first: the change in water density at higher temperatures and thus a corresponding change in the concentration of sodium in the cell volume. The equation for neutron flux density is recalculated using the molal concentration C_{Na-23} (mol kg⁻¹) instead of the molar concentration c_{Na-23} (mol L⁻¹) of sodium in solution:

$$\Phi_n^* = \frac{A_c e^{\lambda_{Na-24} \Delta t}}{\sigma_{Na-23} (1 - e^{-(\lambda_{Na-24} t_{irr})}) C_{Na-23} \rho(T) V_{irr} N_A} \quad (106)$$

where $\rho(T)$ is the density of water (kg L^{-1}), for which the data were obtained from the NIST Chemistry WebBook SRD 69 (Lemmon, et al., 2021) for water held at 25 MPa and are displayed in Figure 71.

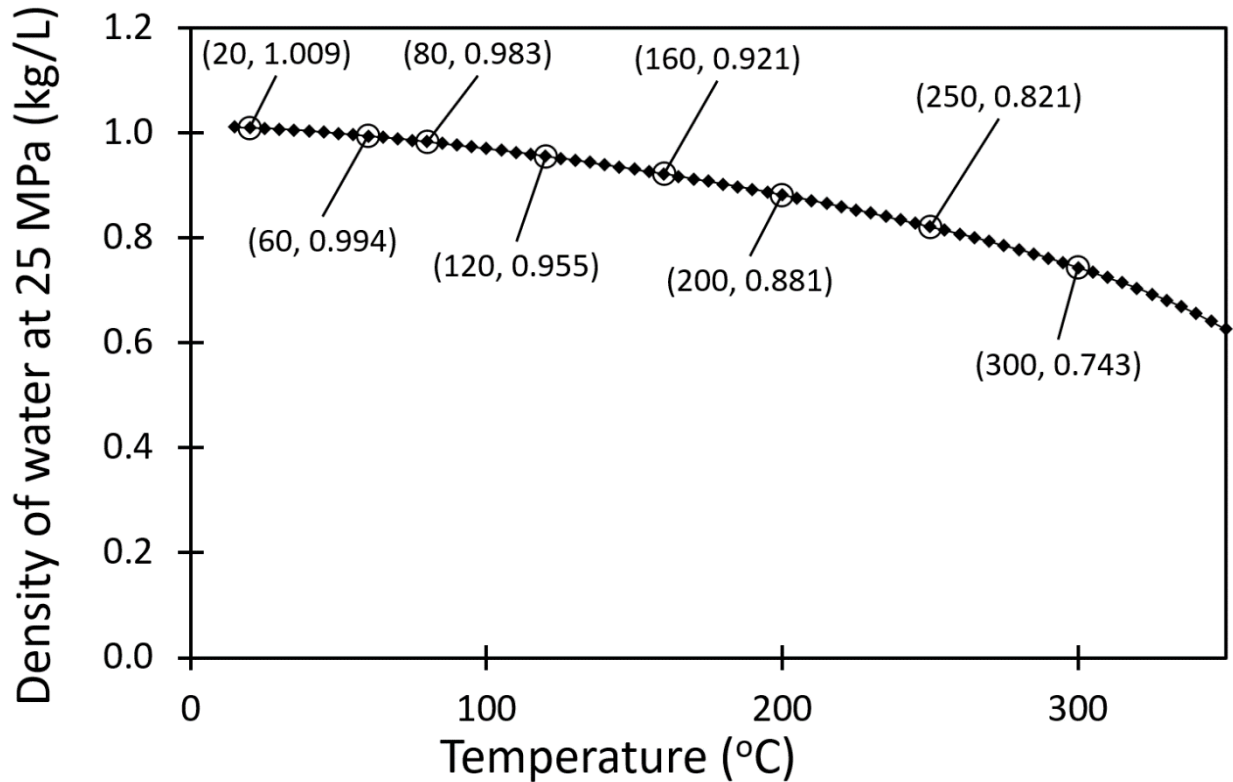


Figure 71. Values of water density for isobaric conditions at 25 MPa, with values displayed at target temperatures for this experiment (values obtained from (Lemmon, et al., 2021)).

The adjusted average neutron flux density Φ_n^* is multiplied by the duration of irradiation t_{irr} to calculate a total neutron exposure value, and the ratio of this value to the corresponding power trend data summation value Ψ is calculated for each sample. These ratios are displayed in Figure 72, plotted versus the same sample ID labels as used in Figure 70.

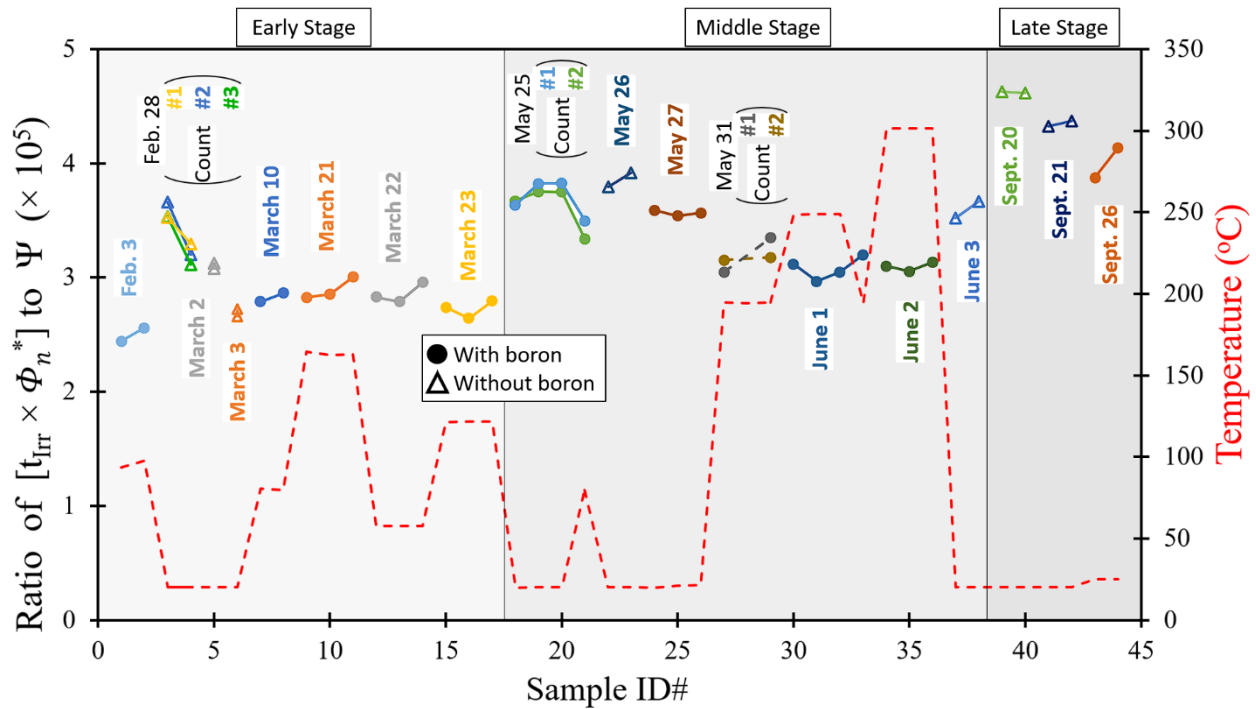


Figure 72. The ratio of the adjusted neutron flux $[t_{irr} \times \Phi_n^*]$ to the power trend data summation Ψ for all samples where ^{24}Na -activation was measured. The different stages of this experimental campaign (early, middle, late) are indicated.

An apparent effect on the ratio by the inclusion/omission of boron was noticed during the early stages of this work. The gamma “blank” solution samples exhibited higher levels of ^{24}Na activation (and consequently higher calculated neutron flux densities) compared to the boronated solution samples, while the reactivity levels of both were very similar as displayed in Figure 70. It was suggested that the boron may be enacting a shielding effect on the sodium, just as boric acid’s purpose as a chemical neutron shim in PWRs is to “shield” uranium atoms from neutrons.

7.1.9 Boron Shielding Effect

Analyzing the ratio of ^{24}Na activation to the power trend data for samples irradiated within the cell revealed a discrepancy between samples containing boric acid and those without. We found for boric acid solutions (typically 0.3 M) that the ratio was higher for the samples without boron used in our investigation of the background gamma dose rate. Therefore, an investigation was

made into the degree of attenuation. The RINSC facility also offers a pneumatically driven “rabbit” system which allows samples to travel through tubes to rest directly adjacent to the core. Solutions were prepared with varying concentrations of boron up to 0.3 M and the same 0.265 mM concentration of Na_2CO_3 used in the typical $^{10}\text{B}(n,\alpha)^7\text{Li}$ experiments for neutron dosimetry, and ca. 5 mL of each solution was contained in four standard small plastic sealed containers which were placed in the rabbit container. The neutron flux density is approximately $2 \times 10^{12} \text{ cm}^{-2} \text{ s}^{-1}$ at the irradiation location, and samples are held there for one minute before being extracted pneumatically and analyzed for ^{24}Na activity with the same equipment as was used for the typical $^{10}\text{B}(n,\alpha)^7\text{Li}$ experiment samples. The first set of results was very unexpected.

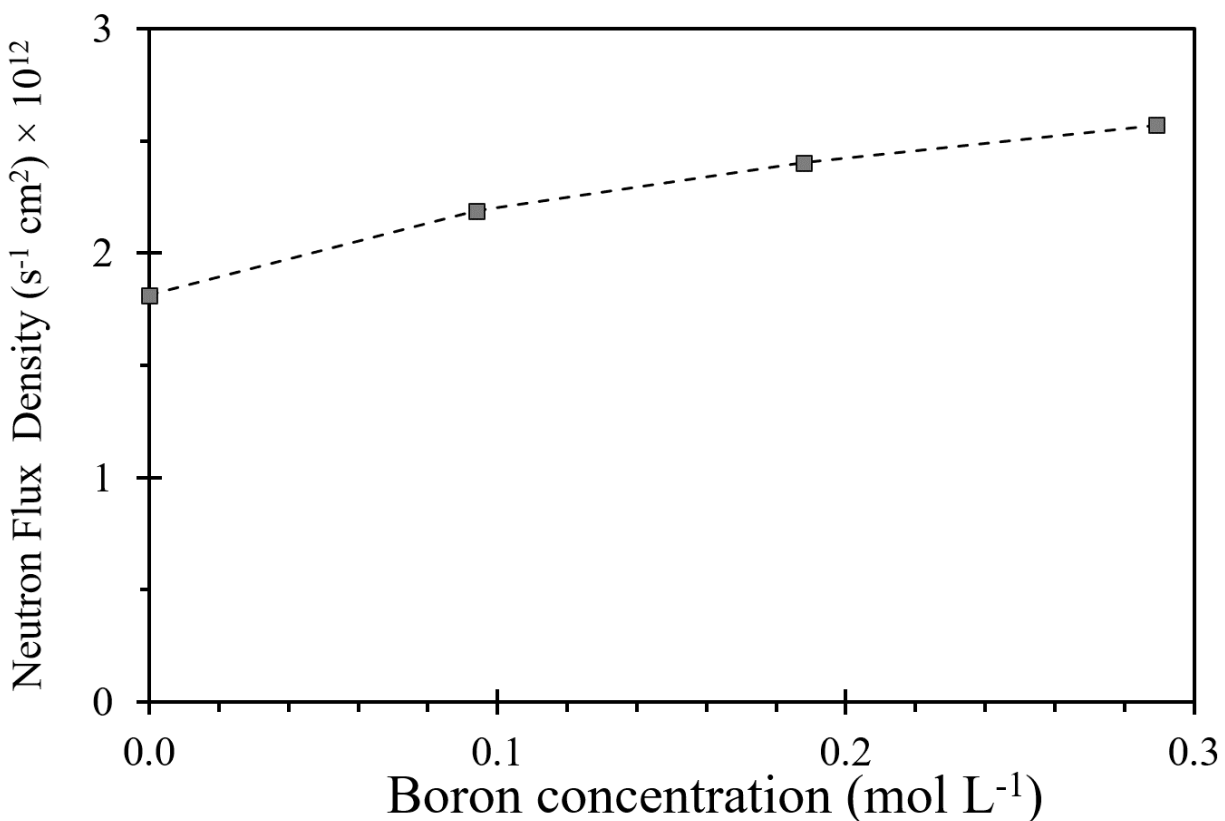


Figure 73. Plot of neutron flux density as calculated from ^{24}Na activation analysis over increasing boron concentration for the first set of measurements wherein all four samples were irradiated simultaneously.

This behavior is surprising, in that it indicates the opposite of what we expected – instead of decreasing the degree of sodium activation with higher amounts of boron, instead this data implies that it increases. This is nonsensical, so we assume there is an experimental error not accounted for. We consider the possibility there is a gradient in the neutron flux density in the rabbit container along the axis the sample containers are stacked within. The samples were rearranged such that the original ordering of 0, 0.1, 0.2, and then 0.3 M of boron now was 0.3, 0, 0.2, and then 0.1 M of boron and were sent through the rabbit system again more than a week later. These samples were counted twice to ensure the spectroscopy equipment was giving precise reports.

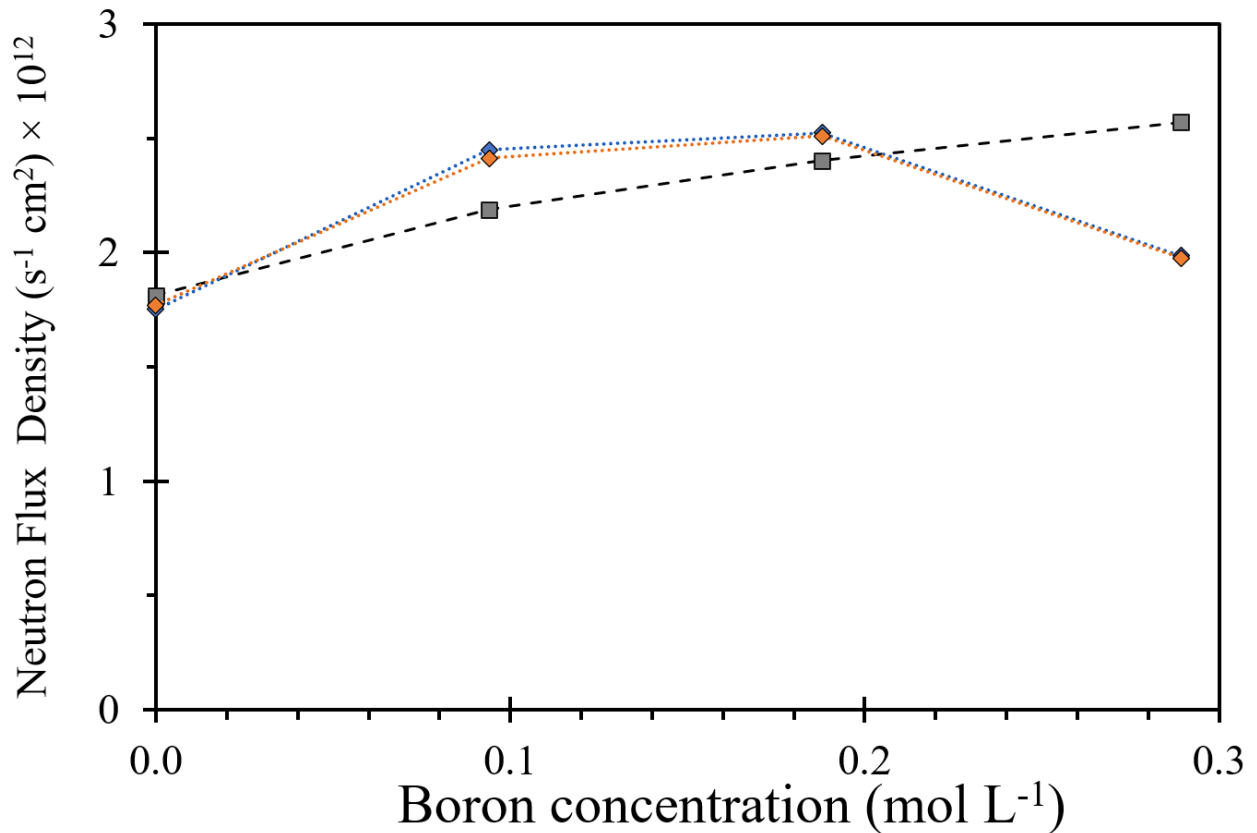


Figure 74. Plot of neutron flux density as calculated from ²⁴Na activation analysis over increasing boron concentration for the second set of measurements (blue and orange diamonds) wherein the ordering of the samples was changed from A,B,C,D to D,A,C,B.

The behavior again appeared illogical, as the sodium within the sample containing no boron had experienced the same neutron irradiation as the sodium within the sample containing the highest. Samples were sent through the rabbit system again more than a week later, but now they were sent through individually.

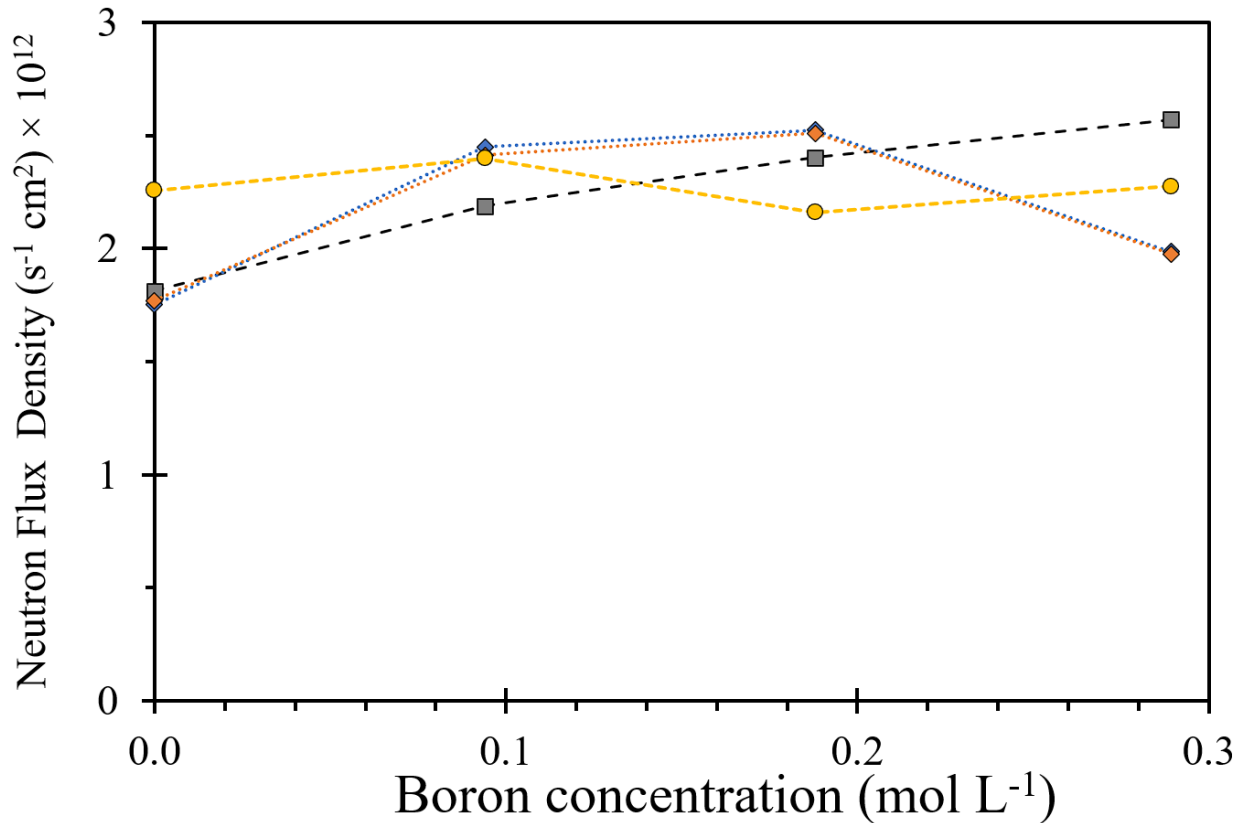


Figure 75. Plot of neutron flux density as calculated from ²⁴Na activation analysis over increasing boron concentration for the second set of measurements (yellow circles) wherein the samples were each sent through individually.

And again, the activation levels do not seem to follow any dependence on the boron concentration. Furthermore, the power trend monitoring data was evaluated for all of the aforementioned samples' irradiation durations and no discrepancy was found – each exhibited an entirely reasonable level of stability from one day to the next and over the course of each full day. Thus the apparent effect on the ratio of the adjusted neutron flux to the power trend data summation

by the inclusion/omission of boron noted in the previous section as well as these results from the rabbit system experimentation both remain frustratingly unexplained.

7.1.10 Room Temperature – effect of LiOH addition (pH)

A linear plot of the hydrogen content detected versus calculated energy deposited in solution samples at room temperature is shown in Figure 76, where the slope fit by linear regression to the data is equal to the G-value for H₂. This value has been corrected for the small amount of H₂ produced by the evaluated gamma background. Fitting only the points for samples without LiOH yields a G(H₂) of $(0.165 \pm 0.006) \mu\text{mol/J}$, fitting only the points for samples with LiOH yields a G(H₂) of $(0.157 \pm 0.005) \mu\text{mol/J}$, and fitting all points yields a G(H₂) of $(0.162 \pm 0.007) \mu\text{mol/J}$. The error bars displayed in the figure are associated with the experimentally estimated uncertainty in the measurements of sodium activation and of hydrogen content, which will be discussed in the next section.

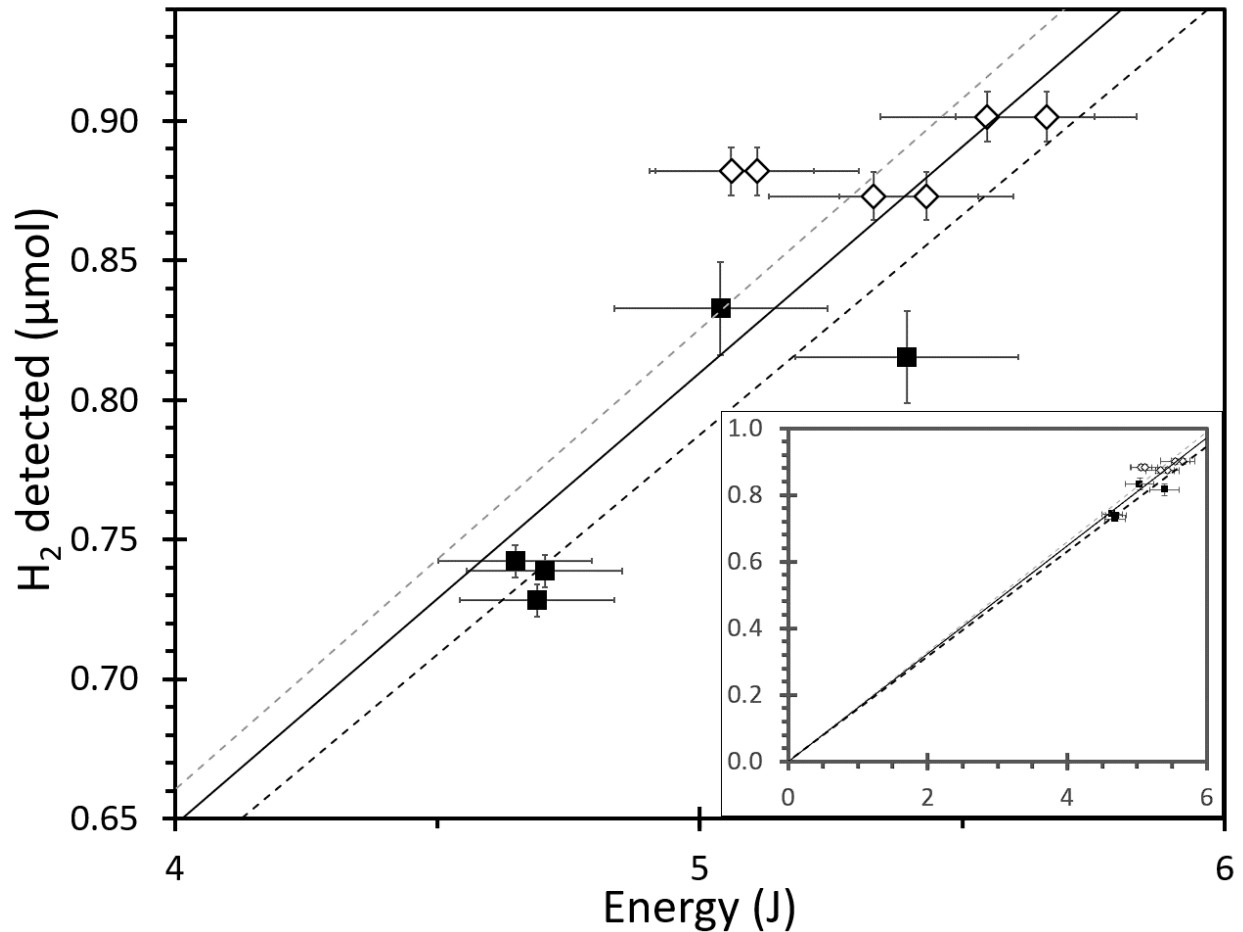


Figure 76. Plot of the room temperature measurements of hydrogen generation by the $^{10}\text{B}(n,\alpha)^7\text{Li}$ reaction after corrections made for gamma background. Points are fit by linear regression to a zero-intercept line for: samples without LiOH (empty diamonds, gray-dashed line), samples with LiOH (filled squares, black-dashed line), and all samples (solid black line). The slope of the lines equates to the G-value.

The investigated effect at room temperature by the omission/inclusion of $^7\text{LiOH}$ to balance the pH of the boric acid solution is found to not be significant. This is expected and in accordance with the work by Buxton and Sellers to confirm how and why boric acid is an ideal nonreactive buffer for use in such systems. Therefore we evaluate all measurements equally regardless of its presence. The $^7\text{LiOH}$ was included in all sample solutions for all experiments at temperatures of 200 °C and above to more closely match PWR chemistry conditions.

7.1.11 Error Analysis

As was mentioned in the previous section, the error bars displayed in Figure 76 are associated with the experimentally estimated uncertainties in the measurements of sodium activation and of hydrogen content. The reports generated by the Genie gamma spectroscopy software have uncertainty values (σ_{Act}) for the detected levels of activated sodium-24, as described in Section 5.9, and these are reflected in the horizontal error bars for the values of energy deposited in the solution as calculated using Equation (99) and the known product energy of each $^{10}\text{B}(n,\alpha)^7\text{Li}$ event. A standard deviation (σ_{H_2}) is computed for the proportionality constants of the three hydrogen calibration measurements performed each day, and this is reflected in the vertical error bars for the values of hydrogen gas detected by the RGA mass spectrometer on that day. The sodium activation uncertainties reported throughout the entirety of this experiment average 3.7% of their measured value, and all σ_{H_2} average 1.6% of their measured proportionality constant. The G-values have been calculated from the hydrogen analysis and sodium activation reports as explained in the discussion for Equation (100), and all results have been plotted in the figure below.

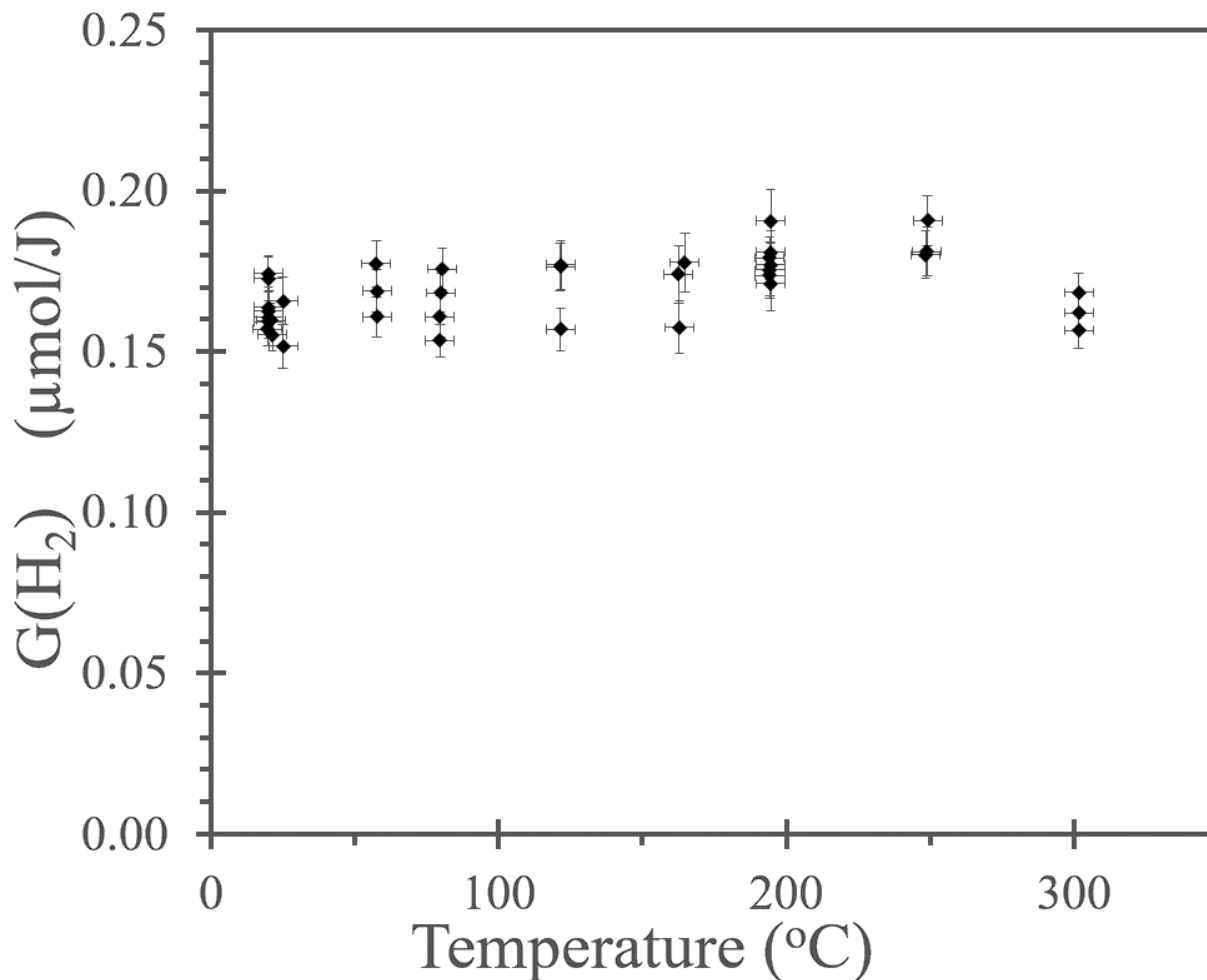


Figure 77. Plot of all calculated G -values for all measurements on the $^{10}\text{B}(n,\alpha)^7\text{Li}$ reaction taken in this work.

The std. deviation error bars in Figure 77 for the G -values were calculated as:

$$\sigma_{G(H_2)} = G(H_2) \times \sqrt{(\sigma_{H_2/H_2})^2 + (\sigma_{Act/Act})^2} \quad (107)$$

However, as the data in Figure 76 and Figure 77 indicate, these calculated errors do not account for the spread of measured values and thus are considered underestimations of the true total experimental uncertainty. Therefore, each G -value is treated equivalently and an average G -value at each temperature is computed along with the standard deviation in each set of points.

7.1.12 G-value for H₂

An average value is calculated from each G(H₂) at a given temperature, and these average values are given in the following table and figure.

Table 4. Table of the final G-values reported in this work for H₂ produced from the ¹⁰B(n,α)⁷Li reaction in aqueous solution at 25 MPa for a temperature range up to 300 °C.

T (°C)	G(H ₂) (μmol/J)	G(H ₂) (#/100eV)	H ₂ molecules/Event
20	0.162 ± 0.007	1.56 ± 0.06	36,600 ± 1,500
60	0.169 ± 0.007	1.63 ± 0.07	38,200 ± 1,500
80	0.165 ± 0.008	1.59 ± 0.08	37,200 ± 1,900
120	0.170 ± 0.009	1.64 ± 0.09	38,500 ± 2,100
160	0.170 ± 0.009	1.64 ± 0.09	38,400 ± 2,000
190	0.180 ± 0.006	1.73 ± 0.06	40,600 ± 1,400
250	0.184 ± 0.005	1.78 ± 0.05	41,600 ± 1,100
300	0.162 ± 0.005	1.57 ± 0.05	36,700 ± 1,100

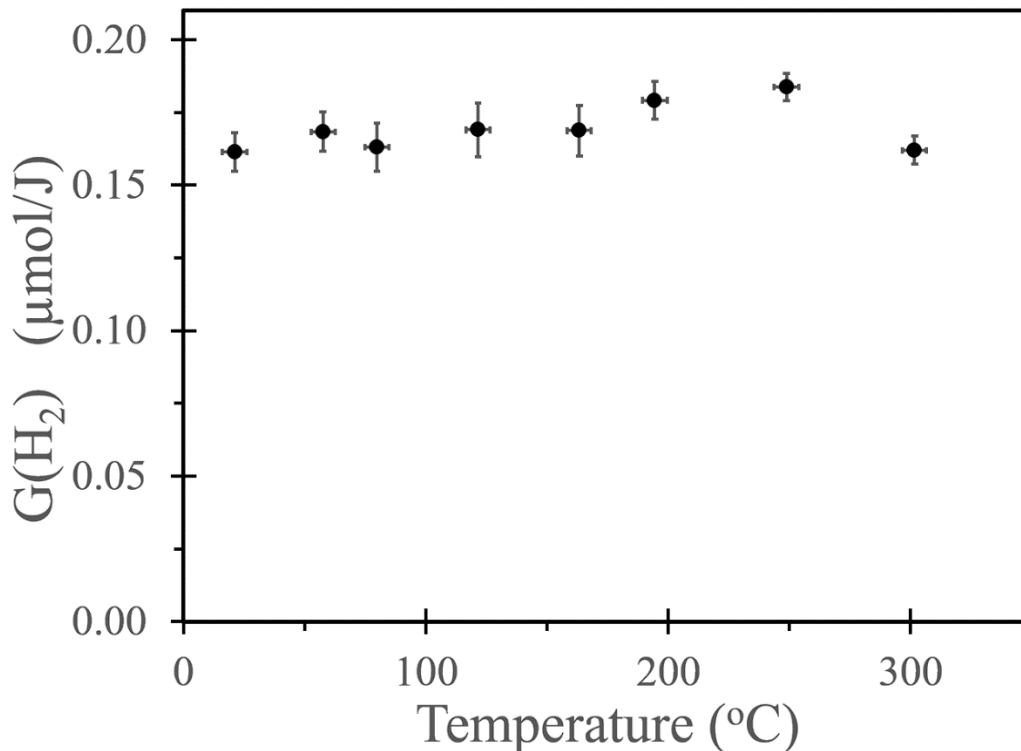


Figure 78. Plot of the final G-values reported in this work for H₂ produced from the ¹⁰B(n,α)⁷Li reaction in aqueous solution at 25 MPa for a temperature range up to 300 °C.

These values and the manuscript detailing this work on evaluating the product yields of the $^{10}\text{B}(n,\alpha)^7\text{Li}$ event in water up to 300 °C have been submitted to the journal of Radiation Physics and Chemistry and are currently under review (Guerin, et al., Submitted 2023, under review).

7.1.13 Comparing to Previous Works

We make a brief comparison of our results to the values reported by Christensen in 2006. As discussed in Section 1.10.1, he provided a compilation on available experimental and simulation results on the H_2 yield by the $^{10}\text{B}(n,\alpha)^7\text{Li}$ reaction at room temperature from Jenks (1965) and from Lefort (1981), along with calculated results for ca. 300 °C from Lundgren (2004) and from Bjergbakke (1984), as well as his own recommended value. These values are plotted alongside our own in Figure 79, showing that some values are within reasonable agreement between different works.

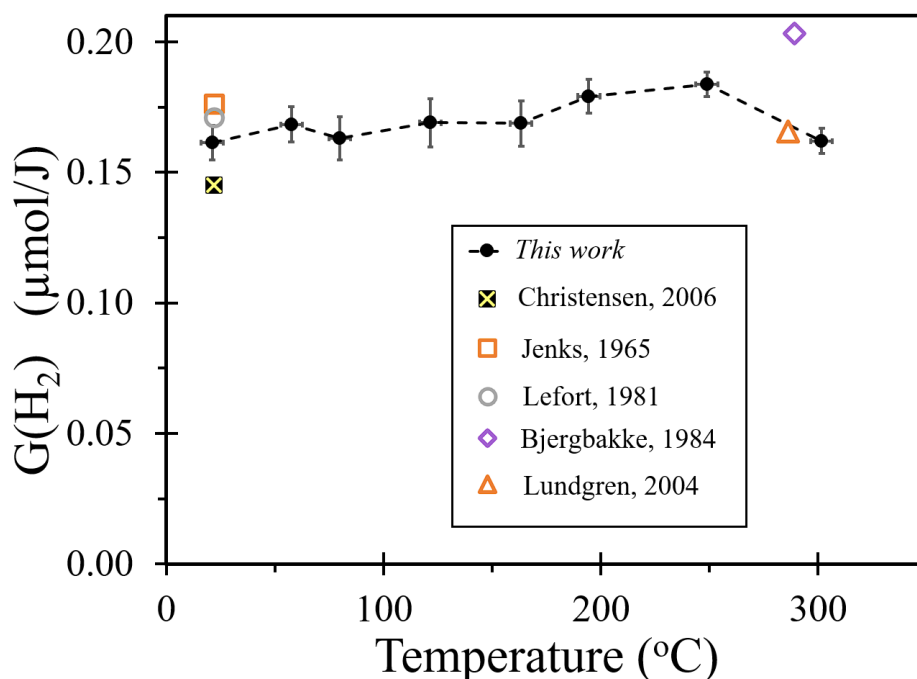


Figure 79. Plot of $G(\text{H}_2)$ values from $^{10}\text{B}(n,\alpha)^7\text{Li}$ reaction as reported in this work, along with comparable results from the 2006 report by Christensen.

In the precursor to the present work, Dietz et al. reported in 2021 the H₂ yield for the same reaction, in a neutral-pH boric acid solution at room temperature. Our system for measuring H₂ yield by ¹⁰B(n,α)⁷Li up to high temperature and pressure is based on their experimental setup used at the NIST Center for Neutron Research BT-2 Neutron Imaging Facility (NIF). As was mentioned in Section 1.10.3 on the precursor to this work, we obtained results at room temperature which indicate a comparable G-value to the work done by Dietz et al. (Figure 80, left). Thanks to an average neutron flux density at the RINSC reactor of $3 \times 10^8 \text{ s}^{-1} \text{ cm}^{-2}$ (nearly $\times 40$ higher than at NIF) and an alternative flowcell construction ($\frac{1}{4}$ -inch tubing), we were able to generate similar levels of H₂ at a much faster rate (Figure 80, right, indicating an increase in the rate of H₂ being generated $\times 13$ more quickly), and with only ca. 2 % gamma contribution estimated as compared to the 29 % correction factor.

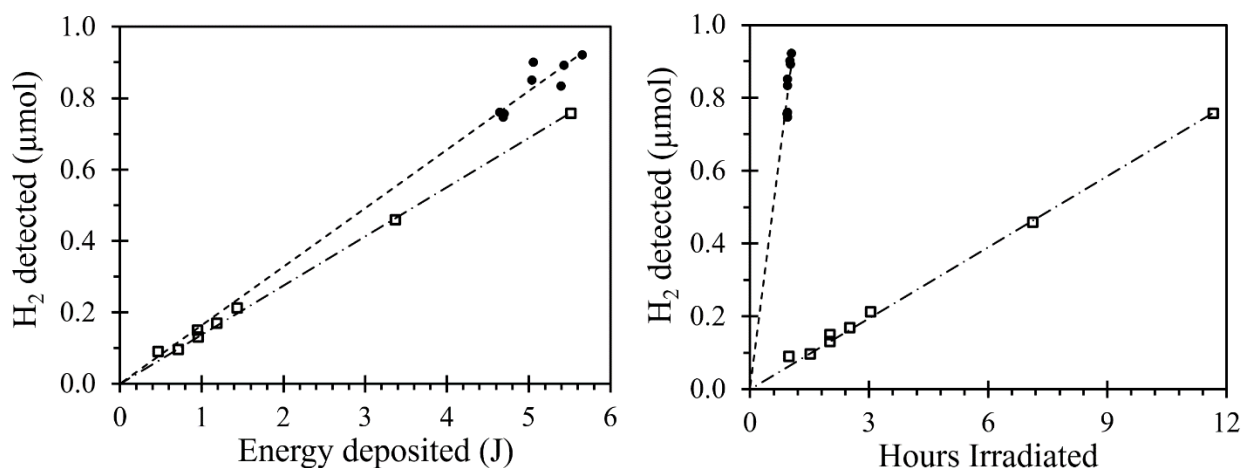


Figure 80. Hydrogen detected at room temperature, plotted versus energy deposited in the solution (left) and as a function of irradiation duration (right), comparing the results of Dietz et al. (□) to the data obtained in this work (•).

Additionally, thanks to optimization of the RGA mass spectrometer settings, we achieved a more desirable S/N ratio compared to their work for detecting the hydrogen entrained in our solution samples. The scale for an H₂ signal typical in the experimentation by Dietz et al. is compared to one of our typical signals, shown in Figure 81.

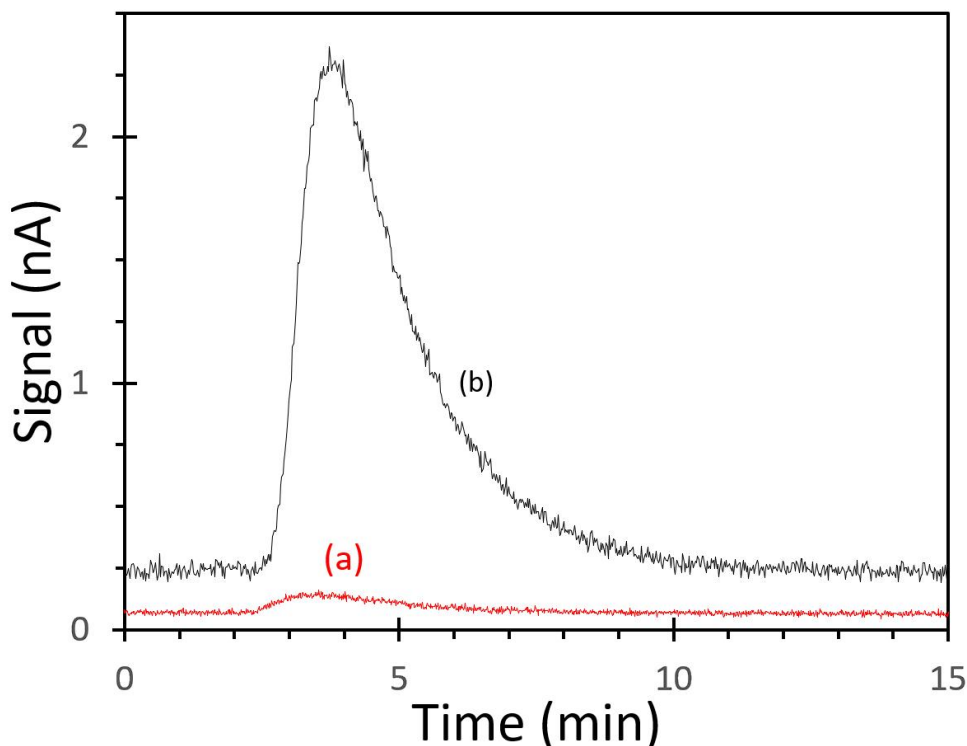


Figure 81. Hydrogen signal detection data for: (a) sample from Dietz *et al.*, irradiated for 3 hours to generate 0.22 μmol of H_2 , and (b) sample from this work, irradiated for 1 hour to generate 0.92 μmol of H_2 . These signals are plotted with the same scale, and so the effect of optimizing the RGA settings is also made obvious.

We also compare our results to the Monte Carlo track chemistry simulations on the radiolysis yields from the $^{10}\text{B}(n,\alpha)^7\text{Li}$ reaction in aqueous solutions up to 350 $^\circ\text{C}$ by Islam *et al.* at Sherbrooke University in 2017, as well as compared to the continuation on that work by Zakaria *et al.* in 2021. As was discussed in Section 1.10.2, the simulations by Islam *et al.* used two different rates above 150 $^\circ\text{C}$ for the bimolecular reaction of the hydrated electron, either using experimental rates measured in alkaline conditions or using rates calculated with an Arrhenius extrapolation from lower temperature data, and the latter case was also applied in the simulations by Zakaria *et al.* which investigated the effects of multiple ionization of water on the Fricke dosimeter. These three simulation results as well as the results by Dietz *et al.* are plotted alongside our own in Figure 82.

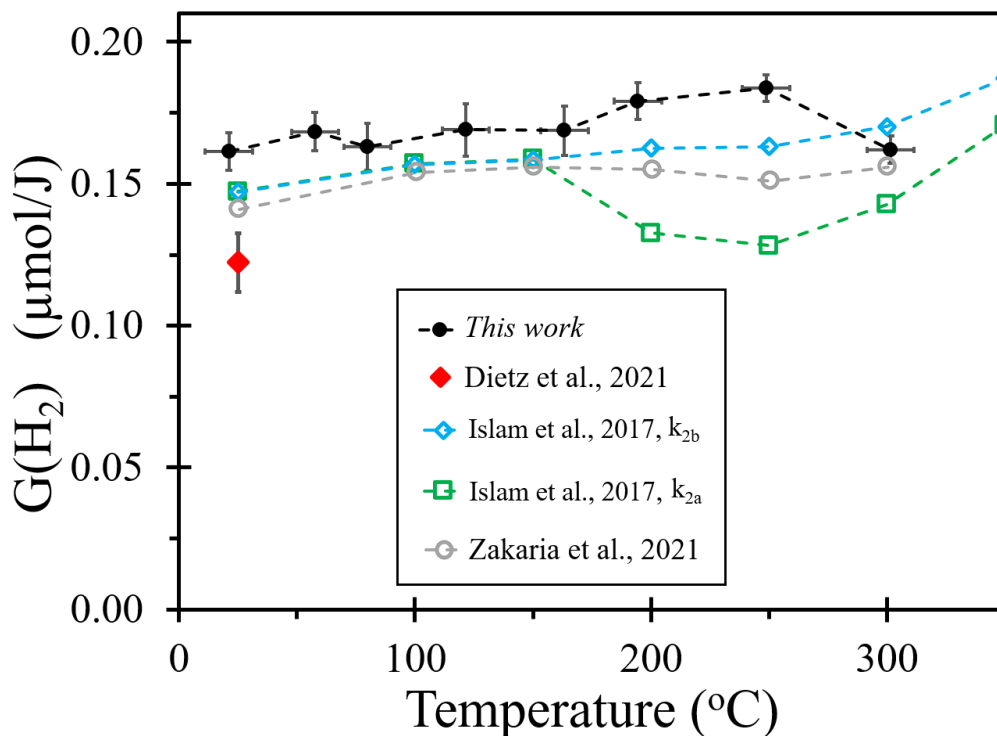
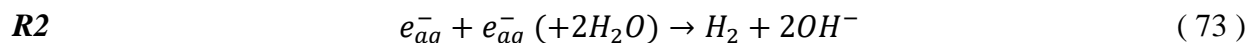


Figure 82. Plot of $G(H_2)$ values from $^{10}B(n,\alpha)^7Li$ reaction as reported in this work, along with comparable experimental results by Dietz et al. and the simulation results by Islam et al. and Zakaria et al.

The simulations using experimental reaction rate numbers compiled the review by Elliot and Bartels in 2009 are plotted as green squares. Agreement is good up to 150 °C. The simulated yield decreases between 150–250 °C because the measured rate constant $k_{(73)}$ for bimolecular reaction of hydrated electrons,



decreases catastrophically in this temperature range, as reported independently by three separate research groups (Elliot & Bartels, 2009). It was expected that this reaction should have significant probability in both high LET tracks (Swiatla-Wojcik & Buxton, 1998; Islam, et al., 2017) and low LET spur recombination (Swiatla-Wojcik & Buxton, 1995; Sanguanmith, et al., 2011) and the same prediction of dip in the H_2 yield above 150 °C is made in both low- and high-LET situations.

With our new high temperature measurements of high LET $^{10}\text{B}(n,\alpha)^7\text{Li}$ radiolysis we see from Figure 82 it is not found experimentally in either case.

Jay-Gerin and coworkers have repeatedly suggested (Sanguanmith, et al., 2011; Butarbutar, et al., 2013; Islam, et al., 2017) that the $k_{(73)}$ reaction rate decrease only occurs in alkaline solutions where the kinetics measurements are made, but not in neutral pH conditions. The second set of simulations plotted as blue circles in Figure 82, calculated by Arrhenius extrapolation from lower temperature data, undeniably produces better agreement between the Sherbrooke simulation and experimental $G(\text{H}_2)$ values. Furthermore, the prompt physio-chemical yield $G_0(\text{H}_2)$ was separated from the overall escape yields $G_{\text{esc}}(\text{H}_2)$, which includes diffusive track recombination like that from reaction **R2**, by using high concentrations of scavengers for the pre-solvated electron (Sterniczuk & Bartels, 2016). It was demonstrated that for High LET alpha particles the difference between prompt and escape yields at room temperature is given as $G_{\text{esc}}(\text{H}_2) - G_0(\text{H}_2) = 0.16 - 0.1 = +0.06 \mu\text{mol/J}$ (LaVerne & Pimblott, 2000; Sterniczuk, et al., 2016). It is then feasible that this already-large fraction of $G_0(\text{H}_2)$ for alpha radiation would become even higher at higher temperatures, and perhaps then the fraction of $G_{\text{esc}}(\text{H}_2)$ coming from reaction **R2** drops, making the “dip” for this case fall below our present experimental detection limit.

7.2 General evaluation of Borate reaction with Hydroxyl radical

Buxton and Sellers were observing their system at single wavelength 420nm, and found no appreciable reaction with $\cdot\text{OH}$ (Buxton & Sellers, 1987). While performing collaborative pulse radiolysis research at NDRL utilizing their 8MeV linear accelerator, during our initial experimentation we observed our system over a wavelength range of 250–530nm and discovered the tail end of a forming radical’s spectrum at wavelengths $>450\text{nm}$. This occurred 1) when borax

was used as the acid-base buffer, 2) in an alkaline system, 3) at wavelengths outside of the expected range for common boric acid species to be absorbing, and 4) during a time regime when all absorbing radiolytic species other than $\cdot\text{OH}$ are gone. Those four facts together lead us to believe it must be the borate molecule reacting with the $\cdot\text{OH}$ to produce some absorbing product borate radical, which then appears to decay away by an as-yet unknown reaction.

Analysis when fitting a single-exponential rise to the pseudo-first-order growth of the borate radical indicates a rate constant on the order of $3 \times 10^6 \text{ mol}^{-1}\text{s}^{-1}$ and a rough Arrhenius plot was generated up to 200 °C. Preliminary analysis of the second order decay of the borate radical has been difficult and no satisfying comprehensive mechanism for the reactions or species has yet been obtained. Likely more side reactions (equilibria, polyborate radical formations, and others...) will need to be considered in order to acquire a complete understanding of the chemistry involved in the decay reaction(s).

7.2.1 Discovering a mystery reaction taking place

During experimentation for measuring the reaction of $\cdot\text{OH}$ with O_2^- in an air-saturated 2 mM borax buffer solution, we observe evidence of an unexpected reaction taking place. Plots of the time-resolved spectral data for the full time range and for short-time are shown below.

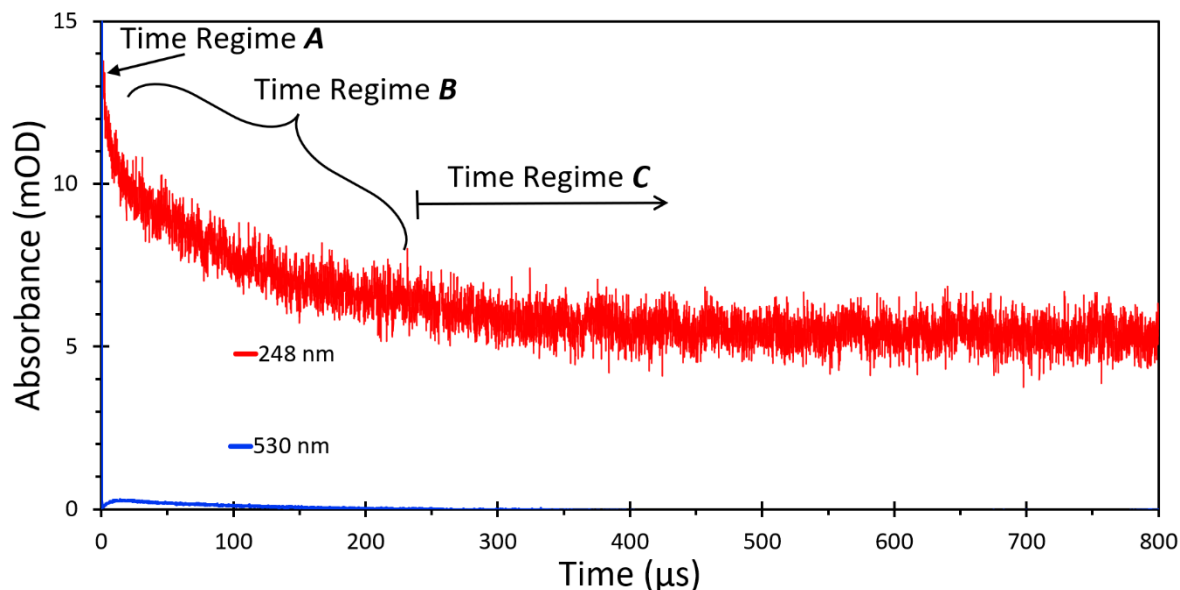


Figure 83. Time-resolved spectral data at 248 and 530 nm over the full time range out to 0.8 ms, with three time regimes indicated, obtained at 75 °C.

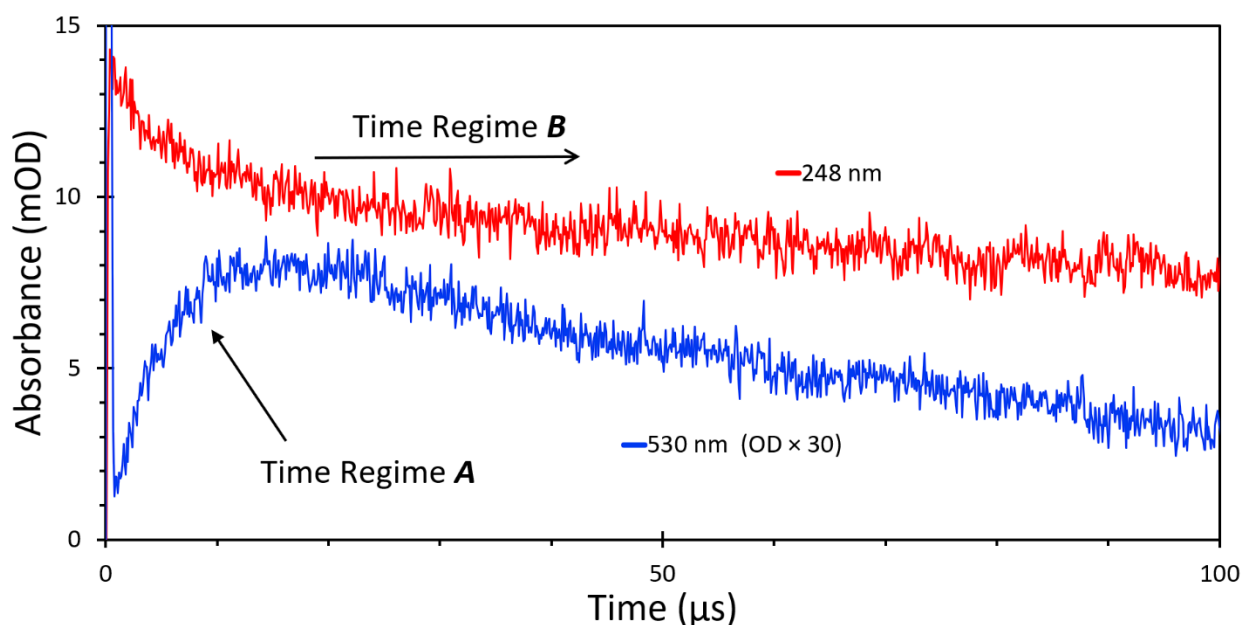


Figure 84. Time-resolved spectral data at 248 and 530 nm over a short-time range, obtained at 75 °C. The 530nm trace (blue) has been scaled up by a factor of 30, and the two shorter time regimes are indicated.

The apparent growth of an absorbing species out in the visible at 530nm was very unexpected. During the time regime A we expect that $\cdot\text{OH}$ are self-recombining to form H_2O_2

(reaction **R4** in Equation (66)) and are reacting with O_2^- in an electron exchange to form O_2 and OH^- (reaction **R17** in Equation (33)). However, these species do not absorb at the 530 nm wavelength, and as it is a borax buffer the only other species present are the boric acid and borate. Boric acid was confirmed nonreactive with $\cdot OH$ and e_{aq}^- (Buxton & Sellers, 1987), so we posited a reaction with the borate and $\cdot OH$ forming an absorbing unknown radical. During time regime **B** we see the radical signal decaying away, we assume from a reaction with O_2^- , and after this regime there is only excess O_2^- remaining.

7.2.2 Identifying initial reactants

During experimentation with borax buffer solutions, by mixing a solution acidified with $HClO_4$ with a solution alkalized with $NaOH$ we identify the species reacting with $\cdot OH$. We observed no growth of any absorbing species at the 530 nm wavelength when flowing only the acidic solution, we observed a small growth of an absorbing species with a similar spectra as was seen in the previous experiment with O_2 and borax when flowing a 50/50 mix of the acidic and alkaline solutions, and we observed a larger growth of the same species when flowing only the alkaline ($pH \approx 10$) solution.

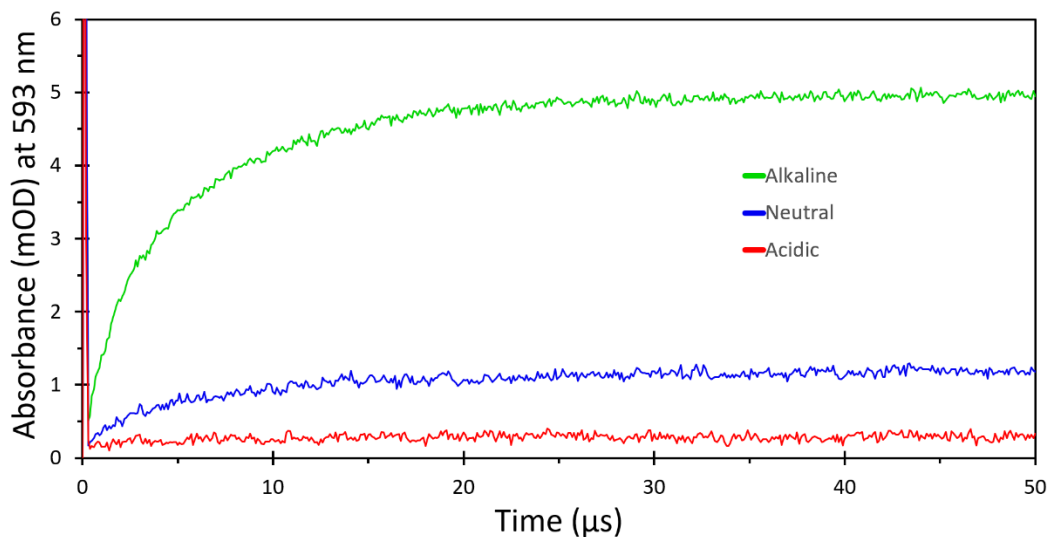


Figure 85. Absorbance signal obtained at 593 nm for mix ratio of acidic:alkaline solutions at 0:1 (acidic), 1:1 (neutral), and 1:0 (alkaline).

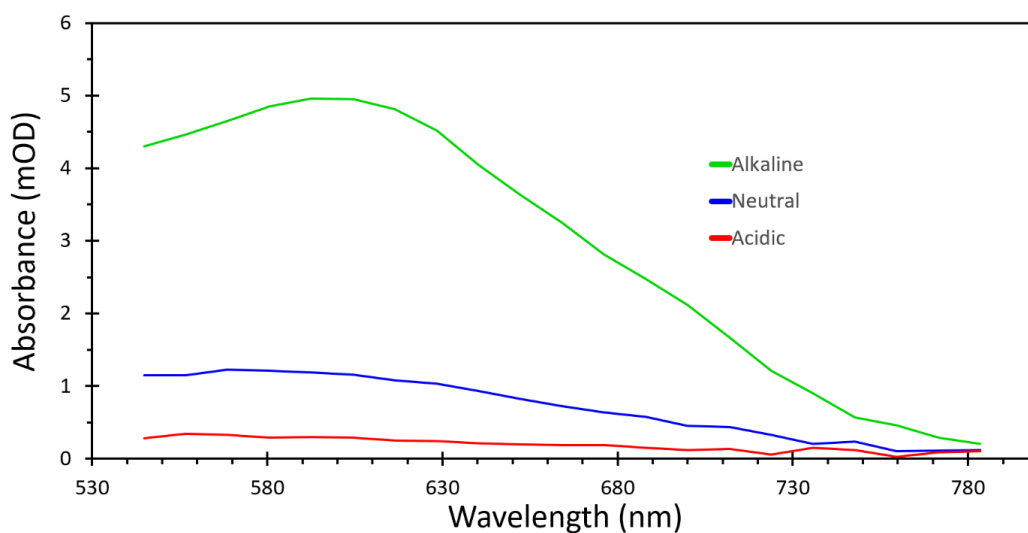


Figure 86. Spectra obtained when averaging the signals in Figure 85 from 40 μs to 50 μs for each wavelength channel monitored during this particular experimental run.

This confirms Buxton and Sellers' conclusion that $\cdot\text{OH}$ does not react with boric acid, however it indicates that the conjugate base is the reactant involved in the formation of this absorbing species through a reaction with the $\cdot\text{OH}$. They overlooked this because they did not do alkaline studies for reactions with $\cdot\text{OH}$, only with e_{aq}^- , and they did not check the visible wavelengths during their experiment (Buxton & Sellers, 1987).

7.2.3 Attempts to evaluate the new radical's REDOX Potential

When the borate's reaction with $\cdot\text{OH}$ was assumed to be an electron abstraction yielding $\cdot\text{B}(\text{OH})_4$ as the product, we attempted to evaluate the radical's REDOX potential by investigating any effect on the rise or decay of the radical through inclusion of chemical agents which would potentially oxidize borate or reduce the product radical. Bromine was selected as a likely contender to oxidize the borate in competition with the $\cdot\text{OH}$, and the agents for reducing the radical were azide, carbonate, iodide, and sulfite.

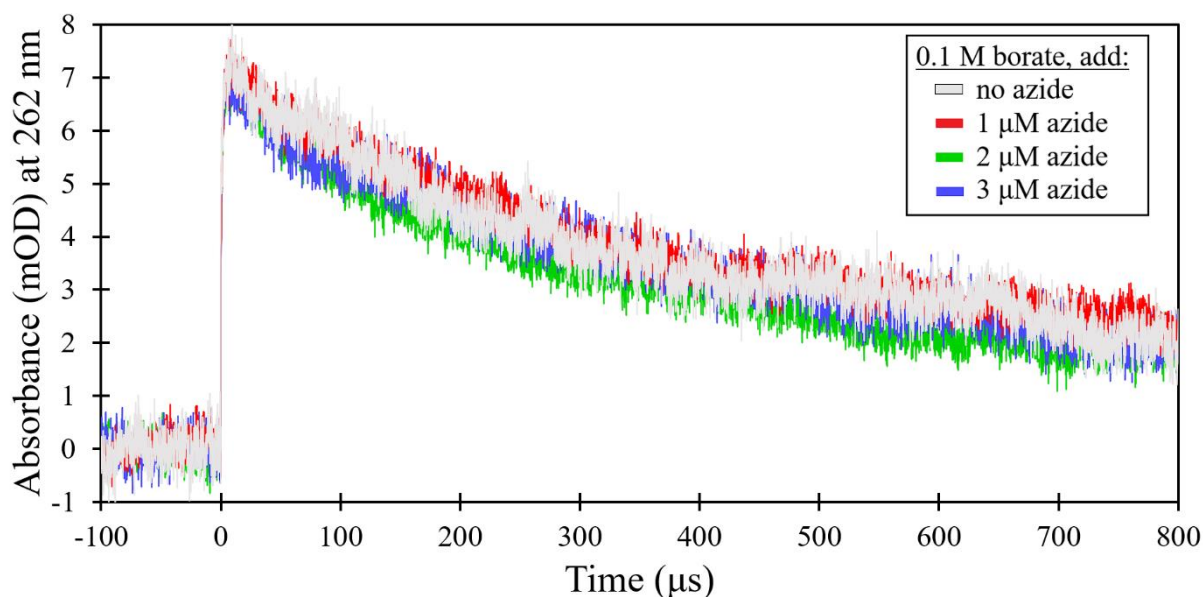


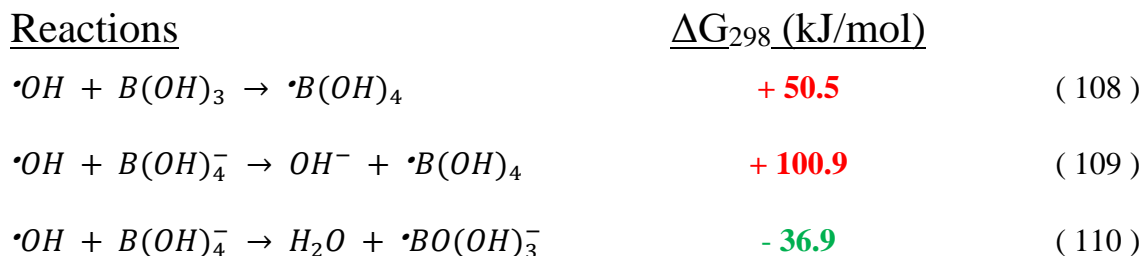
Figure 87. Time-resolved spectral data at 260 nm, displaying the decay rate of the borate radical when no REDOX agent is present (off-white) as compared to its decay when accompanied with different concentrations of azide.

A plot displaying the results of an investigation employing one of these REDOX agents is shown in Figure 87. It is straightforward to interpret that there is no effect on the second order decay of the borate radical by the inclusion of appropriate concentrations of azide, and therefore reaction (83) is not observed occurring. Though more difficult to visually interpret, the implications of the studies using the other chemical agents are the same: no reaction with any of

the agents was distinguishable and so no REDOX potential could be identified for the supposed $\cdot B(OH)_4$ radical.

7.2.4 *Ab initio* calculations for reactions of interest

Ab initio calculations for reactions of interest were provided by our collaborator Dr. Ian Carmichael, the director of the UND Radiation Laboratory.



These calculations indicate that a reaction of boric acid with $\cdot OH$ to produce the borate radical form $\cdot B(OH)_4$ would require a positive change in Gibbs free energy (G), implying it to be an endothermic reaction and thus not spontaneous, which supports Buxton and Seller's observation that a reaction between boric acid and $\cdot OH$ does not take place. The second calculation indicates that a reaction of borate with $\cdot OH$ would not be an electron transfer, as it is similarly an endothermic reaction. Third, a reaction with borate and $\cdot OH$ to form a borate radical $\cdot BO(OH)_3^-$ was calculated to have a negative change in G, implying it is an exothermic reaction and thus thermodynamically possible as a spontaneous reaction. We now assume this to be the reaction causing the growth of an absorbing species observed during our pulse radiolysis experiments.

7.2.5 Ionic Strength Effect Study

No apparent ISE had been observed on the second order decay of the $\cdot BO(OH)_3^-$ radical during the studies performed to evaluate the initial reaction and the subsequent decay of the product or products (the results of which are presented in the next section), which held some sway on our original belief that it was the uncharged $\cdot B(OH)_4$ radical which was produced during the

borate's reaction with $\bullet\text{OH}$. It is now our belief that the lack of ISE evidence was due to the ion pairing phenomenon between the Na^+ ions and the borate, as discussed in Section 1.7.4. The association constant K_A between $B(\text{OH})_4^-$ and Na^+ ions to form $\text{NaB}(\text{OH})_4^0$ over a temperature range (Pokrovski, et al., 1995) is used along with Equation (62) to calculate the ratio of borate anions which have been paired to sodium cations for the concentrations used in the earlier study as well as here by the following equation:

$$\frac{(K_A \times [\text{Na}^+])}{(K_A \times [\text{Na}^+]) + 1} = \frac{[\text{NaB}(\text{OH})_4^0]}{[B(\text{OH})_4^-] + [\text{NaB}(\text{OH})_4^0]} \text{ the ratio of "paired" ions} \quad (111)$$

The association constants and the anion ratio values are given in the table below for the experimental solutions of 0.05 M $\text{Na}_2\text{B}_4\text{O}_7 \cdot 10\text{H}_2\text{O}$ that were alkalized with 0.1 M NaOH (giving them a total concentration of 0.2 M of Na^+) and for the experimental solutions with only 0.05 M borax used in this part of the study (containing 0.1 M of Na^+).

Table 5. Experimentally obtained association constants for $\text{NaB}(\text{OH})_4^0$ from (Pokrovski, et al., 1995), and the percentage of the borate ions which are paired with sodium ions.

T (°C)	pK_A	Paired ions for 0.2 M Na^+	Paired ions for 0.1 M Na^+
75	0.33	30 %	18 %
90	0.36	31 %	19 %
100	0.41	34 %	20 %
125	0.51	39 %	24 %
150	0.57	43 %	27 %
175	0.69	49 %	33 %
200	0.81	56 %	39 %

The higher degree of ion pairing which was present in the previously performed study on the initial reaction and the subsequent decay of the product(s) is thus credited with our failure to

discern any change in the decay as a function of the borax concentration and thereby distinguish an ISE at that time.

Time-resolved spectral data were obtained using select mixing ratios between the solutions described in Section 4.2.6 of 0.05 M borax solution diluted with pure DI water to attain ratios of 1:0, 1:1, 1:3, and 1:7. These results were obtained for temperatures between 100 and 200 °C. Our supposition is that the decay is due to a second order self-recombination reaction between two of the borate radicals R forming a non-absorbing product P.



Thus the rate of this reaction can be expressed in derivative form, and its integrated form, as:

$$\frac{dR}{dt} = -k[R]^2 \quad (113)$$

$$\frac{1}{[R]} = \frac{1}{[R]_0} + kt \quad (114)$$

where k is a second order rate constant ($M^{-1} s^{-1}$), and $[R]_0$ is the initial concentration of the radical.

Multiplying this equation by $1/\varepsilon$ and rearranging Equation (23) to solve for the product of concentration and the extinction coefficient yields the following result:

$$\frac{1}{\varepsilon[R]} = \frac{1}{\varepsilon[R]_0} + \frac{k}{\varepsilon} t \quad (115)$$

$$\varepsilon c = A/\ell \quad (116)$$

$$\frac{\ell}{A} = \frac{k}{\varepsilon} t + \frac{\ell}{A_0} \quad (117)$$

Therefore, a plot of the inverse of the signal ($1/A$) as a function of time will show the decay of the radical's signal as linear with a slope of $\frac{k}{\varepsilon}$. A plot of the inverse signal at 530 nm for four

concentrations of boron is shown in Figure 88, along with the fits by linear regression to the data from 7 to 100 μs . Thus we obtain an estimate of the rate of second order decay.

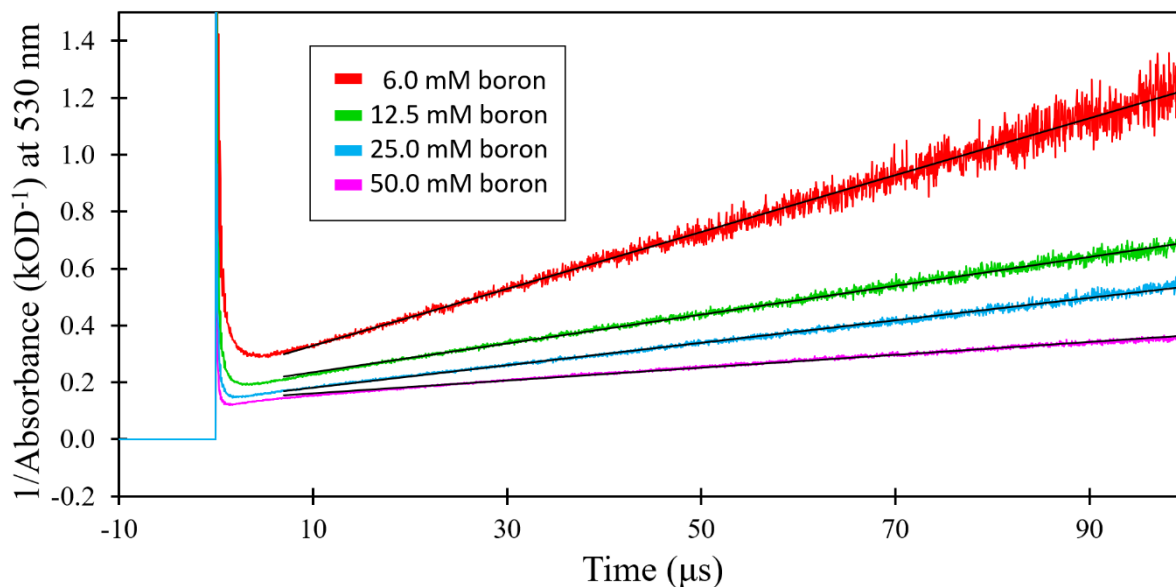


Figure 88. Plot of the inverse of the time-resolved spectral signals at 530 nm, for four concentrations of the borax solution diluted with pure DI, obtained at 100 °C.

These rates are obtained for all samples at each temperature, and are plotted below. The rates are plotted versus the inverse of the total concentration of all boron-containing species, for considering both boric acid and borate. Certainly, we see a slower decay for higher concentrations of boron, and this effect increases with temperature. As detailed in Section 1.5.2, this is not the effect we expect for the ionic strength between negatively charged $\cdot\text{BO}(\text{OH})_3^-$ radicals.

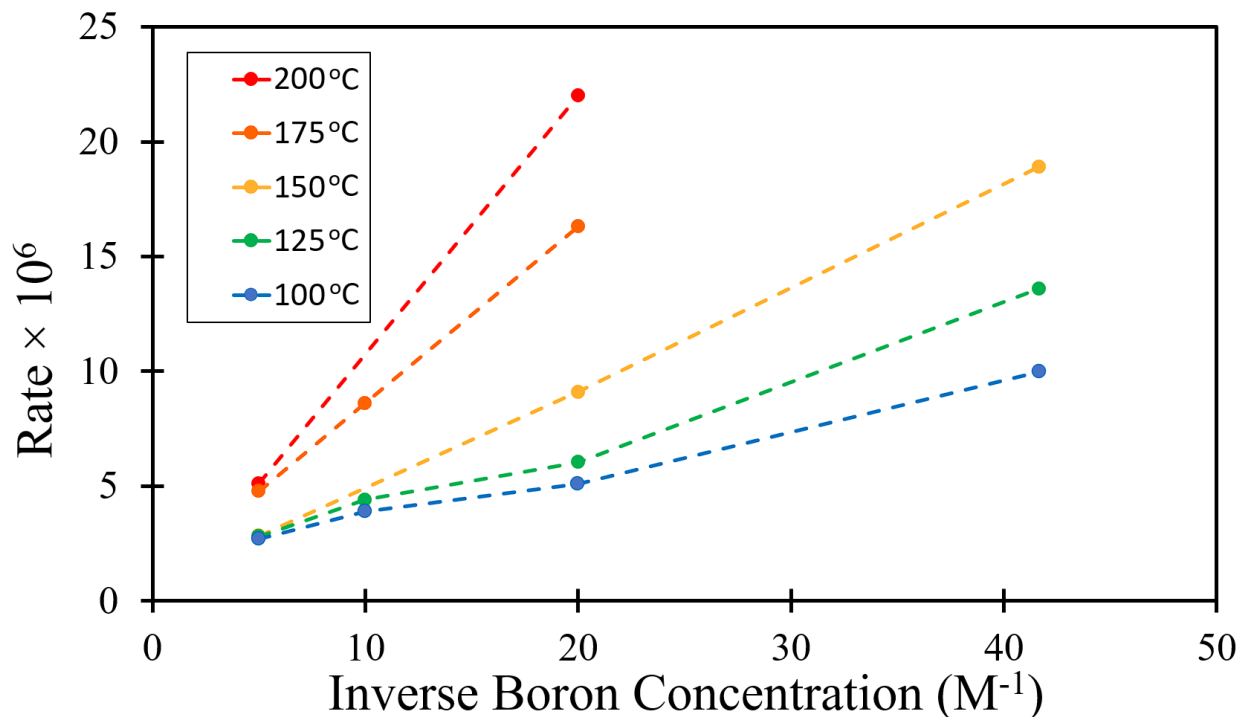


Figure 89. Plot of rates calculated from linear fits to the inverse signal at 530 nm versus the inverse of the boron concentration for temperatures between 100 and 200 °C.

If ion pairs are forming, thus lowering the borate ion's diffusivity and slowing the reaction rate of the second order decay, this might explain the observed concentration effect. Furthermore, as was discussed in Section 1.7.4, there is an effect on the solution's viscosity by varying the borate/boric acid concentration, where an increase in concentration yields an increase in the viscosity. The diffusion of particles through water is proportional to temperature and inversely proportional to viscosity, as given by the Stokes-Einstein equation:

$$D = \frac{k_B T}{6 \pi \eta r} \quad (118)$$

where k_B is the Boltzmann constant, T is the absolute temperature, η is the dynamic viscosity, and r is the radius of the particle. The effect on diffusion by the change in viscosity shown in Figure 25 then amounts to a change of only several percent, whereas we see a much larger effect on the second order reaction rate of the borate radical's decay. Therefore, even if this reaction were

diffusion-limited, the viscosity effect is not large enough to provide an explanation. Alternative considerations involve equilibration among the multiple different species of boric acid, which is known to exist in forms such as a monomer, a dimer, a cyclic trimer, and a cyclic tetramer. Further investigation is necessary for conclusive confirmation.

7.2.6 Calculating the pH of the two main borate solutions

As was described in Section 4.2, two borate solutions were used in the majority of this work studying the reaction of $\cdot\text{OH}$ with the borate: both were mixed with 0.05 M borax, one solution was alkalized with 0.1 M of NaOH to a measured pH of 10.65 at STP. while the other was left unalkalized and had a pH of 9.30 at STP. We provide here calculations of the pH over our temperature range from 25 to 200 °C. The ratio of the concentration of hydroxide ions $[\text{OH}^-]$ and protons $[\text{H}^+]$ in water is defined as:

$$K_w = [\text{OH}^-][\text{H}^+] \quad (119)$$

$$pK_w = -\log_{10} K_w \quad (120)$$

and can be calculated as a function of temperature for molar (mol L^{-1}) concentrations from the data by (Bandura & Lvov, 2006) using the following published equation (Elliot & Bartels, 2009):

$$pK_w = 14.947 + (4.273 \times 10^{-2}) T + (2.115 \times 10^{-4}) T^2 - (5.786 \times 10^{-7}) T^3 + (7.529 \times 10^{-10}) T^4 \quad (121)$$

where T is the temperature given in °C. We convert to molal (mol kg^{-1}) concentrations using the calculated the density of water (kg L^{-1}) as a function of temperature, from the data by (Irvine & Hartnett, 1976), using the following equation also published in the review by Elliot & Bartels, as:

$$\rho = 0.999 + (1.094 \times 10^{-4}) T - (7.397 \times 10^{-6}) T^2 + (2.693 \times 10^{-8}) T^3 - (4.714 \times 10^{-11}) T^4 \quad (122)$$

The EPRI technical report on PWR guidelines (EPRI, 1999) calculates the pH at high temperatures in reactors from (in part) the equilibrium constant for boric acid and borate based on the ratio of their molal concentrations, defined as:

$$K_B = \frac{[B(OH)_4^-]}{[OH^-][B(OH)_3]} \quad (123)$$

which is fit to a polynomial curve that, based on data from (Baes & Mesmer, 1976), can be expressed as a function of temperature as:

$$\log_{10} K_B = \frac{1573.21}{T} + 28.6059 + 0.012078 T - 13.2258 \log_{10} T \quad (124)$$

where T is the absolute temperature (K). Using these equations along with the pH values of our solutions measured at STP, we calculate the pH expected over the temperature range studied while researching the $\cdot OH$ reaction with borate for the two main solutions, displayed below in Figure 90.

Additionally, the percentage of O^- present from the $\cdot OH$ dissociation was similarly calculated over our temperature range, where the ratio of the concentration of $[O^-]$ and protons $[H^+]$ in water is defined as:

$$K_{OH} = \frac{[O^-][H^+]}{[\cdot OH]} \quad (125)$$

and can be calculated as a function of temperature for molar (mol L^{-1}) concentrations from the data by (Buxton, et al., 1988; Elliot & McCracken, 1989) using the following published equation (Elliot & Bartels, 2009):

$$pK_{OH} = 12.383 - (3.02 \times 10^{-2}) T + (1.7 \times 10^{-4}) T^2 - (5.151 \times 10^{-7}) T^3 + (6.96 \times 10^{-10}) T^4 \quad (126)$$

where T is the temperature given in $^{\circ}\text{C}$. Using these values along with those described above for the pH over temperature, we calculate the percentage of O^- dissociated from the $\cdot\text{OH}$ as:

$$\frac{[\text{O}^-]}{[\cdot\text{OH}]} = \frac{K_{\text{OH}}}{[\text{H}^+]} \quad (127)$$

$$\frac{[\text{O}^-]}{[\text{O}^-] + [\cdot\text{OH}]} = \frac{\frac{[\text{O}^-]}{[\cdot\text{OH}]}}{\frac{[\text{O}^-]}{[\cdot\text{OH}]} + 1} = \text{percentage of } \text{O}^- \quad (128)$$

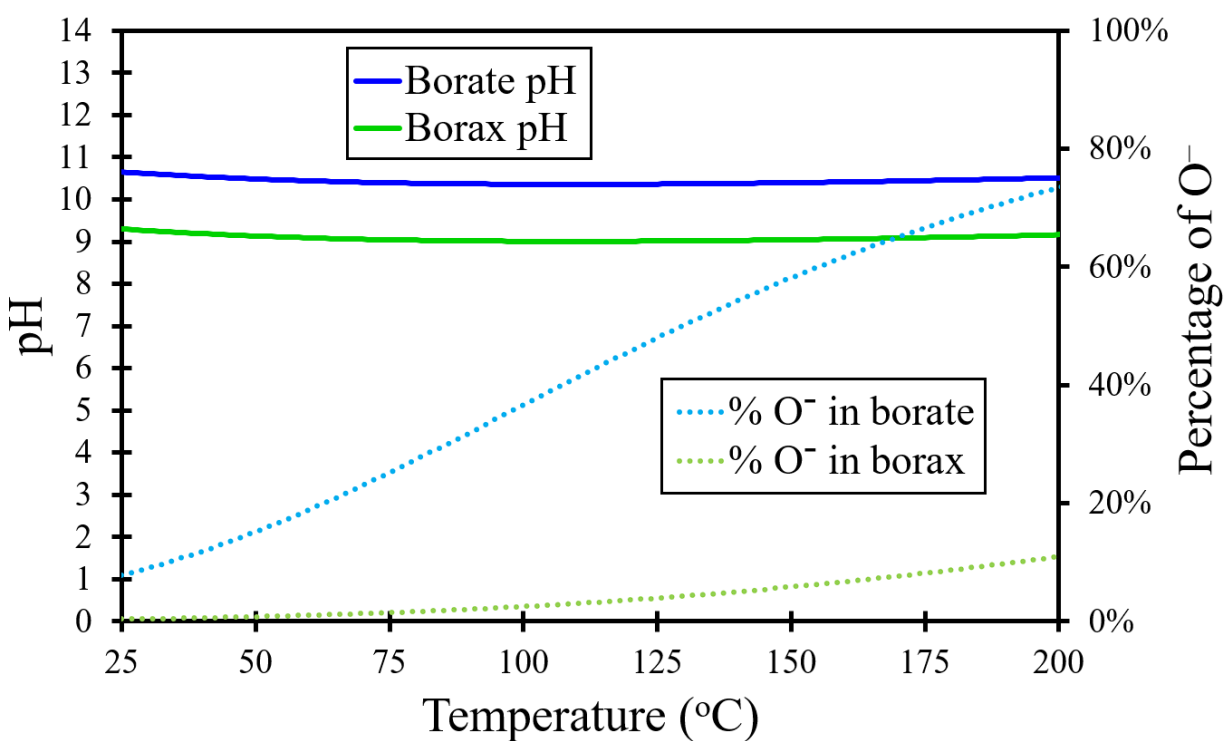


Figure 90. The pH for the two main solutions used (alkalized to borate, and unalkalized borax) while researching the $\cdot\text{OH}$ reaction with borate, along with the percentage of O^- present from the $\cdot\text{OH}$ dissociation, calculated over the temperature range studied.

It is thus apparent that there is a significant fraction of the $\cdot\text{OH}$ dissociating into O^- , which could feasibly react with the borate in the alkalinized solution. We can conclude that O^- and $\cdot\text{OH}$ reaction rates would be similar, since we obtain similar reaction rates with borate from both the alkalinized and unalkalinized borax solutions. The potential of this reaction requires further study.

7.3 Evaluation of Borate's Observed Reaction with $\cdot\text{OH}$

The computational aids IGOR Pro and KinTek Explorer were both employed to evaluate the reaction between borate and $\cdot\text{OH}$ in order to obtain both the rate constants of the initial reaction as well as the decay of the product radical, and the spectra of the species involved. Herein are presented the results of this analytical endeavor.

7.3.1 Initial Fits of the Borate Radical's Growth using IGOR

We obtained an initial estimate of the pseudo-first order reaction's rate constant and the reaction's activation energy. The computational aid IGOR Pro was used to fit the rise of the radical signal at 530 nm to an x-offset exponential rise function, as detailed in Section 6.3.1.1. A plot of the obtained fits for room temperature data is shown in Figure 91, and the Arrhenius plot in Figure 92 over our temperature range up to 200 °C gives an activation energy of $(27.4 \pm 0.4) \text{ kJ mol}^{-1}$ and reaction rate of $(3.82 \pm 0.5) \times 10^6 \text{ M}^{-1} \text{ s}^{-1}$ at room temperature.

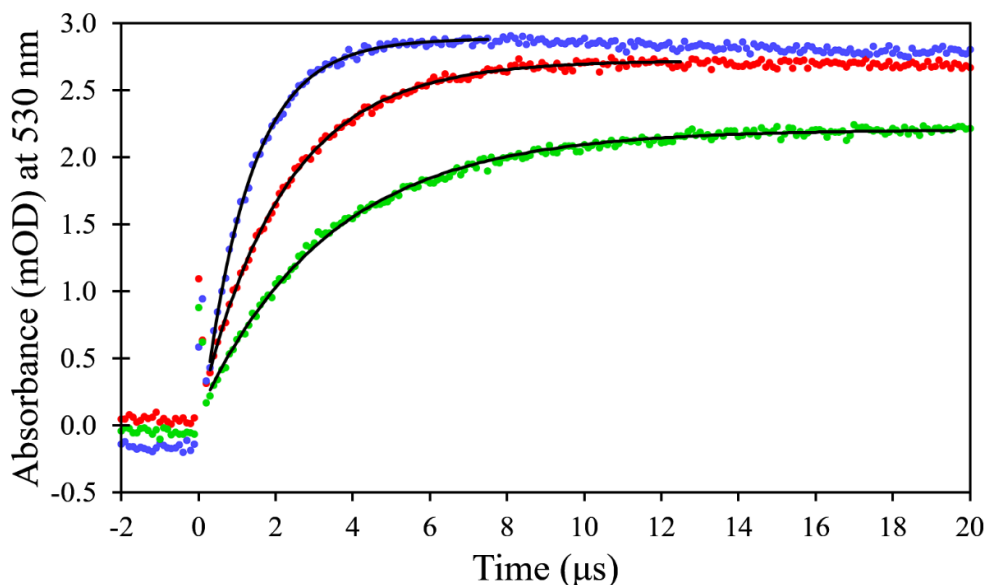


Figure 91. Plot of transient spectrophotometry experiment measurements at NDRL with low dose (ca. 4 ns) at room temperature with borate concentrations of 0.21 M (blue), 0.11 M (red), and 0.05 M (green), as well as trace fits to an x-offset exponential rise function (black) at 530 nm.

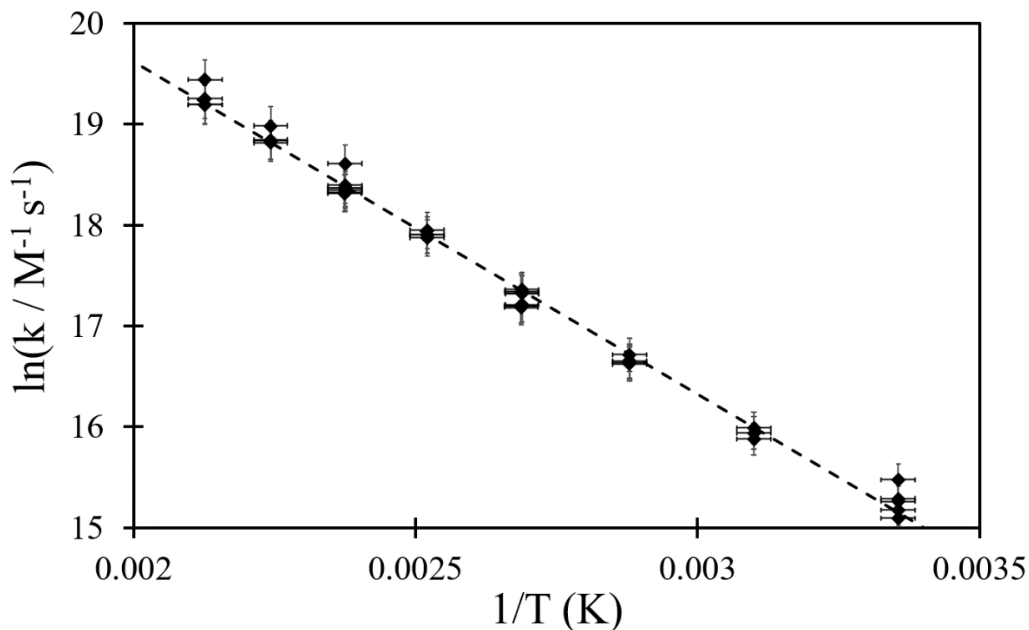


Figure 92. Arrhenius plot for the growth rate of the borate radical from reaction with $\cdot\text{OH}$, where a fit by linear regression computes an activation energy of $(27.4 \pm 0.4) \text{ kJ mol}^{-1}$ and reaction rate of $(3.82 \pm 0.5) \times 10^6 \text{ M}^{-1} \text{ s}^{-1}$ at room temperature.

The data sets collected for UV or Visible wavelength ranges and especially the sets collected at different temperatures were obtained on multiple different days, and thus were subjected to different doses and dose rates by the LINAC along with other interfering conditions, making comparison between them using IGOR somewhat less direct. However, the evolution of the spectrum from room temperature to 175 °C can be observed when normalizing to the highest absorption measured, at the 248 nm wavelength, as is shown in Figure 93.

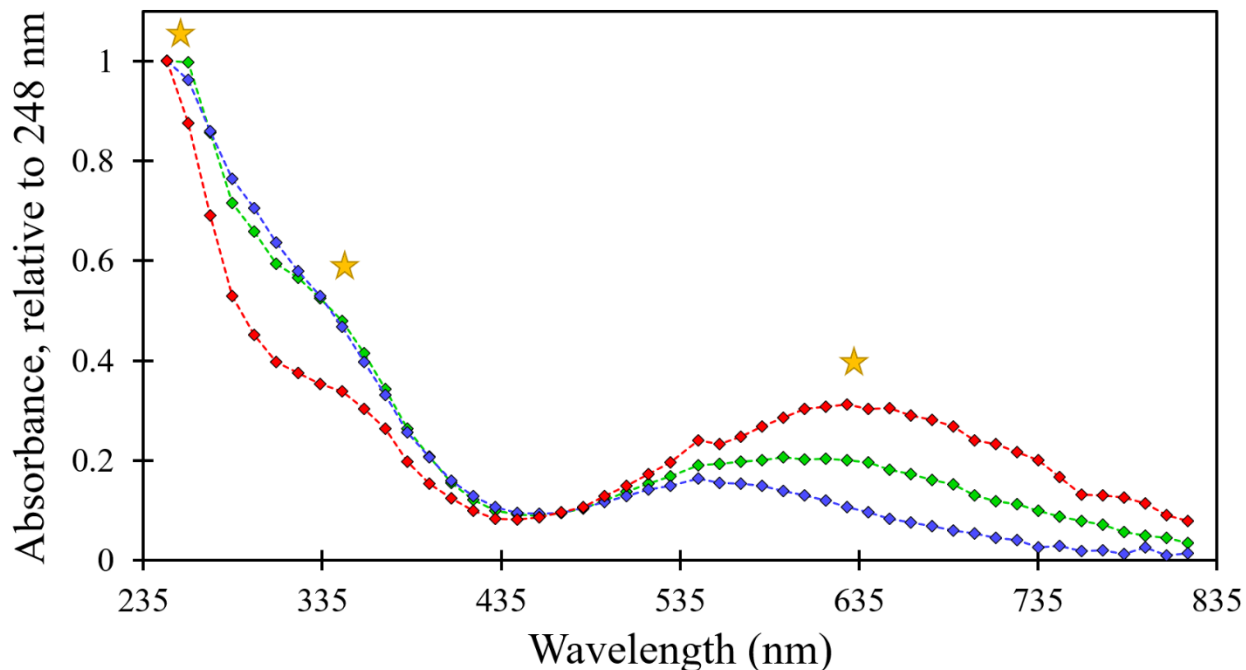


Figure 93. Plot of the borate radical's absorbance over wavelength, relative to 248 nm, obtained at 25 °C (blue), 100 °C (green), and 175 °C (red) which shows three distinguishable peaks at the Deep-UV, the Near-UV, and the Visible wavelength ranges.

Three peaks are distinguishable at distinct wavelength ranges: in the Deep-UV, in the Near-UV, and in the Visible. We observe additional absorbance tending towards the red around 700 nm at 100 °C and higher, which could be either a shift in the radical's spectrum or perhaps a new species appearing, and there is similarly a change in the spectrum near the 330 nm region. The “inverse signal” method for observing the linear behavior of the second order decay for the ISE study is again employed in a brief inquiry to the possibility of additional species. Data obtained at room temperature using the borate solution alkalinized with NaOH for the peaks in the Near-UV and the Visible are plotted in the figure below.

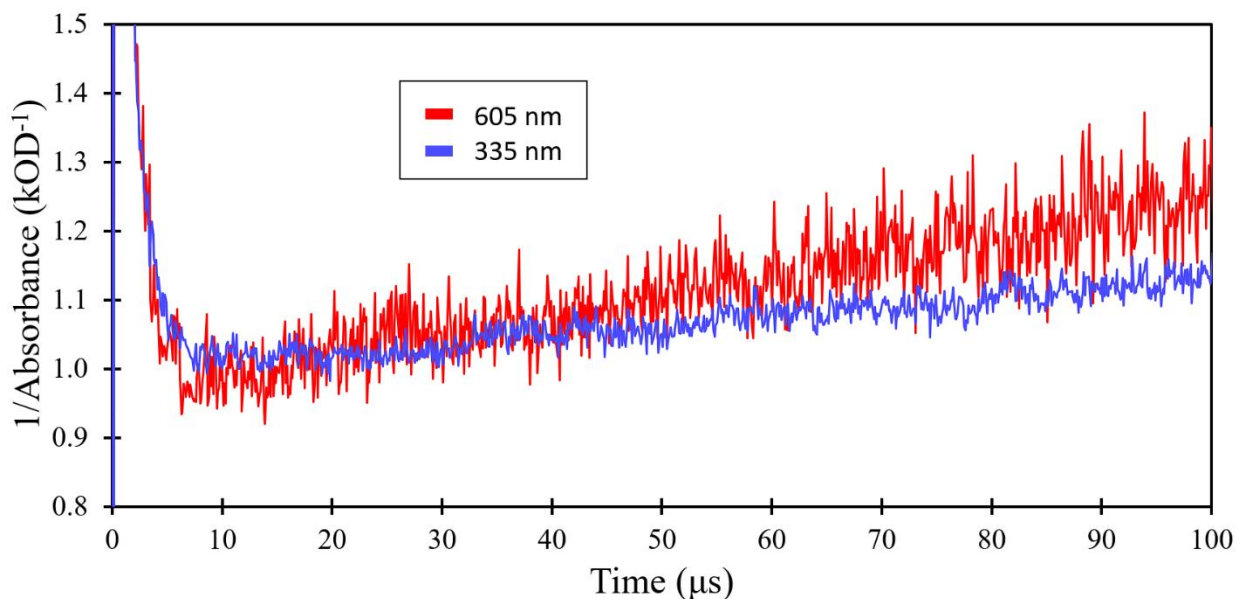


Figure 94. Plot of the inverse of the time-resolved spectral signals at 335 nm (blue) and 605 nm (red), from the alkalized borate solution, obtained at room temperature, normalized to their absorptions at 10 μ s.

As was described in the previous section, plots of the inverse absorbance for second order rates are linear and have a slope that is proportional to $\frac{k}{\epsilon}$ where k is the rate. However, since the ϵ molar attenuation coefficient typically changes with respect to wavelength, direct comparison of the data obtained at 330 nm to that at 600 nm would not be indicative of the relative rates. Instead, we normalize both traces separately to their absorption at 10 μ s (corresponding to the y-intercept of a linear equation), thus enabling meaningful comparison. Clearly these decay rates are not the same, and therefore we more strongly suspect there are multiple radical species. As was discussed in Section 1.7.4 about the work by Tremaine on speciation in boric acid solutions that are nominally 100 % alkalized by NaOH, we expect no polyborate species to be initially present in our 0.05 M borax solutions alkalized by 0.1 M NaOH. Therefore, we expect no significant reactions of \cdot OH with polyborate species as none would be present at the OH-lifetime μ s time scale. Further investigation is necessary for identifying likely reactions and reactants. Evaluation

was attempted using KinTek Explorer along with suggesting a bimolecular recombination of the borate radical which generates a secondary absorbing species.

7.3.2 The Borate Radical's Growth and Decay, Fit using KinTek Explorer

Once we had an estimate for the growth of the initial radical from single-channel analysis using IGOR, we turned to employing KinTek for analysis of multiple compilations of time-resolved spectral data to globally fit all runs in a set together. Sets of data obtained at different temperatures must of course be fit independently due to the rate constants of these reactions being temperature dependent. It must be noted that when globally fitting any set of data for which each experiment does not have the same wavelength domain, KinTek lacks the capacity to solve for a single set of component spectra and would instead solve for the components corresponding to each experiment separately. This presents an obstacle when coupled with the fact that in most cases a set of experiments at a target temperature were acquired on separate days for the UV range (248 to 530 nm, across 24 channels) and the Visible range (545 to 819 nm, across 24 channels). It is feasible that one could manually combine the time-resolved spectral data for equivalent experimental conditions; however, as has been mentioned, the dose rates from the LINAC at NDRL change daily. Thus such an endeavor is made generally impossible for this study, and so sets of data must be fit separately for the two wavelength domains. A third factor which divides the data sets is established by the combination of KinTek's limit allowing only 2000 columns of time-resolved absorption data for the 24 rows of wavelength together with our choices made on the time resolution of the transient spectrometer system. We make the choice to partition high time-resolution data from low-resolution in order to fit the borate radical's short-time rise and long-time decay, respectively, as separate data sets. Therefore, compilations of the multiple sets

of data are distinguished by their temperature, their wavelength domain (UV or Visible), and their timescale (short-time or long-time).

We now cover the topic of deciding the set of observable output functions (what species' behaviors are expected to be perceived) to be fit to the species distinguishable from the deconvolution by SVD for the aforementioned compilations. There are four distinctions made:

- 1) For the short-time regime in the UV, we expect to observe the decay of $\cdot\text{OH}$ as it is consumed by borate, and thus a growth of the product $\cdot\text{BO}(\text{OH})_3^-$ radical.
- 2) For the short-time regime in the Visible, we expect to only observe the growth of $\cdot\text{BO}(\text{OH})_3^-$, since $\cdot\text{OH}$ doesn't significantly absorb in this wavelength range.
- 3) For the long-time regime in the UV, we expect to observe the decay of the borate radical $\cdot\text{BO}(\text{OH})_3^-$ as it is consumed in a bimolecular self-recombination reaction, as well as a growth of the product radical which we enter as the peroxyborate H_4BO_5^- .
- 4) For the long-time regime in the Visible, we expect to observe just the same as in the UV: decay of the borate radical and growth of a supposed peroxyborate species.

An example of an imported time-resolved spectra as well as the SVD results are shown in Figure 95. The decision on how many component species are distinguished is part of KinTek's automatically performed SVD, where it will fit up to five different components and list the magnitude (SV) of each's corresponding eigenvector, indicating greater significance for those with higher values.

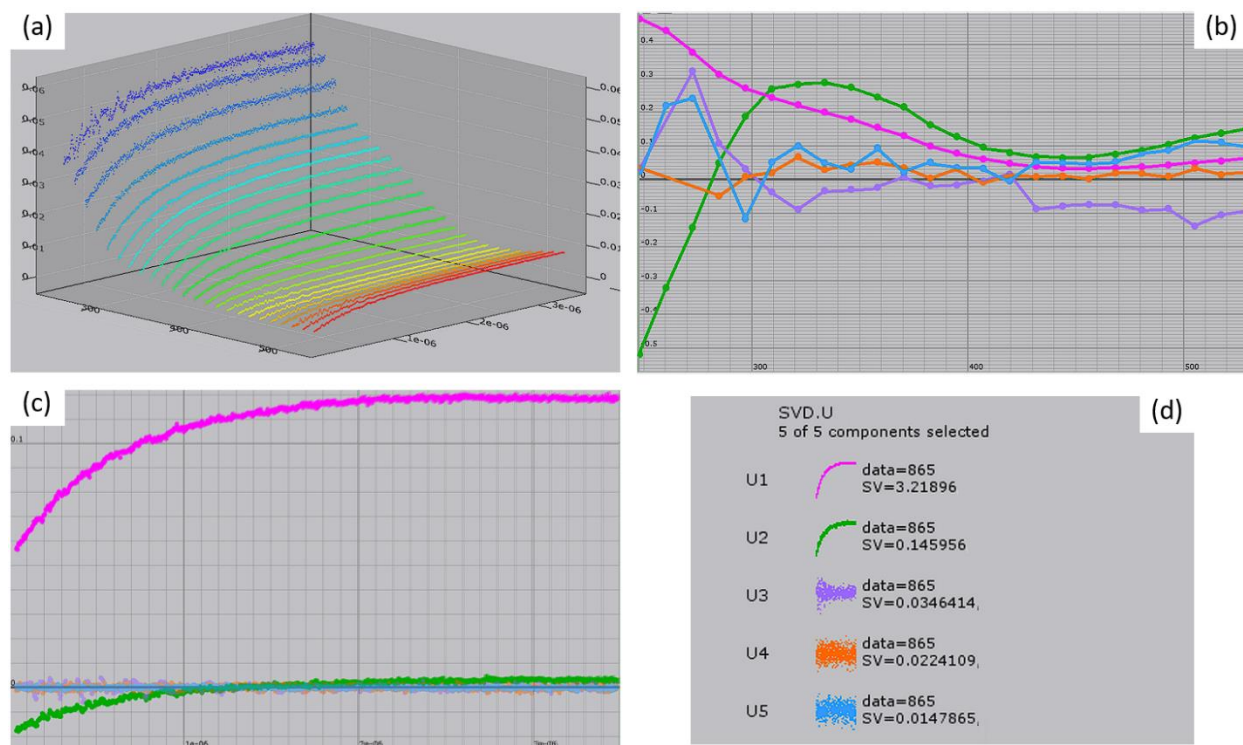


Figure 95. (a) imported time-resolved spectra, (b) the scaled spectra of the five distinguished component species, (c) the signal amplitudes of the five species evolving over time, (d) values from the SVD process corresponding to the absorbance matrix indicating the number of points contained therein and the magnitude of the eigenvector scaling factors (SV).

We can find in Figure 95d that U3, U4, and U5 have very low SV values, indicating that they are most likely only representative of noise, and this can be confirmed visually in Figure 95c where only the traces of U1 and U2 appear to exhibit any significant evolution over time.

The two important conditions to vary in this experiment are the dose and the concentration. Dose was varied to both investigate the initial first-order reaction rate between borate and $\cdot\text{OH}$ and to initiate the second-order chemistry involved in the radical's supposed self-recombination reaction, and the concentration of the borate was varied to establish the reaction rate's dependence on it. Therefore, three distinct experimental conditions are typically used in the global fitting routine: A) high dose and low concentration, B) high dose and high concentration, and c) low dose and high concentration. Most all global fits have at least one data set for each of these three

conditions, and some have additional data sets for the same general conditions though acquired on different days.

A depiction of the full fitting process and results is given in Figure 96–Figure 99 for the time-resolved spectra obtained first for the short-time regime in the UV to observe and fit the $\cdot\text{OH}$ decay and the growth of the $\cdot\text{BO}(\text{OH})_3^-$ borate radical, as well as for the long-time regime in the UV to observe and fit the borate radical decay by self-recombination and the growth of an as-yet unidentified product (for which the placeholder H_4BO_5^- peroxyborate is used).

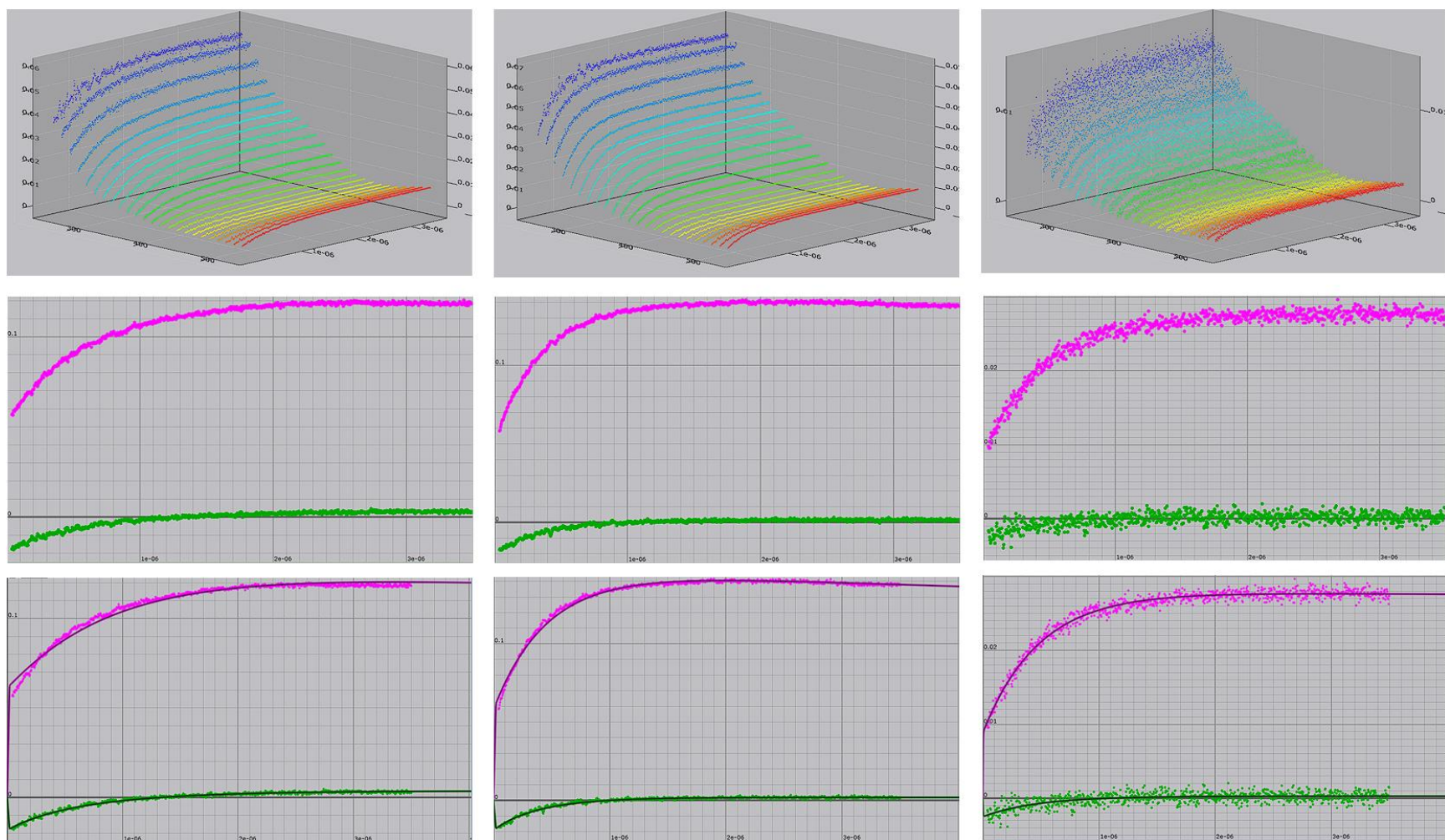


Figure 96. Plots generated by KinTek Explorer for global fitting of time-resolved spectra obtained at 75 °C for short-time in the UV. The columns contain data acquired for the following experimental conditions, from left to right: 2.67 Gy ns⁻¹ for 20 ns and 0.1 M borate, 2.67 Gy ns⁻¹ for 20 ns and 0.2 M borate, 2.12 Gy ns⁻¹ for 4 ns and 0.2 M borate. The rows correspond to different steps in the analysis with KinTek, from top to bottom: imported time-resolved spectra, the signal amplitudes of the two component species evolving over time distinguished by SVD, and the global fitting of the SVD components to the steady-state simulation of the two user-specified observable absorbing species (magenta is the borate radical and green is the [•]OH) using the globally fitted rate constants.

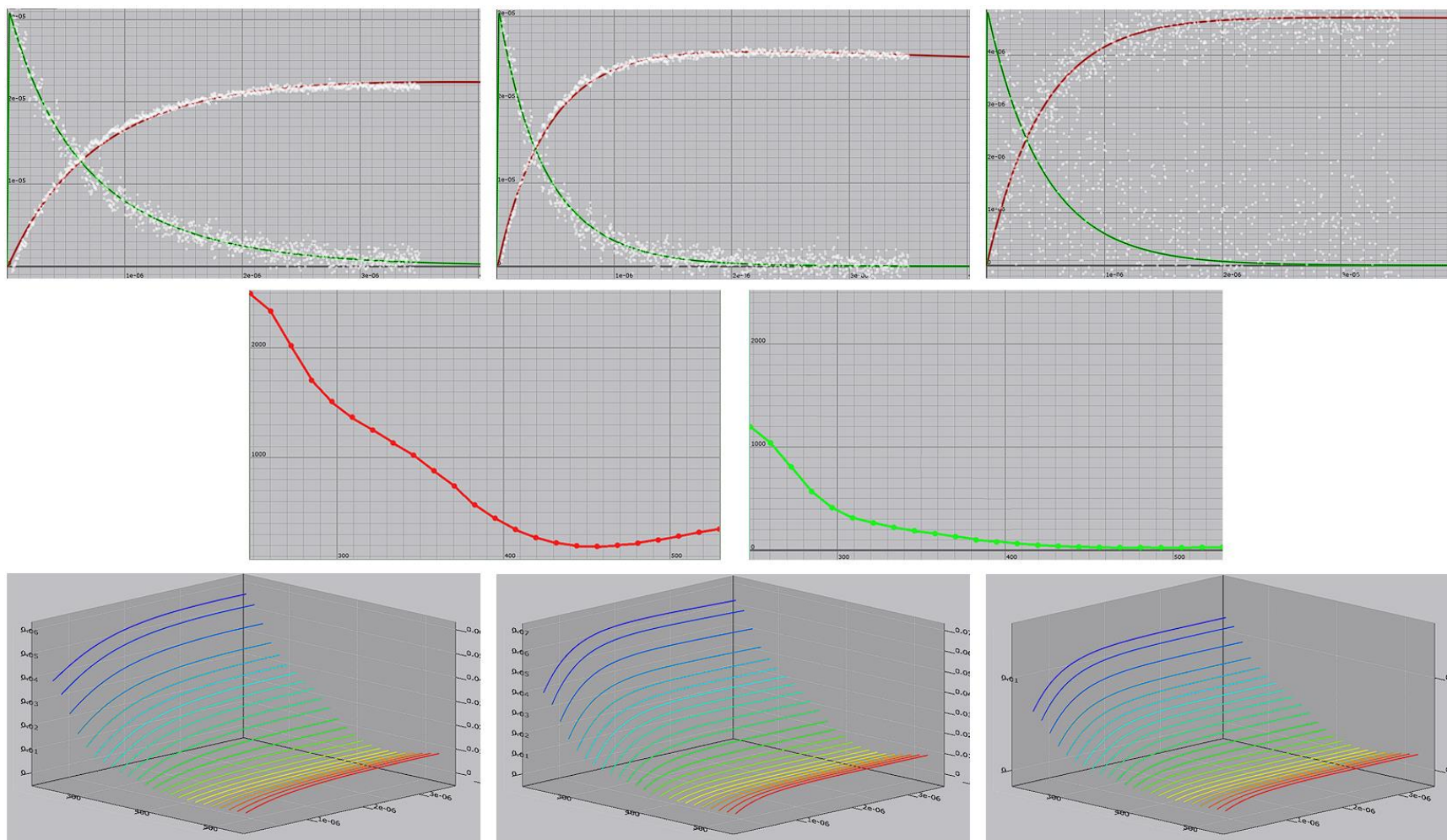


Figure 97. Plots generated by KinTek Explorer for global fitting of time-resolved spectra obtained at 75 °C for short-time in the UV. For the first and last rows, the three columns correspond to the same experimental conditions as in the previous figure. The rows correspond to different steps in the analysis with KinTek, from top to bottom: the fit of experimental data to the steady-state simulation using the two user-specified observable absorbing species (red is the borate radical and green is $\cdot\text{OH}$) using the globally fitted rate constants, the globally fitted spectra of the observables, and the reconstructed time-resolved spectra generated for all three experiments after globally fitting the reaction rate constants and species' spectra.

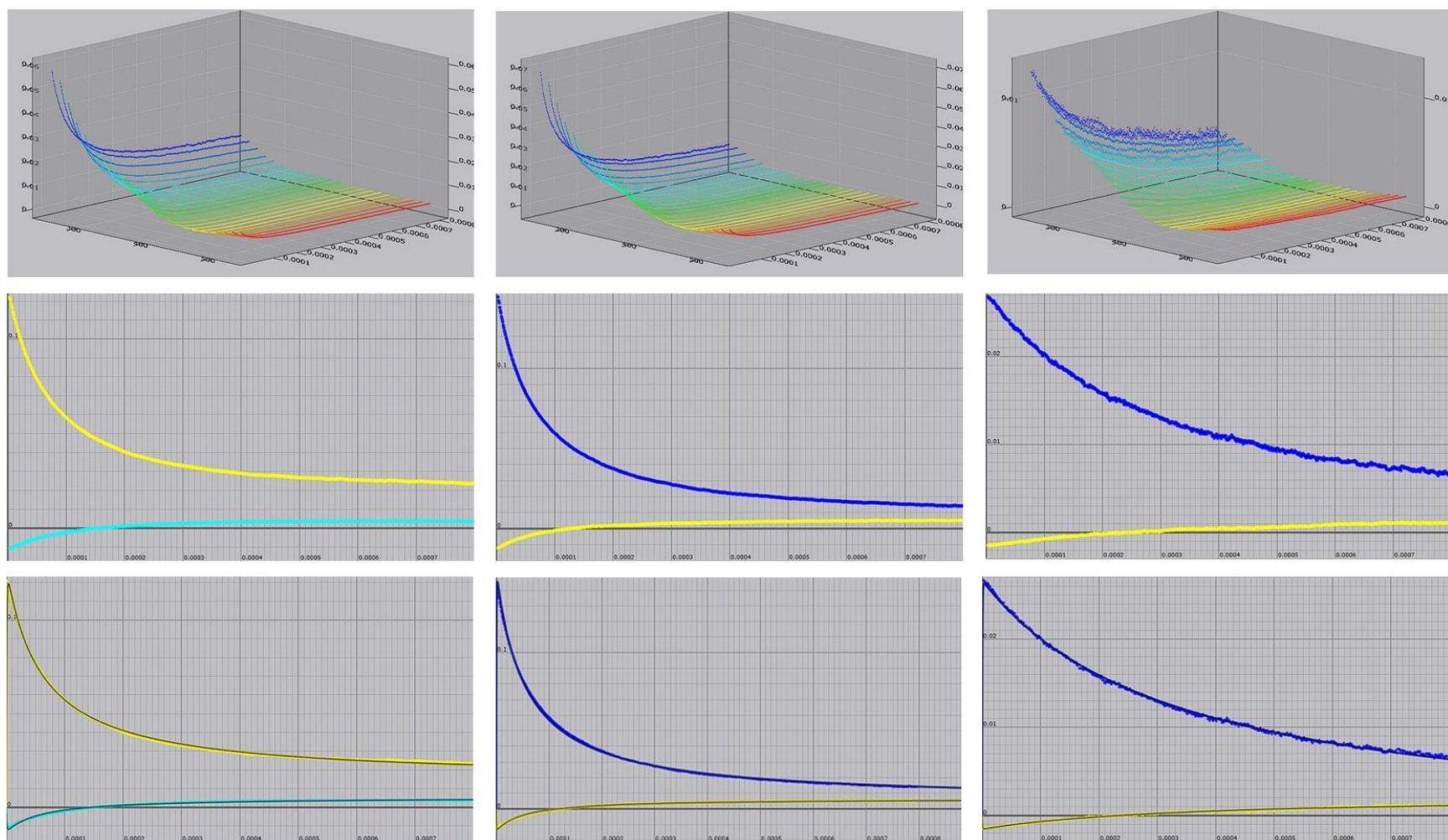


Figure 98. Plots generated by KinTek Explorer for global fitting of time-resolved spectra obtained at 75 °C for long-time in the UV. The columns correspond to the experimental conditions, from left to right: 2.63 Gy ns⁻¹ for 20 ns and 0.1 M borate, 2.63 Gy ns⁻¹ for 20 ns and 0.2 M borate, 1.92 Gy ns⁻¹ for 5 ns and 0.2 M borate. The rows correspond to the same steps in the analysis with KinTek in Figure 96: imported time-resolved spectra, signal amplitude evolution over time (KinTek uses its own arbitrary coloring scheme) by SVD, and fit for the user-specified SVD observables (left plot: yellow is the borate radical and cyan is the peroxyborate; middle and right plots: blue is borate radical and yellow is peroxyborate) to steady-state simulation generated from globally fitted rate constants.

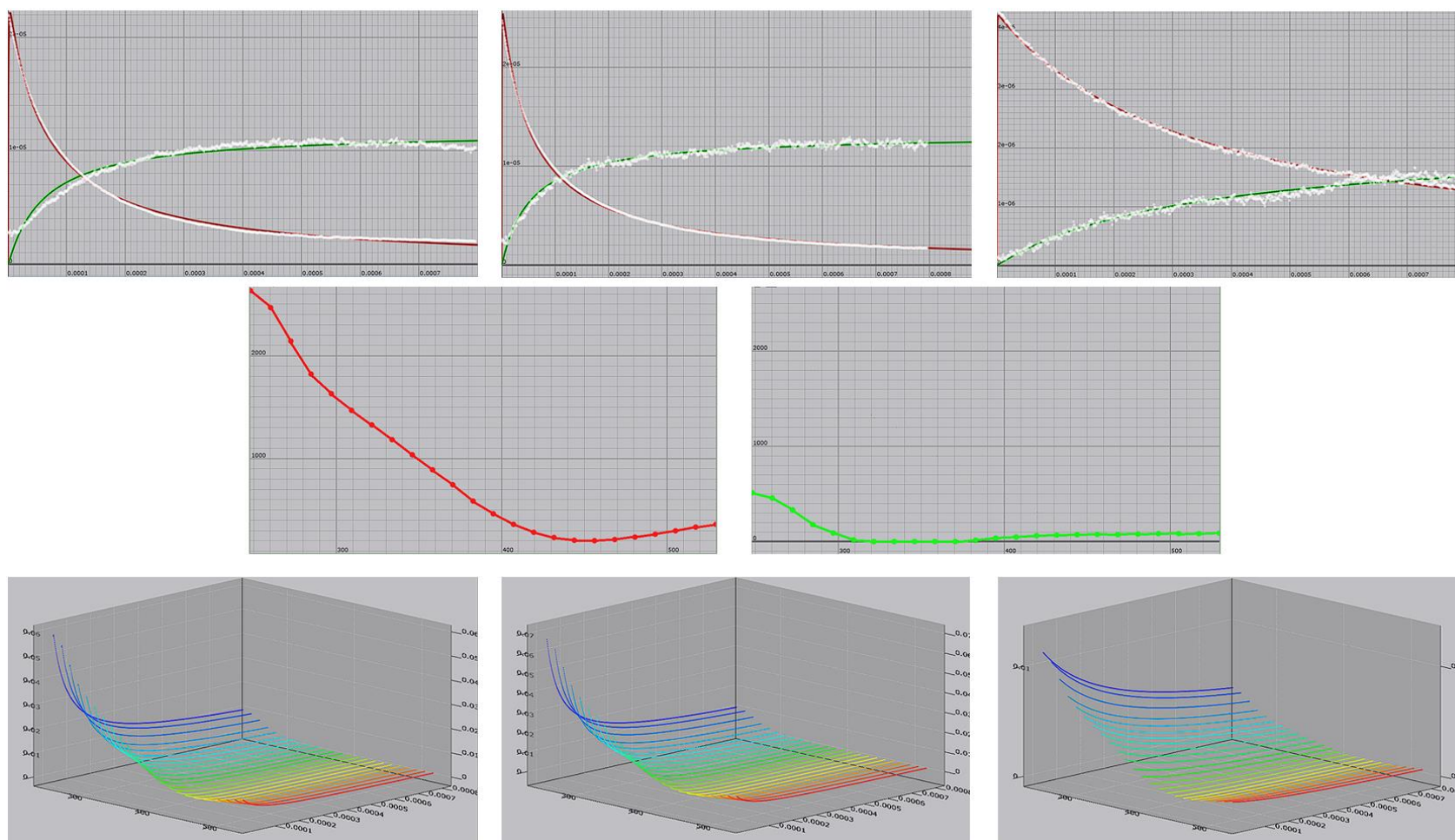
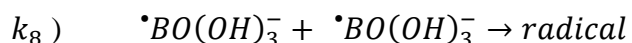
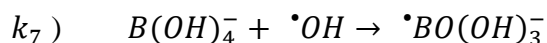


Figure 99. Plots generated by KinTek Explorer for global fitting of time-resolved spectra obtained at 75 °C for long-time in the UV. For the first and last rows, the three columns correspond to the same experimental conditions as in the previous figure. The rows correspond to the same steps in the analysis with KinTek in Figure 97: experimental data fit to the steady-state simulation using the two user-specified observable absorbing species (red is the borate radical and green is peroxyborate) using the globally fitted rate constants, the globally fitted spectra of the observables, and the reconstructed time-resolved spectra generated from the globally fitted reaction rate constants and species' spectra.

Again, we are attempting to globally fit two different rate constants, given below once again. Since the short-time is more significant in fitting k_7 for the rise of the borate radical and has insufficient data to fit k_8 for its decay, we hold the latter as constant during fitting of the short-time data. The reverse case applies when fitting k_8 using long-time data, and so k_7 is held constant then.



An iterative process is thus used to fit both nearly-simultaneously, to the best of our abilities. A rough estimation of the decay rate is obtained using KinTek's impressive immediate feedback by dynamic simulation, wherein users have the ability to scroll a rate constant up or down while concurrently observing the effects in the shape of the computed time dependence of the reactions (Johnson, et al., 2009). This value of k_8 is entered in with the short-time data and held constant, then global fitting for k_7 is performed. The rate constant thereby obtained is similarly entered in with the long-time data and held constant, then global fitting for k_8 is performed. This process needs repeating only 1–3 times before the fitted rate constants both have converged to an acceptable degree. The results from the global fitting of each of the UV/Visible and short-/long-time regimes are thus obtained for all such compilations which have been experimentally acquired over the temperature range from 25 °C to 175 °C, and are shown in the figures below. The error of these values is generated by KinTek's built-in error analysis software through nonlinear regression for each reaction rate constant included in the global fit, and will not be discussed further here.

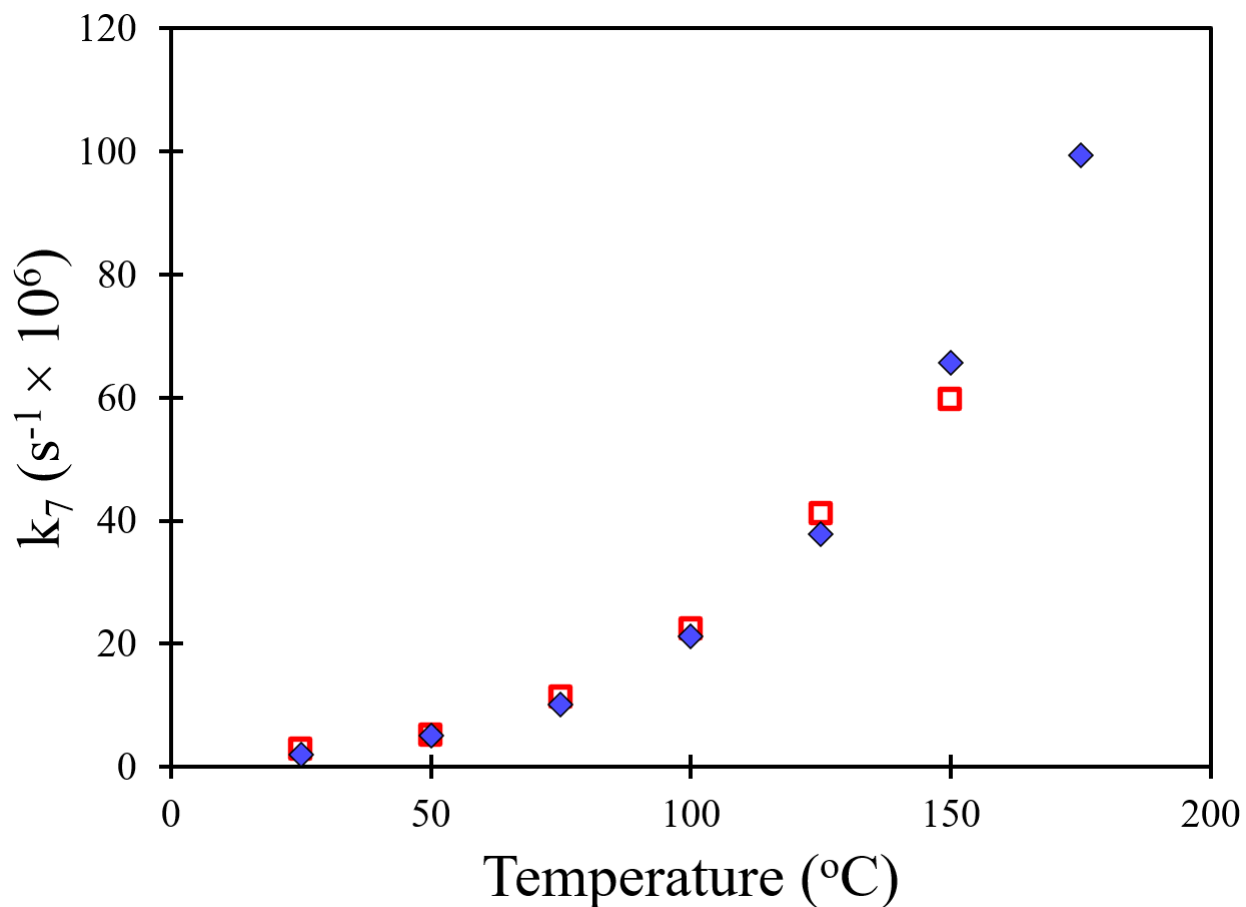


Figure 100. Plot of rate constants from globally fitting k_7 in KinTek using the iterative process of fitting the short- and long-time sets consecutively, while fitting our two wavelength ranges separately. The UV wavelengths in the range of 248 to 530 nm (blue diamonds) and the Visible wavelengths in the range of 545 to 819 nm (red squares) are compared. Error bars generated from KinTek are smaller in both dimensions than the size of the points.

The rates obtained by globally fitting the rates of the initial borate reaction with $\cdot\text{OH}$ separately from the data for the UV range and the Visible range are shown in Figure 100. There is satisfying agreement between the two data sets on this particular rate constant's magnitude and temperature dependence. Therefore they are treated equivalently for fitting to an Arrhenius equation, as plotted in Figure 101.

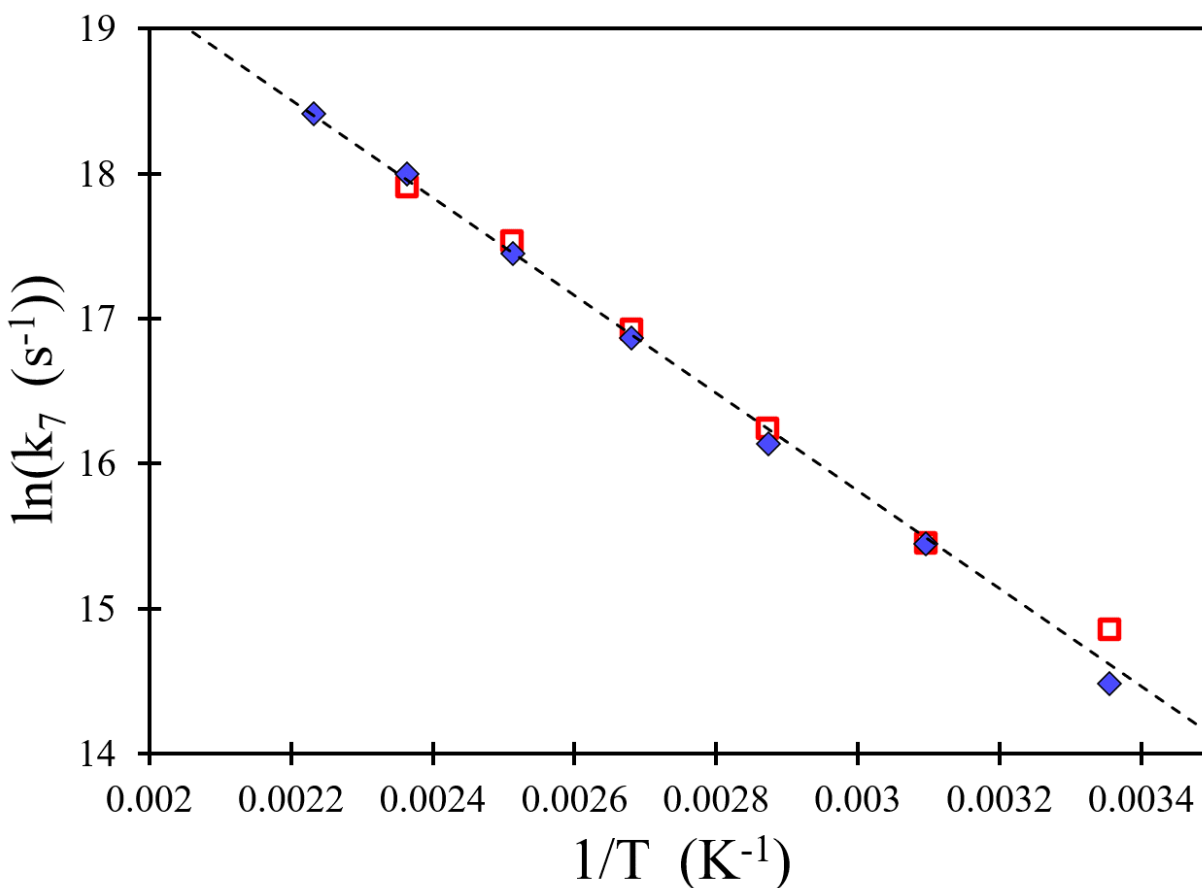


Figure 101. Arrhenius plot of the rate constants from globally fitting k_7 in KinTek. The UV (blue diamonds) and the Visible (red squares) data are fit together, indicating an activation energy of $(28.0 \pm 0.6) \text{ kJ mol}^{-1}$ and room temperature rate constant of $2.24 \times 10^6 \text{ s}^{-1}$.

Agreement with the expected Arrhenius behavior is good, indicating an activation energy of $(28.0 \pm 0.6) \text{ kJ mol}^{-1}$ for the hydrogen atom abstraction from $B(OH)_4^-$ by $\cdot OH$, and its room temperature rate constant to be $2.24 \times 10^6 \text{ s}^{-1}$ (for reference, the measured rate constants at room temperature from the UV and Visible data are $1.95 \times 10^6 \text{ s}^{-1}$ and $2.82 \times 10^6 \text{ s}^{-1}$, respectively). We move on to the fits obtained for the rate of the borate radical decay.

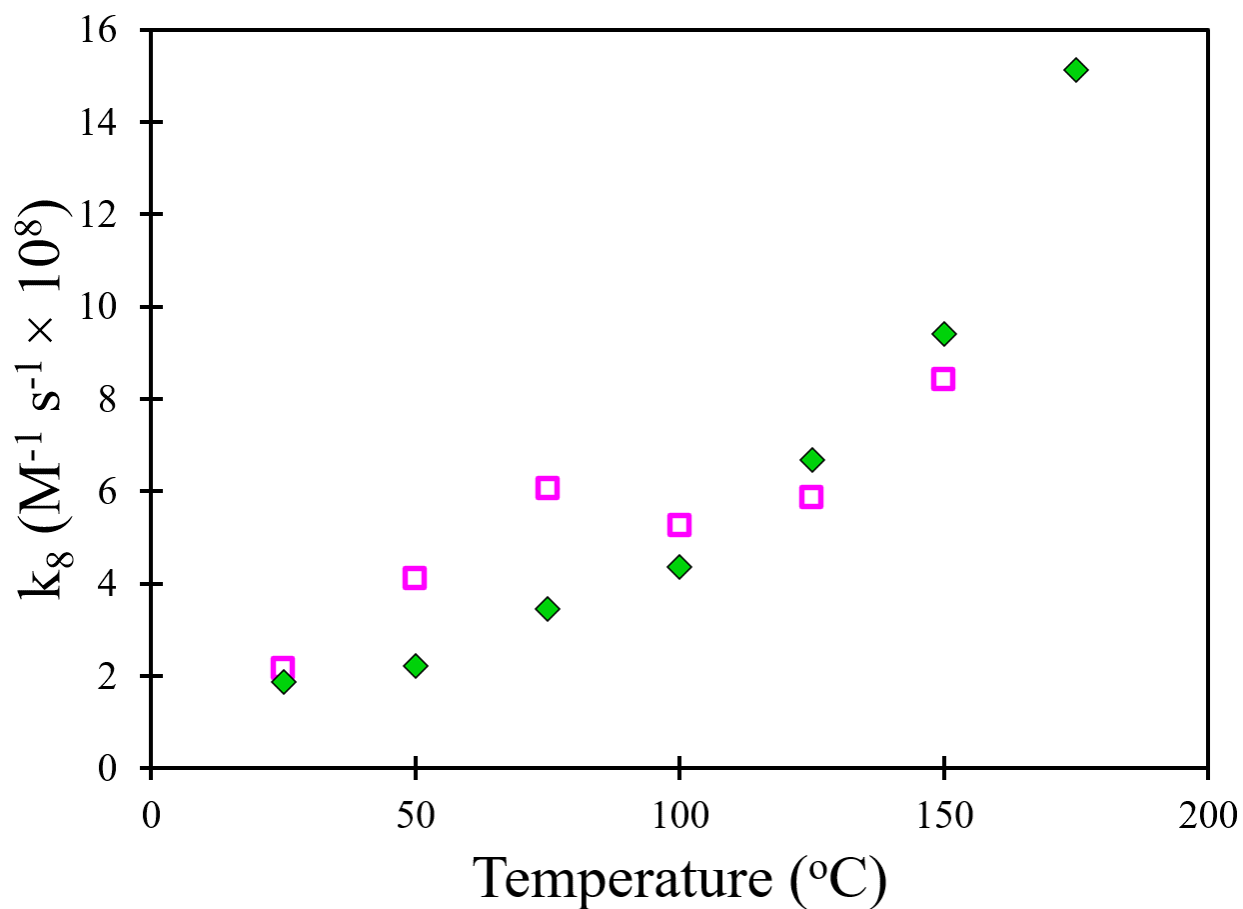


Figure 102. Plot of rate constants from fitting k_8 in KinTek using the iterative process of fitting the short- and long-time sets consecutively, while fitting our two wavelength ranges separately. The UV wavelengths in the range of 248 to 530 nm (green diamonds) and the Visible wavelengths in the range of 545 to 819 nm (magenta squares) are compared. Error bars generated from KinTek are smaller in both dimensions than the size of the points.

Due to the demonstrably poor fits for the decay rate of the borate radical by the proposed bimolecular self-recombination in the Visible range as well as their clear disagreement with the UV fits, we conclude that our model requires refinement before a confident report on the nature of the borate radical's decay can be made. At best, we now offer the UV data fits as rough estimations of the decay rate for the borate radical.

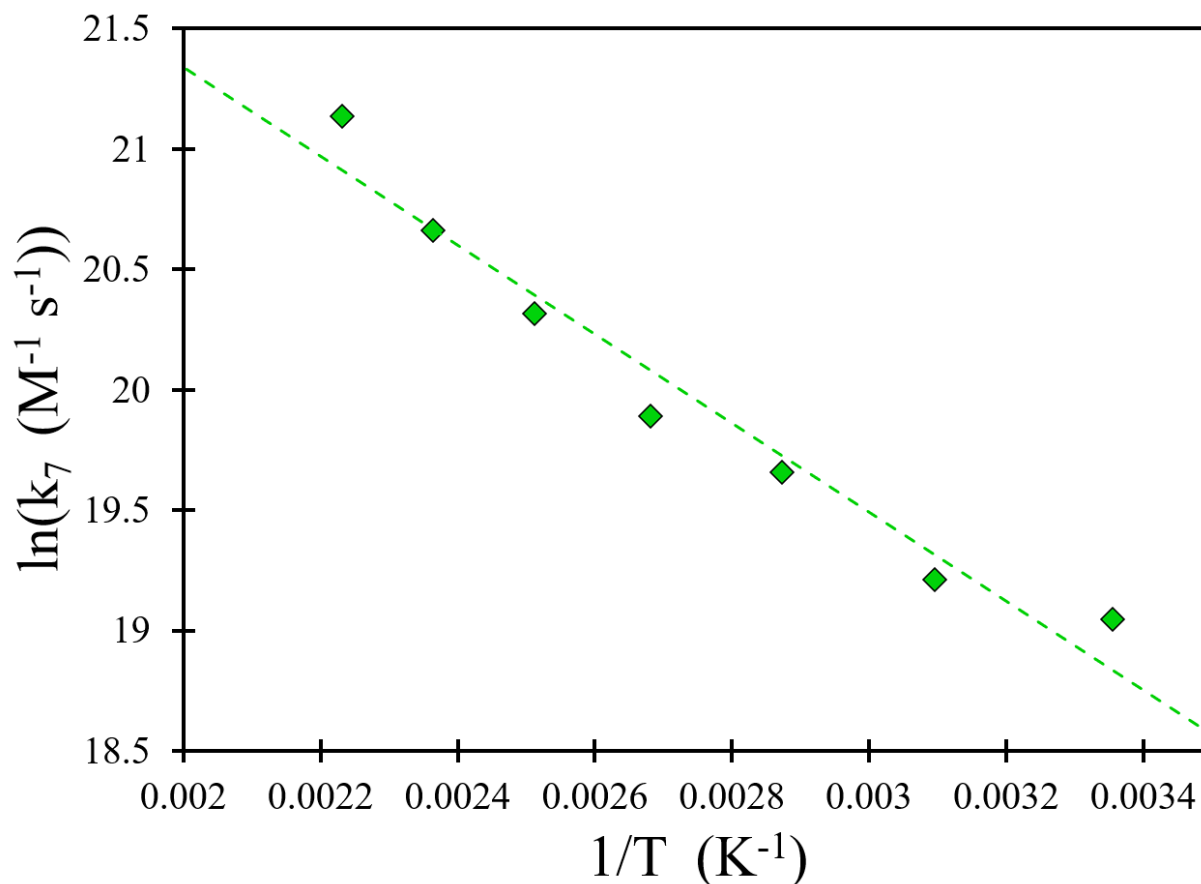


Figure 103. Arrhenius plot of the rate constants from globally fitting k_8 in KinTek. The UV data (green diamonds) is displayed, however the Visible data is omitted. A fit by linear regression indicates an activation energy of $(15.4 \pm 1.5) \text{ kJ mol}^{-1}$ and room temperature rate constant of $1.52 \times 10^8 \text{ M}^{-1} \text{ s}^{-1}$.

Agreement with Arrhenius behavior is less than ideal for the rate of the borate radical's proposed bimolecular self-recombination decay than was obtained for its rate of growth. In this case, the fit by linear regression indicates an activation energy of $(15.4 \pm 1.5) \text{ kJ mol}^{-1}$ and room temperature rate constant of $1.52 \times 10^8 \text{ M}^{-1} \text{ s}^{-1}$ (for reference, the measured rate constant at room temperature was $1.87 \times 10^8 \text{ M}^{-1} \text{ s}^{-1}$).

As was similarly concluded from the study of the ionic strength effect using IGOR in Section 7.3.1, we must consider chemical interactions among the multiple different species of boric

acid which are likely to exist in these conditions. Further investigation is necessary for conclusive confirmation.

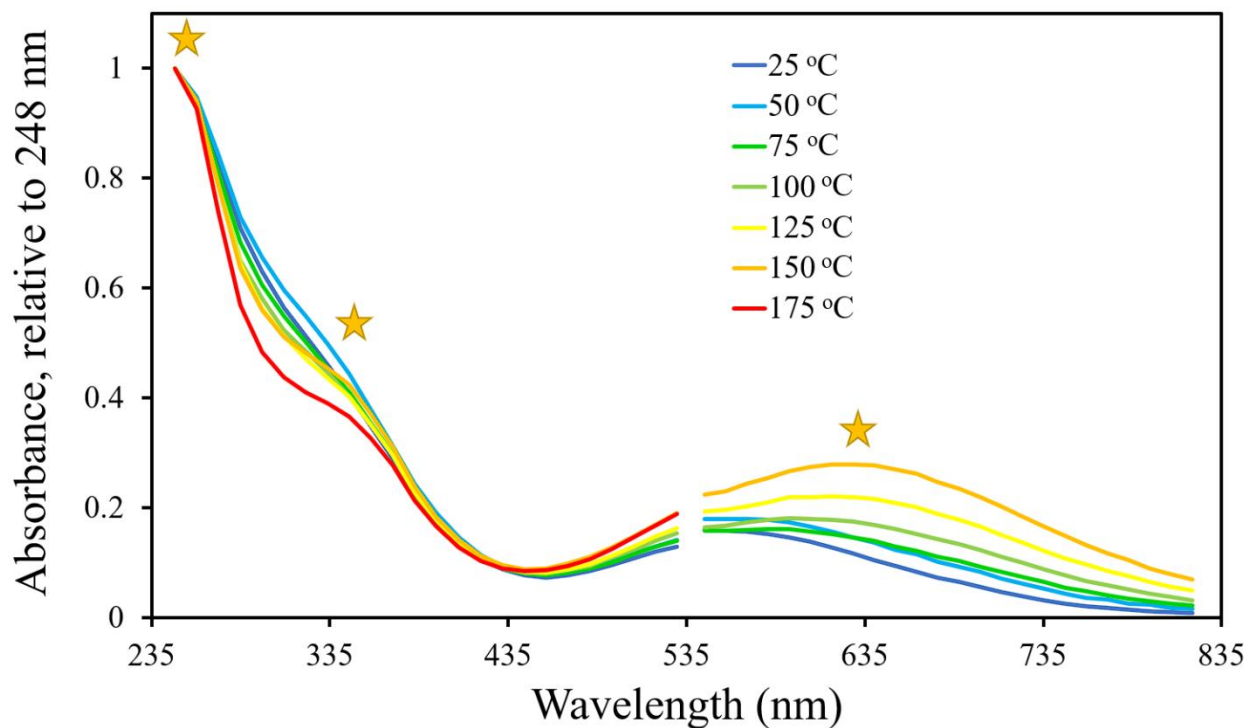


Figure 104. Plot of the borate radical's absorbance over wavelength, relative to 248 nm, obtained from 25 °C to 150 °C in the Visible and up to 175 °C in the UV by KinTek global fitting performed on the radical's short-time rise, from experiments on the alkalized borate solution. Three peaks are distinguishable: in the Deep-UV, in the Near-UV, and in the Visible wavelength ranges.

The fitted spectra for the user-defined observables are generated from KinTek through its global fitting process. Only the spectra of the borate radical are presented here, due to the unsatisfactory fits presented above for the decay reaction's supposed product. Figure 104 shows the evolution of the $\cdot BO(OH)_3$ spectrum from room temperature up to 175 °C can be observed when normalizing to the highest absorption measured, at the 248 nm wavelength. Its behavior resembles the same presented in the spectral analysis performed using IGOR, depicted previously in Figure 93. The same three peaks are distinguishable in the Deep-UV, in the Near-UV, and in the Visible. And we again observe additional absorbance tending towards the red around 700 nm

at 100 °C and higher, along with the similar change in the spectrum near the 330 nm region as temperature increases. These repeated observations therefore further reinforce our proposition of either a shift in the radical's spectrum or perhaps a new species appearing, and there is similarly a change in the spectrum near the 330 nm region.

In summary, we are confident that there is a reaction between the $\cdot\text{OH}$ and borate, and that we have obtained a satisfactory estimation of the rate constant and its temperature dependence as well as the behavior of the product absorbing radical's spectrum evolving with temperature. However, we are left uncertain on the nature of the chemistry surrounding the radical's decay, though rough estimation of the rate at which it occurs has been performed.

This work is expected to be published after a satisfactory overall mechanism is identified, based in part on further study of the literature on the speciation of boric acid at high temperatures likely to be present at our experimental conditions, thus allowing for improvement on these fits obtained by KinTek.

As an additional note, we presume there will be a small correction factor in the energy deposition that must be taken into account when calculating the concentrations and molar extinction coefficients of the radical(s). As was discussed in Section 1.7.4, there is an effect on the solution's density when varying the borate/boric acid concentration, where an increase in concentration results in an increase in the density. For the maximum concentration of 0.2 mol L^{-1} used in this part of the work, this equates to ca. 12 g kg^{-1} . According to the data in Figure 24, the density is expected to change over this concentration range, but only by several percent.

8 Conclusions

The first part of this dissertation presents the first direct measurements for $G(\text{H}_2)$ from the $^{10}\text{B}(n,\alpha)^7\text{Li}$ fission process as a function of temperature up to Pressurized Water Reactor conditions via a stop-flow aqueous solution transport and containment system installed at the Rhode Island Nuclear Science Center. This system was thoroughly evaluated to achieve optimal operational and analytical efficiency, accuracy, and precision. Along with the boron in solution, a sodium-based *in situ* thermal neutron dosimeter was included as well as a scavenger system for preventing interference by radicals of concern.

The second part of this dissertation presents the discovery and evaluation of a reaction between the $\cdot\text{OH}$ radical and the conjugate base form of the boric acid chemical additive used in PWR primary water, over a temperature range up to 200 °C. A continuous-flow aqueous solution system was used in congruence with an electron linear accelerator configured for pulse radiolysis and a transient absorption spectrophotometry system all owned and operated under the widely known and highly regarded Notre Dame Radiation Laboratory.

The reliance on nuclear power plants to supply electricity continues to rise as the world aims to move away from the use of fossil fuels, and we are expected to continue to depend on this low-carbon-emission power supply in our efforts to minimize any sources of anthropogenic impact on the global climate. Their safe operation and the evaluation of component lifetimes as it currently stands already heavily hinges on understanding degradative processes like corrosion and which factors relevant to its regulation must be accounted for. However, ascertaining the radiolytic yield of H_2O_2 at characteristic operational conditions for PWRs from thermal neutron capture by boron – one of the most prevalent chemical species deliberately incorporated within PWR primary water

loops – remains a neglected concern despite its well-known significant enhancement of the corrosion. Additionally, significant reactivity of any of the main boron-containing species with any of the principal radiolytic species produced from the water in these same environments has thus far eluded detection. This is owed to the unfortunate happenstance that such a thorough spectral investigation was not previously feasible at the time when its reactivity was first assessed and so it has remained overlooked.

Hence, the objectives of this dissertation have been twofold: to measure the H₂ product yield by the ¹⁰B(n,α)⁷Li event at PWR primary loop conditions and thus quantify the H₂O₂ yield by the same event, which is expected to be virtually identical; and to perform a more intensive evaluation of the chemistry induced by the forms of boric acid in the same environment.

The temperature dependence of the radiation chemical yield for H₂ via ¹⁰B(n,α)⁷Li has overall good agreement in comparison with previously attained values from simulation over the temperature range, however there is particularly notable disagreement above 150 °C. This demonstrates that the importance of the bimolecular recombination reaction of e_{aq}^- in contributing to H₂ escape yields from spur and track recombination for High LET water radiolysis is significantly overestimated in current models for reactor chemistry. Additionally, in the process of determining the G-value for H₂ by ¹⁰B(n,α)⁷Li we inadvertently encountered several debilitating sources of interference with our measurement efforts. We are thus in a position to offer cautionary advice in the choices of materials, chemical agents, and procedures which are unwise to be included in similar systems without their proper consideration.

The previously unknown chemical reaction between borate $B(OH)_4^-$ and the hydroxyl radical $\cdot OH$ is confirmed and evaluated. The observed borate reaction with $\cdot OH$ exhibits temperature dependence up to 200 °C which is distinctly Arrhenius, the most likely reaction

process and thus the identity of the product radical were confirmed by *ab initio* calculations, and the radical's spectrum evolution over temperature was adequately characterized. The occurrence of this reaction contradicts a long-held belief by those in the reactor chemistry community that boric acid is an ideal inert chemical additive resulting in no significant reactions with any of the most prevalent and reactive radiolytic species. Our model requires refinement before a confident report on the nature of the borate radical's decay can be made, however, rough estimations of the decay rate for the observed radical have been provided here.

Based on assessment of the quality of data acquired, the breadth and depth of considerations with which they were analyzed, and the results obtained therein being comparable to those from other studies, both the objectives of this work have been met.

9 Contribution to Science

The work entailed herein presents information that is in many ways directly contradictory to established theories/conceptions used in models of the chemical kinetics involved within PWRs which are used to predict realistic material corrosion behavior in reactor systems. Our measurements provide information which could be used to construct more accurate models of the chemistry in these systems. This information could also be applicable to the field of medicine, particularly studies aimed at treating some of the most malignant and aggressive brain tumors such as Glioblastoma Multiforme.

9.1 H₂ generation by ¹⁰B(n,α)⁷Li for Reactor Chemistry Models

The temperature dependence of G(H₂) by ¹⁰B(n,α)⁷Li in water was acquired up to 300 °C, and was determined to have weak temperature dependence. Both the sodium dosimeter and the scavenger system were demonstrated to be satisfactorily effective. G-values obtained here at lower temperatures are shown to be in good agreement with simple estimates from previous simulation results initially used for this quantity in reactor models, with previous experiments, and with recent modeling calculations. Detailed Monte Carlo simulations predicted a dip in G(H₂) above 150 °C due to the catastrophic decrease in the reaction rate for bimolecular recombination of e_{aq}^- . Based on all of the experimental evidence we conclude that the importance of this reaction in spur and track recombination is significantly overestimated in the model which Islam et al. employed at Sherbrooke University.

9.2 Critical Hydrogen Concentration

Determining the CHC is important for corrosion engineering of proposed generation IV supercritical water cooled reactors as well as forecasting proper maintenance upkeep in PWRs. Currently, since the CHC is not yet well defined (Bartels et. al., 2012), power plants dissolve much more hydrogen in their primary flow loops than is necessary to suppress the production of oxidative species. This excess hydrogen can endanger a variety of reactor materials with issues of its own, such as hydrogen embrittlement. The overestimation of the CHC by power plants stems from a lack of information on the chemical kinetics associated with the specific chemical system of the plant. In other words, there has not been enough research done on the contributions different types of radiation have on the concentration of hydrogen in order to accurately predict the minimal hydrogen concentration value necessary to be deliberately added into the coolant of a nuclear reactor, such as the excess dissolved hydrogen being produced from the $^{10}\text{B}(n,\alpha)^7\text{Li}$ event's consequential High LET radiolysis. Our measurements represent a contribution to the information required to construct more accurate models of the chemical kinetics within PWRs to be used to predict realistic material corrosion behavior in reactor systems, and to assist in better quantifying the CHC necessary for suppressing oxidative species.

9.3 Reaction of Borate with $\cdot\text{OH}$ for Reactor Chemistry Models

Through the use of pulse radiolysis, the behavior of radicals following irradiation were elucidated to better evaluate the use of borax as a supposedly chemically inert buffer in aqueous solutions. Several aspects of the borate reaction with $\cdot\text{OH}$ were investigated, including a pH study to identify the initial reactants, multiple attempts at discerning the redox potential of the product radical, as well as determination of the initial reaction's rate constant and the product radical's spectra along with efforts to determine the decay reaction(s) of said product as well as their rates.

Although the deductions from some of these inquiries were less constructive, others culminated in more well-grounded findings, and further analysis is ongoing.

Concerning the borate reaction with $\cdot\text{OH}$, we compare this reaction's rate to the rate of the most prevalent reaction between $\cdot\text{OH}$ and an alternate reactive species present, specifically H_2 . Shown in Figure 105 is a plot of the rate of $\cdot\text{OH}$ reactions up to the maximum temperatures typical within PWRs. The rate constants obtained up to 200 °C for the reaction with borate are assumed to increase with Arrhenius behavior and have thus been extrapolated to higher temperatures. The concentration of borate is calculated from the known 0.15 mol L^{-1} concentration of boric acid listed in EPRI guidelines, their recommended pH of 7.3 representative of PWR primary loop conditions, and the temperature-dependent pK_a for the boric-acid-to-borate equilibrium, along with the typical concentration of 1.6 mmol L^{-1} for H_2 . The rate of the reactions are computed as the product of their rate constant and these concentrations.

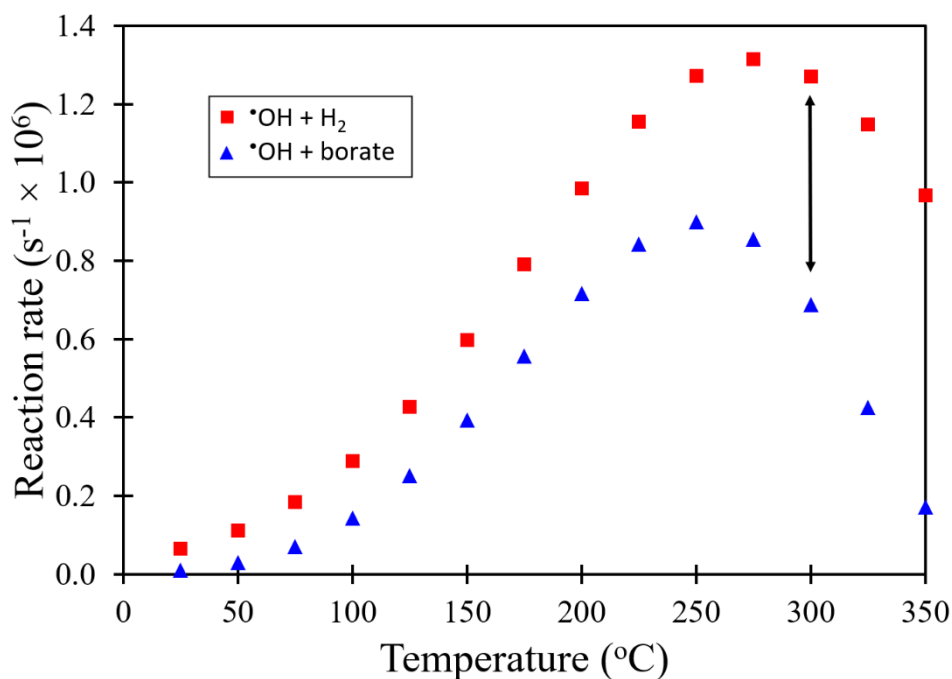


Figure 105. Plot comparing reaction rates for $\cdot\text{OH}$ reacting with H_2 and with borate, over the temperature range experienced in PWRs.

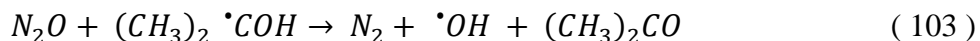
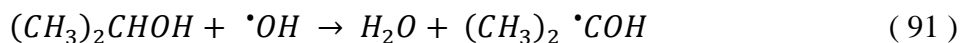
The rate for $\cdot\text{OH}$ reacting with H_2 and with borate is calculated at 300 °C to be 1.3×10^6 and 6.9×10^5 (s^{-1}), respectively. This equates to the borate reaction accounting for greater than a third of all $\cdot\text{OH}$ reactions at these conditions. Our analysis will provide additional data required to construct more accurate models of the chemical kinetics within PWRs concerning this prevalent and reactive chemical form of the boric acid that is so widely used to incorporate the ^{10}B neutron shim in the primary coolant water.

9.4 Contribution to BNCT Research from H_2 generation by $^{10}\text{B}(\text{n},\alpha)^7\text{Li}$

Boron Neutron Capture Therapy has been shown effective for combatting some of the most malignant and aggressive forms of cancer as one of the available modalities utilizing radiation therapy, which is the best (and often the only) viable therapy treatment option for more than half of all cancer patients. Simulations like those by Brandão and Campos in 2009 that used a precise and well-discretized voxel model of a human head demonstrate the feasibility of computational studies which can substitute those performed with real patients. The contribution by boron to the total biological dose rate has been well established as well as the effects of H_2O_2 in the selective destruction of cancer cells. Such simulations for the dosimetric results of BNCT would be improved by additional data for yields of H_2 and H_2O_2 by the $^{10}\text{B}(\text{n},\alpha)^7\text{Li}$ reaction.

9.5 Interference with N_2 for Gamma Dosimetry by Isopropyl

One of the unanticipated sources of interference for our measurements at the RINSC facility was the reaction of the isopropyl radical with the N_2O which was meant to give nitrogen signals interpretable for quantifying the gamma dose. This was no longer feasible due to the release of N_2 in a chain reaction with $(\text{CH}_3)_2 \cdot\text{COH}$ as the carrier, as shown below.



Our experience demonstrates that cautioning against the combination of these chemicals in a system meant for experimentation over an extensive duration is quite appropriate.

9.6 Interference with H₂ Measurements by Corrosion of Cell Materials

Another of the unanticipated sources of interference for our measurements at the RINSC facility was the H₂ produced as a direct result of the oxidative corrosion process undergone by the main tubing materials of both flow cells with the stoichiometry indicated:



Unfortunately, the Zircadyne® 702 cell material was found to undergo an extreme degree of oxidation at temperatures of 200 °C and higher, producing an overabundance of molecular hydrogen in the solution which completely drowned out the H₂ generated by the ¹⁰B(n,α)⁷Li reaction. Although the titanium exhibited much more manageable levels of oxidation, it was still necessary to evaluate the resulting H₂ on the same day as the experimentation at a target temperature. Thus our experience demonstrates the pertinence for cautioning against using these materials even with the proper conditioning treatment to passivate the corrosion rate. Though to be fair, the Zircadyne was not given a chance to be evaluated at high temperatures when not exhibiting what we expect was breakaway corrosion.

10 Future work

10.1 $^{10}\text{B}(\text{n},\alpha)^7\text{Li}$ Chemistry

This is the first study of High LET water radiolysis at high temperatures. In general, it is challenging to study the yields of High LET particles using accelerators. After emission, these heavy ions would then be required to penetrate “windows” in the solution containment cell, and the high pressures needed for liquid studies at high temperature necessitate these windows be thick. As has been discussed, the penetration power of such heavy ions is very weak, and this largely prevents their interaction with the aqueous solution beyond the window. However, neutrons have immensely stronger penetration power and so can ignore any thick outer walls, as is the case in this work. This enables new possibilities in choice for studying alternate product yields by use of an adjusted scavenger system or different target chemical additive. For example, the yields of alternate products from the same $^{10}\text{B}(\text{n},\alpha)^7\text{Li}$ event utilized here could be investigated, such as its yield of e_{aq}^- by adding an acid to react with it to produce $\cdot\text{H}$ and methanol to consume that and give H_2 . Additionally, the prompt physio-chemical H_2 yield could be separated from the recombination event yield by adding a high concentration of NO_3^- nitrate, between 1.0 M and 0.1 M, to prevent any H_2 from forming after the initial event; and this could investigate the curious fact that we see no “dip” in our measured H_2 yield at 200 °C.

10.2 Borate Kinetics

Certainly more work is needed to better illuminate the full chemical mechanism active in the borate solution. We are confident that the borate reacts with $\cdot\text{OH}$, we are fairly convinced that the product radical is $\cdot\text{BO}(\text{OH})_3^-$, and this product has clearly been observed to decay away. There has also been noted the possibility of a reaction with the significantly present O^- that dissociates

from the $\cdot\text{OH}$ in our borax solutions which have been alkalized with NaOH, and further investigation on its reaction with the borate is merited. However, our model of the product being consumed through self-recombination was not sophisticated enough to simulate adequate kinetic behavior for fitting this data. Likely more side reactions such as equilibria along with polyborate radical formation will require consideration, as the borate likely exists in more complex forms than monomers, such as dimers and trimers. The potential for their involvement will need to be reviewed and appropriate models scrutinized once the speciation of the borate under our conditions has been reviewed. Furthermore, the possible presence of any impurities impacting the chemistry should be considered and examined. For example, a likely impurity interred in the NaOH used to alkalize the borax solutions would be carbonate. Despite anticipating this and endeavoring to prevent it, the likelihood is still not dismissible, though an investigation to confirm carbonate's absence or presence is not included in this work.

Additional work is required to push the borate kinetics measurements to higher temperatures. We were limited to 200 °C by concerns of corrosion at higher temperatures when utilizing our stainless steel optical cell. Around the time that this experiment at NDRL was concluding, a new titanium optical cell was under production at the NDRL Machine Shop. This new construction should allow study of the kinetics for the same or similar borated chemical systems at higher temperatures, at least up to 300 °C. The data from such a study would provide further insightful contributions to the scientific community involved in modeling NPP water chemistry, and in particular perhaps elucidate more on the chemical circumstances surrounding the Axial Offset Anomaly phenomenon along with the deposition of corrosion byproducts and the effects of nearby boron-containing species on the incorporation of boron within these deposits.

References

- Allen, C., Borak, T., Tsujii, H. & Nickoloff, J., 2011. Heavy charged particle radiobiology using enhanced biological effectiveness and improved beam focusing to advance cancer therapy. *Mutation Research/Fundamental and Molecular Mechanisms of Mutagenesis*, 711(1-2), pp. 150-157.
- Al-Sheikhly, M., 2017. *Radiation Engineering Manual, for ENMA 655 and ENMA 422*. s.l.:s.n.
- Andrade, C. & Alonso, C., 2001. Andrade, C., and Cruz Alonso. "On-site measurements of corrosion rate of reinforcements. *Corrosion and Building Materials*, 15(2-3), pp. 141-145.
- Applegarth, L., Pye, C., Cox, J. & Tremaine, P., 2017. Raman spectroscopic and ab initio investigation of aqueous boric acid, borate, and polyborate speciation from 25 to 80° C. *Industrial & Engineering Chemistry Research*, 56(47), pp. 13983-13996.
- Armstrong, D. et al., 2015. Standard electrode potentials involving radicals in aqueous solution: inorganic radicals (IUPAC Technical Report). *Pure and Applied Chemistry*, 87(11-12), pp. 1139-1150.
- Arnaut, L., Formosinho, S. & Burrows, H., 2006. Elementary Reactions in Solution. In: *Chemical Kinetics: From Molecular Structure to Chemical Reactivity*. s.l.:Elsevier, pp. 223-250.
- ATI, 2012. *Allegheny Technologies Incorporated Zircadyne Zirconium Technical Data Sheet*. [Online] Available at: <https://www.atimaterials.com/Products/Documents/datasheets/zirconium/alloy/Zircadyne-702-705-2.pdf>
- Auden, E. et al., 2019. Thermal neutron-induced single-event upsets in microcontrollers containing boron-10. *IEEE Transactions on Nuclear Science*, 67(1), pp. 29-37.
- Baes, C. & Mesmer, R., 1976. *The Hydrolysis of Cations*. New York, NY: John Wiley and Sons.
- Baker, C. & Holloway, M., September, 1944. *Note on the origin of the term "barn"*. Los Alamos, USA: Technical Report LAMS-523, Los Alamos National Laboratory.
- Bandura, A. & Lvov, S., 2006. The ionization constant of water over wide ranges of temperature and density. *Journal of physical and chemical reference data*, 35(1), pp. 15-30.
- Bard, A. J. & Faulkner, L. R., 2001. *Electrochemical Methods: Fundamentals and Applications*. New York: John Wiley & Sons, Inc. .
- Bardal, E., 2003. *Corrosion and Protection*. London: Springer Science & Business Media.
- Barr, N. F. & Schuler, R. H., 1959. The dependence of radical and molecular yields on linear energy transfer in the radiation decomposition of 0.8 N sulfuric acid solutions. *Journal of Physical Chemistry*, 63(6), pp. 808-812.
- Bartels, D., Cook, A., Mudaliar, M. & Jonah, C., 2000. Spur decay of the solvated electron in picosecond radiolysis measured with time-correlated absorption spectroscopy. *The Journal of Physical Chemistry A*, 104(88), pp. 1686-1691.

- Bartels, D., Henshaw, J. & Sims, H., 2013. Modeling the critical hydrogen concentration in the AECL test reactor. *Radiation Physics and Chemistry*, Volume 82, pp. 16-24.
- Bartels, D. et al., 2012. *Laboratory and Modeling Studies in Search of the Critical Hydrogen Concentration*. France, French Nuclear Energy Society - SFEN, 'Materials Science and Technology, Non Destructive Testing, Chemistry' Technical Section.
- Barth, R., Soloway, A. & Fairchild, R., 1990. Boron Neutron Capture Therapy for cancer. *Scientific American*, 263(4), pp. 100-107.
- Barth, R., Soloway, A., Fairchild, R. & Brugger, R., 1992. Boron neutron capture therapy for cancer - Realities and prospects. *Cancer*, 70(12), pp. 2995-3007.
- BIPM, Taylor, B. & Thompson, A., 2001. *The International System of Units (SI)*. July 2001 ed. Gaithersburg(MA): US Department of Commerce, Technology Administration, National Institute of Standards and Technology.
- Bjergbakke, E., Sehested, K., Rasmussen, O. & Christensen, H., 1984. *Input Files for Computer Simulation of Water Radiolysis*, DK 4000 Roskilde, Denmark: Risø National Laboratory.
- Blasdale, W. & Slansky, C., 1939. The solubility curves of boric acid and the borates of sodium. *Journal of the American Chemical Society*, 61(4), pp. 917-920.
- Brandão, S. F. & Campos, T. P. R., 2009. *Dosimetric Analysis of BCNT - Boron Neutron Capture Therapy - Coupled to Cf-252 Brachytherapy*. Rio de Janeiro, Brazil, s.n.
- Brown, D. A. et al., 2018. ENDF/B-VIII.0: The 8th Major Release of the Nuclear Reaction Data Library with CIELO-project Cross Sections, New Standards and Thermal Scattering Data. *Nuclear Data Sheets*, 2, Volume 148, pp. 1-142.
- Butarbutar, S. L. et al., 2013. On the Temperature Dependence of the Rate Constant of the Bimolecular Reaction of Two Hydrated Electrons. *Atom Indonesia*, Volume 39, pp. 51-56.
- Butson, M. & Niroomand-Rad, A., 2017. Historical Background, Development, and Construction of Radiochromic Films. In: *Radiochromic Film*. s.l.:CRC Press, pp. 7-32.
- Buxton, G., Greenstock, C., Helman, W. & Ross, A., 1988. Critical Review of rate constants for reactions of hydrated electrons, hydrogen atoms and hydroxyl radicals ($\cdot\text{OH}/\cdot\text{O}^-$) in aqueous solution. *Journal of Physical and Chemical Reference Data*, 17(2), pp. 513-886.
- Buxton, G. & Sellers, R., 1987. Reactivity of the hydrated electron and the hydroxyl radical with boric acid in aqueous solutions. *International Journal of Radiation Applications and Instrumentation. Part C. Radiation Physics and Chemistry*, 29(2), pp. 137-140.
- Buxton, G., Wood, N. & Dyster, S., 1988. Ionisation constants of OH and HO₂ in aqueous solution up to 200 C. A pulse radiolysis study. *Journal of the Chemical Society, Faraday Transactions 1: Physical Chemistry in Condensed Phases*, 84(4), pp. 1113-1121.
- Buxton, G., Wood, N. & Dyster, S., 1988. Ionisation constants of OH and HO₂ in aqueous solution up to 200 C: A pulse radiolysis study. *Journal of the Chemical Society, Faraday Transactions 1: Physical Chemistry in Condensed Phases*, 84(4), pp. 1113-1121.
- Canberra Industries, Inc., 2017. *Model S574 LabSOCS Calibration Software by Mirion Technologies, Inc.* [Online]

- Available at: <https://www.gamdata.se/assets/Uploads/LabSOCS-SS-C40167.pdf>
[Accessed May 2022].
- Canberra Industries, Inc., 2017. *Spectrum Analysis by Mirion Technologies*. [Online]
Available at: <https://www.canberra.com/literature/fundamental-principles/pdf/Spectrum-Analysis.pdf>
[Accessed May 2022].
- Carlson, A. D., 2011. The Neutron Cross Section Standards, Evaluations and Applications. *Metrologia*, 12, 48(6), p. S328.
- Carlson, A. D. et al., 2018. Evaluation of the Neutron Data Standards. *Nuclear Data Sheets*, 2, Volume 148, pp. 143-188.
- Casolaro, P. et al., 2019. Real-time dosimetry with radiochromic films. *Scientific Reports*, 9(1), p. 5307.
- Chatterjee, A. & Holley, W., 1990. A general theory of DNA strand break production by direct and indirect effects. *Radiation Protection Dosimetry*, 31(1-4), pp. 241-247.
- Christensen, H., 1995. Remodeling of the oxidant species during radiolysis of high-temperature water in a pressurized water reactor. *Nuclear Technology*, 109(3), pp. 373-382.
- Christensen, H., 2006. *Fundamental Aspects of Water Coolant Radiolysis*, Stockholm, Sweden: Swedish Nuclear Power Inspectorate.
- Christensen, H. & Sehested, K., 1986. The hydrated electron and its reactions at high temperatures. *The Journal of Physical Chemistry*, 90(1), pp. 186-190.
- Cline, J., Jonah, C. & Bartels, D., 2002. The secondary response distortion in transient absorption spectroscopy. *Review of Scientific Instruments*, 73(11), pp. 3908-3915.
- Coderre, J. & Morris, G., 1999. The radiation biology of boron neutron capture therapy. *Radiation Research*, 151(1), pp. 1-18.
- Cohen, P., 1974. Heat and mass transfer for boiling in porous deposits with chimneys. *AIChE Symposium Series*, 70(138), pp. 71-80.
- Collinson, E., Dainton, F., Smith, D. & Tazuke, S., 1962. Evidence for the negative charge on the "Hydrogen Atom" formed by the action of ionising radiation on aqueous systems. *In Proceedings of the Chemical Society of London*, p. 140.
- Cox, B., 2005. Some thoughts on the mechanisms of in-reactor corrosion of zirconium alloys. *Journal of Nuclear Materials*, 336(2-3), pp. 331-368.
- Crow, M. et al., 1995. Thermal neutron measurements of the Rhode Island Nuclear Science Center reactor after conversion to a compact low enriched uranium core. *Nuclear Instruments and Methods in Physics Research Section A: Accelerators, Spectrometers, Detectors and Associated Equipment*, 365(2-3), pp. 433-445.
- De Laeter, J. et al., 2003. Atomic weights of the elements. Review 2000 (IUPAC Technical Report). *Pure and Applied Chemistry*, 75(6), pp. 683-800.
- Deshon, J., 2004. *PWR Axial Offset Anomaly (AOA) Guidelines, Revision 1, Report No. 1008102*, Palo Alto, CA: EPRI.

- Deshon, J., 2005. *Modeling PWR Fuel Corrosion Product Deposition and Growth Process*, Report No. 1011743, Palo Alto, CA: EPRI.
- Dietz, T. C. et al., 2021. H₂ production in the ¹⁰B(n,α)⁷Li reaction in water. *Radiation Physics and Chemistry*, 3, Volume 180, p. 109319.
- Dwivedi, S. & Vishwakarma, M., 2018. Hydrogen embrittlement in different materials: a review. *International Journal of Hydrogen Energy*, 43(46), pp. 21603-21616.
- Edwards, E. et al., 2007. An apparatus for the study of high temperature water radiolysis in a nuclear reactor: Calibration of dose in a mixed neutron/gamma radiation field. *Review of Scientific Instruments*, 78(12), p. 124101.
- Eliaz, N. & Latanision, R., 2007. Preventative Maintenance and Failure Analysis of Aircraft Components. *Corrosion Reviews*, 25(1-2), pp. 107-144.
- Elliot, A., 1994. Rate constants and G-values for the simulation of the radiolysis of light water over the range 0-300 deg C (No. AECL--11073). *Atomic Energy of Canada Ltd.*
- Elliot, A. & Bartels, D., 2009. *The reaction set, rate constants and g-values for the simulation of the radiolysis of light water over the range 20 deg to 350 deg C based on information available in 2008*. s.l.:Atomic Energy of Canada Limited.
- Elliot, A. & McCracken, D., 1989. Effect of temperature on O- reactions and equilibria: A pulse radiolysis study. *International Journal of Radiation Applications and Instrumentation. Part C. Radiation Physics and Chemistry*, 33(1), pp. 69-74.
- Elliot, A. & Stuart, R., 2008. *Coolant Radiolysis Studies in the High Temperature U-2 Loop in the NRU Reactor*. AECL 153-127160-440-003, Chalk River, Canada: Atomic Energy of Canada, Ltd..
- Ensor, B. et al., 2022. Investigation of breakaway corrosion observed during oxide growth in pure and low alloying element content Zr exposed in water at 360 C. *Journal of Nuclear Materials*, Volume 558, p. 153358.
- EPRI, 1999. *Pressurized Water Reactor Primary Water Chemistry Guidelines: Volume 1, Revision 4*, Palo Alto, CA, USA: Electric Power Research Institute.
- Far West Technology, Inc., 2002. *FWT-60 Series Radiachromic Dosimeters*. [Online] Available at: <https://www.fwt.com/racm/fwt60ds.htm> [Accessed May 2022].
- Ferguson, J., Arcis, H. & Tremaine, P., 2019. Thermodynamics of polyborates under hydrothermal conditions: formation constants and limiting conductivities of triborate and diborate. *Journal of Chemical & Engineering Data*, 64(10), pp. 4430-4443.
- Ferradini, C. & Jay-Gerin, J., 1998. Does multiple ionization intervene for the production of HO₂ radicals in high-LET liquid water radiolysis?. *Radiation Physics and Chemistry*, 51(3), pp. 263-268.
- Fontana, M. G., 2005. *Corrosion Engineering*. 3rd ed. New York: McGraw-Hill Book Company.
- Frattini, P. et al., 2001. Axial offset anomaly: coupling PWR primary chemistry with core design. *Nuclear Energy*, 40(2), pp. 123-135.

- George, K., Wang, S., Nestic, S. & De Waard, K., 2004. Modeling of CO₂ corrosion of mild steel at high pressures of CO₂ and in the presence of acetic acid. *NACE Corrosion*.
- Guerin, S. et al., Submitted 2023, under review. H₂ Generation by the ¹⁰B(n,α)⁷Li Reaction in High Temperature Water. *Radiation Physics and Chemistry*.
- Guzonas, D. et al., 2017. *Materials and Water Chemistry for Supercritical Water-Cooled Reactors*. s.l.:Woodhead Publishing.
- Hada, M. & Georgakilas, A., 2008. Formation of clustered DNA damage after high-LET irradiation: A review. *Journal of Radiation Research*, 49(3), pp. 203-210.
- Hancock, P., 1987. Vanadic and chloride attack of superalloys. *Materials Science and Technology*, 3(7), pp. 536-544.
- Hay, R., 2000. The Kinetic Background. In: *Reaction Mechanisms of Metal Complexes*. Coll House, England: Horwood Publishing, pp. 35-57.
- Hendler, R. & Shrager, R., 1994. Deconvolutions based on singular value decomposition and the pseudoinverse: a guide for beginners. *Journal of Biochemical and Biophysical Methods*, 28(1), pp. 1-33.
- Henshaw, J. et al., October 2006. The Chemistry of Fuel Crud Deposits and Its Effect on AOA in PWR Plants. In *Proc. Int. Conf. on Water Chemistry of Nuclear Reactors System 2006*.
- Henshaw, J. et al., 2006. A model of chemistry and thermal hydraulics in PWR fuel crud deposits. *Journal of nuclear materials*, 353(1-2), pp. 1-11.
- Holley, W., C. A. & Magee, J., 1990. Production of DNA strand breaks by direct effects of heavy charged particles. *Radiation Research*, 121(2), pp. 161-168.
- Irvine, T. & Hartnett, J., 1976. *Steam and Air Tables in SI Units: Including Data for Other Substances with a Separate Mollier Chart for Steam*. First ed. Washington: Hemisphere Publishing Corporation.
- Islam, M. M. et al., 2017. Monte Carlo track chemistry simulations of the radiolysis of water induced by the recoil ions of the ¹⁰B(n,α)⁷Li nuclear reaction. 1. Calculation of the yields of primary species up to 350 °C. *RSC Advances*, 7(18), pp. 10782-10790.
- Janik, D., Janik, I. & Bartels, D. M., 2007. Neutron and β/γ radiolysis of water up to supercritical conditions. 1. β/γ yields for H₂, H atom, and hydrated electron. *Journal of Physical Chemistry A*, 111(32), pp. 7777-7786.
- Janik, I., Bartels, D. & Jonah, C., 2007. Hydroxyl radical self-recombination reaction and absorption spectrum in water up to 350 C. *The Journal of Physical Chemistry A*, 111(10), pp. 1835-1843.
- Jenks, G. H. & Griess, J. C., 1967. *Water Chemistry in Pressurized and Boiling Water Power Reactors (No. ORNL-4173)*, Oak Ridge, Tennessee: Oak Ridge National Laboratory.
- Johnson, K., 2009. Fitting enzyme kinetic data with KinTek global kinetic explorer. *Methods in Enzymology*, Volume 467, pp. 601-626.
- Johnson, K., 2018. *KinTek Global Kinetic Explorer, Instructions for Version 8.0*. Austin, TX: KinTek Corporation.

- Johnson, K., Simpson, Z. & Blom, T., 2009. Global kinetic explorer: a new computer program for dynamic simulation and fitting of kinetic data. *Analytical Biochemistry*, 387(1), pp. 20-29.
- Jonah, C., 2010. An incomplete history of radiation chemistry. In: *Recent trends in radiation chemistry*. Singapore: World Scientific, pp. 1-20.
- Kanjana, K., Haygarth, K. S., Wu, W. & Bartels, D. M., 2013. Laboratory studies in search of the critical hydrogen concentration. *Radiation Physics and Chemistry*, 1, 82(1), pp. 25-34.
- Kanjana, K., Haygarth, K., Wu, W. & Bartels, D., 2013. Laboratory studies in search of the critical hydrogen concentration. *Radiation Physics and Chemistry*, Volume 82, pp. 25-34.
- Kanjana, K., Walker, J. & Bartels, D., 2015. Hydroxymethyl radical self-recombination in high-temperature water. *The Journal of Physical Chemistry A*, 119(10), pp. 1830-1837.
- Katzarov, I. H. & Paxton, A. T., 2017. Hydrogen embrittlement II. Analysis of hydrogen-enhanced decohesion across (111) planes in α -Fe. *Physical Review Materials*, 1(3), p. 033603.
- Kelly, R., Scully, J., Shoesmith, D. & Buchheit, R., 2002. *Electrochemical Techniques in Corrosion Science and Engineering*. New York: CRC Press.
- Koch, G. et al., 2005. Cost of Corrosion in the United States. In: *Handbook of Environmental Degradation of Materials*. s.l.:William Andrew Publishing, pp. 3-24.
- Kondev, F. et al., 2021. The NUBASE2020 evaluation of nuclear physics properties. *Chinese Physics C*, 45(3), p. 030001.
- Kracek, F., Morey, G. & Merwin, H., 1938. *American Journal of Science A*, Volume 35, pp. 143-171.
- Kusumoto, T. & Ogawara, R., 2019. Radiation Chemical Yield of Hydroxyl Radicals for Accelerator-based Boron Neutron Capture Therapy: Dose Assessment of $^{10}\text{B}(n,\alpha)^7\text{Li}$ Reaction Using Coumarin-3-Carboxylic Solution. *Radiation Research*, 5, 191(5), pp. 460-465.
- LaVerne, J. A., 2000. Track Effects of Heavy Ions in Liquid Water. *Radiation Research*, 153(5), pp. 487-496.
- LaVerne, J. A., 2004. Radiation Chemical Effects of Heavy Ions. In: *Charged Particle and Photon Interactions with Matter*. New York: Marcel Dekker, Inc. , pp. 403-429.
- LaVerne, J. A. & Schuler, R. H., 1987. Radiation chemical studies with heavy ions: Oxidation of ferrous ion in the Fricke dosimeter. *Journal of Physical Chemistry*, 91(22), pp. 5770-5776.
- LaVerne, J. & Pimblott, S., 2000. New Mechanism for H₂ Formation in Water. *Journal of Physical Chemistry A*, 104(44), pp. 9820-9822.
- Lefort, M., 1958. Radiation Chemistry. *Annual Review of Physical Chemistry*, 9(1), pp. 123-156.
- Lemmon, E., Bell, I., Huber, M. & McLinden, M., 2021. Thermophysical Properties of Fluid Systems. In: W. Mallard & P. Linstrom, eds. *NIST Chemistry WebBook, NIST Standard*

- Reference Database Number 69. Gaithersburg, MD 20899: National Institute of Standards and Technology.
- Lin, C., 2000. Hydrogen water chemistry technology in boiling water reactors. *Nuclear Technology*, 130(1), pp. 59-70.
- Lin, C. et al., 1991. Decomposition of hydrogen peroxide in aqueous solutions at elevated temperatures. *International Journal of Chemical Kinetics*, 23(11), pp. 971-987.
- Lisovskaya, A. & Bartels, D., 2019. Reduction of CO₂ by hydrated electrons in high temperature water. *Radiation Physics and Chemistry*, Volume 158, pp. 61-63.
- Lisovskaya, A., Kanjana, K. & Bartels, D., 2020. One-electron redox kinetics of aqueous transition metal couples Zn^{2+/+}, Co^{2+/+}, and Ni^{2+/+} using pulse radiolysis. *Physical Chemistry Chemical Physics*, 22(34), pp. 19046-19058.
- Lundgren, K., Wijkström, H. & Wikmark, G., 2004. *Recent developments in the LwrChem radiolysis code*. Intl. Conf. water Chem. Nucl. Reactor Systems, San Fransisco.
- Macdonald, D., 1992. Viability of hydrogen water chemistry for protecting in-vessel components of boiling water reactors. *Corrosion*, 48(3), pp. 194-205.
- Marin, T. W. et al., 2007. Recombination of the Hydrated Electron at High Temperature and Pressure in Hydrogenated Alkaline Water. *Journal of Physical Chemistry A*, Volume 111, pp. 11540-11551.
- MatWeb, 2023. *MatWeb Material Property Data for Titanium Grade 2*. [Online] Available at: <https://www.matweb.com/search/DataSheet.aspx?MatGUID=24293fd5831941ec9fa01dc994973c7&ckck=1> [Accessed 24 February 2023].
- Mezyk, S. & Bartels, D., 1997. Temperature dependence of hydrogen atom reaction with nitrate and nitrite species in aqueous solution. *The Journal of Physical Chemistry A*, 101(35), pp. 6233-6237.
- Mitsui, j. & Siguyama, K., 1973. Neutron Thermalization in Graphite. *Journal of Nuclear Science and Technology*, 10(1), pp. 1-9.
- Morozov, A., Pityk, A., Sahipgareev, A. & Shlepkin, A., 2018. Experimental study of the thermophysical properties of boric acid solutions at the parameters typical of the WWER emergency mode. *Journal of Physics: Conference Series*, 1128(1), p. 012103.
- Morozov, A., Sahipgareev, A., Shlepkin, A. & Soshkina, A., 2020. Determination of the physicochemical properties of boric acid for VVER emergency modes. *IOP Conference Series: Materials Science and Engineering*, 791(1), p. 012016.
- Morozov, A. et al., 2019. Experimental determination of the thermophysical properties of boric acid for VVER emergency regimes. *Atomic energy*, Volume 125, pp. 178-184.
- Mozumder, A., 1999. *Fundamentals of Radiation Chemistry*. San Diego: Academic Press.
- Nedunchezian, K., Aswath, N., Thirupathy, M. & Thirugnanamurthy, S., 2016. Boron neutron capture therapy - A literature review. *Journal of clinical and diagnostic research*, 10(12), p. ZE01.

- Nishina, K. et al., 1979. Neutron diffusion and thermalization parameters; Measurements with graphite and theoretical review. *Memoirs of the Faculty of Engineering, Nagoya University*, 31(1), pp. 47-96.
- NIST, 2019. *CODATA Internationally recommended 2018 values of the Fundamental Physical Constants*. [Online]
Available at: <https://physics.nist.gov/cuu/Constants/index.html>
[Accessed 9 February 2023].
- NIST, 2022. *Atomic Weights and Isotopic Compositions for All Elements*. [Online]
Available at: https://physics.nist.gov/cgi-bin/Compositions/stand_alone.pl
[Accessed January 2023].
- Novelli, F. et al., 2023. The birth and evolution of solvated electrons in the water. *Proceedings of the National Academy of Sciences*, 120(8), p. e2216480120.
- Özbay, D., 2016. *Joint innovative training and teaching/learning program in enhancing development and transfer knowledge of application of ionizing radiation in materials processing*. Reims, France: Hacettepe University Department of Chemistry.
- Peng, S. & Zeng, Z., 2015. Peng, Shangbi, and Zhaoxiong Zeng. "An experimental study on the internal corrosion of a subsea multiphase pipeline. *Petroleum*, 1(1), pp. 75-81.
- Perez, N., 2004. *Electrochemistry and Corrosion Science*. Boston: Kluwer Academic Publishers.
- Pokrovski, G., Schott, J. & Sergeev, A., 1995. Experimental determination of the stability constants of $(\text{NaSO}_4)^-$ and $(\text{NaB}(\text{OH})_4)_0$ in hydrothermal solutions using a new high-temperature sodium-selective glass electrode — Implications for boron isotopic fractionation. *Chemical Geology*, 124(3-4), pp. 253-265.
- Price, G., 1964. A note of the measurement of the transport mean free path of thermal neutrons in graphite by a poison method. *Nuclear Science and Engineering*, 18(3), pp. 410-412.
- Raiman, S., Bartels, D. & Was, G., 2017. Radiolysis driven changes to oxide stability during irradiation-corrosion of 316L stainless steel in high temperature water. *Journal of Nuclear Materials*, Volume 493, pp. 40-52.
- RIAEC, 1992. *Safety Analysis Report for the Low Enriched Fuel Conversion of the Rhode Island Nuclear Science Center Research Reactor*, Narragansett, RI 02882-1197: Rhode Island Atomic Energy Commission.
- RIAEC, January 2017. *Safety Evaluation Report: Renewal of the Facility Operating License for the Rhode Island Nuclear Science Center Reactor. License No. R-95. Docket No. 50-193*, Rhode Island Atomic Energy Commission: United States Nuclear Regulatory Commission, Office of Nuclear Reactor Regulation.
- RINSC, 2023. *State of Rhode Island: Rhode Island Nuclear Science Center - Experimental Facilities*. [Online]
Available at: <http://www.rinrc.ri.gov/research/>
[Accessed 21 February 2023].
- Roentgen, W., 1896. Eine neue Art von Strahlen (On a new kind of rays). In: *Vorläufige Mittheilung Aus den Sitzungsberichten der Würzburger Physik-medice Gesellschaft*

- Würzburg. Würzburg: Stahel'sche K.B. Hof- und Universitätsbuchund Kunsthandlung, pp. 137-147.
- Rutherford, E., 1910. Radium standards and nomenclature. *Nature*, 84(2136), pp. 430-431.
- Sanguanmith, S. et al., 2011. Low-linear Energy Transfer Radiolysis of Liquid Water at Elevated Temperatures up to 350 Degrees C: Monte-Carlo Simulations. *Chemical Physics Letters*, Volume 508, pp. 224-230.
- Sasidharanpillai, S., Arcis, H., Trevani, L. & Tremaine, P., 2019. Triborate formation constants and polyborate speciation under hydrothermal conditions by Raman spectroscopy using a titanium/sapphire flow cell. *The Journal of Physical Chemistry B*, 123(24), pp. 5147-5159.
- Satoh, T. et al., 2004. Effects of hydrogen peroxide on corrosion of stainless steel, (I) improved control of hydrogen peroxide remaining in a high temperature high pressure hydrogen peroxide loop. *Journal of Nuclear Science and Technology*, 41(5), pp. 610-618.
- Sauerwein, W., Wittig, A., Moss, R. & Nakagawa, Y., 2012. *Neutron Capture Therapy - Principles and Applications*. Berlin Heidelberg (Germany): Springer-Verlag Berlin Heidelberg.
- Savolainen, J. et al., 2014. Direct observation of the collapse of the delocalized excess electron in water. *Nature Chemistry*, 6(8), pp. 697-701.
- Schmidt, K. & Bartels, D., 1995. Lack of ionic strength effect in the recombination of hydrated electrons: $e_{aq}^- + e_{aq}^- \rightarrow 2OH^- + H_2$. *Chemical Physics*, 190(1), pp. 145-152.
- Sekine, T. & Baba, H., 1980. *A study of Reactor-Neutron-Induced Reactions: Double Neutron Capture Process and the Systematics of the (n,2n) Reaction*, Japan: Japan Atomic Energy Research Institute.
- Sidhu, T., Agrawal, R. & Prakash, S., 2005. Hot corrosion of some superalloys and role of high-velocity oxy-fuel spray coatings - a review. *Surface & Coatings Technology*, 198(1-3), pp. 441-446.
- Slater, J., 1964. Atomic radii in crystals. *The Journal of Chemical Physics*, 41(10), pp. 3199-3204.
- Spinks, J. & Woods, R., 1990. *An Introduction to Radiation Chemistry*. Third ed. s.l.:John Wiley & Sons, Inc..
- Sterniczuk, M. & Bartels, D. M., 2016. Source of Molecular Hydrogen in High-Temperature Water Radiolysis. *Journal of Physical Chemistry A*, Volume 120, pp. 200-209.
- Sterniczuk, M. et al., 2016. Low LET radiolysis escape yields for reducing radicals and H₂ in pressurized high temperature water. *Radiation Physics and Chemistry*, Volume 121, pp. 35-42.
- Swiatla-Wojcik, D. & Buxton, G., 1995. Modeling of Radiation Spur Processes in Water at Temperatures up to 300-Degrees-C. *Journal of Physical Chemistry*, 99(29), pp. 11464-11471.

- Swiatla-Wojcik, D. & Buxton, G., 1998. Modelling of linear energy transfer effects on track core processes in the radiolysis of water up to 300 degrees C. *Journal of the Chemical Society-Faraday Transactions*, Volume 94.
- Takahashi, K., Cline, J., Bartels, D. & Jonah, C., 2000. Design of an optical cell for pulse radiolysis of supercritical water. *Review of Scientific Instruments*, 71(9), pp. 3345-3350.
- Takahashi, K. et al., 2004. Reaction rates of the hydrated electron with N₂O in high temperature water and potential surface of the N₂O⁻ anion. *Chemical Physics Letters*, 383(5-6), pp. 445-450.
- Tang, Y. & Ballarini, R., 2011. A theoretical analysis of the breakdown of electrostrictive oxide film on metal. *Journal of the Mechanics and Physics of Solids*, 59(2), pp. 178-193.
- Tehan, T., 2000. *The Rhode Island Nuclear Science Center Conversion from HEU to LEU Fuel*, Narragansett, RI (US): Rhode Island Nuclear Science Center.
- Thermo Electron Corporation, 2003. *Total Organic Carbon (TOC) in Drinking Water, Application Note: EN-03001*. [Online] Available at: [http://www.apolloinstruments.fr/AutoFiles/doc/5012_AN_EN-03001_TOC_in_Drinking_water\[1\].pdf](http://www.apolloinstruments.fr/AutoFiles/doc/5012_AN_EN-03001_TOC_in_Drinking_water[1].pdf) [Accessed 27 February 2023].
- Torche, F. & Marignier, J., 2016. Direct evaluation of the molar absorption coefficient of hydrated electron by the isosbestic point method. *The Journal of Physical Chemistry B*, 120(29), pp. 7201-7206.
- Turner, J., 2008. *Atoms, Radiation, and Radiation Protection*. Third, Completely Revised and Enlarged ed. Weinheim, Germany: John Wiley and Sons.
- University of Cambridge, D. o. M. S. & M., 2023. *Materials for Nuclear Power Generation - Moderators*. [Online] Available at: https://www.doitpoms.ac.uk/tlplib/nuclear_materials/moderators.php [Accessed 11 February 2023].
- Visco, G., Campanella, L. & Nobili, V., 2005. Organic carbons and TOC in waters: an overview of the international norm for its measurements. *Microchemical Journal*, 79(1-2), pp. 185-191.
- Wang, P. et al., 2013. Thermodynamic modeling of boric acid and selected metal borate systems. *Pure and Applied Chemistry*, 85(11), pp. 2117-2144.
- Wang, S., Zhang, Z., Miao, L. & Li, Y., 2022. Boron neutron capture therapy: Current status and challenges. *Frontiers in Oncology*, Volume 12, p. 788770.
- Ward, J., Evans, J., Limoli, C. & Calabro-Jones, P., 1987. Radiation and hydrogen peroxide induced free radical damage to DNA. *The British Journal of Cancer*, Volume Supplement 8, p. 105.
- Was, G. & Allen, T., 2019. Corrosion Issues in Current and Next-Generation Nuclear Reactors. *Structural Alloys for Nuclear Energy Applications*, pp. 211-246.
- Was, G., Ashida, Y. & Andresen, P., 2011. Irradiation-assisted stress corrosion cracking. *Corrosion Reviews*, 29(1-2), pp. 7-49.

- Werner, C., 2017. *MCNP Users Manual-Code Version 6.2 (Report LA-UR-17-29981)*, New Mexico: Los Alamos National Laboratory.
- Whitham, K. et al., 1996. Linear accelerator for radiation chemistry research at Notre Dame. *In: IEEE Proceedings Particle Accelerator Conference and International Conference on High Energy Accelerators, Dallas, TX*, Volume 1, pp. 131-133.
- Yokohata, A. & Tsuda, S., 1974. A Solvated Electron Formed from the Water by the Irradiation of the Recoil Particles of $^{10}\text{B}(n,\alpha)^7\text{Li}$ and $^6\text{Li}(n,\alpha)\text{T}$. *Bulletin of the Chemical Society of Japan*, 47(11), pp. 2869-2870.
- Yokoyama, K. et al., 2006. Pharmacokinetic Study of BSH and BPA in Simultaneous Use for BNCT. *Journal of Neuro-Oncology*, 7, 78(3), pp. 227-232.
- Zakaria, A. et al., 2021. Yield of the Fricke dosimeter irradiated with the recoil α and Li ions of the $^{10}\text{B}(n,\alpha)^7\text{Li}$ nuclear reaction: Effects of multiple ionization and temperature. *Canadian Journal of Chemistry*, 99(4), pp. 425-435.
- Zangirolami, D., Oliveira, A. & Ferreira, A., 2010. Thermal and epithermal neutron fluence rates in the irradiation facilities of the TRIGA IPR-R1 nuclear reactor. *Brazilian Journal of Physics*, Volume 40, pp. 47-51.
- Zhou, Y., Fang, C., Fang, Y. & Zhu, F., 2011. Polyborates in aqueous borate solution: a Raman and DFT theory investigation. *Spectrochimica Acta Part A: Molecular and Biomolecular Spectroscopy*, 83(1), pp. 82-87.
- Zieliński, A. & Sobieszczyk, S., 2011. Hydrogen-enhanced degradation and oxide effects in zirconium alloys for nuclear applications. *International Journal of Hydrogen Energy*, 36(14), pp. 8619-8629.
- Zimbrick, J., 2002. Radiation chemistry and the Radiation Research Society: a history from the beginning. *Radiation Research*, 158(2), pp. 127-140.